Explosions of Rotating White Dwarfs

Dissertation zur Erlangung des
naturwissenschaftlichen Doktorgrades
der Bayerischen Julius-Maximilians-Universität Würzburg

vorgelegt von

Jan M. M. Pfannes

aus Dettelbach

Würzburg 2006

Eingereicht am 25.08.2006
bei der Fakultät für Physik und Astronomie

1. Gutachter: Prof. Dr. Jens Niemeyer
2. Gutachter: Prof. Dr. Karl Mannheim
der Dissertation

1. Prüfer: Prof. Dr. Jens Niemeyer
2. Prüfer: Prof. Dr. Karl Mannheim
3. Prüfer: Prof. Dr. Friedrich Reinert
im Promotionskolloquium

Tag des Promotionskolloquiums: 13.12.2006

Doktorurkunde ausgehändigt am ____________________

There's always one more bug This apothegm – well known as part of Murphy's Law – does not apply for computational physics. If not errorless, a working code contains at least two or yet an even number of bugs, each compensating for one another.

Contents

1 Introduction 9

I Theory 11

2 Type Ia supernovae 13
- 2.1 Standard supernovae Ia — “Branch normals” . . . 13
  - 2.1.1 Spectra . . . 13
  - 2.1.2 Light curve . . . 14
  - 2.1.3 Rate . . . 14
- 2.2 “Peculiar” supernovae Ia . . . 14
  - 2.2.1 Phillips relation . . . 16
  - 2.2.2 Evolutionary effects . . . 16
- 2.3 Progenitor scenarios . . . 16
  - 2.3.1 Single-degenerate scenario . . . 17
  - 2.3.2 Double-degenerate scenario . . . 19
- 2.4 Impact on cosmology . . . 19

3 Presupernova evolution of accreting white dwarfs 21
- 3.1 Work on accreting white dwarfs . . . 21
- 3.2 Role of instabilities in the angular momentum transport . . . 22
  - 3.2.1 Eddington-Sweet circulations . . . 22
  - 3.2.2 Shear instabilities . . . 22
  - 3.2.3 Goldreich, Schubert and Fricke instability . . . 23
  - 3.2.4 Magnetic instabilities . . . 23
- 3.3 Physical assumptions . . . 23
- 3.4 Results . . . 24
  - 3.4.1 Thermal evolution of accreting white dwarfs . . . 24
  - 3.4.2 White dwarf spin and angular momentum transport . . . 24
- 3.5 Influence of physical assumptions . . . 27
- 3.6 Limitations of the accretion study . . . 28
- 3.7 Evolution scenarios: loss of angular momentum . . . 29

4 Ignition and propagation of the thermonuclear flame 31
4.1 Initiation of the thermonuclear runaway 31
4.2 Multi- vs. single-spot ignition scenario 32
4.3 Burning modes: detonation vs. deflagration 34
4.3.1 Detonations in the context of type Ia supernovae 34
4.3.2 Deflagrations in the context of type Ia supernovae 35
4.4 Instabilities of thermonuclear flames 36
4.4.1 Rayleigh-Taylor instability 36
4.4.2 Kelvin-Helmholtz instability 37
4.5 Turbulent combustion 37
4.5.1 Turbulent eddy cascade 38
4.5.2 Flamelet burning regime 38
4.5.3 Distributed reaction zone regime 38
4.5.4 Turbulent combustion in type Ia supernovae 39

5 Explosion model formulation 41
5.1 Hydrodynamics 41
5.1.1 Eulerian and Lagrangian coordinates 41
5.1.2 The Reynolds theorem 42
5.1.3 Equations for reactive ideal fluids 44
5.2 Barotropic rotators in a state of permanent rotation 46
5.3 White dwarf matter 48
5.4 Nuclear reactions in white dwarf matter 50

6 Pure deflagrations — the actual state 53
6.1 Enhancements in modelling type Ia supernovae 53
6.2 Influence of physical parameters 56
6.3 Limitations of the pure deflagration model 58

II Numerics 61

7 The combustion model 63
7.1 Burning front modelling 63
7.1.1 The level set method 63
7.1.2 Determination of the burning velocity 64
7.2 Reaction network 66
7.3 Equation of state 68
7.4 Tracer particles 69
7.4.1 Recording the explosion in the moving framework 69
7.4.2 Implementation details 69

8 Initiation of the thermonuclear explosion 71
- 8.1 Static ignition . . . 71
- 8.2 Ignitions at different instants in time . . . 72
  - 8.2.1 Stochastic ignition . . . 72
  - 8.2.2 Implementation details . . . 74

9 Comoving hybrid grid 77
- 9.1 Moving grid transport theorem . . . 77
- 9.2 Grid geometry . . . 79
  - 9.2.1 Implementation details . . . 80
  - 9.2.2 Following a grid expansion . . . 81
- 9.3 Homologous expansion phase . . . 85
- 9.4 Test for hydrostatic stability . . . 86

10 Gravity 89
- 10.1 Gravity in rotating white dwarfs . . . 89
- 10.2 Multipole expansion of Poisson's equation . . . 90
- 10.3 Implementation details . . . 92
- 10.4 The lowest possible expansion order . . . 93

11 The initial rotator model 99
- 11.1 Stationary equilibrium in integral form . . . 99
- 11.2 Implementation details . . . 100
- 11.3 Piecewise polytropic approximation method . . . 105
- 11.4 Transformation between different grids . . . 108
- 11.5 Constructed initial models . . . 110
- 11.6 Distribution of specific angular momentum . . . 113

III Simulations of explosions of rotating White Dwarfs 117

12 Pure deflagrating rapid rotators 119
- 12.1 Following typical explosions . . . 119
- 12.2 Impact of buoyancy . . . 121
- 12.3 Ignition speed in the stochastic ignition scenario . . . 126
- 12.4 Variation of the rotation law . . . 129
  - 12.4.1 $c3$ ignition . . . 129
  - 12.4.2 Stochastic ignition . . . 130
- 12.5 Influence of numerical resolution . . . 132
- 12.6 Shear motion during the explosion . . . 136
- 12.7 Interpretation with respect to spectral features . . . 137

13 Prompt detonation studies **143**
13.1 Prompt detonation of rotators in the past 143
13.2 Following a prompt detonation 144
13.3 Expected spectral features 147
13.4 Postprocessing of the prompt detonation 148
13.5 Detonating rotators: only an exotic scenario? 150

14 Conclusions **151**

15 Zusammenfassung der Arbeit **153**

A Cycle of the hydrodynamics code **159**

B Constructed initial models **161**

C Test of hydrostatic stability **165**

D Impact of buoyancy **167**

Bibliography **169**

1 Introduction

Type Ia supernovae are of great interest not only because they are the main producers of iron group elements and contribute to the mass loss in early galactic evolution. Above all, it is the astounding discovery of the accelerated expanding universe that calls the scientific world's attention to those powerful phenomena. In fact, their high degree of homogeneity and brightness enables their utilisation as standard candles.

Therefore it is all the more surprising that up to now no established explanation for the underlying physics has been found, even though promising progress has been achieved within the last few years. More precisely, a mechanism has to be identified that accounts for a range in explosion strengths in order to explain the deviations from complete homogeneity. The still lacking fundamental understanding may appear dispensable, particularly in light of an empirical correlation that turns out to legitimatise the application of type Ia supernovae as "standardised" candles. But from the theoretical point of view, an understanding of the differences is desirable because the composition of our universe is concerned.

As recent numerical studies reveal, the subsonic combustion of Chandrasekhar mass white dwarfs explains various features that are characteristic for type Ia supernovae. Up to now, these promising deflagration studies have not taken rotation into account. On the one hand, this can be attributed to the fact that adoption of rotation gives rise to the input of a free parameter whose value is unknown. On the other hand, rotation enlarges the computation requirements from the numerical point of view. Just like the formation of type Ia supernovae — mass accretion via a Keplerian disc — suggests, recent studies attest to noticeable rotation of the progenitor stars. The aim of the work presented in this thesis is to explore the possibilities which rotation permits and, at the same time, to ascertain the constraints it entails.

This thesis is organised as follows: the first part addresses the theoretical background necessary for embedding the theme into the type Ia supernova context. The status quo for type Ia supernovae is reviewed as well as studies on accreting white dwarfs and basics of flame ignition and propagation in white dwarf material. Numerical calculations are subject matter of the second part. The tools facilitating the work on explosions of rotating white dwarfs are illustrated. Finally, the results are presented in the third part.

Part I

Theory

2 Type Ia supernovae

2.1 Standard supernovae Ia — “Branch normals”

Unlike core collapse supernovae, supernovae of type Ia (SNe Ia) are attributed to thermonuclear explosions of white dwarfs (WDs) that are completely disrupted by the liberated nuclear energy [HF60]. Their overall properties show a remarkable homogeneity, which led to their utilisation as “standard candles”, i.e., objects whose absolute peak luminosity is known. However, just as the importance of SNe Ia for cosmology became clear and observations were improved and intensified, more and more deviations from the picture of an absolute homogeneous class become apparent. In the following, the basic properties of typical SNe Ia — the so called “Branch normals” [BFN93], representing ~ 64 % [LFT+01] or less of SNe Ia events — are introduced (see [Fil97] or [Lei00] for a more detailed review).

2.1.1 Spectra

SNe Ia are classified by the presence of intermediate-mass elements such as Si, O, Ca, and Mg whose neutral or singly ionised lines are prominent at maximum light, whereas neither H nor He is detected at any time (however, note that SN 2002ic is classified as Ia but shows apparent H features as described, e.g., in Ref. [WBH+04b], possibly caused by the mass donor; cf. section 2.3, [NSD+05] or [HP06]). Those outer stellar regions have an expansion velocity of $\sim 10^9$ cm/s.

Besides Ca II, about 2 weeks after maximum light the spectra are dominated by Fe II lines, indicating an iron-rich core that is now reached by the photosphere. About one month after peak luminosity, emission lines of Fe and Co shape the spectra in the nebular phase.

By examining the spectral evolution, observers concluded that the ejecta has a stratified structure [BBH+05b]. In particular, neither C nor O at low expansion velocities is observed, however their occurrence is predicted by pure deflagration models [BBB+05], [BBH+05a], [MHW+06] (but note that SN 2002cx, “peculiar” (cf. section 2.2) in many respects, exhibits a low-velocity O I line as described in Ref. [JBC+06]). Furthermore — at least to some degree — mixed ejecta are predicted for some events [SMBH05].

If not at all times, at least the late time spectral polarisation is weak (however, refer to section 2.2 for evidence of polarisation).

2.1.2 Light curve

The light curve of SNe Ia initially gave rise to their use as standard candles because the temporal evolution of different events is very similar. In addition, SNe Ia are the brightest among the entire SN group and therefore detectable at high distances. For ~ 20 days [RFL+99], the brightness increases to the maximum magnitude $M_{\mathrm{B}} \approx M_{\mathrm{V}} \approx -19.5 \pm 0.1$ [SST+99]. The bolometric luminosity is $\sim 10^{43}$ erg/s. The most accurate values for absolute magnitudes are obtained from nearby SNe Ia whose distance can be determined independently (e.g., by Cepheids [Sha18]), thus not involving the Hubble constant which in turn can be based upon SNe Ia data [Bra98]. About 2 weeks after maximum, a second maximum in the I-band is characteristic for SNe Ia. The decline, ascribed to the nuclear decay of ^{56}Ni (cf. Eqs. (5.51) to (5.53)), proceeds for ~ 3 magnitudes in 3 to 4 weeks after maximum light and drops exponentially by ~ 1 magnitude per month thereafter.

The amount of ^{56}Ni can be determined by applying *"Arnett's law"* that equates the energy released by nuclear decay and the energy emitted from the surface at maximum light [Arn82], [ABW85]. Attention should be paid to the fact that this equality assumes symmetric ejecta. For a typical SN Ia peak luminosity, an amount of $\sim 0.6\ M_{sun}$ of ^{56}Ni is required [KMP+05].

2.1.3 Rate

SNe Ia occur in all types of galaxies. Whereas the local rate of SNe Ia is about 0.2 events per century per $10^{10}\ L_{B_\odot}$ (for a Hubble constant $H_0 = 75$ km s^{-1} Mpc^{-1} [CET99]), it is found to be dependent on galaxy morphology: young galaxies host ~ 2 times more SNe Ia than early galaxies [NUK+00] because SNe Ia are slightly more efficiently produced in younger stellar populations [BTF94].

However, recent work suggests that the SN Ia rate does not solely depend on the host galaxy stellar mass but also on the star formation rate of the host galaxy (cf. section 2.2.2, [SB05], [SLP+06]).

2.2 "Peculiar" supernovae Ia

As already indicated in the introduction, nearby SNe Ia showing different features, so called "peculiar" SNe Ia, have been observed to accumulate. If SNe Ia are very distant (nowadays SNe Ia observations range up to redshift of $z \lesssim 1.7$), observations are difficult and effected for instance by dust [Wan05] or time dilation [FFL+05]. Very distant SNe Ia are of special interest for cosmologists, but are also afflicted with large error bars in the derived data. The following peculiarities, often occurring together, could be derived for several nearby SNe Ia unambiguously:

A striking feature is the **spread in peak luminosity** that is observed for some

SNe Ia. Whereas the superluminous SN 1991T was assumed to produce $\sim 1.14\ M_\odot$ of ^{56}Ni and only a few intermediate mass elements, the subluminous SN 1991bg merely generated $0.10\ M_\odot$ but plenty of intermediate mass elements [CLV00]. Since mainly the subluminous events cumulate, the affiliation in a new subclass of type Ia supernovae is conceivable.

SNe Ia which reveal at least some degree of **polarisation** have been detected. SN 1996X was polarised to about 0.2 % [WWH97]. The ejecta of the very subluminous SN 1999by [HHWW01] and the normal type SN 2001el [WBH+03] also deviated from spherical symmetry to 0.3 % - 0.8 % and up to 0.7 %, respectively. The polarisation of SN 1999by was even higher if only intermediate mass elements are considered. SN 2004dt with a value of 2 % is one of the most highly polarised SNe Ia ever observed [WBH+04a]. An early detection of SNe Ia seems to be of great importance for verifying polarisation, because this feature nearly disappeared for SN 2001el one week after maximum light [MLS+05].

Polarisation has a considerable impact in the context of rotation since it can help to restrict the geometry of the progenitor [KNW+03]. Also, deviations from spherical symmetry of the ejecta — if axial symmetry is maintained — suggest a rotating progenitor. However, a study of Ref. [LLF+05] reveals that the polarisation of SNe Ia with fast expanding ejecta (cf. the next paragraph) is not of a simple ellipsoidal asphericity.

Some SNe Ia exhibit **high velocity features** (HVFs), i.e., absorption of the prominent Ca II IR triplet for example with velocities ranging from 1.7×10^9 cm/s to 2.9×10^9 cm/s which are much higher than the photospheric component which has a typical velocity of $\sim 1.5 \times 10^9$ cm/s at ~ 1 week before maximum light (cf., e.g., SN 1994D [HBF+99], SN 1999ac [GAA+05], SN 1999ee [MBS+05], SN 2000cx [TBB+04], SN 2001el [KNW+03], SN 2003du [GHF+04], SN 2005cg [QHK+06]).

These features are often attributed to some kind of detonation in the explosion mechanism (cf. section 4.3) that provides sufficient energy for the ejecta acceleration. Also the impact of the interaction with circumstellar material or an accretion disc [KNTW04], [WS06], as well as abundance enhancements (an outer region composed of Si and Ca) are discussed as possible origins of HVFs [TMMN06]. Early detection seems to be important not only in terms of polarisation but also regarding HVFs since far before maximum light, HVFs are shown by so many SNe Ia that they are called "a ubiquitous property" as outlined in Ref. [MBA+05] (cf. also Ref. [GAA+05]).

As described above, those peculiarities are often observed to be correlated. [LLF+05] recently discovered the following trend concerning the increasing strength of line polarisation features:

ordinary or overluminous SN Ia $<$ subluminous SN Ia $<$ SN Ia with HVFs

2.2.1 Phillips relation

The above inhomogeneities among SNe Ia seem to exclude any adoption as standard candles. However, connections between the intensity of spectral lines, expansion velocities, colour, maximum luminosity, and shape of the light curve are known to exist [Bra98]. The most prominent correlation is the *empirical* “Phillips relation” [Psk77], [Phi93]. It states that the peak luminosity is directly linked to the width of the light curve: brighter SNe Ia rise and decline slower than their fainter counterparts, thus possessing a wider light curve. Different methods can be employed to “standardise” the light curves congruently, where the simplest one is the application of a temporal “stretch factor” [PGG+97]. The coherence discovered in a nearby sample of SNe Ia is then assigned to distant SNe Ia.

As the above-mentioned number of correlating features indicates, the necessity of additional corrections to the one-parameter relation emerges when comparing SNe Ia in detail [WSC+06]. See Ref. [GAN+05] for a recent approach.

2.2.2 Evolutionary effects

Besides the dependence of the SN Ia rate on the galaxy type (cf. section 2.1.3), another correlation concerning the stellar population age has been found: the brightest events (SN 199T like) only occur in actively star forming galaxies, while substantially low luminous events (SN 1991bg like) are most prevalent in E/S0 galaxies [HPS+96], [BRB96], [How01], [vLF05]. This behaviour initiated the idea of different evolutionary channels for SNe Ia [SB05], [MDP05].

The possible influence of evolutionary effects is crucial for the utilisation of SN Ia data for cosmology, since events of different age are compared (cf. section 2.4). Recent publications yield no evidence for differences of SNe Ia at various redshifts in terms of spectral or photometrical evolution [MBF+05], [BMP+06], [HHA+05], [BDL+06].

The observation of SNe Ia at high redshifts still is a challenging venture even for the mere classification of the supernova type, so that high accuracy in tackling explosion details can not be expected at present [LHF+05]. In Ref. [KGC+05] the accumulation of slowly declining (and therefore bright) SNe Ia is explained by the bias against the discovery of fast decliners due to their faintness.

2.3 Progenitor scenarios

The progenitor star of a SN Ia can be constrained by the fact that the spectra show neither H nor He lines (cf. section 2.1.1). SNe Ia are observed not only in young populations but also in elliptical galaxies. The former suggests that an evolved progenitor has already ejected its envelope, and the latter excludes progenitors with a mass higher than 8 $M_\odot$. Because no radio or X-ray emission arising from mass accretion onto a heavily bound progenitor is detectable, neutron stars and black holes are ruled out as progenitors.

Consequently, white dwarfs are proposed as SN Ia progenitors. Since WDs simply cool down if not affected by external influences, it is nowadays accepted that the WDs producing a SN Ia have to evolve in a binary system. Neither WDs consisting only of He nor those composed of O, Ne, and Mg contribute to the SN Ia scenario: a WD composed of He is presumed to explode when accreted matter increases its weight up to $M_{\mathrm{WD}} \sim 0.7\ M_\odot$, leaving behind He and ^{56}Ni, but no intermediate mass elements, clearly contradicting observations [NS77], [WTW86]. In contrast, O-Ne-Mg WDs are likely to end up in an accretion induced collapse leading to a neutron star [NK91], [GGI+96].

Therefore, the most likely candidate for a SN Ia progenitor is a WD consisting of primarily C and O (CO WD) that accretes matter in a binary system. Regarding the nature of the companion star, different possibilities have been discussed. On the one hand, the companion could be non-degenerate and supply a mass overflow. On the other hand, it could be also degenerate and merge with the CO WD.

2.3.1 Single-degenerate scenario

A main-sequence star or a giant serves as a mass donor in the single-degenerate scenario. With regard to the WD's explosion mass and the mechanism leading to ignition, different initial conditions are considered in the following models:

1. Chandrasekhar-mass model

2. Super-Chandrasekhar-mass model

3. Sub-Chandrasekhar-mass model

The accreted material reacts to C and O by shell burning until the Chandrasekhar mass is approached in scenarios 1 and 2, which is defined as $M_{\mathrm{Ch}} \simeq 1.456\,(2/\mu_e)^2 M_\odot$ (where the mean molecular weight per electron $\mu_e \approx 2$ in CO WDs [ST83]). M_{Ch} is the maximum possible mass of a WD. For heavier WDs, the pressure gradient no longer balances the gravitational acceleration in the non-rotating case, resulting in the collapse of the star. As described in sections 3.7 and 4.1, central C ignition will initiate a thermonuclear runaway and SN Ia explosion when M_{Ch} is approached within a given period of time that neither nova outbursts nor the crystallisation of the stellar core can prevent. The only significant difference between scenario 1 and scenario 2 is the influence of rapid rotation that theoretically allows for a much higher M_{Ch} in scenario 2. The centrifugal expansion effect counteracts the gravitational acceleration, thus leading to WDs that can be stable up to $\sim 4\ M_\odot$ from the hydrostatic point of view [Jam64], [LO67], [OB68], [Dur75], [DI81].

Whereas the Chandrasekhar-mass model is the preferred progenitor model nowadays — the limiting Chandrasekhar mass explains the homogeneity of SNe Ia convincingly — , the super-Chandrasekhar-mass model as proposed by numerical evolutionary studies of Ref. [YL04] (see chapter 3) is widely considered as "exotic" even though rotation seems plausible in terms of the binary scenario that arranges for mass accretion via an accretion disc rotating at Keplerian value. The progenitor masses are expected to lie in the interval $1.4\ M_\odot \lesssim M_{\mathrm{WD}} \lesssim 2.1\ M_\odot$

The super-Chandrasekhar-mass model is the progenitor scenario underlying this thesis. It is not to be mistaken with the recently proposed scenario of massive He stars ($1.7\ M_\odot \lesssim M \lesssim 2.2\ M_\odot$) that are CO enriched by He shell burning above the core [WB06].

Unlike scenarios 1 and 2, in the sub-Chandrasekhar-mass model a He envelope ($0.1\ M_\odot \lesssim M \lesssim 0.3\ M_\odot$) forms on the surface of the CO WD until a He detonation, propagating downwards and triggering a central explosive CO burning. This occurs before the WD approaches M_{Ch}. Although it is a promising model in terms of matching the frequency of occurrence of SNe Ia statistically [Liv00], the predicted lack of intermediate elements disfavours the model as an explanation for "normal" SNe Ia. Furthermore, no layer of ^{56}Ni with high radial velocities can be observed in the spectra of SNe Ia, even though it predicted by the sub-Chandrasekhar-mass model.

The main challenge of the single-degenerate scenario is the realisation of the successful mass flow of H or He onto the CO WD [CIT98]. Low accretion rates ($\dot{M} \lesssim 10^{-8}\ M_\odot/\mathrm{yr}$) are likely to trigger Nova explosions that reduce the stellar mass instead of increasing it [Bee74], [GTW93]. For high accretion rates ($\dot{M} \gtrsim 10^{-6}\ M_\odot/\mathrm{yr}$) the predicted H or He burning or even the generation of a common envelope contradict observations [NNS79]. However, only recently super-soft X-ray sources have been identified as WDs that steadily accrete H and He [Kv97], [HK03]. Accretion at moderate rates probably causes the formation of a degenerate He layer and thus leads to scenario 3 that brings up different obscurities as explained above. However, for rates of $\dot{M} \gtrsim 10^{-7} - 10^{-6}\ M_\odot/\mathrm{yr}$, recent studies support the possibility of reaching or exceeding M_{Ch} [YL04], [NSKH06].

The detection of a type G0-G2 star at the position of Tycho's SN 1572, moving with more than three times the mean velocity of other stars at that distance and therefore suspected to be the surviving companion, strongly supports the single-degenerate scenario [RCM$^+$04]. Furthermore, numerical studies show that He burning could be more stable than previously assumed [YLS04], mainly caused by the rotationally induced mixing at the CO/He interface (widening the shell source), and centrifugal expansion of the shell source location, in turn favouring a scenario with rapid rotation.

2.3.2 Double-degenerate scenario

Two CO WDs that merge with the emission of gravitational waves are possible progenitors for SNe Ia when their total mass exceeds M_{Ch} [Web84], [IT84]. This scenario naturally explains the absence of hydrogen, and also the rate of predicted events is promising [Liv00]. Although observations for close degenerate mergers possibly reaching M_{Ch} are quite rare [KOW98], recent numerical evolution studies favour this scenario (S.-Y. Yoon, private communication).

However, it is not obvious why the merging of two degenerate WDs should lead to a rather homogeneous class when mass, composition, and angular momentum distribution are presumably different [HN00]. Further, three-dimensional studies suggest that the less massive object is disrupted and forms an accretion disc around the more massive WD [BCPB90], [RS95]. Other investigations of WD mergers indicate that an off-centre ignition causes the C and O to be converted to O, Ne, and Mg, generating a gravitational collapse rather than a thermonuclear disruption [SN85], [WW86], [ML90], [SN98], [SN04].

Besides the described progenitor systems, further scenarios are under discussion, e.g., the *semi-detached* double WD binary model proposed by Ref. [SY05], but found to be inconsistent with observations by Ref. [BBR05].

2.4 Impact on cosmology

Since the late 1990s, SNe Ia used as standard candles have provided evidence for a universe that experiences an accelerated expansion since the time when it was about half of its present age [RFC+98], [PAG+99]. At that time, the predicted *dark energy* took over the kinematics of our universe that was ruled by the matter contribution before. As a consequence of this acceleration, SNe Ia discovered at a redshift of about 1 are systematically dimmer by ~ 0.6 mag as it would be the case in an Einstein-de Sitter universe (i.e., a flat universe that is characterised by a vanishing cosmological constant Ω_Λ).

This discovery is remarkable since the contribution of the dark energy today, $\Omega_\Lambda \sim 0.73$, is comparable to the contribution of matter, $\Omega_M \sim 0.27$ [AGR+06]. The nature of dark energy is not yet established. For example, a positive cosmological constant according to Einstein or Quintessence, i.e., a time dependence on pressure and energy density, w, are under discussion. However, the existence of dark energy is suggested by independent results.

The values of Ω_Λ and Ω_M are supported not only by the SNe Ia data. They are confirmed also from the examination of the cosmic microwave background (CMB) and galaxy clusters. The consistence of these three methods is known as *Cosmic Concordance*. The position of the first Doppler peak as well as the comparison of the

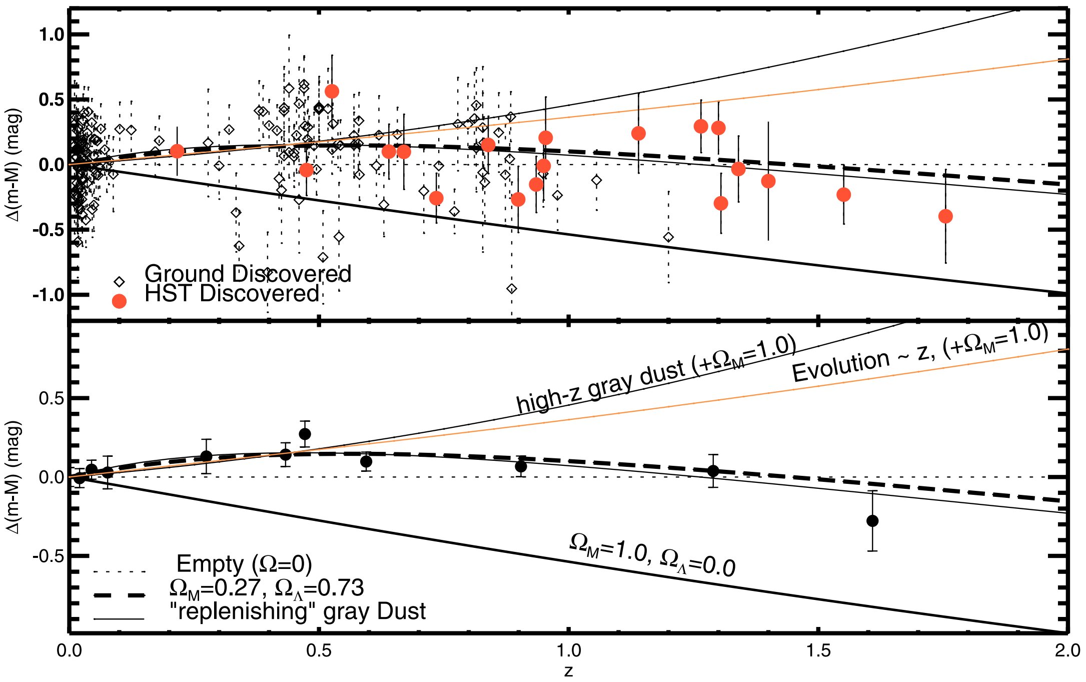

Figure 2.1: Deviations of the luminosities of SNe Ia at different redshifts z from an empty universe are plotted (from [RST+04]). The thick dashed line represents the best fit, namely $\Omega_M = 0.27$ and $\Omega_\Lambda = 0.73$, of the mean SN Ia data in the lower panel.

peak amplitudes for different multipole moments in the CMB angular power spectrum indicate a flat Universe (i.e., the total energy density $\Omega_0 = 1$) and constraint the sum of Ω_M and Ω_Λ [Whi98], [GJC+98], [dAB+00], [SVP+03]. Ω_M is constrained by the evaluation of the mass of galaxy clusters [CYL+98].

A comparative analysis of local SNe Ia to their distant counterparts is unambiguous (see Fig. 2.1). The SNe Ia at redshift $z = 0.5$ are dimmer only by ~ 0.2 mag than local ones compared to those of an empty universe, therefore exhibiting a difference that is of the same order as the intrinsic scatter in peak luminosity (cf. the upper panel of Fig. 2.1, section 2.2). However, a non-monotonic trend confirms the current acceleration whereas explanations by darkening interstellar dust fail [RST+04]: SNe Ia are brighter compared to an empty non-accelerating universe for $z \gtrsim 1.5$.

For this reason, the validity of the empirical Phillips relation as the basic principle for the applicability of the SN Ia data (cf. section 2.2.1) is important more than ever. The origin of diversity among SNe Ia has yet to be determined. Besides theoretical investigations on explosion physics, accurate observations of distant and local SNe Ia have intensified [FRM+05].

3 Presupernova evolution of accreting white dwarfs

In the context of the single degenerate binary system, nowadays the favoured progenitor scenario of SNe Ia, a WD accretes matter from a non-degenerate companion star via a Keplerian disc (cf. section 2.3). Since the average WD mass is $\sim 0.6\ M_\odot$ [ST83], the amount of matter that has to be accreted for C ignition to occur is large (this happens soonest for non-rotating CO WDs close to their Chandrasekhar mass, cf. section 2.3.1). Besides the matter itself also angular momentum is accreted. Therefore it is reasonable to assume that the WD spins up during its accretion phase.

This chapter outlines the work of S.-C. Yoon and N. Langer ([YL04] and Ref. [YL05]), who studied the physics of accreting white dwarfs (AWDs) in detail and claim that in the case of rapid rotation the limiting mass for C ignition or collapse can greatly exceed the value of the Chandrasekhar-mass. The derived rotation laws and temperature profiles serve as templates for the constructed initial models that are described in chapter 11.

3.1 Work on accreting white dwarfs

Early studies on equilibrium models of rotating WDs (e.g., Ref. [Tas78] and references therein) assumed a barotropic equation of state (cf. section 5.2) and implied axial symmetry for both rigid and differential (i.e., radially varying angular velocity Ω) rotators. Rotation is known to change the physics of stars since an additional force, the centrifugal force (cf. Eq. (11.4)), acts outwards and thus has an expanding effect. While the Chandrasekhar mass limit for CO WDs increases only slightly in the case of rigid rotation up to $\sim 1.47\ M_\odot$ (any further mass gain is prevented by mass shedding at the rapidly rotating equator), as outlined in section 2.3.1, it was shown that in principle WDs can be dynamically stable for masses up to $\sim 4\ M_\odot$. In most of the previous studies the angular momentum redistribution during the accretion phase was not derived in detail and thus the employed rotation laws were not necessarily physically motivated.

Yoon's and Langer's stellar evolution code [YL04] considers the effects of accretion-induced heating and energy transport, angular momentum transport by various instabilities and — within limits — the effect of rotation on the WD structure by modifications in the momentum and energy conservation equations. Electron and ion viscosities, relevant for the onset of instabilities, are taken into account. Transport of the accreted angular momentum is treated as a diffusion process.

3.2 Role of instabilities in the angular momentum transport

A star that is initially at rest can be spun up by accretion of angular momentum. The emerging rotation law (i.e., the rotational velocity for each mass element of the star) depends on the angular momentum distribution. If the star accretes the angular momentum at the equator via a Keplerian accretion disc, it has to find its way from the surface layers into the interior in order to induce rapid rotation of the star. However, if the accretion occurs along the field lines in strongly magnetised stars, the gain of matter could take place near the poles and not at the equator, which prevents the star from spinning up efficiently (S.-C. Yoon, private communication).

The study of Ref. [YL04] claims that angular momentum can be transported by Eddington-Sweet circulations and by turbulent diffusion induced by hydrodynamic instabilities. The origin and impact of those mechanisms on AWDs are described below.

3.2.1 Eddington-Sweet circulations

Eddington-Sweet circulations are caused by a thermal imbalance between the equator and the poles of a rotating star. Since the corresponding time scale is shorter than the accretion time scale only in non-degenerate regions, Eddington-Sweet circulations play a role in the WD envelope.

3.2.2 Shear instabilities

The *Dynamical Shear Instability* (DSI) occurs whenever the energy of shear motion dominates over the buoyancy potential. The core of a WD is susceptible to the DSI, because there the buoyancy acceleration g_{buoy} is weaker for two reasons. For g_{buoy}, the following expression holds:

$$g_{\mathrm{buoy}} \;=\; g \cdot \frac{\Delta\,\rho}{\rho}\,, \tag{3.1}$$

where g is the gravitational acceleration and $\Delta\,\rho$ the deviation from the background density ρ. First, strong degeneracy which is predominant in the centre leads to a reduced density contrast, i.e., smaller values of $\Delta\rho/\rho$. Second, the gravitational acceleration is smaller in the stellar interior compared to the outer layers.

The *Thermally Induced Shear Instability* or *Secular Shear Instability* (SSI) is present if the thermal diffusion time scale is shorter than the turbulent viscous time scale. It is important in non-degenerate stars but relevant for WDs only in the outer regions.

3.2.3 Goldreich, Schubert and Fricke instability

The *Goldreich, Schubert and Fricke instability* (GSF) can set in if a star is in a *baroclinic* condition (if the equation of state is baroclinic, in contrast to barotropic (cf. section 5.2) the temperature is an important state variable). Since the temperature has no effect on degenerate matter as long as the thermal energy is below the Fermi energy (cf. section 5.3), the GSF instability is likely to be suppressed in the WD core.

3.2.4 Magnetic instabilities

Magnetic instabilities are potentially important for magnetised WDs, but not considered in Ref. [YL04].

In summary, the strongly degenerate core of WDs is susceptible to the DSI, but other instabilities are relevant only in the non-degenerate outer layers.

3.3 Physical assumptions

The stellar evolution starts with a slowly and rigidly rotating WD whose surface velocity is 10 km/s according to observations of isolated WDs and stellar evolution models [BKN+05].

Three different initial masses, 0.8, 0.9, and 1.0 $M_\odot$ were chosen in Ref. [YL04]. The accretion rate $\dot{M}$ was selected as moderate in the context of the single degenerate Chandrasekhar-mass scenario in Ref. [YL04]. The values 3×10^{-7}, 5×10^{-7}, 7×10^{-7}, and 1×10^{-6} $M_\odot$/yr serve as input values. The accreted matter is modelled to be CO enriched ($X(^{12}C) = X(^{16}O) = 0.487$), i.e., instantaneous conversion from hydrogen or helium by shell burning is assumed.

The value of the accreted angular momentum j_{acc} is obtained as follows. Since non-magnetised WDs in close binary systems are believed to accrete matter through a Keplerian disc, the material should carry j_{acc} of the local Keplerian value at the equator. But earlier studies show that WDs will reach overcritical rotation (involving mass shedding at the equator) well before reaching the Chandrasekhar limit if j_{acc} is Keplerian. This means that the physics of accreting angular momentum is more complicated and the approach has to be modified. It has been shown that the possibility for the shift of $j_{\rm acc}$ back onto the accretion disc by viscous effects exists when the WD rotates near the break-up velocity without preventing an efficient mass accretion [Pac91], [PN91]. In this assumption the following function is applied to the accreted angular momentum:

$$j_{\rm acc} = \begin{cases} f \cdot j_{\rm K} & \text{if} \quad v_{\rm surf} < v_{\rm K} \\ 0 & \text{if} \quad v_{\rm surf} = v_{\rm K} \end{cases} \tag{3.2}$$

Here, $j_{\rm acc}$ is the specific angular momentum carried by the accreted matter, $j_{\rm K}$ and $v_{\rm K}$ are the Keplerian values for the specific angular momentum and the surface velocity, and $v_{\rm surf}$ is the actual surface velocity. f is the dimensionless *angular momentum gain parameter* that determines which fraction of the Keplerian value is allowed to be accreted. The value of f was set to 0.3, 0.5, and 1.0 in the accretion study.

3.4 Results

3.4.1 Thermal evolution of accreting white dwarfs

Rotation has a significant influence on the thermal evolution of WDs. As a consequence of the centrifugal expansion effect, rotating WDs are cooler than their non-rotating counterparts. The thermal structure is of great importance with respect to the WD spin, since it influences the redistribution of angular momentum by affecting the stability criterion for the onset of the DSI (cf. section 3.2.2).

Fig. 3.1 shows the thermal evolution of an accreting WD. In contrast to non-rotating WDs in which the central temperature rises rapidly within the accretion phase, it remains nearly constant in the rotating case. Moreover, if frictional energy dissipation $\dot{E}_{\rm rot}$ is considered, the star becomes hotter.

The accretion-induced heating is a sensitive function of the accretion rate $\dot{M}$. For a higher accretion rate, the WD becomes hotter. The existence of an absolute temperature maximum as suggested by Fig. 3.1, is caused by the accretion induced heating. It is located in the outer layers of the degenerate core. Since it moves outwards as the WD gains mass, it plays a key role in the transportation of angular momentum from the envelope into the core.

3.4.2 White dwarf spin and angular momentum transport

Fig. 3.2 displays typical profiles of the angular velocity during the accretion process. In [YL04] it was shown that all models rotate *differentially* while gaining in mass.

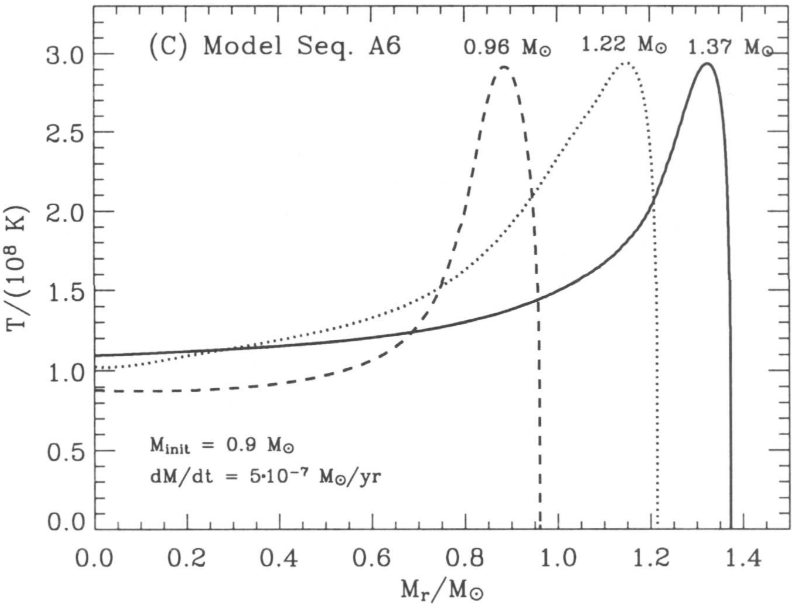

Figure 3.1: Temperature as a function of the radial mass coordinate of an accreting WD at three different instants in time. Unlike the non-rotating case, the central temperature is relatively low and rises only slightly with mass. The outer layers exhibit the typical accretion induced peak in temperature (from [YL04]).

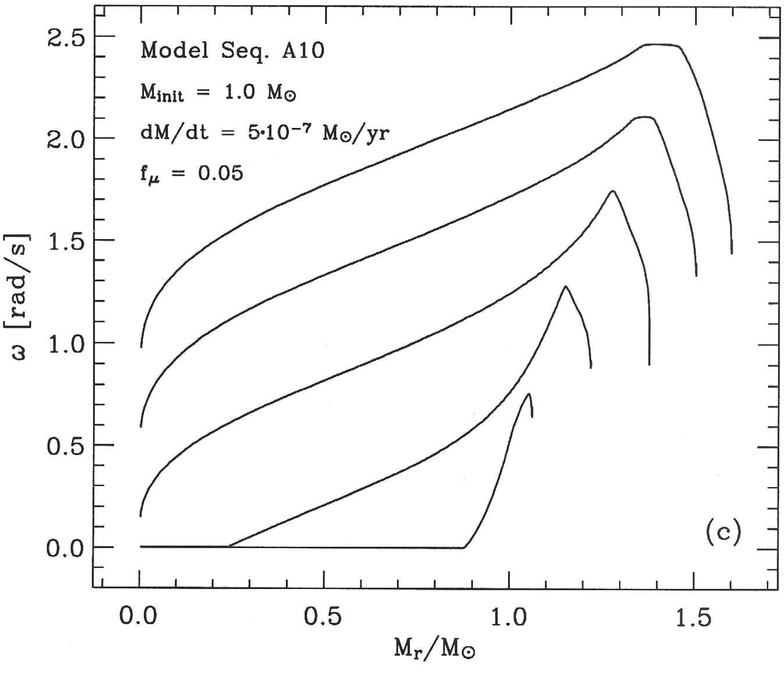

Figure 3.2: Angular velocity (here denoted by ω) as a function of the radial mass coordinate of an accreting WD at five different instants in time. Soon after the onset of accretion a characteristic absolute maximum in ω develops in the outer layers (from [YL04]).

An absolute maximum in angular velocity $\Omega_{\rm peak}$ arises. Its value is in the range of 1.5 rad/s $\lesssim \Omega_{\rm peak} \lesssim$ 6.5 rad/s when the central density of the WD reaches the ignition density of 2.0×10^9 g/cm^3. The corresponding total masses are ~ 1.5 and $\sim 2.1\ M_\odot$, respectively. Since $\Omega_{\rm peak}$ is located neither in the centre nor at the surface, it causes a shear factor that is positive in the core and negative in the envelope:

$$\sigma \equiv \partial\Omega \,/\, \partial(\ln r) > 0 \quad \text{in the core} \tag{3.3}$$

$$\sigma < 0 \quad \text{in the envelope} \tag{3.4}$$

The maximum in Ω is attributed to the fact that the slowly rotating inner part contracts faster than the rapidly rotating surface layers as the total mass increases. Since angular momentum is transported in the direction of decreasing Ω, the peak prevents the envelope from slowing down efficiently by an inward angular momentum transport. It was therefore found that the outer layers rotate fast or even at Keplerian velocity during the accretion phase. As a result, much of the accreted angular momentum $j_{\rm acc}$ is not accepted by the star (i.e., $j_{\rm acc} = 0$; cf. Eq. (3.2)): only 40 % of $j_{\rm acc}$ is accreted by the WD when it reaches 1.4 $M_\odot$.

Yoon and Langer claim that the degenerate core of an accreting WD rotates differentially as a function of shear strength σ near the threshold value for the onset of DSI, $\sigma_{\rm crit}$. Since any other mechanism for the transportation of angular momentum is too slow, stronger shear will decay to $\sigma_{\rm crit}$ via DSI. So there exists an inner dynamical shear-unstable region and an outer region dominated by SSI and Eddington-Sweet circulations. An interface which may be thought to divide these both regions is located below the position of the peak temperature and therefore in a region containing a strong temperature gradient which reduces DSI by enhancing the buoyancy. Thus, when the maximum in temperature moves outwards during accretion, and in addition stronger degeneracy which is caused by mass gain reduces the inner buoyancy, the interface moves outwards. As a consequence, the unstable DSI region also rises towards the surface and hence more angular momentum can be transported from the outer layers into the core. Altogether, the peak in Ω moves outwards.

The main conclusions regarding the angular velocity profile are:

- Accreting WDs rotate differentially throughout their evolution.
- DSI is the most important mechanism for the angular momentum transport in the highly degenerate core.
- The angular momentum gain from the accreted matter and the spin-up are closely related to the restructured angular momentum and thermal evolution of the WD as its mass increases.

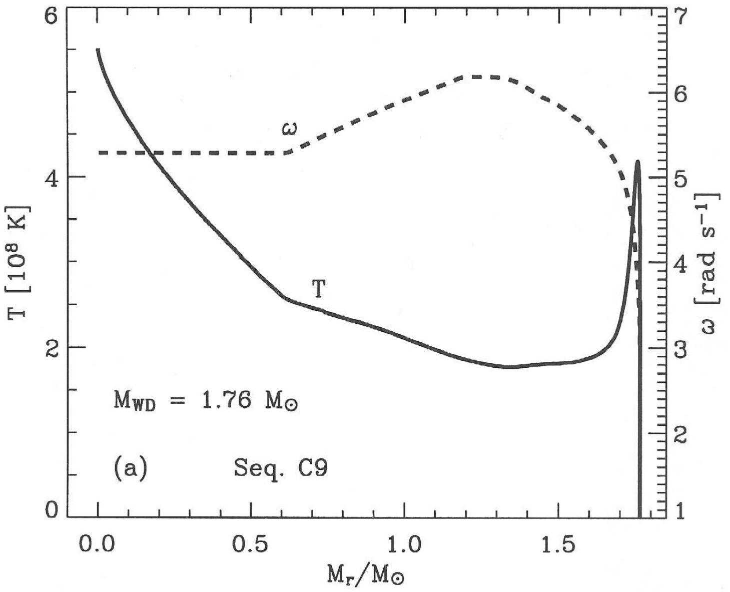

Figure 3.3: Temperature and angular velocity (here denoted by ω) as a function of the radial mass coordinate of an accreting WD prior to ignition. The convective core (enclosing the mass $\gtrsim 0.6\ M_\odot$) rotates rigidly, and the temperature in the core rises due to simmering C burning (cf. section 4.1; from [YL04]).

It is important to note that the profile in angular momentum will not correspond to Fig. 3.2 when thermonuclear runaway begins. Before ignition, a phase of convective motion arises in the centre (cf. section 4.1) leading to a very efficient transportation of angular momentum. Thus a rigidly rotating inner component will form in the inner part of the WD. A possible angular velocity profile of the progenitor prior to thermonuclear runaway is shown in Fig. 3.3.

3.5 Influence of physical assumptions

The influence of different assumptions for various physical quantities or parameters (that were introduced in section 3.3) was investigated in Ref. [YL04] and is listed here. It turned out that

- the higher the initial mass, the higher the mass M_β at a certain value of β. The latter is defined as

$$\beta \equiv \frac{E_{\text{rotation}}}{|W|} , \tag{3.5}$$

  where E_{rotation} is the kinetic energy of the rotation and W the gravitational energy. This relationship is a consequence of the fact that less matter and thus angular momentum has to be accreted to reach M_β if a WD is initially more massive.

- the lower the angular momentum gain parameter f (cf. Eq. (3.2)), the higher is M_β, since less angular momentum is accreted per unit time.
- the higher the accretion rate, the higher is M_β, since more angular momentum (but not matter) is rejected by condition (3.2).
- chemical gradients hardly have any effect in WDs unlike in non-degenerate stars.

3.6 Limitations of the accretion study

The validity of the study of Ref. [YL04] is limited by several physical assumptions.

It is suited only for non-magnetised WDs. Magnetised WDs are potentially susceptible to magnetic instabilities. Further, the accretion mechanism may be different (not via a Keplerian disc). It might well be the case that a strongly magnetised WD will not suffer a rapid speed up or/and decelerate by the magnetic force.

The study also may have duration limits because of the one-dimensional approach. The study of Ref. [YL04] states that it should work accurately up to about 60 % of the Keplerian rotation, while above that value the centrifugal force might be underestimated. However, the central regions are treated properly since it can be shown that the inner dense core (where $\rho \gtrsim 0.05\ \rho_c$) remains nearly spherical (also see Figs. 11.2, B.1 to B.7). The neglect of nuclear shell burning by the assumption of instantaneous conversion of the accreted matter is shown to have nearly no influence.

The diffusion process that describes the transportation of angular momentum in Ref. [YL04] is based on the assumption of shell like rotation. The authors claim that the shell like dependence of Ω which is inevitable by the nature of a one-dimensional code might not be appropriate for rotating WDs. Actually, in section 5.2 it is shown that rotating WDs with a barotropic equation of state display cylindrical rather than shell like rotation. For this reason, an accurate rewriting of AWD rotation laws (cf. section 11.1) does not have top priority in this thesis.

Yoon and Langer argue that those limitations might alter some details but do not affect the qualitative conclusion of the study, which is formulated with the following words: “Accreting WDs will rotate differentially and can grow beyond the canonical Chandrasekhar mass without suffering central C ignition, unless they lose angular momentum through secular instabilities” [YL04].

3.7 Evolution scenarios: loss of angular momentum

All accreting WD models discussed in the study of Ref. [YL04] had so much angular momentum at the end that they could not serve as SN Ia progenitors: The value of their total angular momentum J was so large that the central density was always too low to initiate C ignition as a consequence of centrifugal expansion. In section 4.1, the conditions for successful C ignition, namely the ignition density of $\rho_{\text{ignite}} \sim 2 \times 10^{9}$ g/cm^3 and the simultaneously necessary ignition temperature of $T_{\text{ignite}} \sim 1 \times 10^{9}$ K, are mentioned.

An efficient way to lose angular momentum is the gravitational wave radiation reaction called the *Chandrasekhar, Friedmann and Schutz* (CFS) instability, to which rapidly rotating compact stars are secularly susceptible. The authors show that the r -mode, whose restoring force is the coriolis force, might be important for the evolution of accreting WDs. The necessary value of β (cf. Eq. (3.5)) for the onset of this mode can be as low as $\lesssim 9$ % within a sufficiently short time scale compared to the accretion time scale. Unlike other modes of the CFS instability that demand higher values of β for their initiation, the r -mode can be a promising mechanism to remove angular momentum from the outer layers of a rotating WD (where most of it is located) by gravitational wave radiation.

Since the CFS instability is likely damped in the presence of strong viscosity (but not necessarily the secularly unstable modes), different scenarios on the final fate of accreting WDs are discussed by the authors [YL05]. Fig. 3.4 shows possible evolutionary paths denoted by the letters A to D, each of which correspond to different physical consequences. In the following the accretion time scale is labelled τ_{acc}, the time scale for loss of angular momentum due to r -mode instability $\tau_{\text{J}_{\text{loss}}}$.

- A: $\tau_{\text{J}_{\text{loss}}} < \tau_{\text{acc}}$

  If a sufficient amount of mass and angular momentum is accreted, the working r -mode instability removes angular momentum. As soon as the total angular momentum J is small enough, C ignition starts (A_1). If the mass flow ceases due to a limited budget in the binary system, path A_2 is followed.

- B: $\tau_{\text{J}_{\text{loss}}} > \tau_{\text{acc}}$

  In this case, the evolution critically depends on the angular momentum accretion efficiency. If it is very efficient, the growth will continue until the mass budget is exhausted. Since ignition is delayed, the final fate is determined by $\tau_{\text{J}_{\text{loss}}}$. If it is short enough, C ignition may occur in a liquid state of the star, producing a SN Ia (B_1). Otherwise if $\tau_{\text{J}_{\text{loss}}}$ is long, the WD core crystallises, leading to an electron-capture induced collapse resulting in a neutron star (B_2). But since a relatively large value for $\tau_{\text{J}_{\text{loss}}}$ leads to ignition densities

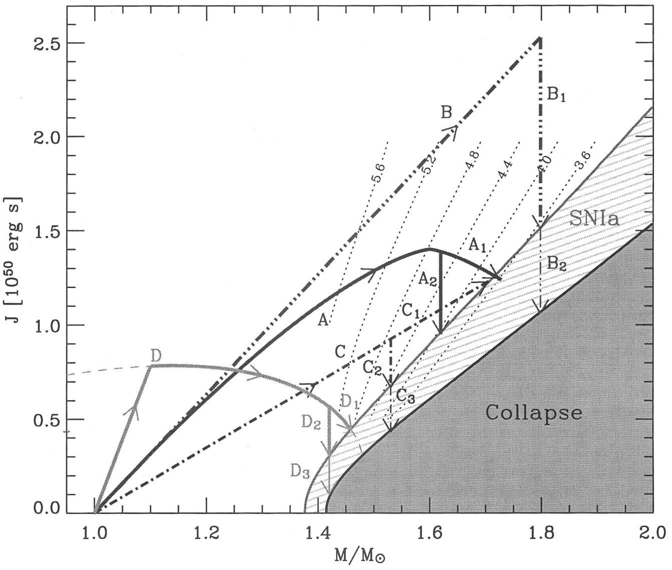

Figure 3.4: Possible evolutionary paths for accreting WDs. In dependence of the interplay of the accreted mass and accreted or rather lost angular momentum J, the final outcome varies between a SN Ia and the forming of a neutron star (from [YL05]).

of $\rho_{\text{ignite}} \gtrsim 2 \times 10^9$ g/cm^3, which results in neutron-rich iron group elements, path B_1 is probably not a major evolutionary path.

- C: $\tau_{\mathrm{J}_{\text{loss}}} > \tau_{\text{acc}}$ and low j_{acc} - efficiency

  If angular momentum is not efficiently accreted, even for $\tau_{\mathrm{J}_{\text{loss}}} > \tau_{\text{acc}}$, a SN Ia explosion is possible, either within the accretion phase (C_1) or delayed due to limited available matter (C_2).

- D: Extreme angular momentum transport efficiency

  The existence of rigidly rotating WDs through extremely efficient transport of angular momentum by magnetic torques is possible. In this case the total angular momentum J has a maximum at 1.13 $M_\odot$. Since its time scale is only short enough for more massive WDs, the r -mode instability cannot remove angular momentum, but the necessary decrease of angular momentum could be achieved by transferring it back to the accretion disc. The SN Ia progenitor masses of path D are limited to the narrow interval of $1.38\ M_\odot \lesssim M \lesssim 1.46\ M_\odot$.

The different evolutionary paths suggest that the progenitor masses for SNe Ia may not have a constant value but a wide range even within certain path/s that is/are realized by nature. The minimum mass is the canonical value of 1.38 $M_\odot$, the maximum achievable mass remains uncertain (but it is presumed that it cannot exceed 2.1 $M_\odot$ by much).

4 Ignition and propagation of the thermonuclear flame

This chapter introduces the basics concerning the ignition and combustion of WDs. After a brief illustration of the pre-supernova WD (section 4.1), different ignition scenarios are discussed in section 4.2. The propagation of two possible burning modes is described in section 4.3. Section 4.4 presents instabilities of thermonuclear flames that are required for the turbulent combustion, which is described in section 4.5. In part II of this thesis, the numerical realisation of the relevant physics is layed out.

4.1 Initiation of the thermonuclear runaway

The energy of a pre-supernova WD is basically determined by three contributions [IBHN06]: compressional heating, nuclear burning, and neutrino emission. When a WD reaches the central density of $\rho_c \sim 2 \times 10^9$ g/cm^3 as the result of steady mass accretion (cf. chapter 3), it exceeds the *ignition line* in the (ρ_c, T_c) - plane [YL03], [LHT+06]. By definition, at that time the produced nuclear energy e_{nuc} exactly balances the energy e_ν that is removed from the core by emission of plasmon neutrinos. Henceforth, compressional heating proceeds and e_{nuc} becomes greater than e_ν. For the next ~ 1000 yrs, convective motion starts and delays heating of the core [HN00]. The final values are of the order of $v_{\mathrm{convect}} \sim (3-10) \times 10^6$ cm/s [WWK04], [WW04]. But since the WD cannot get rid of the energy by radiation or by expansion, the centre of the convective core that finally encloses about half of the mass of the star grows steadily hotter. The cooling of the stellar core by convective motion is maintained as long as the convective turnover time scale is smaller than the nuclear time scale τ_{nuc}. The latter is introduced in Ref. [WWK04] and denotes the time that is required to significantly reduce the carbon abundance in an isolated region of the fluid. As soon as more energy is produced in the core than can be transferred by convective motion to the outer stellar layers, the cooling mechanism breaks down. A thermonuclear runaway leads to the explosion of the entire star when the central temperature reaches $\sim 10^9$ K.

Up to this point, the formation scenario of the ignition is widely accepted. However, clarification in several upcoming points, each of which significantly influencing the SN explosion, is still missing: *where* does ignition actually start inside the star, *how many* ignition points are these, and most elementary, what is the *burning mode* (a possible change of the mode during the explosion is not yet considered)?

4.2 Multi- vs. single-spot ignition scenario

The initiation of burning is found to have a strong impact on the explosion outcome [LAH05]. Different possibilities have been discussed for the location and number of seeds initiating the flame: the single-point central ignition, the single-point off-centre ignition, and the multi-point ignition that happens in a certain region within the WD interior. Knowledge about the ignition scenario is not only crucial for the determination of the burning mode. Small regions of sparks distributed in the core are thought to lead to a multi-spot ignition whereas an extended hot region favours the creation of a detonation front (cf. section 4.3). Numerical simulations have shown that variation of the ignition parameters (number, extent and location of the flame seed) has a strong impact on the calculated results [NHW96], [RHN02b], [RH05a]. It turned out that for deflagration models a singular event that initiates an off-centre deflagration fails to unbind the WD and that the explosion is more energetic for an increased number of ignition points. However, a maximum energy output is achieved for a moderate number of ignitions. An even greater number prevents a strongly wrinkled flame surface and therefore the energy release is less [SN06], [RHNW06]. The study of Ref. [HS02] finds no evidence for multiple spot or strong off-centre ignition, maybe as the consequence of an artefact of the employed numerical scheme as described in Ref. [WWK04].

The latter reference, together with subsequent publications, [WW04] and [KWG06], favour off-centre multi-spot ignition. In the following, the main idea of these ignition studies is presented since they serve as an input for the ignition routine employed in this thesis which is introduced in section 8.2. A combination of stellar mixing-length theory and Rayleigh-Benard convection is used to derive an estimate for the beginning of the runaway: temperature fluctuations relative to an adiabatic background state that are caused by convective motion produce the ignition points. It is important to know whether motion leading to the temperature excess in fluid regions is approximately isotropic (described by a Kolmogorov power spectrum) or obeys a dipole jet flow pattern. A parabolic temperature profile is assumed for the adiabatic background:

$$T_a(r) \simeq T_0 \left(1 - \frac{r^2}{\Lambda^2}\right) , \tag{4.1}$$

where $\Lambda = 7.35 \times 10^7$ cm for the central density of $\rho_c = 2 \times 10^9$ g/cm^3. Then the typical temperature excess gained by fluid elements on their way through the hot core regions δT_b relative to the background temperature for the isotropic case is given by

$$\frac{\delta T_b}{T_a} \sim \left(\frac{\Lambda}{R}\right)^{4/7} \left(G\,\rho_0\,\delta_P\,\tau_{\mathrm{nuc}}^2\right)^{-3/7} \tag{4.2}$$

and for the dipole jet by

$$\frac{\delta T_b}{T_a} \sim \left(\frac{\Lambda}{R}\right) \left(G\,\rho_0\,\delta_P\,\tau_{\mathrm{nuc}}^2\right)^{-1/2} \ . \tag{4.3}$$

Here R is interpreted as the mixing length, δ_P is the derivative of the logarithm of density relative to pressure, τ_{nuc} the nuclear time scale and G is Newton's gravitational constant.

The hottest fluctuations are found *not* to be located at the centre but within a shell of radius $\sim$ 100 km in the isotropic case and clustered along the flow axis in one side of the hemisphere in the dipole case. This is explained by the fact that the material heats up when it is transported through the region of high temperature background, therefore reaches the maximum in temperature somewhat later. In addition, it turns out that a dipole flow, although likely in the non-rotating WD as a consequence of the convective pre-supernova motion, is eliminated by even a very moderate degree of rotation (angular velocity $\Omega \lesssim 0.2$ rad/s).

The multi-point ignition scenario is also favoured by a numerical study which considers the evolution of fully resolved temperature fluctuations [IBHN06]. A fluid element that is hotter than the surroundings has lower density. It rises as a consequence of buoyancy and is exposed to fragmentation processes on its way towards the stellar surface. Whether this temperature fluctuation succeeds in igniting the material depends on the nuclear time scale τ_{nuc}. Only if τ_{nuc} is smaller than the dispersion time scale, ignition results. Otherwise, the temperature fluctuation fragments before ignition can occur. In accordance with Ref. [WWK04], the ignition points are found to have a typical size of $\sim$ 1 km. Furthermore, dispersion turns out to be more efficient for higher temperature fluctuations because they develop much faster than their colder counterparts. In the context of a certain probability distribution function (PDF) for the temperature fluctuations [KWG06], this has a clear consequence for the number of ignition points. The production of higher temperature fluctuations is less likely because their occurrence is confined to the tail of such a PDF. Since hotter fluctuations are more likely to fail to ignite, the multi-point ignition scenario is favoured.

For the numerical studies presented in this thesis, different ignition conditions have been employed. Both the number and the location of the ignitions have been varied. The implementation of the ignition is described in chapter 8.

4.3 Burning modes: detonation vs. deflagration

Detonations and *deflagrations* are two fundamentally different burning modes [LL91]. A combustion front proceeds as a detonation if the thin reaction zone at the interface between burnt and unburnt material propagates as a shock wave which compresses the fuel. In contrast, a deflagration (also called *flame*) moves subsonically in the unburnt material. It is sustained by the equilibrium between heat diffusion and energy generation.

Unlike detonations that do not allow the expansion of unburnt material, deflagrations are strongly affected by turbulent velocity fluctuations of the fuel [HN00].

4.3.1 Detonations in the context of type Ia supernovae

The burning mode that was initially proposed for SNe Ia was detonation [Arn69]. In this scenario, the over pressure created by the heat of the burning products is sufficiently high to form a shock wave that ignites the fuel by compressional heating. Since the burning front moves at the speed of sound in this case, the star has no time to expand. Therefore most of the the WD matter has such high densities (cf. section 5.3, Table 11.2) that it is burnt to iron group elements (IGEs). However, the detonation of a WD hardly produces any intermediate mass elements (IMEs), which is clearly contradicted by the observed spectra of SNe Ia (cf. section 2.1.1, [Fil97]).

This observational evidence against detonations as the explosion mechanism for SNe Ia is also supported by investigations of the explosion ignition. In Refs. [BK86], [Woo90], [NW97], and [Nie99] it is argued that for a successful initiation of a detonation, a flat temperature gradient and consequently shallow gradient of the nuclear time scale, $\mathrm{d}\,\tau_{\mathrm{nuc}}/\mathrm{d}r$, is needed. As soon as the thermonuclear runaway (cf. section 4.1) is initiated at the hottest point, adjacent regions are burnt by a combustion wave with a phase velocity $v_{\mathrm{ph}} = (\mathrm{d}\,\tau_{\mathrm{nuc}}/\mathrm{d}r)^{-1}$. If v_{ph} is comparable to the speed of sound and the isothermal region is broad enough, a detonation occurs. However, the existence of these conditions are questionable since many hot ignition points should occur as a result of the convective fluid motion rather than such a plateau in temperature (cf. section 4.2).

Rapid rotation of the progenitor star changes the situation insofar as it affects the condition of equilibrium of the progenitor situation: more material is located at lower densities compared to the non-rotating star (cf. section 11.5). Nevertheless, rotation has not yet solved the problem of the overproduction of heavy elements [Ste90]. It is shown in chapter 13 that, by employing a very different but physically motivated rotation law (cf. chapter 3), it is possible to construct rotating WDs that do produce a significant amount of IMEs when detonated. Since also a large amount of IGEs emerges from the promptly detonated rotators, this model certainly does not serve as the main explosion scenario. However, if different explosion mechanisms are involved in SNe Ia events, the addressed progenitors could be responsible that energetic events such as SN 1991T [MDT95] produce at least $\sim 1\ M_\odot$ of IGEs and $\sim 0.2 - 0.3\ M_\odot$ IMEs (P. Mazzali, private communication).

Deflagration-to-detonation transition

Motivated by the occurrence in terrestrial experiments, a *delayed detonation* has been proposed [Kho91], [WW94]. When allowing for such a *deflagration-to-detonation transition* (DDT), the star can expand due to the foregoing deflagration. A considerable amount of IMEs is generated when the detonation is delayed.

Although consistent with kinematics as well as spectra, light curves and nucleosynthesis, the conditions for such a transition are questionable in the context of WD matter [Nie99]. Therefore the criterion for switching the burning mode remains a parameter that is not well understood up to now (however, see Ref. [GN05] for a simulation employing a physically motivated transition criterion).

A possible deflagration-to-detonation transition is not further examined in the framework of this thesis. In contrast, whether the features of SNe Ia can be explained with as few as possible hypothetical assumptions is explored.

4.3.2 Deflagrations in the context of type Ia supernovae

The SN Ia model $W7$ [NTY84] marks the start of promising deflagration models. Unlike the previously introduced detonations, deflagrations propagate subsonically: an equilibrium of energy generation and heat diffusion is necessary in order to form a deflagration flame which consists of two zones as a first approximation. In the *diffusion zone* (that may be small in the context of degenerate WD matter due to efficient heat transport), the material is heated up to ignition temperature. Combustion takes place in the attached *reaction zone*. As soon as the energy generation rate — depending on the temperature with a large exponent — is on par with the relatively constant heat conduction rate (this occurs at $T \sim 1 \times 10^9$ K [TW92], [IBHN06]), thermonuclear runaway is initiated.

Unlike a detonating WD, a WD that is burned by a flame expands during the explosion. Since the flame "reaches" the fuel at lower densities, a significant amount of IMEs can be produced. However, a laminar (i.e., undisturbed) flame that moves with the laminar speed s_{lam} would extinguish as a result of the stellar expansion before a sufficient amount of energy is released, not even resulting in a complete unbinding of the WD ($s_{\text{lam}} \approx 10^7$ cm/s $\approx 1\ \%\ c_{\text{sound}}$ [TW92]). Although heat conduction is very effective in WDs and thus the propagation velocity of laminar flames fast, it is small compared to the speed of sound with values up to $\lesssim 10^9$ cm/s in a dense WD close to M_{Ch}.

But due to the very high Reynolds numbers of WD material ($Re \sim 10^{14}$ [NH95b]), the flow is likely to be highly turbulent. This has a significant impact on the flame that is susceptible to instabilities on various length scales and therefore does not propagate with a laminar but a turbulent velocity s_{tur} ($> s_{\text{lam}}$) for most the time of the SN Ia explosion [NH95a], [NH95b]. The great challenge of the described pure deflagration scenario is to employ an approach to determine s_{tur} by means of plausible physical assumption instead of considering it as free parameter [Dam39], [NH95b], [SNH06], [SNHR06]. Good agreement with observations is obtained if $s_{\text{tur}} \lesssim 0.3\ c_{\text{sound}}$ [HN00].

4.4 Instabilities of thermonuclear flames

As described in the previous section, the flame in WD matter is subject to turbulent motion. This turbulence is caused by hydrodynamical instabilities which are presented in this section.

4.4.1 Rayleigh-Taylor instability

In the presence of a gravitational field, two uniform fluids with different densities that are separated by a horizontal boundary are Rayleigh-Taylor (RT) unstable. The following growth rate is derived by linear perturbation theory [Cha61], [BDR+04]:

$$n_{\text{RT}} = \sqrt{g\,k\,\frac{\rho_2 - \rho_1}{\rho_2 + \rho_1}} \qquad (4.4)$$

where g is the gravitational acceleration from medium 2 with density ρ_2 towards medium 1 with density ρ_1 and k is the wave number of the perturbation. The fluid is susceptible to RT instability if the root of Eq. (4.4) is positive, i.e., $\rho_2 > \rho_1$.

The RT instability, also called *buoyancy* instability, influences the SN Ia event since in a star that is ignited at or near the centre, hot and therefore less dense ashes will be surrounded by denser fuel outside. Any perturbation of the flame surface leads to the formation of the typical RT mushroom structures. The RT instability is inhibited as soon as the star expands significantly as a result of the explosion.

As derived in Ref. [Cha61], rigid rotation stabilises the RT instability for small wave numbers in a density stratification that increases exponentially in the opposite direction of gravity. The suppression of the RT instability by rotation is also confirmed by a recent numerical study of Ref. [COZK02].

For the velocity v_b of a buoyant bubble, the following expression holds [DT50],

[GL88], [Rea84]:

$$v_b = c_1 \sqrt{\frac{\mathrm{At}\, g\, D}{2}} \tag{4.5}$$

where the dimensionless constant c_1 is about 0.5, D is the bubble diameter, g the gravitational acceleration (that has to be replaced by g_{eff}, i.e., the gravitational acceleration that is corrected by the centrifugal acceleration in rotating stars), and At is the Atwood number:

$$\mathrm{At} = \frac{\rho_2 - \rho_1}{\rho_2 + \rho_1} > 0 \tag{4.6}$$

From Eq. (4.5) it is clear that the velocity of rising bubbles is faster if the density contrast is higher, the gravitational acceleration is stronger, or the extension of the buoyant material is larger.

4.4.2 Kelvin-Helmholtz instability

Given the case that two fluid layers move — as in the case of RT instability where rising ashes penetrate into infalling fuel — against each other and form a shear flow, a surface of tangential discontinuity exists. It can be shown [LL91] that perturbations of this shear flow will grow by the rate

$$n_{\mathrm{KH}} = k\, \Delta v_t \frac{\sqrt{\rho_1\, \rho_2}}{\rho_1 + \rho_2}\,, \tag{4.7}$$

where Δv_t is a jump in the tangential velocity, ρ_1 and ρ_2 the densities of medium 1 and 2, respectively, and k is the wave number of the perturbation.

In the SN Ia context, the Kelvin-Helmholtz (KH) instability (or *shear* instability) arises as a secondary instability resulting from the RT instability. It further increases the flame surface that was enhanced by the RT perturbation. Additional shear in the azimuthal direction is present in differential rotators. However, since the angular velocity profiles of pre-supernova WDs do not contain jumps (cf. section 3.4.2), rotational shear is negligible compared to the flame shear.

4.5 Turbulent combustion

It is mentioned in section 4.3.2 that an undisturbed flame is too slow to unbind the WD. But the flame that burns the WD material is wrinkled by turbulent motion that results from the instabilities presented above. Consequently, the flame surface and thus the energy release are enhanced. The basics of this *turbulent combustion* is given below.

4.5.1 Turbulent eddy cascade

For a better understanding of the turbulence effect that is present on different length scales, the idea of a turbulent eddy cascade is helpful [Ric22], [Kol41], [Fri95]. A fluid of low viscosity is susceptible to the formation of turbulent motion. Energy that is injected into such a fluid causes turbulence that can be considered as turbulent eddies on the macroscopic scale. These eddies produce successively smaller eddies and the energy is carried to smaller scales. Below a certain length scale the flow is essentially laminar because dissipative effects dominate. At the so-called *Kolmogorov scale*, the energy put into the system at the macroscopic scale is dissipated by viscous effects. If the turbulent cascade obeys Kolmogorov's energy spectrum, where the energy for wave numbers k drops as $k^{-5/3}$, the turbulent velocity $v'(l)$ — that is identified as the eddy velocity — decreases for smaller length scales l. A Kolomgorov spectrum emerges for an overwhelming majority of technical and numerical experiments [ZWB⁺05].

Depending on the flame thickness δ that marks the relevant length scale for turbulent combustion in SNe Ia and the strength of turbulence on this scale, i.e., $v'(\delta)$, burning takes place in different burning regimes [Pet99].

4.5.2 Flamelet burning regime

Concerning the deflagration process in SNe Ia, the large scale perturbations of the RT instability drive the turbulence on a length scale comparable to the stellar radius of the WD. If the turbulent velocity on the length scale of the flame thickness is much slower than the laminar burning velocity of the flame, i.e., $v'(\delta) \ll s_{\mathrm{lam}}$, the flame becomes at most slightly distorted, thus enhancing the surface, but the flame profile (cf. section 4.3.2) is *not* affected or even destroyed. This bending of the flame takes place from the largest length scale (where the RT instability acts) down to the *Gibson scale* l_{gibs}. The latter is defined to be the scale where the turbulent velocity is equal to the laminar burning speed:

$$v'(l_{\mathrm{gibs}}) = s_{\mathrm{lam}} \tag{4.8}$$

The flame surface increases on length scales greater than l_{gibs} but it remains planar on length scales that are smaller than l_{gibs}. There, eddies rotate more slowly than s_{lam} (cf. section 4.5.1). Thus they are simply burnt by the flame. Therefore, in the so called *flamelet burning regime*, the flame proceeds with laminar speed but with an enhanced surface, which gives rise to an increase of the energy generation rate.

4.5.3 Distributed reaction zone regime

For stronger turbulence, l_{gibs} becomes smaller according to Eq. (4.8) if s_{lam} remains constant. As soon as l_{gibs} has dropped to the order of magnitude of the flame width δ, turbulent eddy motion affects the internal flame structure, changing the microscopic flame profile. As long as only the diffusion zone is influenced — it may be broader for typical flames — burning takes place in the *thin reaction zone regime*. If additionally the very thin reaction zone is influenced, the flame resides in the *broken reaction zone regime* (both regimes are summarised as *distributed zone reaction regime*).

This combustion theory is derived for deflagrations where the Prandtl number Pr is near unity (Pr is the ratio of the kinematic viscosity to the thermal diffusivity). In degenerate WD matter heat conduction dominates over viscous effects and Pr is accordingly smaller, 10^{-5} to 10^{-1} [NP84]. Therefore, the burning mechanism eventually "skips" the thin reaction zone regime by directly changing from the flamelet to the broken reaction zone regime.

At the transition from the flamelet to the distributed zone reaction regime, a switch in burning modes from deflagration to detonation (cf. 4.3.1) could be possible [NK97], [LHW$^+$00]. Furthermore, burning could be quenched as soon as the flame resides in the distributed zone reaction regime.

4.5.4 Turbulent combustion in type Ia supernovae

The flame velocity is a crucial parameter for SNe Ia. In sections 4.5.2 and 4.5.3 it is explained that the flame is affected in different ways, depending on the strength of turbulence.

In the flamelet regime the flame starts in matter with high densities ($\rho \sim 10^9$ g/cm^3). As long as l_gibs is greater than the length scale of the stellar radius R, it propagates with s_lam which can be determined by a fully resolved numerical study of Ref. [TW92]. As soon as RT motion introduces turbulent motion and $l_\mathrm{gibs} \lesssim R$, the thin flame is wrinkled. In that stage of the explosion, the flame width δ is $\sim 10^{-5}$ cm and s_lam is $\sim 10^7$ cm/s [TW92]. The burning regime does not change before the burning to IGEs is finished, which is completed in $t \lesssim 1.0$ s [Rei01].

As time passes, the star expands and the flame becomes thicker and the laminar burning speed slower ($\delta \sim 1$ cm, $s_\mathrm{lam} \sim 10^4$ cm/s). In addition, turbulence becomes stronger, so that the distributed reaction zone regime is reached. Eventually this transition occurs before the density has dropped below $\rho \lesssim 10^7$ g/cm^3 when burning ceases (cf. section 7.2). Thus the burning to IMEs that follows the iron burning could be affected by a different burning mode ([ZWR$^+$05]; W. Schmidt, in preparation). However, in the absence of a DDT, the energetics of the SN Ia event will not be influenced significantly since most of the energy is liberated during the iron burning.

As mentioned in section 4.5.2, the burning velocity in the flamelet regime is s_lam, but above l_gibs the flame does not proceed in a smooth way. Its surface is wrinkled depending on the strength of turbulence. Since the smallest resolved numerical scale Δ is always greater than l_{gibs} for three-dimensional full star studies, the increased surface on scales between Δ and l_{gibs} has to be considered in a special way. It can be achieved by the intuitive approach that derives a (higher) turbulent velocity s_{tur} by equating consumption rate of the real flame and the under resolved flame [Dam39]:

$$s_{\mathrm{tur}} \;=\; s_{\mathrm{lam}} \frac{A_{\mathrm{tur}}}{A_{\mathrm{lam}}} \;, \tag{4.9}$$

where A_{tur} is the wrinkled flame surface of the turbulent flame and A_{lam} the smaller smoothed flame surface in the model. Thus, in order to determine the numerical flame velocity s_{tur}, the unaccessible quantity A_{tur} has to be derived by a further approximation. By considering a Bunsen flame, an expression for A_{tur} is derived in Ref. [Dam39]. The conical flame surface A_{tur} is obtained from the following expression, where v' is the gas velocity at the nozzle of a Bunsen burner whose nozzle surface corresponds to A_{lam} :

$$A_{\mathrm{tur}} \;\approx\; A_{\mathrm{lam}} \frac{s_{\mathrm{lam}} + v'(\Delta)}{s_{\mathrm{lam}}} \;, \tag{4.10}$$

leading to

$$s_{\mathrm{tur}}(\Delta) \;=\; s_{\mathrm{lam}} + v'(\Delta) \;. \tag{4.11}$$

Although different results for the determination of the turbulent burning speed s_{tur} exist (cf. Eq. (7.4)), it is agreed that for strong turbulence (i.e., $v'(\Delta) \gg s_{\mathrm{lam}}$), $s_{\mathrm{tur}}(\Delta)$ decouples from s_{lam} and is proportional to the velocity fluctuations $v'(\Delta)$ [Shc43], [Poc94].

In terms of modelling turbulent combustion in hydrodynamics simulations, the determination of $s_{\mathrm{tur}}(\Delta)$ is necessary. For the simulations presented in chapter 12, $s_{\mathrm{tur}}(\Delta)$ is obtained by the application of a subgrid scale model that is introduced in section 7.1.2.

5 Explosion model formulation

Relevant physical facts and equations that are needed in order to model explosions of rotating WDs are explained in this chapter. The derivation of the hydrodynamics equations is followed by the presentation of properties of rotating stars and the physics of combustion in WD material.

5.1 Hydrodynamics

5.1.1 Eulerian and Lagrangian coordinates

Different coordinate systems exist for the description of stellar interiors in the continuum limit [Tas78], [Mü94], [Sch01]. Two of them, *Eulerian* and *Lagrangian* coordinates, are introduced in the following, because they are the limiting cases of the coordinate system used in the framework of this thesis (cf. chapter 9).

Let $\boldsymbol{x} = (x_1, x_2, x_3)$ be a fixed location in space expressed in *Eulerian* (or spatial) coordinates. Then the velocity of a fluid particle at this position is given by

$$\boldsymbol{v} = \boldsymbol{v}(\boldsymbol{x}, t) \ . \tag{5.1}$$

When using Lagrangian (or *material*) variables, each fluid particle is labelled by its original position $\boldsymbol{x}_0 = (x_1^0, x_2^0, x_3^0)$ at a certain time t (say $t = 0$). Then the actual position $\boldsymbol{x}$ is not an independent but a dependent variable. It is determined as a function of the independent variables $\boldsymbol{x}_0$ and t:

$$\boldsymbol{x} = \boldsymbol{x}(\boldsymbol{x}_0, t) \ , \tag{5.2}$$

and the velocity of the fluid parcel is given by

$$\boldsymbol{v}(\boldsymbol{x}_0, t) = \frac{\partial \boldsymbol{x}}{\partial t} \ . \tag{5.3}$$

Any scalar, vector, or tensor quantity a which is a function of the spatial variables $(\boldsymbol{x}, t)$ is also a function of the material variables $(\boldsymbol{x}_0, t)$ by the transformation given in Eq. (5.2). But $x(\boldsymbol{x}, t)$ denotes the value of a that is felt by a fluid particle at the location $\boldsymbol{x}$ instantaneously, and $a(\boldsymbol{x}_0, t)$ is the value of a by a mass element initially at the location $\boldsymbol{x}_0$ at time t.

When using spatial variables, the *spatial derivative* is given by

$$\frac{\partial a}{\partial t} \equiv \left.\frac{\partial a}{\partial t}\right|_{\boldsymbol{x} = const.} \tag{5.4}$$

and the *material derivative* by

$$\frac{\mathrm{D} a}{\mathrm{D} t} \equiv \left.\frac{\partial a}{\partial t}\right|_{\boldsymbol{x}_0 = const.} . \tag{5.5}$$

Whereas Eq. (5.4) defines the rate of change of a to an observer located at the fixed point $\boldsymbol{x}$, Eq. (5.5) measures the rate of change of a as one follows a mass element along its path.

With the convention of Eqs. (5.4) and (5.5), the velocity of the fluid $\boldsymbol{v}$ (Eq. (5.3)) is

$$\boldsymbol{v} = \frac{\mathrm{D}}{\mathrm{D} t} \boldsymbol{x} . \tag{5.6}$$

Thus the transition from Lagrangian to Eulerian coordinates proceeds as follows:

$$\begin{aligned} \frac{\mathrm{D}}{\mathrm{D} t} a(\boldsymbol{x}, t) &= \frac{\partial}{\partial t} a(\boldsymbol{x}, t)\,|_{\boldsymbol{x}_0} = \frac{\partial}{\partial t} a\big(\boldsymbol{x}(\boldsymbol{x}_0, t), t\big)\,\big|_{\boldsymbol{x}_0} \\ &= \frac{\partial}{\partial t} a(\boldsymbol{x}, t)\,|_{\boldsymbol{x}} + \mathrm{grad}_{\boldsymbol{x}}\, a(\boldsymbol{x}, t) \cdot \frac{\partial}{\partial t} \boldsymbol{x}(\boldsymbol{x}_0, t)\,\big|_{\boldsymbol{x}_0} \end{aligned} \tag{5.7}$$

or in short

$$\frac{\mathrm{D}}{\mathrm{D} t} a = \frac{\partial}{\partial t} a + (\boldsymbol{v} \cdot \mathrm{grad})\, a \tag{5.8}$$

Eq. (5.8) expresses the rate of change with time of an arbitrary function $a(\boldsymbol{x}, t)$ to an observer travelling with the fluid particle, located at point $\boldsymbol{x}$ at the instant t.

5.1.2 The Reynolds theorem

Considering the rate of change with time of a in an arbitrary material volume $V(t)$, one obtains (following the notation of [Tas78], the symbol $\mathrm{d}/\mathrm{d}t$ designates a derivative of a function that only depends on time):

$$\frac{\mathrm{d}}{\mathrm{d} t} \int\limits_{V(t)} a(\boldsymbol{x}, t)\, \mathrm{d}V = \frac{\mathrm{d}}{\mathrm{d} t} \int\limits_{V_0} a(\boldsymbol{x}_0, t)\, J\, \mathrm{d}V_0 = \int\limits_{V_0} \left(\frac{\partial a}{\partial t} J + a \frac{\partial J}{\partial t} \right) \mathrm{d}V_0 \tag{5.9}$$

Here J denotes the Jacobian of the transformation relating the element of volume $\mathrm{d}V(t)$ to the corresponding element $\mathrm{d}V_0$ in material variables:

$$J = \frac{\partial\,(x_1, x_2, x_3)}{\partial\,(x_1^0, x_2^0, x_3^0)} \tag{5.10}$$

Its temporal derivative is computed to be [Mai05]

$$\frac{\partial\,J}{\partial\,t} = J\,\mathrm{div}\,\boldsymbol{v}\ . \tag{5.11}$$

Therefore Eq. (5.9) becomes

$$\frac{\mathrm{d}}{\mathrm{d}\,t}\int\limits_{V_0} a\,J\,\mathrm{d}V_0 = \int\limits_{V_0} J\left(\frac{\partial\,a}{\partial\,t} + a\,\mathrm{div}\,\boldsymbol{v}\right)\mathrm{d}V_0\ . \tag{5.12}$$

Accordingly, the *Reynolds theorem* can now be derived:

$$\frac{\mathrm{d}}{\mathrm{d}\,t}\int\limits_{V(t)} a\,\mathrm{d}V = \int\limits_{V(t)}\left(\frac{\mathrm{D}\,a}{\mathrm{D}\,t} + a\,\mathrm{div}\,\boldsymbol{v}\right)\mathrm{d}V = \int\limits_{V(t)}\left[\frac{\partial\,a}{\partial\,t} + \mathrm{div}\,(a\,\boldsymbol{v})\right]\mathrm{d}V \tag{5.13}$$

Using Gauss's theorem, the Reynolds theorem (Eq. (5.13)) can be rewritten:

$$\frac{\mathrm{d}}{\mathrm{d}\,t}\int\limits_{V(t)} a\,\mathrm{d}V = \frac{\partial}{\partial\,t}\int\limits_{V_t} a\,\mathrm{d}V + \oint\limits_{S(t)} a\,\boldsymbol{v}\cdot\boldsymbol{n}\,\mathrm{d}S \tag{5.14}$$

Here $\boldsymbol{n}$ is the vector normal to the surface $S = S(t)$ surrounding the material volume. The Reynolds theorem (Eq. (5.14)) illustrates that the rate of change (Eq. (5.9)) is the sum of two distinct contributions. On the one hand it consists of the rate of change over a fixed volume V_t (coinciding with the material volume $V(t)$ at instant t), and on the other hand of a contribution of the flux of a over the bounding surface $s(t)$.

Let $B(a)$ be the rate of change of a:

$$\frac{\mathrm{d}}{\mathrm{d}\,t}\int\limits_{V(t)} a\,\mathrm{d}V = B(a) \tag{5.15}$$

Then the general form of a balance equation with the source term $s(a)$ in Eulerian form follows from Eq. (5.13):

$$\frac{\partial\,a}{\partial\,t} + \mathrm{div}\,(a\,\boldsymbol{v}) = b(a)\ , \tag{5.16}$$

where the source $B(a)$ is

$$B(a) = \int\limits_{V(t)} b(a)\,\mathrm{d}V \ . \tag{5.17}$$

For the special case of the conservation of the quantity $\int_{V(t)} a\,\mathrm{d}V$ in Eq. (5.9) (i.e., the temporal derivative is zero), the *continuity equation* can be derived:

$$\frac{\partial\, a}{\partial\, t} + \operatorname{div}(a\,\boldsymbol{v}) = 0 \tag{5.18}$$

I.e., the two components on the right side of Eq. (5.14) either exactly balance or both are zero in case of conservation.

5.1.3 Equations for reactive ideal fluids

Although diffusive processes play an important role in SNe Ia — deflagrational burning is allowed by heat diffusion — it is sufficient to treat the fluid not as real (as described by the Navier-Stokes equation) but as ideal (i.e., free of dissipation and diffusion). This approximation holds since both viscous dissipation and diffusion processes act only on scales much smaller than the resolved ones. That is, the numerically introduced discretisation error is greater than the error caused by the omission of viscosity. Therefore, the formally simpler Euler equations are used in this work to model the flow of stellar material.

From Eq. (5.16), the set of *reactive Euler equations including gravitation* describing fluids in the limit of dissipation absence can be derived:

- equation of *mass conservation* (also known as continuity equation)

$$\frac{\partial}{\partial\, t}\rho + \nabla(\boldsymbol{v}\,\rho) = 0 \tag{5.19}$$

- equation of *momentum balance*

  The momentum of a local fluid element is not conserved but changed by external forces and thus obeys a balance equation. In absentia of any dissipation, the only present source terms are caused by the pressure gradient and the gravitational acceleration (that are quoted on the right hand side, respectively):

$$\frac{\partial}{\partial\, t}(\rho\,\boldsymbol{v}) + \nabla(\rho\,\boldsymbol{v})\,\boldsymbol{v} = -\nabla p - \rho\,\nabla\Phi_g \tag{5.20}$$

- equation of *energy balance*

  The total energy, defined as the sum of kinetic and internal energy of a local fluid element follows the subsequent relationship, where the source term $\rho\, S$ is caused by energy release of reactive burning:

  $$\frac{\partial}{\partial\, t}\rho\, e_{\text{tot}} \;+\; \nabla\left(\boldsymbol{v}\,\rho\, e_{\text{tot}}\right) \;=\; -\nabla(\boldsymbol{v}\, p) \;-\; \rho\,\boldsymbol{v}\,\nabla\Phi_g \;+\; \rho\, S \;, \tag{5.21}$$

  where e_{tot} is the specific value of the total energy.

The gravitational potential is obtained from Poisson's equation in the Newtonian limit (cf. chapter 10):

$$\nabla^2\,\Phi_g(\boldsymbol{r}) \;=\; 4\pi\, G\,\rho(\boldsymbol{r}) \tag{5.22}$$

The reactive source term S in Eq. (5.21) depends on the species' reaction rates $\boldsymbol{q}$ which in turn are usually given as functions of ρ, T and the mass fraction of the species $\boldsymbol{X}$:

$$S \;=\; f(\boldsymbol{q}) \tag{5.23}$$

$$\boldsymbol{q} \;=\; \boldsymbol{f}(\rho, T, \boldsymbol{X}) \tag{5.24}$$

The included species and the corresponding reaction rates involved in the executed simulations are specified in section 7.2.

For the balance of species, the following equation holds:

$$\frac{\partial}{\partial\, t}(\rho\,\boldsymbol{X}) \;+\; \nabla(\boldsymbol{v}\,\rho\,\boldsymbol{X}) \;=\; \boldsymbol{q} \tag{5.25}$$

The pressure and temperature must be specified as functions of ρ and the specific internal energy $e_{\text{int}} = e_{\text{tot}} - \boldsymbol{v}^2/2$ in order to have a complete set of hydrodynamical equations. Those additional relations are given by the equation of state (EOS, cf. sections 5.3 and 7.3 for the EOS of WD matter and the numerical implementation of the EOS, respectively) :

$$p \;=\; p\,(\rho, e_{\text{int}}, \boldsymbol{X}) \tag{5.26}$$

$$T \;=\; T\,(\rho, e_{\text{int}}, \boldsymbol{X}) \tag{5.27}$$

5.2 Barotropic rotators in a state of permanent rotation

An equation of state is called *barotropic* if the pressure depends only on the density:

$$p \;=\; p\,(\rho) \tag{5.28}$$

The physics of rotating stars simplifies whenever a barotropic equation of state may be applied. Eq. (5.28) states that isobaric surfaces coincide with the surfaces of constant density, the isopycnic surfaces. A special case of barotropy, the polytropic equation of state (11.9), is introduced in section 11.2.

The pressure of WDs depends, in general, on the density, the temperature and the chemical composition. Nevertheless, a barotropic relation between pressure and density is thought to be well suited for describing the physics of WDs, since most of the electrons in the interior are so highly degenerate that in spite of possibly high internal temperatures the complete independence of the temperature is a good approximation [Tas78].

The following assumptions are made for the rotating stars used in this thesis:

1. The star is isolated in space and rotates about a fixed axis in space with the angular velocity Ω.
2. The system is stationary, i.e., the density of each mass element does not change in time when performing a cyclic motion.
3. Friction that might occur in differential rotators is neglected.
4. Electromagnetic forces are neglected.

A star satisfying these conditions is said to describe a *state of permanent rotation* for an inertial observer [Tas78].

Conservation of mass together with the restriction of temporal constant density demand *axial symmetry* of the rotating system. If the star is required to rotate about the z-axis in cylindrical coordinates (s, ϕ, z) and the centre of the rotator coincides with the origin of the coordinate system, the components of the velocity are

$$v_s = 0\ , \qquad v_\phi = \boldsymbol{\Omega}\ s\ , \qquad v_z = 0\ , \tag{5.29}$$

where the angular velocity is

$$\boldsymbol{\Omega} = \boldsymbol{\Omega}\,(s, z)\ . \tag{5.30}$$

The components of the equations of motion follow from Eq. (5.20):

$$\frac{1}{\rho}\frac{\partial p}{\partial s} = -\frac{\partial \Phi_g}{\partial s} + \boldsymbol{\Omega}^2 s \tag{5.31}$$

$$\frac{1}{\rho}\frac{\partial p}{\partial z} = -\frac{\partial \Phi_g}{\partial z} \tag{5.32}$$

Here ρ, p, and Φ_g are the density, pressure, and the gravitational potential, respectively. When eliminating Φ_g in Eqs. (5.31) and (5.32), one finds that

$$\frac{\partial}{\partial z}\left(\boldsymbol{\Omega}^2 s\right) = \frac{\partial}{\partial z}\left(\frac{1}{\rho}\right)\frac{\partial p}{\partial s} - \frac{\partial}{\partial s}\left(\frac{1}{\rho}\right)\frac{\partial p}{\partial z}\,, \tag{5.33}$$

and with Eq. (5.29) it follows that

$$2\,\frac{\partial \boldsymbol{\Omega}}{\partial z}\,\boldsymbol{v} = \nabla\frac{1}{\rho} \times \nabla p\,. \tag{5.34}$$

From Eq. (5.34) it is clear that the condition of barotropy (coincidence of isopycnic and isobaric surfaces) is given if and only if

$$\frac{\partial \boldsymbol{\Omega}}{\partial z} = 0\,. \tag{5.35}$$

Therefore we can draw an important conclusion: the rotation law of a WD that obeys a barotropic equation of state (5.28) depends only on distance s to the rotation axis:

$$\boldsymbol{\Omega}_{\mathrm{WD}} = \boldsymbol{\Omega}(s) \tag{5.36}$$

Note that Eqs. (5.35) and (5.28) are equivalent statements when describing rotating objects.

If the condition (5.35) holds, then an *equatorial plane of symmetry* which is perpendicular to the axis of rotation can be proven to exist [Tas78]. This property is also known as *Lichtenstein Theorem.*

A further useful property of barotropic stars can be seen when the *effective gravity* $\boldsymbol{g}_{\mathrm{eff}}$, i.e., the gravitational attraction corrected for the centrifugal acceleration, is introduced. In cylindrical coordinates the forces are:

$$\begin{aligned} g_s &= -\frac{\partial \Phi_g}{\partial s} + \Omega^2 s \\ g_z &= -\frac{\partial \Phi_g}{\partial z} \end{aligned} \tag{5.37}$$

Then Eqs. (5.31) and (5.32) can be rewritten:

$$\frac{1}{\rho}\nabla p = g_s + g_z = \boldsymbol{g}_{\mathrm{eff}} \tag{5.38}$$

Thus for a star in the state of permanent rotation, the effective gravity is always orthogonal to the isobaric surfaces. Furthermore, if the equation of state is barotropic, the effective gravity also is orthogonal to the isopycnic surfaces.

This section closes with four statements, any of which imply the validity of the other three if the state of permanent rotation is to be guaranteed [Tas78]:

1. The angular velocity is constant over cylinders centred about the axis of rotation.
2. The effective gravity can be derived from a potential.
3. The effective gravity is normal to the isopycnic surfaces.
4. The isobaric and isopycnic surfaces coincide.

5.3 White dwarf matter

A WD results from a main sequence star with a mass $M \lesssim 8\ M_\odot$ that has ejected its envelope after the expiration of nuclear reactions. It resides in an equilibrium of gravity and pressure due to degenerate electrons. The mean masses and radii of WDs are $M \sim 0.6\ M_\odot$ and $R \sim 10^{-2}\ R_\odot$, respectively. The mean density is $\rho \sim 10^{7}$ g/cm^3, and the temperature has a constant value between 10^{7} and 10^{8} K that slowly drops when the WD cools [UB99].

The situation becomes different for WDs in binary systems (a considerable number of WDs occur in binaries [Wei68]). WDs can gain weight by mass accretion. If the mass reaches the Chandrasekhar limit (cf. section 2.3.1), the electron pressure is no longer balanced by gravity and the collapse to a neutron star or a black hole occurs. WDs suffering a SN Ia explosion approach M_{Ch}, thereby reaching central densities in the range of 10^{8} to 10^{10} g/cm^3 and a central temperature of $\sim 10^{9}$ K.

WD matter is characterised by electron degeneracy. The electron gas causes high heat conductance, which leads to an isothermal condition of an isolated star. Since the thermal energy of the electrons, about 10 keV, is much lower than the Fermi energy E_{F} ($\sim$ 1 MeV), temperature variations have no effect on the density and pressure profiles. In particular, the degeneracy avoids cooling by expansion when the temperature rises. Only $\sim$ 0.5 % of the mass has (or rather $\sim$ 24 % of the radius encloses) densities less than 10^{6} g/cm^3 that are non-degenerate and thus the adiabatic index $\gamma = 5/3$ there (see Fig. 11.1, [ST83]).

A pre-supernova WD can be modelled by a polytropic EOS (Eq. (11.9)) with an adiabatic index of $\gamma = 4/3$ that describes the highly relativistic electrons in the stellar core [Ste90]. However, for the model of the WDs presented in this thesis, an approach that is not limited to a certain density regime (i.e., not assuming a fixed value of γ) is used (cf. section 11.3).

As soon as the thermonuclear runaway is initiated, the EOS is more complicated. The thermodynamical properties are composed of several contributions [Cox68], [ST83]:

- **Photon gas**: According to the Stefan-Boltzmann law, the photon field contribution is comparable to the internal energy of electrons and nuclei for $T \sim 10^{9}$ K. The energy e_γ and pressure p_γ of a photon gas with temperature T is given by

  $$e_\gamma = \frac{4\,\sigma}{c}\,T^{4} \quad \text{and} \tag{5.39}$$

  $$p_\gamma = e_\gamma\,/\,3\,, \tag{5.40}$$

  where σ is the Stefan-Boltzmann constant and c the speed of light. The photon gas is important especially in hot ashes and at lower densities.

- **Electron gas**: Near the stellar centre, the Fermi energy has such a high value that relativistic effects become important. Furthermore, due to the high temperatures reached during the explosion, degeneracy may be lifted. Therefore the equation of state has to describe an arbitrarily degenerate and relativistic electron gas.

  The energy e_e and pressure p_e for the electrons is given by the following equations:

  $$e_e = \frac{8\,\pi\,\sqrt{2}}{h^3}\,m_e^4\,c^5\,\beta^{5/2}\,\left[F_{3/2}(\eta,\beta) + \beta\,F_{5/2}(\eta,\beta)\right] \tag{5.41}$$

  $$p_e = \frac{16\,\pi\,\sqrt{2}}{3\,h^3}\,m_e^3\,c^5\,\beta^{3/2}\,\left[F_{3/2}(\eta,\beta) + \frac{1}{2}\,\beta\,F_{5/2}(\eta,\beta)\right] \tag{5.42}$$

  Here F_k denote the relativistic Fermi integrals:

  $$F_k(\eta,\beta) = \int\limits_0^\infty \frac{x^k\,(1+\frac{1}{2}\,\beta\,x)^{1/2}}{\mathrm{e}^{-\eta+x}+1}\,\mathrm{d}\,x \tag{5.43}$$

  The parameters η and β indicate the strength of degeneration and relativistic effects, respectively. They are defined as

  $$\eta = \frac{E_\mathrm{F}}{k\,T} \qquad \text{and} \qquad \beta = \frac{k\,T}{m_e\,c^2}\,, \tag{5.44}$$

  where k is the Boltzmann constant and m_e the electron mass.

- **Electron-positron-pair creation**: For $T \gtrsim 10^{9}$ K, i.e., in the hot ashes, the photons' energy suffices to create electrons and positrons. The contributions of the additional leptons to energy and pressure have the same form as Eqs. (5.41) and (5.42), but the Fermi integrals (Eq. (5.43)) are replaced by a modified expression [Cox68]:

$$\tilde{F}_k(\eta,\beta) = F_k(\eta,\beta) + F_k\left(-\eta - \frac{2}{\beta},\, \beta\right) \tag{5.45}$$

- **Baryonic gas**: The nuclei are completely ionised but not relativistic for $T \lesssim 10^{10}$ K and can therefore be described by the Maxwell-Boltzmann equation. The energy density e_n and pressure p_n are

$$e_n = \frac{3}{2} R\, T\, \rho \sum_i \frac{X_i}{A_i} \qquad \text{and} \tag{5.46}$$

$$p_n = 2/3\, e_n\ , \tag{5.47}$$

  where A_i is the atomic mass of nucleus i and the summation is carried out for all chemical species.

Since the direct evaluation of the Fermi integrals (Eq. (5.43) and (5.45)) is too time consuming to be carried out during the simulation, state values are tabulated (cf. section 7.3).

5.4 Nuclear reactions in white dwarf matter

A complex network involving hundreds of nuclei and more than 3000 nuclear reactions and photodisintegration leads to heavy nuclei up to the iron group [HT96]. The procedure of nuclear burning can be approximately merged in the following reactions.

The accretion induced compression causes a rise of the central temperature. For $T \gtrsim 10^9$ K explosive carbon burning sets in:

$$^{12}\mathrm{C} + {}^{12}\mathrm{C} \longrightarrow {}^{20}\mathrm{Ne} + \alpha \tag{5.48}$$

Due to the following rise in temperature, the photon field becomes sufficiently energetic to photodissociate neon when $T \gtrsim 1.5 \times 10^9$ K:

$$^{20}\mathrm{Ne} + \gamma \longrightarrow {}^{16}\mathrm{O} + \alpha \tag{5.49}$$

The liberated α particles are captured by the remaining heavy ions:

$$^{16}\text{O}\,(\alpha,\gamma)\;^{20}\text{Ne}\,(\alpha,\gamma)\;^{24}\text{Mg}\,(\alpha,\gamma)\;^{28}\text{Si} \tag{5.50}$$

At even higher temperatures, oxygen fusion (^{16}O + ^{16}O) sets in. Once the temperature exceeds $T \gtrsim 3 \times 10^9$ K, photodisintegration plays an important role for all nuclei. A complex series of photodissociation and α capture reaction follows, converting silicon into iron group elements.

In this state of *Nuclear Statistical Equilibrium* (NSE), mainly radioactive nickel ^{56}Ni is generated: unlike in the *thermal equilibrium*, where every reaction is balanced by its reverse reaction, in NSE the weak reactions, expressed by the electron abundance Y_e, are suppressed. Thus NSE depends not only on density and temperature, but also weakly on Y_e [HT99].

Consequently for SNe Ia the more strongly bound ^{54}Fe is not favoured but ^{56}Ni is as long as $Y_e \sim 0.5$ since the resulting $^{54}\text{Fe}+2\,\text{H}$ are bound even less. However, when considering high WD densities of $\rho \gtrsim 3 \times 10^9$ g/cm^3, Y_e is decreased by electron capture and the production of ^{54}Fe is favoured [THRT04].

The burning mode (i.e., deflagration or detonation; cf. section 4.3) arising in the WD affects its temperature (see Fig. 13.2). Higher temperatures are achieved if the WD is burnt by a detonation. Since the NSE depends on temperature, it may be reached differently for deflagrations and detonations. Table 13.2 shows that the high temperatures arising from detonations lead to a narrow peak of the preferred iron group isotope.

Whereas the reactive SN Ia explosion lasts for $\lesssim 1.5$ s, the characteristic light curve is observable for many weeks (cf. section 2.1.2). It is powered by the electron capture decay of ^{56}Ni to radioactive ^{56}Co, that in turn undergoes electron capture (81 %, Eq. (5.52)) and β^+ decay (19 %, Eq. (5.53)), to stable ^{56}Fe, whose half-life periods are 6.1 and 77 days, respectively [TAC67], [CM69]:

$$^{56}\text{Ni} + e^- \longrightarrow\; ^{56}\text{Co} + \bar{\nu}_e \tag{5.51}$$

$$^{56}\text{Co} + e^- \longrightarrow\; ^{56}\text{Fe} + \bar{\nu}_e \tag{5.52}$$

$$^{56}\text{Co} \longrightarrow\; ^{56}\text{Fe} + e^+ + \nu_e \tag{5.53}$$

The energy for the light curve results from γ radiation that is emitted by the excited states of ^{56}Co and ^{56}Fe.

6 Pure deflagrations — the actual state

The actual state of SN Ia simulations based on the pure deflagration scenario, which is the underlying explosion mechanism of the main focus of this thesis, is outlined.

6.1 Enhancements in modelling type Ia supernovae

During the last years, the pure deflagration model which is presented in part II of this thesis in its current implementation, has resulted in significant progress as far as an understanding of SNe Ia is concerned.

Transition to three spatial dimensions
In the past, the energy release in hydrodynamics simulations of SNe Ia was always below expectations. Due to the transition to three spatial dimensions (together with a more realistic reaction network as described in the next paragraph), the energetics could be brought in line with values suggested by observations [RHN02a]. In particular, the WDs in all exploding WD models are unbound which prohibits a contraction at a later time. This is due to the fact that in two-dimensional cylindrical coordinates, (s, ϕ, z), axial symmetry is assumed, i.e., any dependence on the azimuthal angle ϕ is excluded. Although two-dimensional calculations are favourable in terms of computing capacities, they are not capable of treating turbulent motion in a correct manner. Turbulence as an elementary property of flames in WD material (cf. section 4.5) cannot develop along the direction of ϕ. A consideration of the third spatial dimension is required for a realistic model, because the flame surface is increased by additional structures that can not be shaped assuming axial symmetry. A three-dimensional model results in a more energetic explosion. This can be seen in Fig. 6.1 which contrasts the evolution of the total energy for both two-dimensional cylindrical and three-dimensional Cartesian coordinates.

More realistic burning network
Unlike the early version of the hydrodynamics code that treated burning as a one-step reaction from fuel to ashes, the current description of burning is more realistic. The consideration of α-particles and a species representing intermediate mass elements (IMEs; cf. section 7.2 for details) has led to more powerful explosions. This

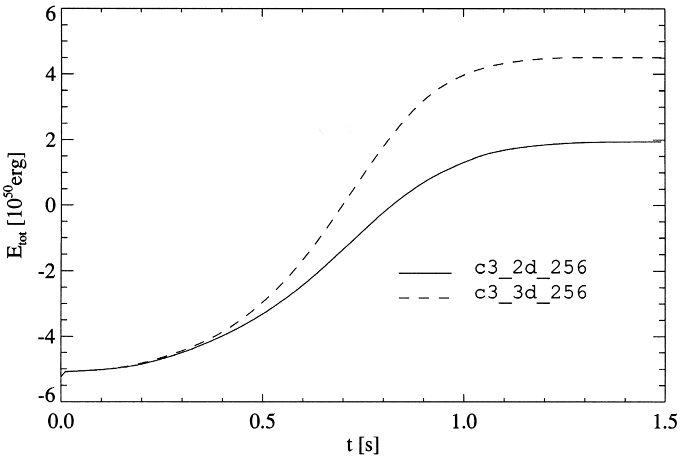

Figure 6.1: A noticeably greater amount of energy is released in three-dimensional simulations. The plots compare the total energy evolution of a non-rotating star which is ignited by the $c3$ ignition (cf. section 8.1) in two (solid line) and three (dashed line) spatial dimensions (from [Rei01]).

is due to the fact that α-particles reduce the temperature and thus buoyant effects. A longer residence of the flame in the stellar material is the consequence.

Improved derivation of the turbulent burning velocity

A crucial quantity for the simulation of flames in full star simulations is the turbulent burning velocity s_{tur} (cf. sections 4.5.4 and 7.1.2). It turned out that the production of turbulence is largely confined to the regions near the flame front and the interior ash regions [SNHR06]. This fact of pronounced anisotropy requires a localised modelling of the physics that can not be resolved.

In order to derive s_{tur}, a localised subgrid scale model is employed. By considering several contributions in the computation of s_{tur}, energy generation is significantly enhanced. Moreover, less unburnt fuel remains (see Figs. 6.2(a) and 6.2(b), respectively).

Enhanced burning by multi-spot ignition

A further increase of released energy is obtained by employing the multi-spot ignition that became possible with higher resolution of the central stellar region [RHN02b], [SN06], [RHNW06]. Fig. 6.3 compares the energetics of a WD ignited under various conditions. The central $c3$ ignition (cf. section 8.1) releases noticeably less energy compared to the temporally delayed stochastic multi-spot ignition with high values of the ignition rapidity C_e (cf. section 8.2). This trend is also evident for the amount of iron group elements (IGEs) whose generation is the main energy source of the SN Ia event.

Stochastic ignition is also capable of alleviating a general problem of the deflagration scenario, namely the presence of fuel at low expansion velocities, i.e., near the

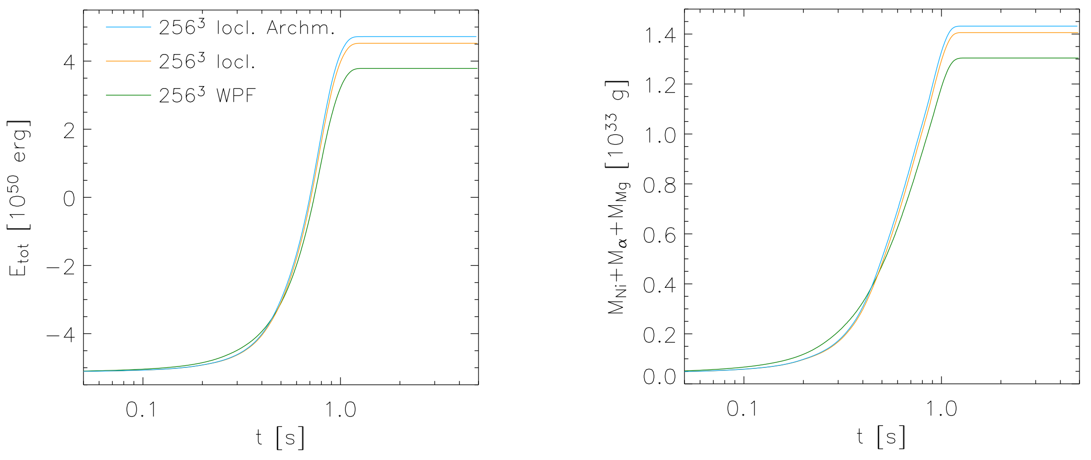

(a) (b)

Figure 6.2: Evolution of the total energy (Fig. 6.2(a)) and the burnt material (Fig. 6.2(b)) in a three-dimensional simulation with 256 cells per octant. The green line ("WPF") denotes the previously employed subgrid scale model, the orange line ("locl.") and the blue line ("locl. Archm.") represent the localised model and the localised model considering buoyancy effects, respectively. The localised subgrid scale model produces a more energetic explosion and the burning of more fuel (from [SNHR06]).

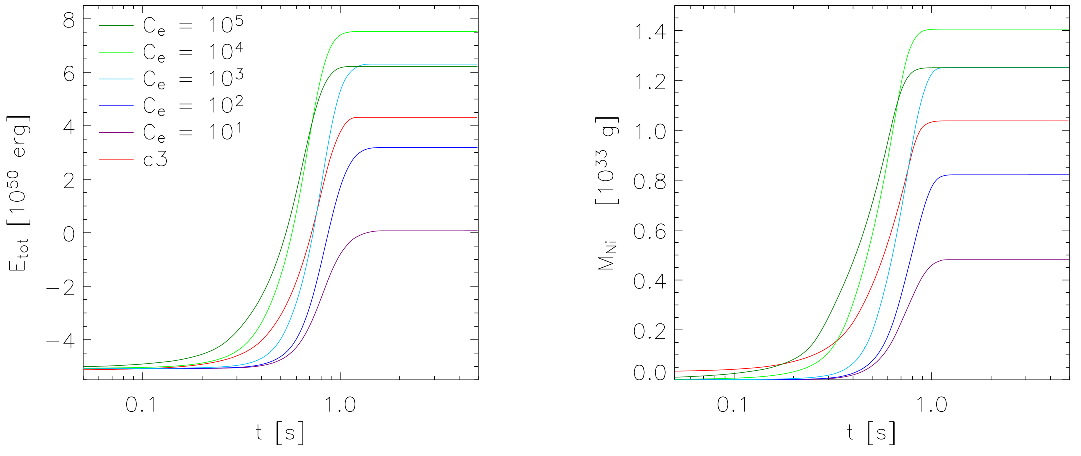

(a) (b)

Figure 6.3: Evolution of the total energy (Fig. 6.3(a)) and the amount of IGEs ("Ni", Fig. 6.3(b)) for the central $c3$ ignition and the stochastic multi-spot ignitions with various ignition speeds "C_e". Compared to the $c3$ ignition, a more energetic explosion and more IGEs are obtained by the multi-spot ignition with $C_e = 10^4$ (from [SN06]).

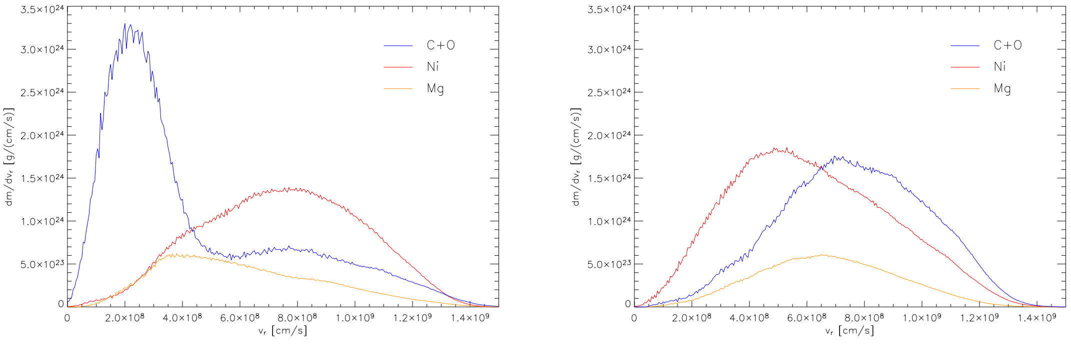

(a) (b)

Figure 6.4: Probability density functions in radial velocity space for a full star simulation with $C_e = 10^2$ (Fig. 6.4(a)) and $C_e = 10^5$ (Fig. 6.4(b)) at $t = 5.0$ s. More ignition points alleviate the problem of unburnt material at low radial velocities (from [SN06]).

stellar centre. Fig. 6.4 shows that the amount of slow unburnt material is reduced significantly for a high number of ignition points (i.e., a large value of C_e).

The ejecta are found to exhibit velocities up to $\sim 14 \times 10^8$ cm/s which compares fairly well with observations (apart from the existence of HVFs; cf. section 2.2).

6.2 Influence of physical parameters

In order to check the capability of the deflagration model to explain the empirically established correlation between peak luminosity and light curve shape (cf. section 2.2.1), parameter studies have been carried out. The influence of physical quantities of the progenitor star that are not well determined by stellar evolution theory or may change for different SN Ia events has been investigated in detail [RH04], [THR05] [RGH05]. The impact of the carbon-to-oxygen ratio, the central density prior to ignition and the metallicity of the progenitor have been analysed. Another parameter of importance may be the rotation of the progenitor, which is the main topic of this thesis (cf. part III).

Carbon-to-oxygen ratio

For two reasons, the carbon-to-oxygen ratio was assumed to be a principal source of peak luminosity variations by influencing the production of ^{56}Ni, i.e., the energy source of the SN Ia (cf. section 5.4): On the one hand, the laminar burning velocity rises for a higher carbon fraction X(^{12}C) (cf. Eq. (7.3)). On the other hand, the lower binding energy for ^{12}C compared to ^{16}O leads to a greater energy release.

However, the influence of X(^{12}C) (which was varied over the range of $0.3 < \mathrm{X}(^{12}\mathrm{C}) < 0.6$) turned out to be nearly inexistent. A mechanism between the nucleosynthesis and turbulent flame evolution was found that almost balances any effect

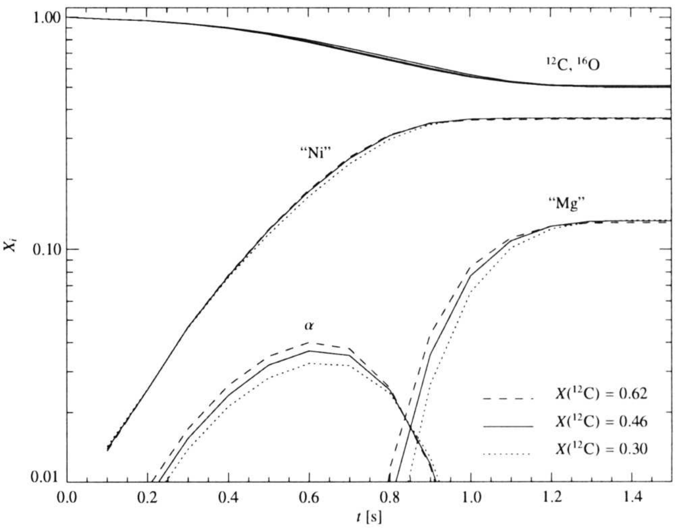

Figure 6.5: Evolution of the chemical species for an exploding WD with different carbon-to-oxygen ratios. The amount of IGEs ("Ni") is nearly unaffected by X(^{12}C), because a self-regulating mechanism between nucleosynthesis and turbulent flame evolution is established. Note the higher amount of α-particles for greater X(^{12}C) (from [RH04]).

on the amount of generated ^{56}Ni. The higher value of X(^{12}C) leads to a higher temperature and thus to a higher amount of α-particles (see Fig. 6.5), which in turn causes lower temperatures and higher stellar densities. Burning is suppressed due to these effects. Although the progenitor's carbon-to-oxygen ratio affects the energy release of SN Ia explosions and therefore the ejecta velocities, it has little effect on the peak luminosity which is determined by the ^{56}Ni mass.

Central density

Just like X(^{12}C), the central density ρ_c affects the energy release of the models and thus the expansion velocity of the SN Ia ejecta. A higher value of ρ_c results in a more vigorous explosion (see Fig. 6.6) which is thought to originate only marginally from the laminar burning velocity (cf. Eq. (7.3)). The influence of ρ_c both on the energetics and the composition has been found primarily in two different observations. For higher ρ_c, more material is present at sufficiently high densities that can potentially be burnt to IGEs, resulting in a stronger explosion. Furthermore, higher gravitational acceleration g_{buoy} (see Eq. (3.1)) is experienced by the flame. Thus the turbulent cascade (cf. section 4.5.1) develops more quickly and the turbulence-induced boost of the flame propagation velocity sets in earlier. It is found that more IGEs and less IMEs are obtained for higher values of ρ_c .

Metallicity

The metallicity is found to have a large influence on the amount of ^{56}Ni. Changes of the metallicity of the progenitor star were tested by means of different ^{22}Ne mass

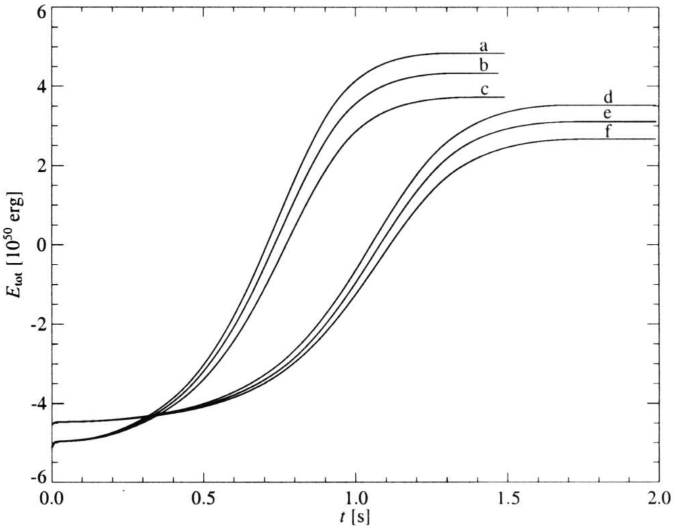

Figure 6.6: Evolution of the total energy for the initial central stellar density for $\rho_c = 2.6 \times 10^9$ g/cm^3 (lines a, b, and c) and $\rho_c = 1.0 \times 10^9$ g/cm^3 (lines d, e, and f). X(^{12}C) is 0.62 (a and d), 0.46 (b and e), and 0.30 (c and f) (from [RGH05]).

fractions in the initial composition assumed in a postprocessing run of the simulation data. Different values for X(^{22}Ne) represent different metallicities since the stellar metallicity affects mainly the initial CNO abundances. During the pre-explosive H burning they are converted to ^{14}N and the He burning to ^{22}Ne. A linear dependence of the ejected ^{56}Ni mass on the progenitor's metallicity is found, with a variation of $\sim 25\%$ in the metallicity range of 0.1 $Z_\odot$ to 3.0 $Z_\odot$:

$$M(^{56}\mathrm{Ni}) \;\simeq\; 0.45\ M_\odot - 0.031\ \frac{Z_{\mathrm{CNO}}}{Z_\odot} \tag{6.1}$$

However, the amplitude of the variation of the ^{56}Ni mass cannot account for all the variations in peak luminosity of SNe Ia.

6.3 Limitations of the pure deflagration model

The pure deflagration model still cannot account for all observed characteristics. As stated in the previous section, the explosion mechanism is fairly robust and cannot explain the diversity of ^{56}Ni that is suggested by observations (cf. section 2.2). The maximum amount of ^{56}Ni never exceeds $\sim 0.5\ M_\odot$ in the deflagration simulations, however, it is $\gtrsim 1\ M_\odot$ for the brightest events.

Whereas the fact of a relatively low amount of ^{56}Ni could be explained by the hypothesis that the low number of those extremely bright events suggests a totally different explosion mechanism, a further obstacle for the acceptance of the pure deflagration model is the fact that currently too little IMEs, not more than $\lesssim 0.3\ M_\odot$, are produced. This in turn might be an effect of the numerical representation of the flame (cf. section 4.5). The burning to IMEs could proceed in the distributed reaction zone regime (cf. section 4.5.3) when the turbulent fluid motion affects the internal structure of the flame, which is thicker at this stage. But since the numerical flame description (cf. section 7.1.1) is successively worse for increasing flame width, the flame may be represented in an incorrect manner for the burning in the distributed reaction zone regime [RH05b]. At the beginning, this problem was postponed since burning beyond the flamelet regime was neglected, and the lack of IMEs was explained by an excess of leftover fuel that is potentially converted to intermediate mass elements. But recent studies show that, even for very efficient burning in the distributed burning zone regime, the amount of intermediate elements can hardly be increased. This is explained by the fact that once a noticeable stellar expansion is initiated by the early burning stage, the flame cannot get ahead of the WD's expansion at a later time.

Limitations on the pure deflagration model are also given from spectral observations. Leftover fuel is predicted not only in the outer layers but also close to the centre by the model and, moreover, is more or less distributed all over the star. This mixing is a consequence of the burning process that is shaped by the large scale Rayleigh Taylor instability. As mentioned in section 6.1, the multi-point ignition scenario helps to reduce C and O at the centre, and some SNe Ia may even highlight that feature. Furthermore, mixed ejecta are not ruled out completely. However, it is questionable whether the predicted degree of mixing is in agreement with the bulk of observations of SNe Ia. HVFs (cf. section 2.2), i.e., ejecta at velocities of $v \gtrsim 1.5 \times 10^9$ cm/s cannot be explained very well by the pure deflagration model.

For these reasons, it is questionable whether the pure deflagration model can explain strong SNe Ia events. Up to now, the impact of rotation on the flame had not been investigated. It is presented in chapter 12.

Part II

Numerics

7 The combustion model

The hydrodynamics code PROMETHEUS employed here was written in 1989 [FMA89] and has been developed over 17 years. This chapter describes the numerical method that enables the modelling of WD explosions. The modifications and extensions of the code that were necessary for this work are presented in the following chapters.

The interested reader is referred to the following theses; [Ste90], [Nie95], [Rei01], [Rö03], [Sch04], and [Gol04]; and the corresponding publications for further details on PROMETHEUS.

7.1 Burning front modelling

7.1.1 The level set method

In principle, the reactive Euler equations (Eqs. (5.19) to (5.27)) together with equations describing diffusion of energy and species across the burning front contain the physics needed for the treatment of flames. But fully resolved numerical simulations of the flame are much too time consuming for three-dimensional full star simulations. Typical grid spacings ($\Delta \gtrsim 10^5$ cm) are at least 5 orders of magnitude larger than the flame width ($\delta \lesssim 10^0$ cm). The challenge is to find a model that imitates the behaviour of microphysical processes and can be applied on the simulation grid scale. Then the required knowledge of the microphysical processes can be obtained by experiments or fully resolved numerical studies, carried out on small computational domains.

The widely employed *reaction-diffusion approach* artificially smears out the transition region between fuel and ashes to resolve the flame numerically [Kho93]. A major shortcoming is that the formation of turbulent flame structures is shifted towards greater scales since the flame thickness on the numerical grid is not small but several grid cells wide.

The *level set method* , introduced in Ref. [OS88] and applied to SN Ia calculations in Ref. [RHN⁺99], provides better spatial confinement since it treats the flame as a sharp discontinuous surface that divides fuel from ashes in the three-dimensional computational domain. It is convenient to associate the flame at position $\boldsymbol{r}$ with the moving zero-isosurface $\Gamma(t)$ of the so called G-equation that is defined to be -1 in fuel and 1 in ashes:

$$\Gamma(t) \;\equiv\; \{\, \boldsymbol{r} \mid G(t, \boldsymbol{r}) = 0 \,\} \tag{7.1}$$

In order to identify $\Gamma(t)$ with the burning front, $G(t, \boldsymbol{r})$ has to evolve according to the burning front propagation. This propagation can be separated into two parts. On the one hand, the front is advected by the fluid motion with a speed $\boldsymbol{v}$. On the other hand, it burns with the burning speed s normal to the flame surface:

$$\frac{\partial G}{\partial t} = -(\boldsymbol{v} + s\,\boldsymbol{n})\,(-\boldsymbol{n}\,|\nabla G|) = (\boldsymbol{v}\boldsymbol{n} + s)\,|\nabla G| \tag{7.2}$$

The burning speed s depends on the burning mode and the background state of the WD matter.

7.1.2 Determination of the burning velocity

Deflagration

As described in section 4.5.4, the velocity of a flame depends on the burning regime. The laminar burning speed s_{lam} was obtained by Ref. [TW92], who performed fully resolved numerical studies of flame propagation in CO matter, resulting in an expression for s_{lam} with an error of $\lesssim 10\%$:

$$s_{\mathrm{lam}} = 9.2 \cdot 10^{6}\ \mathrm{cm/s} \left(\frac{\rho}{2 \cdot 10^{9}\ \mathrm{g/cm^3}} \right)^{0.805} \left[\frac{X(^{12}\mathrm{C})}{0.5} \right]^{0.889} \tag{7.3}$$

Here, $\mathrm{X}(^{12}\mathrm{C})$ denotes the mass fraction of carbon and ρ the density of the fuel. Eq. (7.3) defines the flame velocity when it propagates undisturbed. As soon as turbulent motion emerges in the flamelet regime, the burning speed s becomes greater than s_{lam}. The magnitude of the velocity fluctuations on the grid scale, $v'(\Delta)$, determine the turbulent flame propagation speed $s_{\mathrm{tur}}(\Delta)$ (cf. section 4.5.2), which is given by the following relation [Poc94] for the conditions in this thesis:

$$s_{\mathrm{tur}}(\Delta) = s_{\mathrm{lam}} \sqrt{1 + \frac{4}{3} \left(\frac{v'(\Delta)}{s_{\mathrm{lam}}} \right)^{2}} \tag{7.4}$$

As mentioned in Refs. [SNH06] and [SNHR06], the subgrid scale model that computes $v'(\Delta)$ contains several contributions:

- The **rate of production** term describes the energy that is transferred through the turbulence cascade from resolved to unresolved scales. It is determined *locally*, therefore no specific turbulence energy spectrum such as Kolmogorov's has to be assumed.
- A specific **Archimedian force** term takes account of buoyancy effects caused by macroscopic Rayleigh-Taylor motion on unresolved scales.

$\log(\rho,\ \mathrm{g/cm^3})$	7.5	8.0	8.5	9.0
$D\ [10^9\mathrm{cm/s}]$	1.143	1.160	1.220	1.323

Table 7.1: Velocity D of the detonation front as a function of density, as obtained by Ref. [Sha99]

- Turbulent energy is converted into heat by a **rate of dissipation** term.
- The **rate of diffusion** term incorporates the transport on unresolved scales that superimposes the macroscopic advection.

$v'(\Delta)$ and therefore $s_{\mathrm{tur}}(\Delta)$ decrease with increasing resolution since more and more details of the flame surface are resolved when the number of grid cells is increased. In terms of SNe Ia explosions, it turns out that s_{tur} in highly resolved studies is of the order $\sim 0.1\ c_{\mathrm{sound}}$.

Detonation

Just like the laminar burning velocity for deflagrations, the propagation velocity D for detonations can be determined by fully resolved numerical studies. Simulations with detailed nuclear networks yield an endothermal behaviour of the Si reaction for densities $\rho > 2 \times 10^7$ g/cm^3. Thus detonations in that density regime are of pathological type. For less dense material, the reactions are found to be exothermal and the detonation velocity is identified as the Chapman Jounguet-velocity, i.e., the local speed of sound of ashes [Kho89], [Sha99].

For this work, D is obtained as follows. Within the density regime of $10^{7.5}$ g/cm^3 $\leq \rho \leq 10^{9.0}$ g/cm^3, the four values listed in Table 7.1 and published in Fig. 2 of Ref. [Sha99] are linearly interpolated. Below $\rho = 10^{7.5}$ g/cm^3, D is set to the constant value of 1.143×10^9 cm/s because the transition to the local speed of sound produces an abrupt change in D. Note that burning ceases for $\rho < 10^{7.0}$ g/cm^3 in the detonation model (cf. section 7.2).

For densities $\rho > 10^{9.0}$ g/cm^3 that occur early, D is extrapolated from Ref. [Sha99] by the following fit, returning D in units of 10^9 cm/s:

$$D \;=\; 6.048 \;-\; 1.299 \cdot \log(\rho) \;+\; 0.086 \cdot \big(\log(\rho)\big)^2 \tag{7.5}$$

Note that densities greater than $10^{9.3}$ g/cm^3 do not occur in the employed WD progenitor models. The evolution of D with respect to density is plotted in Fig. 7.1.

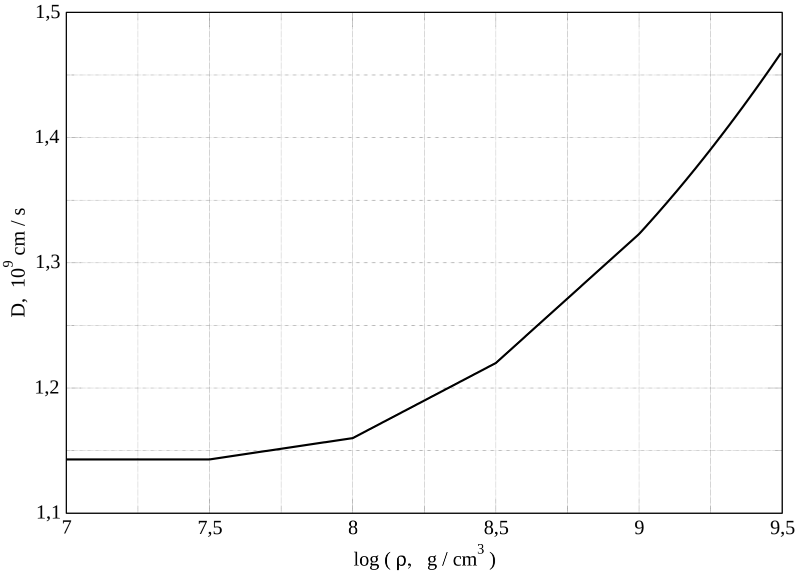

Figure 7.1: Velocity of the detonation front D as a function of density, following Ref. [Sha99]

7.2 Reaction network

As outlined in section 5.4, the nucleosynthesis involved in SNe Ia explosions is very complex. Moreover, the majority of reactions take place on extremely short time scales compared to the explosion duration. In other words, once the thermonuclear runaway is initiated, the nuclear time scale τ_{nuc} is much smaller than the hydrodynamical time scale τ_{dyn} ($\tau_{\mathrm{dyn}} \approx 0.1$ s, [NW97]). There are technical obstacles that prohibit the solution of the complete nuclear reaction equations (Eqs. (5.23) to (5.25)). Even if only the energetically important fast reactions in the flame were resolved temporally — which is already very demanding in terms of computing power —, the internal structure of the flame itself has to be resolved in detail which is not possible for three-dimensional calculations (cf. section 7.1.1 and chapter 9).

Since the priority of this study is on the realistic modelling of the explosion hydrodynamics, the burning mechanism in the hydrodynamics code is treated in a simplified manner [Rei01]. The underlying idea is the following: as long as the proper amount of energy release of all participating fast reactions is guaranteed when the flame burns through the WD and if the average molecular weight of fuel and ashes is roughly correct, the complex reaction network can be reduced to a coarse effective network. Such an effective network contains single nuclei that represent groups of elements having similar binding energies and molecular masses: a mixture of *carbon and oxygen* (C+O, “fuel”; throughout this work, always an equal fraction of carbon and oxygen is assumed; cf. section 6.2), *intermediate mass elements* (IMEs) represented by ^{24}Mg, *iron group elements* (IGEs) represented by ^{56}Ni, and α-*particles*.

The implementation is done as follows:

- At high densities, $\rho > 5.25 \times 10^{7}$ g/cm^3, CO is burnt to ^{56}Ni, releasing 7.86×10^{17} erg/g. Since NSE (cf. section 5.4) allows for the production of α-particles in dense hot ashes, the overall energy release can be delayed. The generation of α-particles is controlled by a NSE data table provided by H.-Th. Janka. It requires 7.274×10^{17} erg/g. The α-particles are converted to ^{56}Ni during the later expansion of the star and thus can be considered as an energy buffer.
- At lower densities ^{24}Mg is produced, releasing 4.18×10^{17} erg/g. It is not clear if burning to IMEs completely takes place in the flamelet burning regime or if the transition to the distributed reaction zone regime already affects the burning of WD matter (cf. sections 4.5.3 and 4.5.4). Further, the impact of such a transition (quenching the flame or triggering a DDT; cf. section 4.3.1) is unknown. Depending on the burning mode (cf. section 4.3), the criterion for burning to cease is chosen differently:
    - For *detonations* whose reaction zone is not affected by any turbulent motion, burning is stopped at densities below 10^{7} g/cm^3. This density threshold for burning is motivated by the study of a numerically resolved detonation front propagating in WD matter. It was shown that burning ceases for $\rho \lesssim 10^{7.5}$ g/cm^3 [Mai05].
    - The *flame* profile may be wrinkled heavily or even destroyed upon arrival in the distributed reaction zone regime. Therefore, a qualitative criterion is chosen to stop magnesium burning in deflagrations (following W. Schmidt, in preparation). The time scale of thermal diffusivity, roughly of the order $\delta / s_{\mathrm{lam}}$ (where δ is the flame thickness and s_{lam} the laminar flame velocity) is approximately equal to the nuclear time scale τ_{nuc} (cf. section 4.1):

    $$\tau_{\mathrm{nuc}} \approx \frac{\delta}{s_{\mathrm{lam}}} \tag{7.6}$$

    This time scale is compared to the time scale of turbulent diffusivity that is associated with the eddy turnover time on the grid scale $\tau_{\mathrm{turb}}(\Delta)$. As soon as the ratio of τ_{nuc} (which grows steadily for less dense fuel) to $\tau_{\mathrm{turb}}(\Delta)$ (which becomes shorter for stronger turbulence) exceeds a certain value C^*, burning is stopped:

    $$\frac{\tau_{\mathrm{nuc}}}{\tau_{\mathrm{turb}}(\Delta)} = C \,, \quad \text{no burning for} \quad C \geq C^* \tag{7.7}$$

For the simulations presented here, C^* was set to 1. However, much higher values for C^* did not produce significantly more IMEs (W. Schmidt, in preparation). τ_{nuc} in Eq. (7.6) is obtained by inter- and extrapolated values of δ and s_{lam} tabulated in Ref. [TW92].

- Once magnesium burning is terminated, the leftover CO remains unaffected.

A more detailed knowledge of the chemical composition of the ejecta can be obtained by making use of the tracer particle method (cf. section 7.4).

The unnaturally sharp transition densities for the burning procedure were derived from data of a W7 run provided by K. Nomoto and therefore are rather phenomenological. The outcome of the postprocessing of tracer particles may be considered as a test for the validity of such transition densities that have a potentially large impact on the simulation. However, it is important to bear in mind that such a test is not independent of the assumed transition densities since they do affect the value of the energy release.

The handling of the burning may be one of the most inaccurate parts of the simulation. Further work on the verification of the above described assumptions may yield clarification.

7.3 Equation of state

The relevant contributions to the equation of state (EOS; Eqs. (5.26) and (5.27)) for an exploding WD are listed in section 5.3. The numerical computation of the relativistic Fermi integrals for the electron and the electron-positron-pair creation contributions (Eqs. (5.43) and (5.45), respectively) is very demanding in terms of computational power. For this reason, the energy density and pressure for the lepton and the photon contributions are tabulated for a regular grid in the $(\log T, \log \rho)$ plane. The range of these employed tables is given by $3 \leq \log_{10} T\,[\mathrm{K}] \leq 11$ and $-5 \leq \log_{10} \rho\,[\mathrm{g/cm^3}] \leq 11$. It is important to note that the EOS is derived for an electron number fraction of $Y_e = 0.5$, i.e., for an equal number of protons and neutrons. Since the maximum density does not exceed 2×10^9 g/cm^3, this assumption is suited for WDs considered in this study. However, neutronisation begins to become important for $\rho \gtrsim 3 \times 10^9$ g/cm^3, causing a lower Y_e by electron capture. This influences not only the EOS but also the NSE (cf. section 5.4). Therefore, the present implementation is not capable of simulating WDs that are more massive but still conceivably SN Ia progenitors [LHT$^+$06].

As it will be shown in section 11.3, the bilinear interpolation scheme employed to extract the desired values is problematic: not only the values of pressure or energy density, but also their derivatives are needed, which are piecewise constant. Although it demands more computational effort, this is avoided by a higher order interpolation scheme.

7.4 Tracer particles

7.4.1 Recording the explosion in the moving framework

As outlined in section 7.2, it is possible to obtain more detailed information of the species generated during the explosion a posteriori. Provided that the energy release of a coarse grid network is adequate to treat the hydrodynamical evolution of an exploding star properly, a detailed nucleosynthesis calculation can be carried out by making use of the tracer particle method. Fluid elements with a given mass are labelled and their advected motion is followed during the SN Ia event while the corresponding values of position (or velocity components), density, temperature, and nuclear energy are tabulated continuously. For the calculations presented in this work, output is written roughly once per (physical) millisecond. The tracer particles are identified exactly with fluid elements in Lagrangian variables (cf. section 5.1.1).

In addition to the extraction of a a more detailed species composition from the tracer particles' information, also synthetic spectra and light curves can be generated with the help of radiation transfer codes [Rei01].

7.4.2 Implementation details

Regarding accurate statistics, attention should be paid to a proper discretisation of the tracer particles. Due to the fact that their masses do not change over time, the stellar material should be divided into bits of equal masses instead of equal volumes. Otherwise, a large number of tracer particles is “lost” in low density regions that are not important for the burning process and furthermore, the tracer particles possess enormous differences in weight.

This requirement is easily met for a spherical star by integrating the mass from the centre outwards, thereby recording the thickness $\Delta r(m)$ of concentrical shells containing an identical amount of mass Δm. After remapping the Lagrangian tracer grid that is equidistant in differential mass $\Delta m(r)$, azimuthal angle ϕ , and $\cos\theta$ (where θ is the polar angle) onto the Cartesian grid of the hydrodynamics simulation, an interpolation routine ensures that even in coarsely resolved regions the tracer data is derived accurately during the explosion. It turned out that a completely regular alignment of the tracer particles at the beginning of the explosion causes problems in the postprocessing analysis. This can be avoided by displacing the tracer particles slightly from their regular positions.

The situation is different for rotating stars that do not exhibit spherical symmetry because the density stratification is not only a function of r but of s and z in cylindrical coordinates. Moreover, the resolution of the rotating stars is coarse (cf. section 11.4). Any interpolation within a rotating initial model turned out to be too inaccurate to obtain stellar volumes of identical masses Δm. Therefore, the tracer particles were selected in the same way as for the non-rotating star. But $\Delta r(m)$ derived for the non-rotating star was changed in order to account for the shape of the rotator. This was achieved by increasing the radii containing m so that the elongated equatorial radius of a rotator can be identified with the artificially increased surface of the non-rotating star. Subsequently, the masses of all tracer particles were calculated explicitly.

The fact that the masses (that are computed according to the (r, ϕ, θ)-grid that the tracer particles span initially) are no longer identical is a disadvantage. For the extreme case of a tracer particle that is located outside the stellar poles but still closer to the centre than the equator, the mass vanishes. The situation is aggravated even if only a small number of tracer particles is employed. The calculation of the tracer volumes on the (r, ϕ, θ)-grid by assuming Cartesian boxes becomes increasingly imprecise for an ever decreasing number of tracer particles, since it only holds in the limit of small Δr, $\Delta\phi$, and $\Delta\theta$. In particular, this shortcoming arises for the detonation events (cf. chapter 13), where the number of tracer particles has to be held small. This limitation is necessary to avoid a postprocessing overload caused by a large number of tracer particles which reside in the computationally time consuming NSE (cf. section 5.4) as a consequence of high temperatures and densities. Therefore, the sum of all tracer masses differs from the stellar mass by $\lesssim 2.5$ % when setting only 3375 tracers (i.e., 15 zones each in radial, azimuthal and polar directions). The deviation caused by the coarse Lagrangian grid cannot be reduced noticeably by increasing the resolution of the hydrodynamics grid which provides more precise density values for the calculation of the tracer particles' masses.

8 Initiation of the thermonuclear explosion

In order to investigate the impact of certain ignition situations, different methods depending on the burning mode (cf. section 4.3) as well as on the numerical resolution have been used to initiate the burning front in the hydrodynamics simulations.

8.1 Static ignition

A convenient approach to model the start of the thermonuclear runaway in hydrodynamics simulations is to burn a certain region instantaneously to ashes. Due to the very different time scales of the convective phase and the explosion ($\lesssim 1000$ yrs vs. $\lesssim 1.5$ s, respectively), the initial configuration cannot simply be evolved by starting the hydrodynamics code prior to ignition and then following the temperature fluctuations (however, note the approach described in section 8.2). The position and extent of that region burnt at $t = 0$ s, i.e., at the onset of the explosion tracking, has to be motivated by ignition studies (cf. section 4.2).

A frequently used initial flame morphology is the $c3$ configuration. It represents a central ignition that already has developed instabilities in order to avoid a long latency of their growth to a noticeable degree [RHN02a]. With three bulges in azimuthal direction in each hemisphere, the flame has already emerged into a strong axial symmetric sinusoidal perturbation (see Fig. 8.1). Besides the fact that the $c3$ ignition is reproducible and ensures similar conditions even if initiated in different initial models (it may be chosen to enclose an equal volume of ashes for all

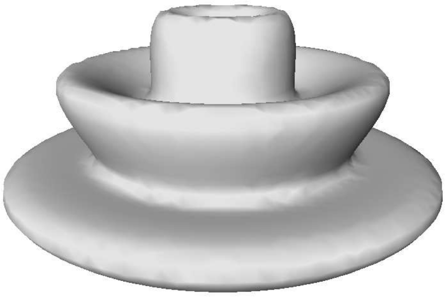

Figure 8.1: Flame surface for the $c3$ configuration in the upper hemisphere of a star

stars), a major advantage of the $c3$ ignition is the applicability for coarse numerical resolutions.

Provided that the grid is sufficiently fine (bubbles with radius smaller than ~ 2 grid spacings Δ will not evolve but dissolve for numerical reasons), the employment of a large number of bubbles at $t = 0$ s is a promising realisation of the multi-spot ignition scenario [RHNW06].

The detonations initiated in the framework of this thesis are started with a spherically burnt region, which were usually ignited exactly at the centre, whereas the radius is chosen to be twice the grid spacing Δ.

8.2 Ignitions at different instants in time

8.2.1 Stochastic ignition

In an extension to the static ignition approach, the stochastic ignition model, initiating flame seeds at different instants in time as described in Ref. [SN06], was applied. A snapshot of the bubbles that are stochastically placed in a delayed manner near the stellar centre within the first tenths of a second can be seen in Fig. 12.12(a).

According to Eq. (4.1), the background temperature of the WD models are determined by the following formula:

$$T_a(r) \;=\; \max\left\{T_0\left[1-\frac{r^2}{\Lambda^2}\right],\, T_{\text{ext}}\right\}\;, \tag{8.1}$$

where r is the distance to the centre, $\Lambda = 7.35\times 10^7$ cm is the extension of the convective zone for WDs with central density of 2×10^9 g/cm^3 and T_{ext} is the temperature profile of the WD without the convective temperature peak for the interior regions. According to Figs. 3.1 and 3.3, T_{ext} possesses an accretion induced peak at the surface layers for accreting WDs. This outer peak is assumed not to be significant in terms of the ignition process because the corresponding temperature of the region heated by accretion is $\lesssim 5\times 10^8$ K for all models.

The temperature fluctuations relative to the background temperature, $\delta T_b/T_a$, are computed according to Eqs. (4.2) and (4.3) for the isotropic and the dipole case, respectively. The contained parameter Λ/R (where R is the mixing length) is set to unity in all calculations, allowing for ignitions to occur in the entire convective region.

The ignition algorithm is based upon the Poisson process, which yields the following expression for the probability of i ignitions within the time interval δt:

$$P_{t,r}(i,\delta t) \;=\; \frac{(\nu_{t,r}\;\delta t)^{\,i}}{i\,!}\,\exp\left(-\nu_{t,r}\;\delta t\right) \tag{8.2}$$

Here, $\nu_{t,r}$ is a function of the temperature excess δT_b and the thermodynamic background state. As explained in the following, an expression for $\nu_{t,r}$ can be derived. For a region of approximately equivalent background state, the number of ignitions per unit time increases proportionally with the volume of fuel. Since concentric shells contain material with roughly the same background state, the ignition probability in shells with width $\delta r \ll R$, denoted by $P_{t,r,\delta r}(i, \delta t)$, is considered in the following.

The ignition probability $P_{t,r,\delta r}(i, \delta t)$ is increased if either the sampling time δt or the ratio of the fuel volume relative to a unit volume is increased. $\nu_{t,r}$ in Eq. (8.2) is a function of shell mean values:

$$\nu_{t,r,\delta t} \;=\; \langle \nu_{t,r}\ \Theta[G(t,r)] \rangle_{\,r,\delta r}\ \frac{3\, r^{\,2}\, \delta r}{r_b^3} \tag{8.3}$$

Here, $G(t,r)$ results from the G-equation (cf. Eq. (7.2)), i.e., $\Theta[G(t,r)]$ is unity in fuel and zero in ash regions. Furthermore, the angle bracket $\langle\ \ \rangle_{\,r,\delta r}$ denotes the average of the quantity $\nu_{t,r}$ that is yet to be determined over shells of radius r and thickness δr. The expression is normalised by a sphere with radius r_b enclosing the central burning region.

$\nu_{t,r,\delta t}$ represents an inverse time scale (cf. Eq. (8.2)) and is non-zero only in unburnt material. It can be approximated by the following expression, which computes the average quantities of the shell that are important for the ignition process:

$$\langle \nu_{t,r}\ \Theta[G(t,r)] \rangle_{\,r,\delta r} \;=\; \chi_{u,r,\delta r}(t)\ \cdot\ C_e\, \frac{S_{\mathrm{nuc}}}{c_P\ \delta T_b}\ , \tag{8.4}$$

where c_P is the heat capacity for the average temperature and S_{nuc} the nuclear energy generation rate for the average mass density of unburnt material within a particular shell. $\chi_{u,r,\delta r}(t)$ represents the volume fraction of the unburnt fluid of the cell at instant t. The only free parameter of the model, C_e, is called the *exponentiation parameter* and controls the overall speed of the ignition process.

Strictly speaking, this procedure cannot be applied to very deformed stars since it postulates spherical symmetry of the central burning region. But not only do the elongated rotators deviate from spherical symmetry, also the initially spherical non-rotating WDs are no longer symmetric as soon as the ignition process is started because of the mixing of fuel and ashes caused by turbulent combustion. However, it turns out that the spatial variation of the background state variables of unburnt material contained within a thin spherical shell at an instant in time is small. Moreover, it is shown that for densities $\rho \gtrsim 0.05\ \rho_c$ the WD remains almost spherical. This observation justifies the implementation of the ignition process even for rotating WDs (cf. section 11.5, [Ste90], [YL05]).

Furthermore, a derivation of the dipole jet flow (cf. section 4.2) conditions from spherical shells is not coherent in detail but is a sufficiently good approximation as long as the ignition sites are placed according to the flow scheme.

8.2.2 Implementation details

The ignition routine, which is called every second hydrodynamical time step, operates as follows:

- The number of possible ignitions in each shell (the burning region was divided into 24 equidistant concentric shells for most of the simulations done for this thesis) is determined according to Eqs. (8.2), (8.3), and (8.4). Note that for the two possible modes, *isotropic turbulence* and *dipole jet flow* (cf. section 4.2), the calculation differs in the expression for the temperature fluctuations δT_b (Eqs. (4.2) and (4.3), respectively) and furthermore in the value of r_b in Eq. (8.3) (Eqs. (24) and (27) in Ref. [WW04], respectively).
- Determination of the ignition location:
  - In the isotropic case, the chosen ignition locations are uniformly distributed within the corresponding shell.
  - For the jet flow, the distribution of polar angles θ is not uniform because more ignitions should occur when convective material has flowed through the centre, thereby heating up. Consequently, ignition sites are thought to be clustered along the rotational axis in one of the hemispheres (cf. section 4.2). This is implemented by the following choice of θ:

    $$\theta \;=\; \pi \cdot (\, rand \,)^{\,\mathrm{D_e}} \tag{8.5}$$

    Here, *rand* is a function which returns uniformly distributed numbers in the range between 0 and 1 and $\mathrm{D_e}$ is the *dipole ignition exponent*. For $\mathrm{D_e} = 1$, equipartition in θ is achieved. In the simulations of this thesis, $\mathrm{D_e} = 1/3$, yielding a pronounced appearance in the southern hemisphere (in the convention that the position vector for $\theta = 0$ points towards the North Pole in spherical coordinates).

  At the elected positions, an ignition is “planned”, i.e., a bubble with radius $3\,\Delta$ (where Δ is the time-dependent grid spacing) is placed. Note that this ignition only leads to burning if it is placed within unburnt matter. Furthermore, note that an ignition does not necessarily form a sphere. Particularly, when a lot of ignitions have already been successfully set, a new incineration often leads only to a minor increment of burnt material by causing a new buckle on the already burnt material.

- If the maximum density occurring in the star drops below 0.5×10^{9} g/cm^3, ignitions are no longer initiated. Depending on the initial model as well on the explosion strength and therefore on the total number of ignitions, this typically occurs for $t \lesssim 0.7$ s.

9 Comoving hybrid grid

The computational grid employed in this study is neither fixed in time (Eulerian grid) nor tracks individual fluid elements (Lagrangian grid) but describes a different approach (cf. section 5.1.1). Since the region of interest, initially a WD of radius $\sim 2 \times 10^8$ cm, expands steadily once the explosion is initiated (size of the computational domain $\sim 5 \times 10^9$ cm after $t = 5$ s), it is convenient to follow this expansion with a comoving hybrid grid.

Both an Eulerian and a Lagrangian grid show major disadvantages in the context of SNe Ia explosions. If the grid is static, either the explosion simulation is limited to a short interval in time since material escapes beyond the domain boundaries early or the resolution is generally very coarse (note that the Eulerian implementation of a grid whose cells increase in the outer regions exponentially corrects this problem to a certain degree; however, a non-uniform grid evokes different problems, e.g., for the implementation of a subgrid scale model; cf. section 7.1.2). Additionally, the adoption of an *adaptive mesh refinement* approach is not favourable since the explosive burning in a SN Ia soon becomes highly structured due to turbulent motion that develops *everywhere*. In this case, refinement would simply be too costly. If the grid follows the turbulent fluid motion (and thus prevents any unphysical diffusion), it becomes contorted after a short time in the presence of turbulence and grid tangling occurs. The latter can only be avoided by assigning a new grid, which is a complicated procedure with respect to the conservation of quantities [Mü94].

The comoving grid described in the following is well suited for simulating SNe Ia. By virtue of the adaptiveness of the hybrid implementation it is above all advantageous for aspherical explosions that occur for rapidly rotating progenitor stars. In the following, the impact on the equations of hydrodynamics is introduced. Then the grid geometry itself is described. Implementation details and a stability test close the chapter.

9.1 Moving grid transport theorem

When using a moving grid, the hydrodynamics equations change [Mü94], [Rö05]. The necessary modifications are derived in this section.

In a similar way to the fluid velocity (Eq. (5.6)), a *grid velocity* $\boldsymbol{v}_{\rm grid}$ is introduced:

$$\boldsymbol{v}_{\rm grid} \;=\; \frac{\mathbb{D}}{\mathbb{D}\,t}\,\boldsymbol{r}_{\rm grid} \tag{9.1}$$

$\mathbb{D}/\mathbb{D}t$ is the *moving grid derivative*, defined as the derivative with respect to fixed values of the moving grid; $\boldsymbol{r}_{\rm grid} = (r_1^{\rm grid}, r_2^{\rm grid}, r_3^{\rm grid})$ denotes the position of the grid coordinate. The *relative velocity* $\boldsymbol{v}_{\rm rel}$ between fluid and moving grid is

$$\boldsymbol{v}_{\rm rel} \;=\; \boldsymbol{v} \;-\; \boldsymbol{v}_{\rm grid}\ . \tag{9.2}$$

From Eq. (9.2) it is clear that Eulerian and Lagrangian coordinates represent the limiting cases of $\boldsymbol{v}_{\rm grid} = 0$ and $\boldsymbol{v}_{\rm grid} = \boldsymbol{v}$, respectively.

According to Eq. (5.8), which relates Lagrangian to Eulerian coordinates,

$$\frac{\mathbb{D}}{\mathbb{D}\,t}\,a \;=\; \frac{\partial}{\partial\,t}\,a \;+\; (\boldsymbol{v}_{\rm grid}\cdot{\rm grad})\,a \tag{9.3}$$

relates the moving grid to Eulerian time derivative of a quantity a. Furthermore, corresponding to the Jacobian (Eq. (5.10)) of the transformation relating an Eulerian volume element to the corresponding element in material variables, the Jacobian $J_{\rm grid}$ transforms the initial volume ${\rm d}V_{\rm grid}^0$ into its moving grid volume ${\rm d}V_{\rm grid}$:

$${\rm d}V_{\rm grid} \;=\; J_{\rm grid}\,{\rm d}V_{\rm grid}^0 \tag{9.4}$$

Corresponding to the derivation of the Reynolds theorem (Eqs. (5.13) and (5.14)), the *moving grid transport theorem* is obtained:

$$\begin{aligned}\frac{\rm d}{{\rm d}\,t}\int\limits_{V_{\rm grid}(t)} a\,{\rm d}V_{\rm grid} \;&=\; \int\limits_{V_{\rm grid}(t)}\left(\frac{\mathbb{D}\,a}{\mathbb{D}\,t} \;+\; a\,{\rm div}\,\boldsymbol{v}_{\rm grid}\right){\rm d}V_{\rm grid}\\ &=\; \int\limits_{V_{\rm grid}(t)}\left[\frac{\partial\,a}{\partial\,t} \;+\; {\rm div}\,(a\,\boldsymbol{v}_{\rm grid})\right]{\rm d}V_{\rm grid}\end{aligned} \tag{9.5}$$

Inserting the general form of a balance equation in Eulerian form (Eq. (5.16)) into Eq. (9.5), the expression that defines the set of equations of hydrodynamics with the appropriate quantities a and source terms $B(a)$ can be written as follows:

$$B(a) \;=\; \int\limits_{V_{\rm grid}(t)} b(a)\;{\rm d}V_{\rm grid} \;=\; \frac{\partial}{\partial\,t}\int\limits_{V_{{\rm grid}\ t}} a\;{\rm d}V_{\rm grid} \;+\; \int\limits_{V_{\rm grid}(t)} {\rm div}\,(a\,\boldsymbol{v}_{\rm rel})\;{\rm d}V_{\rm grid} \tag{9.6}$$

$$\;=\; \frac{\partial}{\partial\,t}\int\limits_{V_{{\rm grid}\ t}} a\;{\rm d}V_{\rm grid} \;+\; \oint\limits_{S_{\rm grid}(t)} a\,\boldsymbol{v}_{\rm rel}\cdot\boldsymbol{n}\;{\rm d}S_{\rm grid} \tag{9.7}$$

The moving grid theorem describes the rate of change of a quantity a that, similar to Eq. (5.14), consists of two contributions: the rate of change over a fixed volume $V_{\mathrm{grid}\,t}$ (coinciding with the grid volume $V_{\mathrm{grid}}(t)$ at instant t) and the contribution of the flux of a on the boundary surface $S_{\mathrm{grid}}(t)$.

By comparing Eq. (9.7) with Eq. (5.14) is is clear that the changes in the implementation of the reactive Euler equations (cf. section 5.1.3) are only minor: the advected fluid velocity $\boldsymbol{v}$ has to be replaced by the relative velocity $\boldsymbol{v}_{\mathrm{rel}}$ whereas the velocities implied in the quantity a, i.e., in the form of momentum and energy density, remain unchanged.

9.2 Grid geometry

Although a grid that expands uniformly in space (i.e., all grid spacings are equal at a certain instant) is capable to follow an explosion, it has a major shortcoming [Rö05]. First, the resolution of the central part that is important for the explosion is initially high but is much lower as soon as the WD expands. Second, due to the implementation of the flame ignition that does not consider pressure equilibrium between fuel and ashes, the time step of the simulation is soon limited by shock waves that move towards the boundaries of the computational domain.

Therefore a different approach was followed. The grid is initially set up with a fine central resolution and an exponentially increasing cell width outwards. The fine grid encloses the region where the flame resides (or is capable of being ignited, cf. section 8.2). As soon as the thermonuclear runaway is started, the grid expands rectilinearly on the basis of two contributions: the inner part moves to follow the radial motion $v_{\mathrm{r,\,flame}}$ of a shell with radius r_{flame} which contains the outermost flame position, and the outer part expands to follow the expansion of the star with velocity $v_{\mathrm{r,\,WD}}$ where the star's surface is found at the radius r_{WD}. The velocities of the grid's supporting points are then defined in the following way:

$$v^{x}_{\mathrm{grid}} = \begin{cases} v_{\mathrm{r,\,flame}} \cdot \dfrac{x}{r_{\mathrm{flame}}} & \text{for} \quad x \leq r_{\mathrm{flame}} \\[2ex] v_{\mathrm{r,\,WD}} \cdot \dfrac{x}{r_{\mathrm{WD}}} & \text{for} \quad x > r_{\mathrm{flame}} \end{cases} \tag{9.8}$$

Here x denotes the x- component of the distance to the centre of the computational domain where the shells — tracking the flame and the surface of the WD — are centred. The grid velocities in y- and z- direction are computed accordingly.

Since the flame burns faster than the WD expands, the equally spaced flame grid will penetrate into the non-equidistant outer grid and increase the number of flame grid cells at the cost of outer cells.

9.2.1 Implementation details

For the successful realisation of this procedure, several aspects had to be considered in the implementation. First, the surface radius r_{WD} in Eq. (9.8) has to be found. Since neither the pressure nor the temperature vanish at the surface for numerical reasons and since rapidly rotating WDs are not spherical, a procedure to determine r_{WD} must be found: the radius of a sphere enclosing a certain amount of mass is chosen to be r_{WD}. Then $v_{\mathrm{r,\,WD}}$ is the mean radial velocity of a sufficient amount of cells lying on that spherical surface. When the enclosed mass approaches the total stellar mass, this procedure also works accurately for very deformed stars. In practise, the enclosed mass was chosen to be about 99.8 % of the total stellar mass.

Similarly, the outermost position of the flame r_{flame} is defined as a mean value of flame positions located on a shell. Due to numerics, taking only the radial velocity of the cell containing the flame that is farthest from the origin is problematic. Instead, mean values of a certain number of cells lying outside and housing the flame are taken for obtaining r_{flame} and $v_{\mathrm{r,\,flame}}$.

In addition, since the flame burns outwards efficiently at the beginning, the inner grid with equidistant spacing expands at the cost of the outer grid with non-equidistant spacing. But since the star itself does not start to expand before a sound crossing time, the size of the computational domain could shrink although all grid points move outwards. This is due to the fact that the outermost and largest cells may be cancelled when the grid is rearranged with respect to the increasing number of equidistant cells of the flame grid. Therefore, Eq. (9.8) is replaced by a more complex expression:

- expansion of the *entire* grid with velocity $v_{\mathrm{r,\,WD}}$ when the flame is located deep within the equidistant flame grid, or
- expansion of the *entire* grid with velocity $v_{\mathrm{r,\,flame}}$ when the
    1. flame tends to extend beyond the star, or
    2. WD tends to extend beyond the computational domain, or
    3. flame tends to extend beyond the equidistant flame grid as a consequence of an underestimated value of $v_{\mathrm{r,\,flame}}$ (additionally, $v_{\mathrm{r,\,flame}}$ is increased by the factor 1.4 in this condition)
- else expansion as a *hybrid* grid as described by Eq. (9.8)

A benefit of the hybrid grid is its enormous flexibility for the explosion at run time. However, when doing the analysis one has to keep in mind that the dynamics of an individual simulation creates its own grid (in general, the relationship holds that more energetic events cause higher radial velocities and therefore are subject to coarser resolution compared to weak explosions), making direct comparisons difficult even for an identical initial grid.

Recapitulating, it is found that the grid motion does not cause numerical problems even if the expansion is done in a unsteady way (cf. the 3rd condition of the second item in the criteria of choices).

9.2.2 Following a grid expansion

Figs. 9.1, 9.3, and 9.5 show a cross section of the yz-plane of the computational grid of the “14AWD4 $C_e = 5 \times 10^4$ ” explosion model which can be viewed as representative in terms of grid expansion. The corresponding density profiles are plotted in Figs. 9.2, 9.4, and 9.6 as a cross section along the rotational axis, where the flame is displayed by a white thick line. For the sake of clarity only every 4th grid line is drawn. Mirror symmetry at the equatorial plane of the star is assumed, i.e., just one hemisphere is calculated (only positive coordinate values of the z-axis).

The grid consists of $256^2 \times 128$ cells that initially span a volume of $(2 \cdot 5.43 \times 10^8\ \mathrm{cm})^2 \times (5.43 \times 10^8\ \mathrm{cm})$. The number of equidistant cells enclosing the flame is 80^3 per octant. The resolution of the flame grid is $\Delta x = 7.50 \times 10^5$ cm at $t = 0.05$ s (see Fig. 9.8). The red circle denotes r_{flame}, the outermost position of any cell containing the flame, and is thus always enclosed by the equidistant flame grid. The blue line represents r_{WD} and contains nearly all the mass of the WD. It is used to expand the outer non-equidistant grid region.

While the flame burns outwards, it occupies more and more cells. The number of equidistant cells has increased to 97^3 per octant at $t = 0.5$ s (see Fig. 9.3). The flame grid resolution then is $\Delta x = 1.82 \times 10^6$ cm, and the size of the computation domain has shrunk to 4.36×10^8 cm (see Fig. 9.7).

In the homologous expansion phase (cf. section 9.3; $t = 5.0$ s, see Fig. 9.5), the number of equidistant cells is 106^3 (total of 128^3) per octant. $\Delta x = 7.58 \times 10^7$ cm. The computational domain extends up to 1.24×10^{10} cm in every spatial direction. When burning has ceased ($t \gtrsim 1.5$ s), the level set (i.e., the white thick line; cf. section 7.1.1) no longer represents the flame but a borderline between fuel and ashes that drift outwards. r_{flame} is greater than r_{WD} as soon as any burnt material passes the region containing most of the mass. Compared to non-rotating explosions, this usually happens much sooner for explosions of rotating stars since the flame breaks out of the WD in the polar regions earlier.

Note that the computation domain shrinks near the beginning (up to $t \sim 0.6$ s, see Fig. 9.7). This behaviour seems surprising as both r_{flame} and r_{WD} increase with time. It is explained by the fact that the number of equidistant grid cells increases at the cost of outer elongated grid cells when the flame travels initially outwards. The expansion of the WD that is not possible before a sound crossing time magnifies the domain in the following.

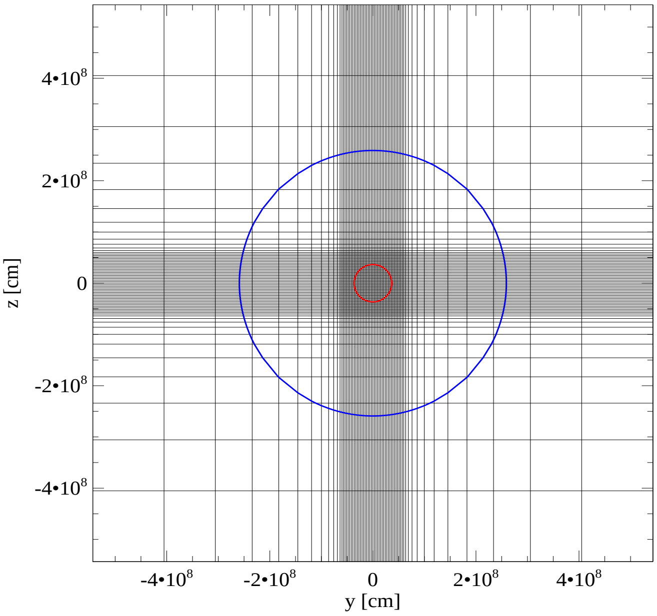

Figure 9.1: Grid of the "14AWD4 $C_e = 5 \times 10^4$" explosion model at $t = 0.05$ s. The number of equidistant cells per octant is 80^3 with a total of 128^3. $r_{\rm WD} = 2.59 \times 10^8$ cm (blue circle) moves outwards with $v_{\rm WD} = 0.00$ cm/s, $r_{\rm flame} = 3.6 \times 10^7$ cm (red circle) moves outwards with $v_{\rm flame} = 6.0 \times 10^7$ cm/s. For the sake of clarity, only every 4th grid line is drawn.

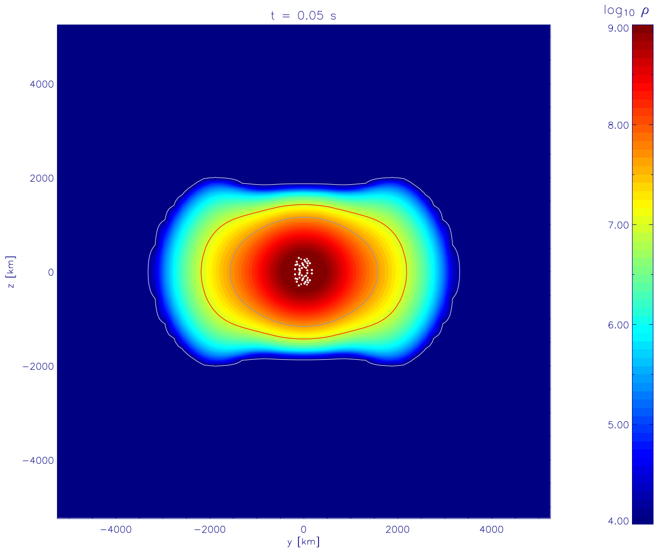

Figure 9.2: Density contours and the flame (white thick contour line) of the "14AWD4 $C_e = 5 \times 10^4$" explosion at $t = 0.05$ s. The grey thick contour line encloses densities greater than 5.25×10^7 g/cm^3, the red line greater than 1.05×10^7 g/cm^3, and the white line greater than 10^4 g/cm^3. Equatorial symmetry is assumed.

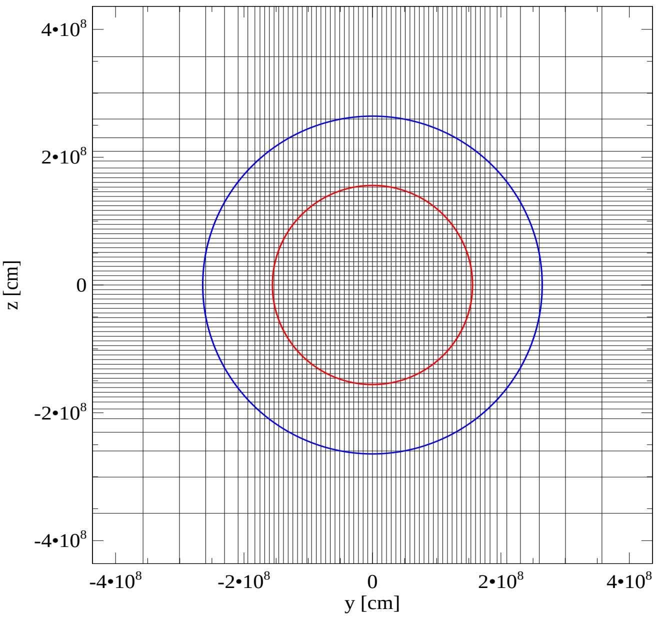

Figure 9.3: Grid of the "14AWD4 $C_e = 5 \times 10^4$ " explosion model at $t = 0.50$ s. The number of equidistant cells per octant is 97^3 with a total of 128^3. $r_{\mathrm{WD}} = 2.64 \times 10^8$ cm (blue circle) moves outwards with $v_{\mathrm{WD}} = 9.8 \times 10^7$ cm/s, $r_{\mathrm{flame}} = 1.55 \times 10^8$ cm (red circle) moves outwards with $v_{\mathrm{flame}} = 5.11 \times 10^8$ cm/s. For the sake of clarity, only every 4th grid line is drawn.

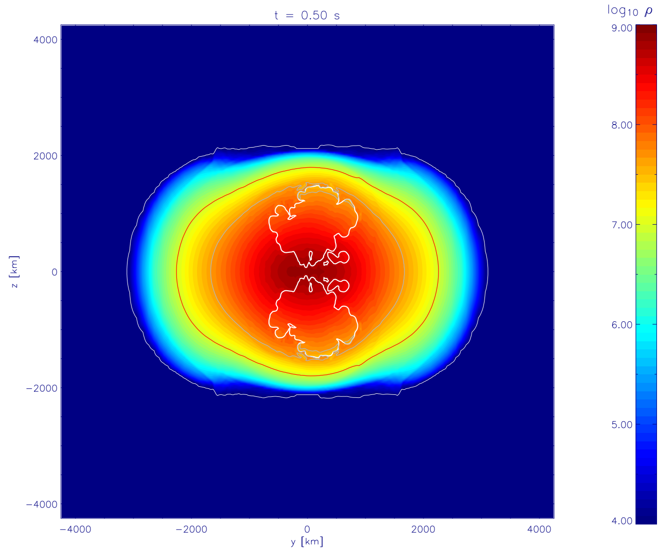

Figure 9.4: Density contours and the flame (white thick contour line) of the "14AWD4 $C_e = 5 \times 10^4$ " explosion at $t = 0.50$ s. Equatorial symmetry is assumed.

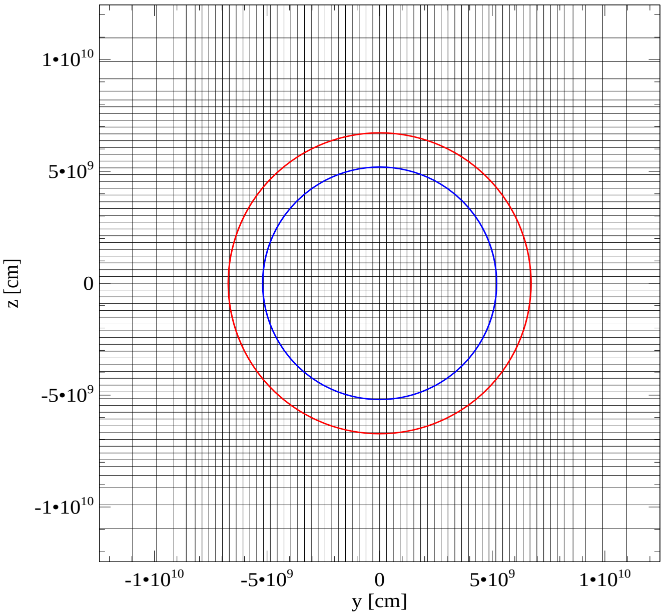

Figure 9.5: Grid of the “14AWD4 $C_e = 5 \times 10^4$ ” explosion model at $t = 5.00$ s. The number of equidistant cells per octant is 106^3 with a total of 128^3. $r_{\mathrm{WD}} = 5.196 \times 10^9$ cm (blue circle) moves outwards with $v_{\mathrm{WD}} = 1.143 \times 10^9$ cm/s, $r_{\mathrm{flame}} = 6.724 \times 10^9$ cm (red circle) moves outwards with $v_{\mathrm{flame}} = 1.489 \times 10^9$ cm/s. For the sake of clarity, only every 4th grid line is drawn.

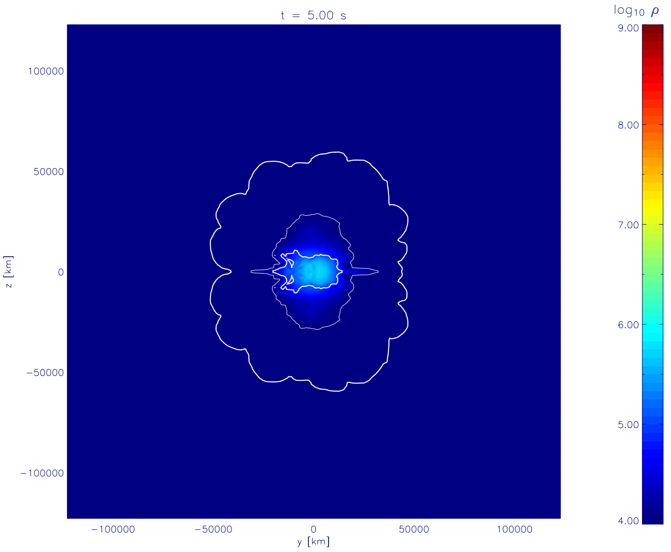

Figure 9.6: Density contours and the flame (white thick contour line) of the “14AWD4 $C_e = 5 \times 10^4$ ” explosion at $t = 5.00$ s. Equatorial symmetry is assumed.

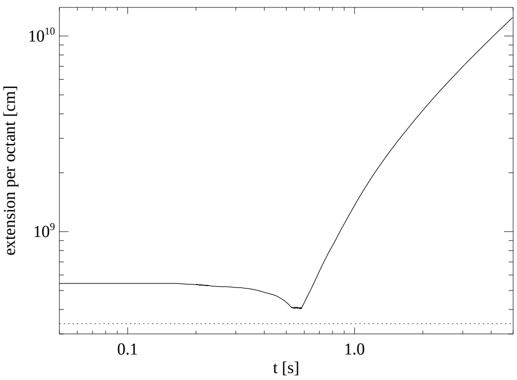

(a) domain extension

Figure 9.7: Temporal evolution of the computational domain size per octant for the "14AWD4 $C_e = 5 \times 10^4$ " explosion. The dashed line represents the initial equatorial radius of the 14AWD4 rotator.

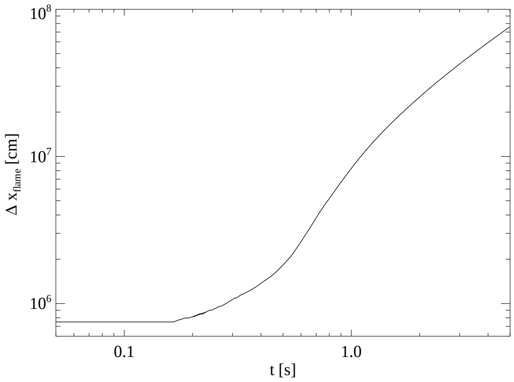

(a) flame grid spacing

Figure 9.8: Temporal evolution of the cell size of the equidistant flame grid of the "14AWD4 $C_e = 5 \times 10^4$ " explosion model

9.3 Homologous expansion phase

The moving grid enables one to follow the explosion. Although the burning process in terms of SNe Ia is finished after ~ 1.5 s (see the evolution of E_{nuc} in Fig. 9.9), the subsequent expansion phase may have a significant impact on the synthetic spectra until the *homologous* expansion is reached [Rö05].

The homologous or self-similar expansion is characterised by a fluid velocity that is proportional to the central distance r :

$$v(r) \;\propto\; r \tag{9.9}$$

As soon as Eq. (9.9) is fulfilled at every location $\boldsymbol{r}$, the relative positions of the ejecta do not change anymore. The instant of reaching homologous expansion can be estimated by a comparison of the different contributions to the total energy. Most of the energy released in the explosion is needed to stem the initially high gravitational attraction of the star. As a result of the expansion, the WD cools and has excess kinetic energy. Therefore, the homologous phase is indicated by a small amount of gravitational and internal energies compared to the kinetic energy.

Fig. 9.9 shows that after $t = 5$ s, both the gravitational energy ($E_{grav}^{5\,\mathrm{s}} = -0.89 \times 10^{50}$ erg) and internal energy ($E_{int}^{5\,\mathrm{s}} = 0.22 \times 10^{50}$ erg) are small compared to the kinetic energy ($E_{kin}^{5\,\mathrm{s}} = 7.70 \times 10^{50}$ erg). Although this trend becomes even clearer

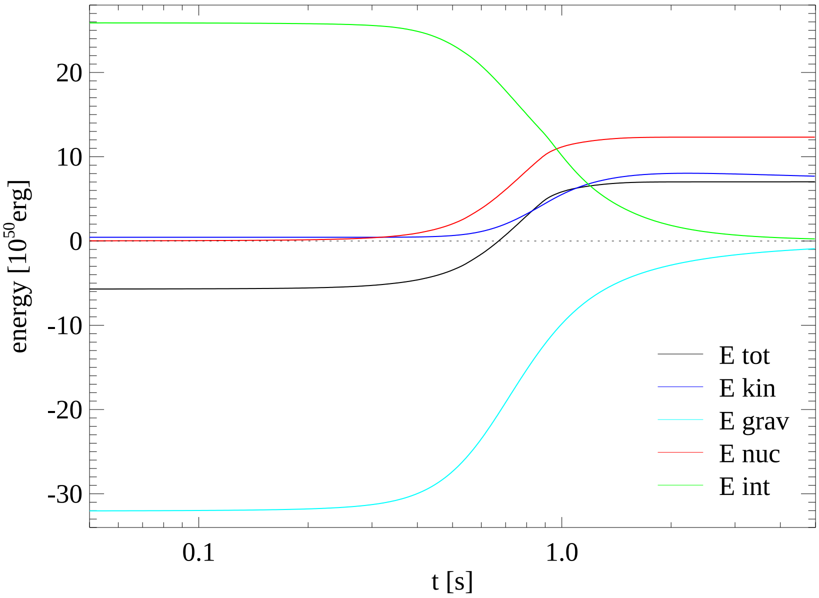

Figure 9.9: Temporal evolution of the different energy contributions of the 8rigid model (stochastic ignition: $C_e = 5 \times 10^3$) is plotted. At $t = 5$ s both the gravitational and internal energy are small compared to the kinetic energy.

after $t = 10$ s [Rö05], due to the cost of three-dimensional calculations all simulations for this thesis were stopped after $t = 5$ s which is nevertheless a good approximation for the instant when homologous expansion is achieved.

9.4 Test for hydrostatic stability

A star in hydrostatic equilibrium (i.e., fulfilling the temporally constant version of Eq. (5.20)) remains unchanged. However, in practice the numerical discretisation will cause fluctuations in the density and velocity profiles sooner or later, especially when the star rotates rapidly. In addition to effects of the hydrodynamical setup such as the flux splitting scheme [Mü94], several mechanisms, not necessarily strictly distinguishable from each another, may contribute (cf. sections 10.4 (approximated gravitational potential), 11.3 (oscillation of state variables), and 11.4 (interpolation effects)).

Axially symmetric motion follows an orbit that can only be approximated by small alternating perpendicular steps on a Cartesian grid. The smaller these steps are, the more accurately an axially symmetric motion can be described. Unless the grid spacing is fine enough, problems regarding the rotation occur.

It was tested whether rapid rotators remain stable on the grid structure that

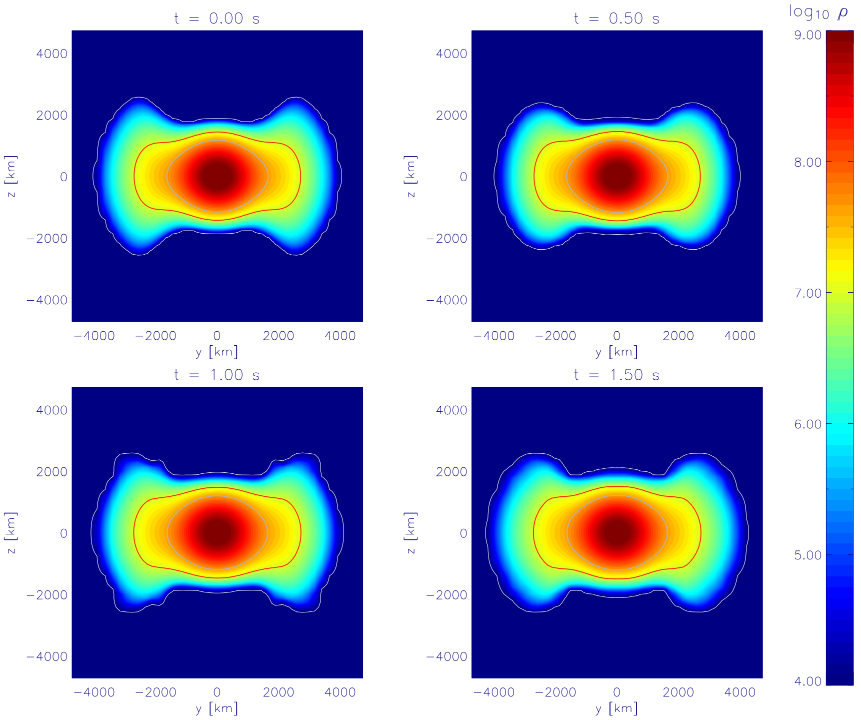

Figure 9.10: Density contours for the 20AWD3 model during the test for hydrostatic stability. Equatorial symmetry is assumed.

was used for the SNe Ia simulations for the period of nuclear burning. For the hydrostatic stability test the grid introduced in section 9.2 was used. However, no temporal motion of the grid was allowed since neither expansion nor contraction of the star occur as long as hydrostatic equilibrium is maintained. The simulations were followed up to $t = 1.5$ s, the time when burning would have stopped if the WD had been ignited.

A comparison of density contours at different instants serves as a simple check for hydrostatic stability. Figs. 9.10, C.2, and C.3 show the density profiles of the 20AWD3, 10AWD1, and 8rigid rotators in the yz-plane (rotation axis in z-direction), respectively. The grey thick contour line encloses densities of $\rho > 5.25 \times 10^7$ g/cm^3, the red thick line $\rho > 1.05 \times 10^7$ g/cm^3, and the white outer line marks $\rho = 10^4$ g/cm^3. Up to $t = 1.0$ s, the contour lines retain their shape except at the surface. Later the WDs' core density becomes lower. Two reasons are responsible for amplified deviations in the outer layers. First, the resolution of the grid is worse there (see panel for $t = 1.00$ s in Fig. 9.10 where the grid structure affects the stellar surface). Second, no pressure gradient is considered below the threshold density of $\rho = 10^{-3}$ g/cm^3.

Figs. 9.11, C.1(a), and C.1(b) show the absolute value of the radial velocities $|v_{\rm rad}|$

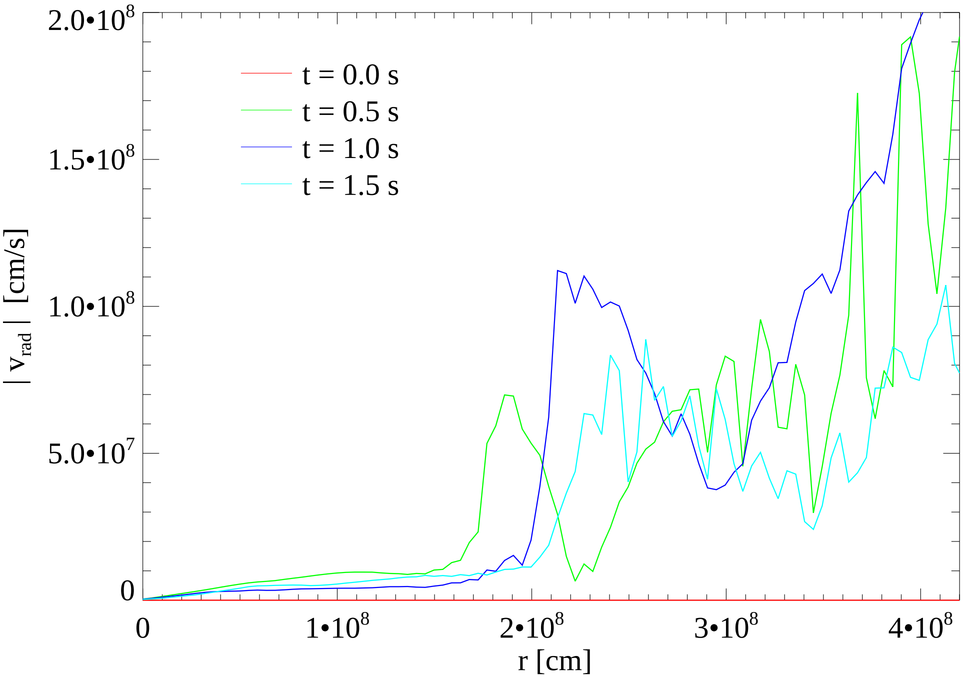

Figure 9.11: Modulus of the radial velocity as function of the central distance at four different times for the 20AWD3 model

that are averaged at certain distances from the stellar centre r in one section of the three-dimensional domain. The restriction of axial symmetry for the WD models in equilibrium (cf. section 5.2) does not allow for any radial motion, therefore $|v_{\mathrm{rad}}|$ indicates instabilities caused by the grid among other things.

Similar to the simulations without rotation [Rei01], the highest radial velocities occur in the outer regions whereas the value of $|v_{\mathrm{rad}}|$ in the central region is low. The missing pressure gradient in the pseudo-vacuum surrounding the star causes high infalling velocities of less dense matter. The radial velocities in the inner region are at all instants found to be $\lesssim 4 \times 10^7$ cm/s and therefore an order of magnitude lower than the characteristic velocities due to nuclear burning. The high radial velocities resulting for inner regions in the analysis for the 20AWD3 model (see Fig. 9.11) are explained by the low value of the polar radius (cf. Table 11.2). It causes biased statistics since high $|v_{\mathrm{rad}}|$ at the polar surface appear at distances r that are important for burning near the equatorial plane (see the broad bulge of material enclosed by the red line in Fig. 9.10).

Since the mass fraction of the problematic surface regions is negligible and furthermore burning does not take place there, the stability of all discretised models on the grid can be assumed.

10 Gravity

The gravitational force compensates for the counteracting pressure gradient and the centrifugal force, both acting outwards, within a rotating star in hydrostatic equilibrium.

This chapter describes an efficient way to compute the gravitational potential of deformed rotators in hydrodynamics simulations that cannot be approximated by a radially symmetric matter distribution due to their oblate shapes.

10.1 Gravity in rotating white dwarfs

In order to account for the effect of self-gravity, the gravitational potential $\Phi_g(\boldsymbol{r})$ has to be computed. Although WD matter prior to carbon ignition has high densities ($\rho_c \sim 2 \times 10^9$ g/cm^3 [LHT$^+$06]), it is sufficiently low to work in the Newtonian limit [Dem98] [1].

In this limit, $\Phi_g(\boldsymbol{r})$ is obtained via Poisson's equation

$$\nabla^2 \, \Phi_g(\boldsymbol{r}) = 4\pi \, G \, \rho(\boldsymbol{r}) \ , \tag{10.1}$$

where the source $\rho(\boldsymbol{r})$ is the density distribution at position $\boldsymbol{r}$ and G is Newton's gravitational constant, i.e., $\Phi_g(\boldsymbol{r})$ is derived from a density distribution by a homogeneous second-order elliptic partial differential equation. The integral form of Eq. (10.1) directly leads to Φ_g at point $\boldsymbol{r}$:

$$\Phi_g(\boldsymbol{r}) = - \, G \int\limits_V \frac{\rho(\boldsymbol{r}')}{|\boldsymbol{r} - \boldsymbol{r}'|} \, \mathrm{d}\boldsymbol{r}' \tag{10.2}$$

As can be seen from Eq. (10.2), the density values $\rho(\boldsymbol{r'})$ of all positions $\boldsymbol{r'}$ contribute to the solution of $\Phi_g(\boldsymbol{r})$. Density changes at arbitrary distances from $\boldsymbol{r}$ will immediately affect the value of $\Phi_g(\boldsymbol{r})$.

---

[1] The potential influence of general relativistic (GR) effects has been calculated both by generating a rotating WD with a code that considers GR effects [KEH89], and by examining the localised Schwarzschild radii, i.e., the Schwarzschild radii derived for enclosed matter along the line centre − stellar surface . In both cases, the consideration of GR effects turned out to be dispensable.

Because of this highly non-local nature of Eq. (10.2), the computation of $\Phi_g(\boldsymbol{r})$ in hydrodynamics simulations is costly even with the power of today's supercomputers. The hydrodynamics code PROMETHEUS processes the gravitational accelerations whenever a "hydro sweep" is executed (see appendix A), i.e., a one-dimensional subroutine (obtained by the method of "dimension-splitting", see Ref. [Mü94]) is solved. Since for a three-dimensional simulation three hydro sweeps which change the source $\rho(\boldsymbol{r})$ are executed for each increment of time, $\Phi_g(\boldsymbol{r})$ has to be calculated triply per time increment. Therefore, $\Phi_g(\boldsymbol{r})$ must be derived efficiently. Solving (10.2) directly whereby the interactions of all computational grid cells must be considered makes great demands on the CPU power in three spatial dimensions. Furthermore it is not possible on a computer cluster with distributed memory since intensive communication is necessary, more precisely the interchange of all density values.

10.2 Multipole expansion of Poisson's equation

A multipole expansion of $\Phi_g(\boldsymbol{r})$ can be an efficient method in order to deal with the non-locality of Eq. (10.2) when it is justifiable to terminate the expansion at a low order. Every deviation of the density stratification from spherical symmetry demands inclusion of higher order terms. However, WDs that are noticeably deformed by rotation exhibit cylindrical symmetry (cf. section 5.2), which favours the method of a multipole expansion. $\Phi_g(\boldsymbol{r})$ can be computed to high precision by expanding $\Phi_g(\boldsymbol{r})$ only up to low order terms (cf. section 10.3 and Ref. [Fli93]).

The Green's function for Eq. (10.2) expanded in spherical harmonics $Y_l^m(\theta, \phi)$ looks as follows [Jac98]:

$$\frac{1}{|\boldsymbol{r}-\boldsymbol{r}'|} = 4\pi \sum_{l=0}^{\infty} \sum_{m=-l}^{l} \frac{1}{2l+1} \frac{r_<^l}{r_>^{l+1}} \, Y_{lm}^*(\theta', \phi') \, Y_{lm}(\theta, \phi) \,, \tag{10.3}$$

where

$$r_< \equiv min\{|\boldsymbol{r}|\,, |\boldsymbol{r}'|\} \tag{10.4}$$
$$r_> \equiv max\{|\boldsymbol{r}|\,, |\boldsymbol{r}'|\} \tag{10.5}$$

and the components of $\boldsymbol{r}$ and $\boldsymbol{r}'$ are expressed in spherical coordinates (r, θ, ϕ) about the density distribution's centre of mass $\boldsymbol{r}_{cm}$ [Nol99]:

$$\boldsymbol{r}_{cm} = \frac{\int\limits_V \boldsymbol{r}\,\rho\,(\boldsymbol{r})\,\mathrm{d}^3\boldsymbol{r}}{\int\limits_V \rho\,(\boldsymbol{r})\,\mathrm{d}^3\boldsymbol{r}} = \frac{\int\limits_V \boldsymbol{r}\,\rho\,(\boldsymbol{r})\,\mathrm{d}^3\boldsymbol{r}}{M_{total}} \tag{10.6}$$

The expansion about the centre of mass assures that low-multipole terms dominate in Eq. (10.3).

The spherical harmonic functions with the parameters l and m are

$$Y_{lm}(\theta,\phi) \;\equiv\; (-1)^m \sqrt{\frac{2l+1}{4\pi}\frac{(l-m)!}{(l+m)!}}\; P_{lm}\cos(\theta)\; e^{im\phi}\;, \tag{10.7}$$

where P_{lm} are Legendre polynomials. With Eq. (10.3) Poisson's equation (10.2) is as follows:

$$\begin{aligned}\Phi_g(\boldsymbol{r}) = -\,4\pi G \sum_{l=0}^{\infty}\sum_{m=-l}^{l} \frac{1}{2l+1} \Bigg\{ & Y_{lm}(\theta,\phi)\;\times \qquad (10.8)\\ & \left[\, r^{\,l} \int\limits_{r\,<\,r'} \frac{\rho(\boldsymbol{r}')\; Y^*_{lm}(\theta',\phi')}{r'^{\;l+1}}\; d^3\boldsymbol{r}' \;+\; \frac{1}{r^{\;l+1}} \int\limits_{r\,>\,r'} \rho(\boldsymbol{r}')\; Y^*_{lm}(\theta',\phi')\; r'^{\;l}\; d^3\boldsymbol{r}' \,\right] \Bigg\}\end{aligned}$$

The sum over m of the products of the spherical harmonic functions (10.7) for a given value of l becomes

$$\begin{aligned}\sum_{m=-l}^{l} Y^*_{lm}(\theta',\phi')\; Y_{lm}(\theta,\phi) = \frac{2l+1}{4\pi} \Bigg[& P_{l0}(\cos\theta)\; P_{l0}(\cos\theta') \;+ \qquad (10.9)\\ & 2\sum_{m=1}^{l} \frac{(l-m)!}{(l+m)!}\; P_{lm}(\cos\theta)\; P_{lm}(\cos\theta')\;\; \cos\Big(m(\phi-\phi')\Big) \Bigg]\;.\end{aligned}$$

Finally, with this expression and the usage of a trigonometric identity for the difference in azimuthal angles, $\phi-\phi'$, Eq. (10.8) turns into

$$\begin{aligned}\Phi_g(\boldsymbol{r}) = -G\sum_{l=0}^{\infty} P_{l0}(\cos\theta) & \left[r^l\;\mu^{e,out}_{l0}(r) + \frac{1}{r^{l+1}}\;\mu^{e,in}_{l0}(r)\right] - \qquad (10.10)\\ 2G\sum_{l=1}^{\infty}\sum_{m=1}^{l} P_{lm}(\cos\theta) & \Bigg[(r^l\cos m\phi)\;\mu^{e,out}_{l0}(r) \;+\; (r^l \sin m\phi)\;\mu^{o,out}_{lm}(r) \;+\\ & \frac{\cos m\phi}{r^{l+1}}\;\mu^{e,in}_{lm}(r) \;+\; \frac{\sin m\phi}{r^{l+1}}\;\mu^{o,in}_{lm}(r)\Bigg]\;,\end{aligned}$$

where the integrals in (10.8) are substituted by the source moments $\mu_{lm}(r)$:

$$\mu_{lm}^{e,in}(r) \equiv \frac{(l-m)!}{(l+m)!} \int\limits_{r>r'} r'^{\,l} \;\; \rho\,(\boldsymbol{r'})\; P_{lm}(\cos\theta')\cos m\phi' \; \mathrm{d}^3\boldsymbol{r'} \tag{10.11}$$

$$\mu_{lm}^{o,in}(r) \equiv \frac{(l-m)!}{(l+m)!} \int\limits_{r>r'} r'^{\,l} \;\; \rho\,(\boldsymbol{r'})\; P_{lm}(\cos\theta')\sin m\phi' \; \mathrm{d}^3\boldsymbol{r'} \tag{10.12}$$

$$\mu_{lm}^{e,out}(r) \equiv \frac{(l-m)!}{(l+m)!} \int\limits_{r<r'} \frac{1}{r'^{\,l+1}} \, \rho\,(\boldsymbol{r'})\; P_{lm}(\cos\theta')\cos m\phi' \; \mathrm{d}^3\boldsymbol{r'} \tag{10.13}$$

$$\mu_{lm}^{o,out}(r) \equiv \frac{(l-m)!}{(l+m)!} \int\limits_{r<r'} \frac{1}{r'^{\,l+1}} \, \rho\,(\boldsymbol{r'})\; P_{lm}(\cos\theta')\sin m\phi' \; \mathrm{d}^3\boldsymbol{r'} \tag{10.14}$$

The superscripts e and o stand for *even* and *odd* in accordance with the symmetry of the trigonometric functions cos and sin that act on the azimuthal angle. *in* and *out* denote the *inner* and the *outer* source moments.

The advantage of using a multipole expansion is due to the fact that the source moments (Eqs. (10.11) to (10.14)) which have to be calculated in order to obtain $\Phi_g(\boldsymbol{r})$ in Eq. (10.10) can be evaluated within a local domain: the radial contribution of each computational cell to the source moments is determined independently and added to the 5-dimensional moment vector containing all source moments with the following form:

$$\mu_{lm}^{e/o\,,\,in/out}(r) = \mu \Big(\, r \; , \; e/o \; , \; in/out \; , \; l \; , \; m \, \Big) \tag{10.15}$$

Once all contributions of a local domain have been calculated, a single data exchange with all other domains suffices to complete (10.15) by summing up all contributions, and Eq. (10.10) can be solved easily.

10.3 Implementation details

The implementation of the moment vector (10.15) requires a discretisation in its radial distance from r_{cm}. The number of entries in the moment vector is

$$n_{\mathrm{entries}} = (n_{\mathrm{radial}} + 1) \cdot 2 \cdot 2 \cdot (l_{max} + 1) \cdot (m_{max} + 1) \; . \tag{10.16}$$

In order to minimise the size of the vector (10.15) that is to be exchanged, the discretisation in r must be sufficiently coarse. Test calculations have shown that for reasonable accuracy in computing $\Phi_g(\boldsymbol{r})$, it is reliable to determine n_{radial} as follows:

$$n_{\text{radial}} = \text{int}\left(\frac{2 \cdot R_{\text{diagonal}}}{(\Delta x_{min}\ \Delta y_{min}\ \Delta z_{min})^{1/3}}\right) + 1 \tag{10.17}$$

Here $\Delta[xyz]_{min}$ are the smallest grid spacings and R_{diagonal} is the length of the diagonal across the cubic irregular computational grid that changes in size over time (see chapter 9).

Note that the speed of the multipole algorithm in parallel operation might be improved if working with a non optimised compiler by rearranging the multi-dimensional moment array (10.15) to a one-dimensional vector with n_{entries} positions.

10.4 The lowest possible expansion order

In order to determine the the lowest possible expansion order of the Poisson equation for which the capability to reproduce $\Phi_g(\boldsymbol{r})$ accurately is still guaranteed, reference values are needed. The direct output from the multipole algorithm with different limiting parameters l and m, $\Phi_{g\,lm}^{\text{mpole}}$, was compared to the values obtained by means of the rotating initial model Φ_g^{inimod} (see chapter 11) [2].

Due to the implied symmetries of the rotating initial models (cf. section 5.2), it is adequate to do this test on a cylindrical (s,z)-grid for one quadrant of the star: equatorial symmetry leads to contributions of even l only, axial symmetry implies that m is zero. Attention is drawn to the fact that both symmetries are not warranted once the WD is ignited. However, the deviations from axial and equatorial symmetry due to burning are assumed to be relatively small.

The percentage deviation dev of $\Phi_{g\,l0}^{\text{mpole}}$ from the reference value Φ_g^{inimod} is defined as follows:

$$dev(s,z) \equiv \frac{\Phi_g^{\text{inimod}}(s,z) - \Phi_{g\,l0}^{\text{mpole}}(s,z)}{\Phi_g^{\text{inimod}}(s,z)} \cdot 100 \tag{10.18}$$

The deviations were calculated by comparing the values of $\Phi_{g\,lm}^{\text{mpole}}(s,z)$ with those of the initial model $\Phi_g^{\text{inimod}}(s,z)$ that initially had to be interpolated from $\Phi_g^{\text{inimod}}(ir,it)$ in adaptive spherical coordinates for the (s,z)-grid of the hydrodynamics code (see section 11.4). As $\Phi_g^{\text{inimod}}(ir,it)$ is accessible only for positions within the stellar surface, $dev(s,z)$ was computed only for that region.

Statistical evaluations [BSMM99] of two WD models, namely the critical rigid rotator ("8rigid") and a rotating accreting white dwarf ("10AWD1"), cf. section

---

[2] Note that $\Phi_g(\boldsymbol{r})$ for the initial model solver had been also derived by a multipole expansion beforehand. The values $l_{max} = 10$ and $m_{max} = 0$ are set in the initial model solver.

8rigid	$l_{max} = 0$	$l_{max} = 2$	$l_{max} = 4$
$\bar{x}$ $[10^{-3}\,\%]$	– 124.31	9.81	6.71
$\tilde{x}$ $[10^{-3}\,\%]$	– 0.89	8.72	6.38
s $[10^{-3}\,\%]$	4.33	0.25	0.03
$min.$ $[10^{-1}\,\%]$	– 10.5214	−0.1769	– 0.1757
$max.$ $[10^{-1}\,\%]$	5.4887	2.0369	2.0041

Table 10.1: Arithmetic mean ($\bar{x}$), median ($\tilde{x}$), standard deviation (s), minimal ($min.$) and maximal ($max.$) values of dev for the 8rigid model

10AWD1	$l_{max} = 0$	$l_{max} = 2$	$l_{max} = 4$
$\bar{x}$ $[10^{-3}\,\%]$	– 284.77	28.86	16.60
$\tilde{x}$ $[10^{-3}\,\%]$	113.58	20.31	15.13
s $[10^{-3}\,\%]$	1.84	0.37	0.81
$min.$ $[10^{-1}\,\%]$	– 35.0678	−1.0691	– 0.0443
$max.$ $[10^{-1}\,\%]$	19.1973	3.7763	4.2393

Table 10.2: Arithmetic mean ($\bar{x}$), median ($\tilde{x}$), standard deviation (s), minimal ($min.$) and maximal ($max.$) values of dev for the 10AWD1 model

11.5, are summarised in Tables 10.1 and 10.2, respectively. $\bar{x}$ is the arithmetic mean, $\tilde{x}$ the median, s the standard deviation, and $min.$ the most negative and $max.$ the most positive value ever arising for $dev(s, z)$. In the case of a monopole algorithm ($l_{max} = 0$), there are noticeable deviations of $\Phi_{g\,00}^{\text{mpole}}$ from the desired value of Φ_g^{inimod}. These deviations decrease roughly by an order of magnitude when taking the quadrupole term ($l = 2$) into account, whereas the inclusion of the octupole terms ($l_{max} = 4$) only produces a tiny further improvement.

Taking a closer look when the truncation of the expansion takes place after the quadrupole terms, one can see that the mean deviation from Φ_g^{inimod} is much less than one-tenth of a percent. Also the standard deviation of dev is relatively small, less than 3% of the mean value. This implies that the gravitational potential is approximated very well for $l_{max} = 2$. The median has approximately the same value as the mean, which means that most of the deviations are small and very few large outliers occur.

Tables 10.1 and 10.2 show that the 8rigid model is generally better approximated by low order terms of the multipole expansion than the 10AWD1 model. This is due to the fact that the former star has a “more spherical” shape whereas the rotation law proposed for AWDs (see section 11.5 and appendix B), more precisely the maximum in angular velocity, causes a characteristic deepening at the poles.

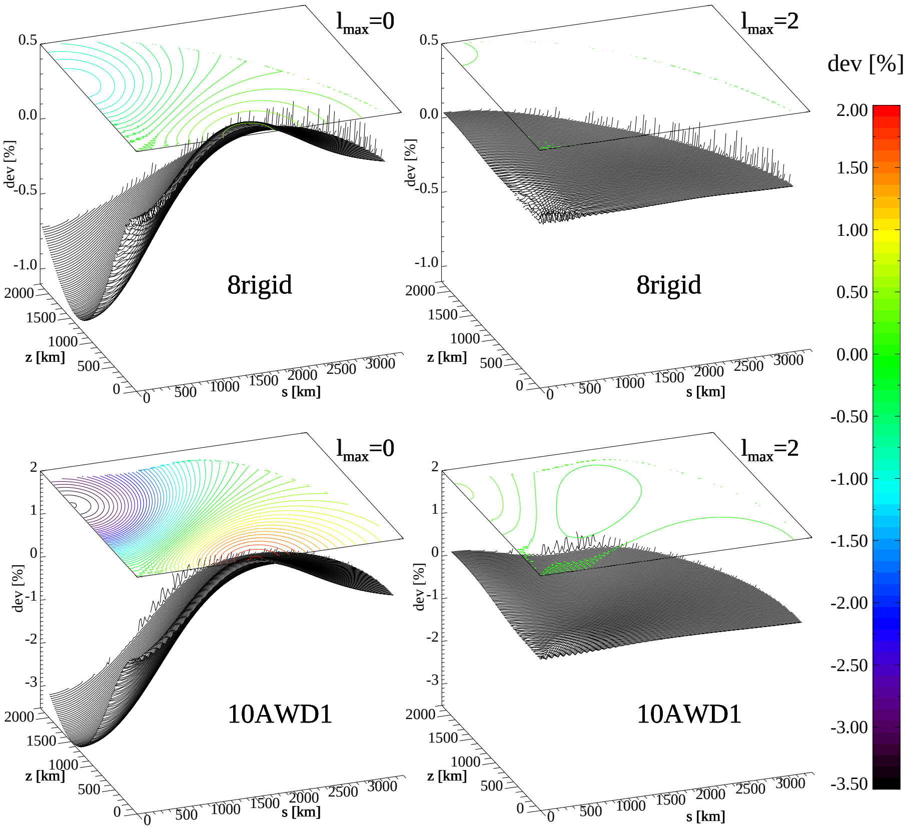

Figure 10.1: Deviations of $\Phi_{g\,l0}^{\mathrm{mpole}}$ from Φ_g^{inimod} in percent for the 8rigid and 10AWD1 rotators as a function of l_{max} within the star

This can also be seen in Fig. 10.1, where the spatially resolved value for $dev(s,z)$ is plotted for both WD models each with $l_{max}=0$ and $l_{max}=2$ within the star. In addition, the illustration shows the shape of the rotators as a projection on the top surface of the figure which, in turn, display contour lines of $dev(s,z)$. $\Phi_g^{\mathrm{inimod}}(s,z)$ is generally over estimated (dev negative) for $l_{max}=0$ in the region from the centre ($s=0, z=0$) to the pole $(0, r_{pol})$, and underrated in the region from the centre to the equator $(r_{equ}, 0)$.

Noticeable deviations from Φ_g^{inimod} occur at the surface of the star. This observation can be explained by the fact that the interpolation scheme in Φ_g^{inimod} and ρ used in the computation of $\Phi_{g\,l0}^{\mathrm{mpole}}$ on the (s,z)-grid does not work as accurately at the stellar surface as inside the star (cf. section 11.4).

Except for the central region, where the deviations show a slightly alternating fashion between adjacent grid points and the just mentioned outliers at the stellar surface, $dev(\boldsymbol{r})$ is a very smooth function in space. This means that neighbouring values of $\Phi_{g\,l0}^{\mathrm{mpole}}(\boldsymbol{r})$, even if they deviate slightly from $\Phi_g^{\mathrm{inimod}}(\boldsymbol{r})$, behave in the same manner. Consequently, since the gravitational accelerations $\boldsymbol{g}_{\mathrm{grav}}$ needed for the hydrodynamics simulation are obtained as the spatial derivatives of $\Phi_g(\boldsymbol{r})$, a low order multipole expansion for the gravitational potential is very promising:

$$\boldsymbol{g}_{\mathrm{grav}}(\boldsymbol{r}) \;=\; -\nabla\,\Phi_g(\boldsymbol{r}) \tag{10.19}$$

A survey reveals that taking octupole terms into account increases the computation time of the Poisson algorithm by about 10 percent when equatorial symmetry is assumed, and from Eq. (10.16), it is apparent that the memory that is to be transmitted between cluster machines would increase by a factor 5/3 even for the constriction to axial symmetry. Since the computational effort was to be kept small and the octupole terms do not increase the accuracy to a high degree, l_{max} was limited to 2 for all simulations of this investigation. For economical reasons, a possibly emerging dependence of $\rho(\boldsymbol{r})$ on the rotation angle ϕ is not considered, i.e., m is set to 0. Initially it is nonexistent due to axial symmetry. During the hydrodynamical simulation it is thought to be small (this assumption should not be worse than the common practice of employing a monopole Poisson algorithm for non-rotating stars).

The predictions of the analysis of Eq. (10.18) on the multipole algorithm's capability to solve $\Phi_g(\boldsymbol{r})$ for rotating stars accurately remain speculative unless the influence of the limitation of the multipole expansion to a certain value of l_{max} is studied. Fig. 10.2 shows the density profile of the 10AWD1 rotator (for which the approximated potential was worse with $l_{max} = 2$ compared to 8rigid). The upper left panel represents the star at $t = 0$ s, i.e., at the beginning of a hydrodynamical simulation. Without discretisation errors and with the correct forces on each mass element, the density profiles should not change over time (cf. section 9.4). The error resulting from a low order multipole Poisson algorithm becomes visible since the test for hydrostatic stability was carried out for different values of l_{max}: the lower left panel makes clear that a monopole algorithm is not able to compute $\Phi_g(\boldsymbol{r})$ to the demanded accuracy since the density stratification changes within the time span of 1.5 s (i.e., some time longer than it takes an exploding WD to unbind). The grey contour line at $\log_{10}(\rho) = 7.72$ and the red line at $\log_{10}(\rho) = 7.02$ represent densities up to which burning to iron group elements (IGEs) and approximately burning to intermediate mass elements (IMEs) takes place (cf. section 7.2), respectively. The white outer line at $\rho = 10^4$ g/cm^3 represents the stellar surface. For $l_{max} = 0$ both the grey and the red line are shifted in the polar direction by about 80 km. For $l_{max} = 2$, however, the contour lines up to $\rho \approx 10^6$ g/cm^3 are preserved. The fact that the WD keeps its shape with $l_{max} = 2$ (and that the octupole terms do not visibly improve the result) justify the truncation of the multipole expansion after the quadrupole term.

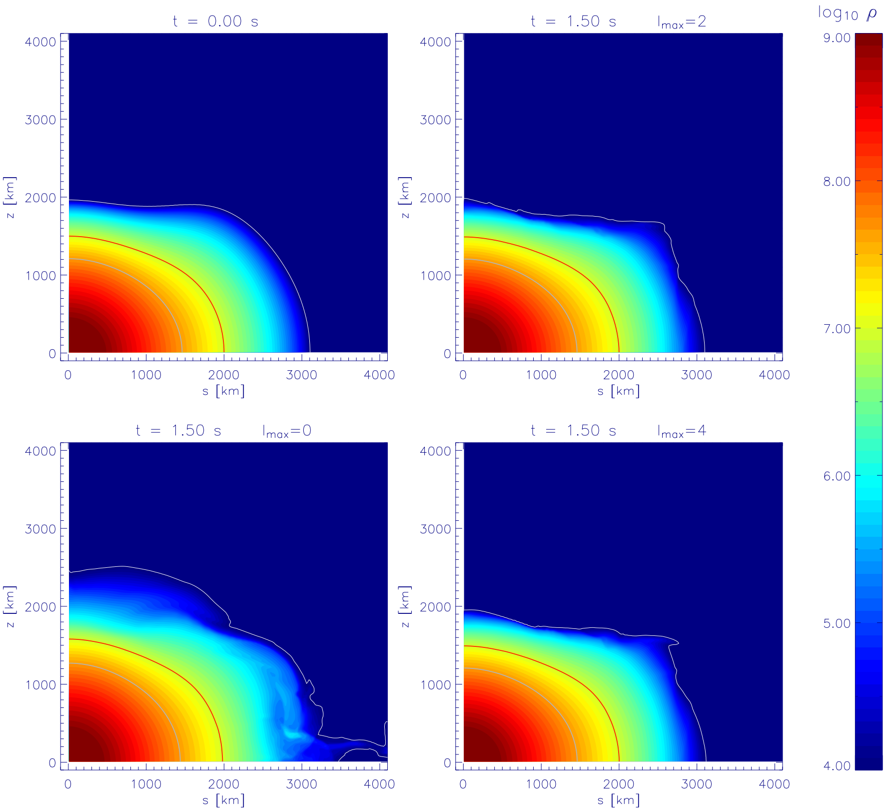

Figure 10.2: Test for hydrostatic stability of the 10AWD1 model for various values of the limiting parameter l_{max}. Densities greater than those enclosed by the red line will approximately burn to IMEs, those enclosed by the grey line to IGEs if the star is ignited.

11 The initial rotator model

In order to simulate the explosion of a rotating star, a rotating density stratification in hydrostatic equilibrium had to be generated, serving as the input for the hydrodynamic simulation. This chapter explains the method used for the construction of the rotators.

11.1 Stationary equilibrium in integral form

For an arbitrary set of coordinates, the stationary equilibrium of a self-gravitating and rotating gas in differential form is written as [EM85]

$$-\,(\boldsymbol{v}\nabla)\boldsymbol{v} \;=\; \frac{1}{\rho}\nabla p \;+\; \nabla\Phi_g \;, \tag{11.1}$$

where ρ is the density, p the pressure, $\boldsymbol{v}$ the fluid velocity (cf. Eq. (5.20)) and Φ_g the gravitational potential that is described by Poisson's equation (10.1):

$$\Delta\Phi_g = \begin{cases} 4\,\pi\,G\,\rho\;, & \text{inside}\;, \\ 0\;, & \text{outside}\;. \end{cases} \tag{11.2}$$

When the star is in a state of permanent rotation (cf. section 5.2), the fluid velocity $\boldsymbol{v}$ in cylindrical coordinates $(s,\;\phi,\;z)$ is given by

$$\boldsymbol{v} = s\;\Omega(s)\;\boldsymbol{e}_\phi\;, \tag{11.3}$$

where s is the distance from the rotation axis. With Eq. (11.3), the equation of equilibrium (11.1) reduces to

$$\frac{1}{\rho}\nabla p = \;-\;\nabla\Phi_g \;+\; s\;\Omega^2(s)\;\boldsymbol{e}_s\;. \tag{11.4}$$

The second term on the right hand is called *centrifugal acceleration*. Solving Eq. (11.4) directly raises severe problems [HE82], since the boundary conditions must be treated properly: the gravitational potential and the pressure have to be finite at the centre, the gravitational potential has to be zero at infinity and the pressure is zero at the surface of the rotator. Therefore it is convenient to employ the Poisson integral instead of Eq. (10.1), which has the following shape in spherical polar coordinates (r, θ, ϕ) when axial and equatorial symmetry is applicable (cf. section 5.2):

$$\begin{aligned}\Phi_g(\boldsymbol{r}) &= -\, G \int\limits_V \frac{\rho(\boldsymbol{r'})}{|\boldsymbol{r}-\boldsymbol{r}'|}\, \mathrm{d}\boldsymbol{r'} \\ &= -\, 4\pi G \int\limits_0^\infty r'^{\,2}\mathrm{d}r' \int\limits_0^{\pi/2} \sin\theta'\mathrm{d}\theta' \sum_{n=0}^{\infty} f_{2n}(r, r') \\ &\qquad \cdot\; P_{2n}(\cos\theta) P_{2n}(\cos\theta')\rho(r', \theta')\end{aligned} \tag{11.5}$$

Here P_{2n} are the even Legendre polynomials and

$$f_{2n}(r, r') = \begin{cases} r'^{2n}/r^{2n+1} & \text{for} \quad r \geq r' \,, \\ r^{2n}/r'^{2n+1} & \text{for} \quad r < r' \,. \end{cases} \tag{11.6}$$

Since Eq. (5.35) holds, the centrifugal force component in Eq. (11.4) can be obtained from a centrifugal potential Φ_c:

$$\Phi_c = -\int^{s} \Omega^2(s')s'\mathrm{d}s' \tag{11.7}$$

Integrating Eq. (11.4) yields

$$\int \frac{1}{\rho}\, dp \;+\; \Phi_g \;+\; \Phi_c \;=\; C \,, \tag{11.8}$$

where C is the constant of integration. Eq. (11.8) is an equation for which the incorporation of the boundary conditions is straightforward.

11.2 Implementation details

Eqs. (11.7) and (11.8) indicate that the implementation of the integral equation describing stationary equilibria is easiest when the (reciprocal value of the) density can be integrated analytically with respect to the pressure and when the rotation law $\Omega(s)$ is an analytical square integrable function.

The first condition is fulfilled for a special case of a barotropic equation of state, the polytropic equation of state:

$$p \;=\; \kappa\,\rho^{\gamma} \;=\; \kappa\,\rho^{1+\frac{1}{n}} \tag{11.9}$$

Here κ is the polytropic constant and γ the adiabatic index. Instead of γ the polytropic index $n = 1\,/\,(\gamma - 1)$ is often cited. Both κ and γ have to be chosen adequately for the physical system of interest.

A flexible approach to incorporate the rotation law motivated by the physics of chapter 3 is to employ a polynomial representation (which is terminated after the 5th order in the following):

$$\Omega(s) \;=\; \begin{cases} \Omega_c & \text{for} \quad 0 \le \bar{s} \le \bar{s}_{\text{rigid}} \\ \Omega_c \;+\; c_1\,\bar{s} \;+\; c_2\,\bar{s}^2 \;+\; c_3\,\bar{s}^3 \;+\; c_4\,\bar{s}^4 \;+\; c_5\,\bar{s}^5 & \text{for} \quad \bar{s}_{\text{rigid}} < \bar{s} \le \bar{s}_{\max} \end{cases} \tag{11.10}$$

Here $\bar{s}$ is the normalised distance from the rotation axis and $\bar{s}_{\text{rigid}}$ the normalised distance from the rotation axis out to the position for which the angular velocity has a constant value of Ω_c :

$$\bar{s} \;\equiv\; \frac{s}{r_{\text{surf}}^{\text{equator}}} \qquad \text{and} \qquad \bar{s}_{\text{rigid}} \;\equiv\; \frac{s_{\text{rigid}}}{r_{\text{surf}}^{\text{equator}}} \tag{11.11}$$

As will become clear later, from a numerical point of view that it is favourable to use the normalised value of the distance from the rotational axis. As a result of the normalisation, the maximal value of $\bar{s}$, namely $\bar{s}_{\max}$, is equal to one. Since rigid rotation is believed to occur in the pre-supernova convective core due to a very efficient exchange of angular momentum [YL04], rigid rotation of the interior may be assumed: s_{rig} denotes the distance out to which Ω is constant. The polynomial coefficients c_1 to c_5 have to be determined according to the desired rotation law.

In order to check the accuracy of the code by means of a comparison with different numerical methods that are employed for finding the equilibrium configurations [Hac86], [KEH89], the widely employed *j-const.* (11.12) and *v-const.* (11.13) rotation laws have also been implemented:

$$\Omega(s) \;=\; \Omega_c\,/\,(1 + s^2/A^2) \tag{11.12}$$

$$\Omega(s) \;=\; \Omega_c\,/\,(1 + s/A) \tag{11.13}$$

The length scale parameter A in Eqs. (11.12) and (11.13) specifies a distance from the rotation axis up to which rotation is roughly rigid. The names of these two rotation laws are attributed to the fact that the limiting case of $A \to 0$ in Eqs. (11.12) and (11.13) yields a mass distribution with constant specific angular momentum or constant track velocity, respectively.

According to Ref. [YL05], neither *j-const.* nor *v-const.* rotation are expected to occur among WDs in the history of the single-degenerate scenario. This study claims that those rotation laws may be considered as artificial merely since the rotation is so highly differential that the shear is much greater than allowed by the critical value for the onset of the dynamical shear instability.

Following these specifications, Eq. (11.8) becomes

$$\frac{\gamma}{\gamma-1}\,\kappa\,\rho^{\,\gamma-1} \;+\; \Phi_g \;+\; \Phi_c \;=\; C\;, \tag{11.14}$$

where the gravitational potential Φ_g is determined by Eq. (11.5) and the centrifugal potential Φ_c (11.7) appears as follows:

$$\begin{aligned}
\Phi_c \;=\; & -\int\limits_0^{s_{\text{rigid}}} \Omega_c^2\, s'\mathrm{d}s' - \int\limits_{s_{\text{rigid}}}^{s_{max}} \Omega^2(s')s'\mathrm{d}s' \;= \\
-\Bigg\{ & \frac{1}{2}\,\Omega_c^2\, s^2 \;+\; \frac{2}{3}\,\Omega_c c_1\,(s^3 - s^3_{\text{rigid}})\big|_{s\,>\,s_{\text{rigid}}} + \\
& \frac{1}{4}\left(2\,\Omega_c c_2 + c_1^2\right)\,(s^4 - s^4_{\text{rigid}})\big|_{s\,>\,s_{\text{rigid}}} + \\
& \frac{2}{5}\,(\Omega_c c_3 + c_1 c_2)\,(s^5 - s^5_{\text{rigid}})\big|_{s\,>\,s_{\text{rigid}}} + \\
& \frac{1}{6}\left(2\,\Omega_c c_4 + 2\,c_1 c_3 + c_2^2\right)\,(s^6 - s^6_{\text{rigid}})\big|_{s\,>\,s_{\text{rigid}}} + \\
& \frac{2}{7}\,(\Omega_c c_5 + c_1 c_4 + c_2 c_3)\,(s^7 - s^7_{\text{rigid}})\big|_{s\,>\,s_{\text{rigid}}} + \\
& \frac{1}{8}\left(2\,c_1 c_5 + 2\,c_2 c_4 + c_3^2\right)\,(s^8 - s^8_{\text{rigid}})\big|_{s\,>\,s_{\text{rigid}}} + \\
& \frac{2}{9}\,(c_2 c_5 + c_3 c_4)\,(s^9 - s^9_{\text{rigid}})\big|_{s\,>\,s_{\text{rigid}}} + \\
& \frac{1}{10}\left(2\,c_3 c_5 + c_4^2\right)\,(s^{10} - s^{10}_{\text{rigid}})\big|_{s\,>\,s_{\text{rigid}}} + \\
& \frac{2}{11}\,c_4 c_5\,(s^{11} - s^{11}_{\text{rigid}})\big|_{s\,>\,s_{\text{rigid}}} + \frac{1}{12}\,c_5^2\,(s^{12} - s^{12}_{\text{rigid}})\big|_{s\,>\,s_{\text{rigid}}} \Bigg\}
\end{aligned} \tag{11.15}$$

From Eq. (11.14) it is clear that for a given rotation law (Eq. (11.10)) and a given value of the adiabatic index γ (in Eq. (11.9)), the rotating configuration is completely determined by the following quantities:

- κ (or central pressure) ,
- central density ρ_c and
- central angular velocity Ω_c .

It is reasonable to specify the central angular velocity Ω_c for a rotating model, particularly when the rotation law is of the form (11.10) and Ω_c serves as zeroth order input. But the axis ratio a,

$$a = \frac{r_{\text{surf}}^{\text{pol}}}{r_{\text{surf}}^{\text{equator}}} \,, \tag{11.16}$$

was chosen to specify a model instead of Ω_c. This approach complicates the process of finding of an equilibrium configuration with a desired rotation law since Ω_c cannot be predetermined but has to be obtained by choosing an adequate value of a, in general by trial and error. It is advantageous that equilibria configurations can be deformed by a desired degree in a dimensionless manner.

Following the study of Ref. [EM85], Eq. (11.14) is discretised on a two-dimensional grid with n_t equidistant angular supporting points in the interval of $0 \leq \theta \leq \pi/2$ (equatorial symmetry is assumed without loss of generality, cf. section 5.2) and n_r equidistant but angular dependent radial supporting points:

$$\theta_i = \frac{\pi}{2}\,\frac{i-1}{n_t-1} \,, \qquad i = 1, ..., n_t \tag{11.17}$$

$$r_{ij} = r_j(\theta_i) = r_{\text{surf}}(\theta_i)\,\frac{j}{n_r} \,, \qquad j = 1, ..., n_r \tag{11.18}$$

The index $j = 1$ refers not to the centre but to the total number of n_t radial supporting points that are located adjacent to the centre.

The discretised equilibrium equation now reads

(i) in the centre:

$$\frac{\gamma}{\gamma-1}\,\kappa\,{\rho_c}^{\gamma-1} + \Phi_g(0) = C \,, \tag{11.19a}$$

where the central gravitational potential $\Phi_g(0)$ is given by

$$\Phi_g(0) = -\,4\pi G \sum_l \sin\theta_l\,\Delta\theta_l \sum_m r_{lm}\,\Delta r_{lm}\,\rho_{lm} \,. \tag{11.19b}$$

(ii) for $1 \leq i \leq n_t$ and $1 \leq j \leq n_r$:

$$\frac{\gamma}{\gamma - 1} \, \kappa \, {\rho_{ij}}^{\gamma-1} \quad + \quad (\Phi_g)_{ij} \quad + \quad (\Phi_c)_{ij} \quad = \quad C \ , \tag{11.20a}$$

where the density ρ_{ij} and the gravitational potential $(\Phi_g)_{ij}$ are given by

$$\rho_{ij} = \rho(r_{ij}, \theta_i) \ , \tag{11.20b}$$

$$\begin{aligned} (\Phi_g)_{ij} = - \ \ 4\pi G \sum_l \sin\theta_l \ \Delta\theta_l \sum_m r_{lm}^2 \ \Delta r_{lm} \\ \cdot \sum_n f_{2n,lm}^{ij} \ P_{2n}(\cos\theta_i) \ P_{2n}(\cos\theta_l) \ \rho_{lm} \end{aligned} \tag{11.20c}$$

with

$$f_{2n,lm}^{ij} = f_{2n}(r_{ij}, r_{lm}) \ , \tag{11.20d}$$

and the centrifugal potential $(\Phi_c)_{ij}$ is obtained via Eq. (11.15) by replacing s with $(r_{ij} \, \sin\theta_i)$.

(iii) at the surface, i.e., for $1 \leq i \leq n_t$ and $j = n_r$:

$$\rho_{i,n_r} = \rho(r_{i,n_r}, \theta_i) = 0 \ . \tag{11.21}$$

n is the index of all Legendre polynomials. $\Delta\theta_l$ and Δr_{lm} are the angular and radial grid spacings (the indices l and m correspond to the inner loop in angular and radial direction arising in the calculation of the gravitational potential), respectively.

Eqs. (11.19a), (11.20a), and (11.21) form a system of $(n_r + 1) \cdot n_t + 1$ nonlinear equations for the $(n_r+1) \cdot n_t + 2$ unknowns, namely $n_t \cdot n_r$ densities ρ_{ij}, the n_t surface radii r_{i,n_r}, the integration constant C, and the central angular velocity Ω_c. Together with the additional Eq. (11.16), an equilibrium model is uniquely determined.

The nonlinear system of equations is solved by the Newton-Raphson iteration scheme. Since a sufficiently good initial guess is demanded for a Newton-Raphson algorithm to converge [PTVF03], a sequence of models is computed, starting from a non-rotating spherical star that becomes more and more deformed while the axis ratio (Eq. (11.16)) decreases steadily, e.g., by the factor 1/1.05. The previous less deformed and initially a spherical model serves as input for the construction of each deformed model. The convergence of a model is taken to be complete when the relative change of any variable of the nonlinear system is less than ϵ, e.g., 10^{-4}. Unlike the self-consistent field approach [Hac86] which allows for convergence even when starting with a uniform density configuration, the primary slightly rotating density profile has to be supported by a stratification that obeys the equation of state (EOS) of a WD (cf. section 5.3) fairly well.

A disadvantage of this method is the fact that the distribution of angular momentum changes from model to model within a particular sequence since the rotation law is a spatial function that has to be determined a priori, however, the shape and mass of the rotators change from model to model. This results in a different distribution of specific angular momenta [Ste90].

Particularly when choosing a rotation law in polynomial form such as Eq. (11.10), it is convenient that the distance from the rotation axis s is normalised to the equatorial radius of the star, $r_{\text{surf}}^{\text{equator}}$ (cf. Eq. (11.11)). Severe problems arise when the star becomes more and more deformed so that a non-normalised s in Eq. (11.10) exceeds the value for which the coefficients of the rotation law are derived (that is when $s > r_{\text{surf}}^{\text{initial}}$). This causes negative or very high values for the angular velocity Ω.

11.3 Piecewise polytropic approximation method

This method is introduced for a polytropic EOS (Eq. (11.9)). Since a WD can be described with a polytropic equation of state only within certain density regimes when γ and κ remain constant (the value of γ in Eq. (11.9) is 4/3 in the relativistic degenerate core but 5/3 in the non-degenerate envelope), it is necessary to replace Eq. (11.9) by a more realistic yet barotropic equation of state.

A straightforward way to do this is presented in Ref. [ME85]. Eq. (11.9) is partitioned into $N-1$ intervals for N monotonically increasing density values, $\rho_1 < ... < \rho_{d-1} < \rho_d ... < \rho_N$, that each obey a polytropic relation to pressure via desired values of γ and κ :

$$p \;=\; \kappa_d \, \rho^{\gamma_d} \quad \text{for} \quad \rho_d \le \rho \le \rho_{d+1} \quad \text{where} \quad d = 1, ..., N-1 \tag{11.22}$$

Here κ_i and γ_i are the interval dependent polytropic constant and adiabatic index, respectively. The interval dependent adiabatic indices γ_d and polytropic constants κ_d are obtained for a given density ρ_d by employing the equation of state of the hydrodynamics program describing WD matter (cf. section 5.3). Together with the input values at a certain temperature T_d, the EOS then supplies the values of the density dependent pressure p_d and adiabatic index γ_d. The temperature must be a unique function of the density for barotropy. The temperature profile used for this thesis was suggested by detailed studies of accretion (cf. Figs. 3.1 and 11.1, [YL04]) and the convective pre-supernova core (cf. Eq. (4.1)). By calling the EOS subroutine for each density ρ_d, a table of corresponding ρ_d, p_d, and γ_d is constructed.

Then the polytropic constants κ_d can be obtained via the relation

$$\kappa_d \;=\; \frac{p_d}{{\rho_d}^{\gamma_d}} \;. \tag{11.23}$$

To assure a uniform tabulation, the steps in ρ, as proposed by the study of Ref. [ME85] are defined as follows:

$$\log\left(\rho_d\right) = \log\left(\rho_{d-1}\right) \;+\; \frac{\log\left(\rho_N\right) - \log\left(\rho_2\right)}{N-2} \qquad \text{for} \quad 3 \leq d \leq N \tag{11.24}$$

In this work, the values of ρ_1, ρ_2, and ρ_N in g/cm^3 were chosen to be 0, 100, and 10^{10}, respectively. The total number of steps N was 10000.

Fig. 11.1 shows the input values for the EOS, i.e., temperature and density, in the upper panel. Due to the convective core, the temperature drops roughly parabolically with respect to distance from the centre (see Eq. (4.1)), which can be seen in the the plotted dependence on density. Furthermore, there exists a local maximum in temperature at large radius, representing the accretion induced heating of the rotator. The lower panel shows the resulting adiabatic index. Obviously, γ is not a smooth monotonic function of density but shows steps and oscillations. This behaviour is caused by the fact that for the employed EOS, the pressure is tabulated for density and temperature (cf. section 7.3) and obtained by a bilinear interpolation scheme (i.e., linear interpolation in density and in temperature). This kind of interpolation is not fully satisfying since not only the interpolated values (i.e., pressure) but also derivatives of interpolated values are used in order to obtain the adiabatic index γ:

$$\gamma \;=\; \frac{\rho}{p}\,\frac{\mathrm{d}\left(\log p\right)}{\mathrm{d}\left(\log \rho\right)} \tag{11.25}$$

The shape of γ causes no problems regarding numerical convergence or hydrostatic stability. Nevertheless a higher order interpolation routine [TS00] should be employed for the state variables in the future since irregularities arising in expressions such as (11.25), which contains the speed of sound, potentially lead to a variety of problems.

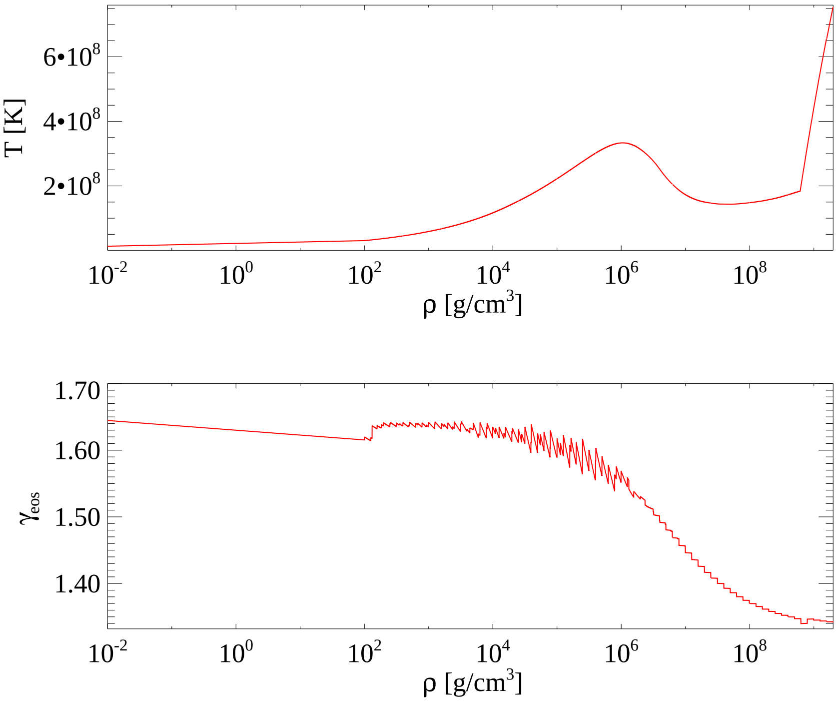

Figure 11.1: The adiabatic index γ as used in the piecewise polytropic method is plotted versus density ρ (lower panel) for an accreting WD temperature profile (upper panel). The steps and oscillations of γ arise from a low order interpolation scheme of the state variables.

In addition to the changes in the first term in Eq. (11.14), namely replacing κ and γ by κ_i and γ_i, this equation has to be modified for the piecewise polytropic approximation method in one more aspect. Since the effective potential $(\Phi_g + \Phi_c)$ is required to be continuous at the interval boundaries, the constant of integration C in Eq. (11.14) is no longer independent of the density but has to obey the following condition:

$$\frac{\kappa_{d+1}\,\gamma_{d+1}}{\gamma_{d+1}-1}\,\rho_d{}^{\gamma_{d+1}-1} - C_{d+1} \;=\; \frac{\kappa_d\,\gamma_d}{\gamma_d-1}\,\rho_d{}^{\gamma_d-1} - C_d \qquad \text{for} \quad d = 1, ..., N-1 \tag{11.26}$$

C_N is identical to C of Eq. (11.14), which is one of the variables of the nonlinear system to be determined.

The corresponding code has been compared with the results of the *Self Consistent Field* method [KEH89] that describes a completely different approach to finding equilibria configurations for the case of a polytropic equation of state and the *j-const.* rotation law. Only tiny deviations were observed, therefore the adequacy of this method is confirmed.

11.4 Transformation between different grids

As stated above, the order of the nonlinear set of equations to be solved is $n_v = (n_r + 1) \cdot n_t + 2$. Since n_v increases with the number of both radial and angular supporting points n_r and n_t, the introduced method is limited to low resolution. On the one hand, it is costly in terms of CPU time to factorise the Jacobian matrix at every step of the Newton-Raphson iteration scheme. The matrix is occupied at nearly each position, furthermore it obeys an irregular pattern, which favours the costly Gaußian elimination scheme of the triangular decomposition in order to solve the linear system of equations. On the other hand, the required working memory becomes enormous for increased resolution. For $n_r = 44$ and $n_t = 16$ the size of the matrix is 4.2 megabytes when working with 8 byte precision, for $n_r = 130$ and $n_t = 110$ it is increased to more than 1.6 gigabytes. This is a severe limitation since Gaußian elimination cannot efficiently be parallelised. Note that different modifications of the Newton-Raphson iteration scheme exist that demand fewer factorisation steps at the cost of convergence or can be restricted to a given amount of working memory at the cost of computational effort [Kan03].

Due to these limitations it is important to use an accurate method for the interpolation of the rotating initial model values (densities and angular velocities) from adaptive spherical coordinates (Eqs. (11.17) and (11.18)) on the rectangular coordinate system with which the SN Ia explosion is followed.

The interpolation proceeds as follows (see Ref. [Ste90] for a similar approach):

1. Each coordinate X of the rectangular grid, i.e., $X(x, y, z)$, is converted into the corresponding comoving coordinate $X(r_{rect}, \theta_{rect})$:

$$r_{rect} = \sqrt{x^2 + y^2 + z^2} \tag{11.27}$$

$$\theta_{rect} = \arctan\left(\frac{\sqrt{x^2 + y^2}}{z}\right) \tag{11.28}$$

2. According to Eq. (11.18), the indices i_{small} and i_{large} that correspond to the enclosing angles, are found such that:

$$\theta_{i_{small}} \leq \theta_{rect} < \theta_{i_{large}} \tag{11.29}$$

3. The corresponding radial indices $j_{fit,\,i}$ are found such that:

$$r_{(j_{fit,\,i})}(\theta_i) \leq r_{rect} < r_{(j_{fit,\,i})+1}(\theta_i) \quad \text{for} \quad i = i_{small} \quad \text{and} \quad i = i_{large} \tag{11.30}$$

4. The spacing values for the four point radial stencil for both enclosing radial vectors $r_j(\theta_{i\,small})$ and $r_j(\theta_{i\,large})$ are computed, each of them being equally spaced in the radial direction by $\Delta_{i\,small}$ and $\Delta_{i\,large}$:

$$\begin{aligned}
\Delta_{1,\,i} &= r_{rect} - r_{(j_{fit,\,i})-1}(\theta_i) \\
\Delta_{2,\,i} &= r_{rect} - r_{(j_{fit,\,i})} \quad (\theta_i) \\
\Delta_{3,\,i} &= r_{rect} - r_{(j_{fit,\,i})+1}(\theta_i) \\
\Delta_{4,\,i} &= r_{rect} - r_{(j_{fit,\,i})+2}(\theta_i) \quad \text{for} \quad i = i_{small} \quad \text{and} \quad i = i_{large}
\end{aligned} \tag{11.31}$$

5. The quartic mean for the quantity $\bar{Q}^{rect}$ (being either the density ρ or the track velocity v_{rot}) of both enclosing radial vectors is computed:

$$\begin{aligned}
\bar{Q}_i^{rect} = \Bigg(&- \frac{\Delta_{2,\,i}\,\Delta_{3,\,i}\,\Delta_{4,\,i}}{6} \cdot Q_{(j_{fit,\,i})-1} \\
&+ \frac{\Delta_{1,\,i}\,\Delta_{3,\,i}\,\Delta_{4,\,i}}{2} \cdot Q_{(j_{fit,\,i})} \\
&- \frac{\Delta_{1,\,i}\,\Delta_{2,\,i}\,\Delta_{4,\,i}}{2} \cdot Q_{(j_{fit,\,i})+1} \\
&+ \frac{\Delta_{1,\,i}\,\Delta_{2,\,i}\,\Delta_{3,\,i}}{6} \cdot Q_{(j_{fit,\,i})+2} \Bigg) \cdot \Delta_i^{-3} \\
&\text{for} \quad i = i_{small} \quad \text{and} \quad i = i_{large}
\end{aligned} \tag{11.32}$$

6. The quadratic angular mean of $\bar{Q}_{i_{small}}$ and $\bar{Q}_{i_{large}}$ is obtained:

$$\bar{Q}^{rect} = \bar{Q}^{rect}_{i_{small}} + \frac{\theta_{rect} - \theta_{i_{small}}}{\theta_{i_{large}} - \theta_{i_{small}}} \cdot \left(\bar{Q}^{rect}_{i_{large}} - \bar{Q}^{rect}_{i_{small}} \right) \tag{11.33}$$

7. The track velocity is computed as follows:

$$v_{rot} = \Omega\big(r_j(\theta_i)\sin\theta_i\big) \cdot r_j(\theta_i)\sin\theta_i \tag{11.34}$$

8. The stencil (11.32) for the radial quartic interpolation scheme that demands two neighbouring supporting points outside and inside is modified if the considered point is too close to the centre or the surface (and thus less than two points are available for the one-sided interpolation). This guarantees a usable interpolation (which is asymmetric in that case).

Integral quantities as the total mass, gravitational energy or kinetic energy may be used in order to check the accuracy of this interpolation method (cf. Table 11.1).

	inimod	promet	inimod	promet	inimod	promet
	M $[M_\odot]$		E_{grav} $[10^{51}\text{erg}]$		E_{rot} $[10^{50}\text{erg}]$	
8rigid	1.4661	1.4653	-3.2074	-3.2040	4.4164	4.4122
10AWD1	1.6374	1.6362	-3.6701	-3.6649	1.7484	1.7465
11AWD2	1.7428	1.7410	-4.0330	-4.0242	2.6252	2.6216
20AWD3	2.0150	2.0131	-4.5283	-4.5184	4.4652	4.4597
22AWD3 *	2.0687	2.0680	-4.5004	-4.4967	4.5549	4.5541
14AWD4	1.7911	1.7897	-4.1419	-4.1353	2.9907	2.9871
$16j_{const}$adr05	1.8025	1.8012	-4.2779	-4.2714	3.1631	3.1598
$16v_{const}$adr02	1.7067	1.7057	-4.0605	-4.0556	2.3929	2.3908

Table 11.1: The total mass M, gravitational energy E_{grav}, and kinetic energy E_{rot} as given from the initial model algorithm ("inimod") and obtained by the hydrodynamics code Prometheus ("promet") at $t = 0$ s. The difference is caused by the remapping of the discrete densities and velocities that underlie those quantities from adaptive spherical coordinates on a (non-equidistant) Cartesian grid. The resolution of the initial model algorithm was 90 radial and 80 angular supporting points, the resolution of the hydrodynamics code was 128^3 cells per octant (* 50^3 cells per octant).

Both the initial model algorithm and the hydrodynamics code compute those quantities in a separate manner (on different coordinate systems) from the densities and velocities of the supporting points. The agreement was satisfying since deviations typically arose only in the 3^{rd} digit, and these deviations could even be further decreased by using a grid that is finer in the outer regions for the hydrodynamics code (cf. chapter 9).

11.5 Constructed initial models

Since rapid rotation of accreting WDs is not guaranteed (it is a common belief that the presence of strong magnetic fields potentially decelerates WDs [YL04]) and the possible shape of the rotation law may vary to a large degree for different assumptions in the accretion model or simply from star to star (cf. chapter 3), the initial models employed for this study were chosen to cover a broad range of possible rotation laws and, accordingly, masses. Tables 11.2 and 11.3 summarise quantities of the most frequently used models. Note that differential rotators can become heavier than the critical rigid rotator since Ω is allowed to have a high value within the star and to drop towards the equatorial surface. As a consequence, overcritical rotation is avoided. However, it sets in when the gravitational force is no longer able to compensate for the centrifugal force, initially at the equator (the effective gravity no longer points inward). Then mass shedding at the equator occurs.

model	8rigid	10AWD1	11AWD2	20AWD3	22AWD3	14AWD4
Ω_c [rad/s]	0.37242	1.5999	4.6074	3.9847	3.6791	4.5934
c_1	0	7.3470	4.5	-18.823	-18.823	-16.265
c_2	0	62.006	-15	196.62	196.62	162.39
c_3	0	-275.25	9	-563.38	-563.38	-480.84
c_4	0	342.62	0	600.25	600.25	531.85
c_5	0	-137.09	0	-218.51	-218.51	-2.0081
$\bar{s}_{\mathrm{rigid}}$	1	0	0	0	0	0.2
$r_{equator}/r_{pol}$	1.477	1.629	1.710	2.183	2.407	1.796
Ω_{peak} [rad/s]	Ω_c	4.4126	4.5158	5.2236	4.9013	5.1986
M [$M_\odot$]	1.4661	1.6374	1.7428	2.0150	2.0687	1.7911
M_{high} [$M_\odot$]	1.302	1.393	1.481	1.469	1.409	1.490
M_{high}/M [%]	88.8	85.1	85.0	72.9	68.1	83.2
M_{med} [$M_\odot$]	0.126	0.180	0.200	0.401	0.449	0.227
M_{med}/M [%]	8.6	11.0	11.5	19.9	21.7	12.7
r_{pol} [10^8cm]	2.1721	2.0180	1.8985	1.8836	1.9214	1.8833
$r_{equator}$ [10^8cm]	3.2092	3.2871	3.2471	4.1116	4.6240	3.3822
E_{int} [10^{51} erg]	2.5878	2.7395	2.8895	2.9604	2.9153	2.9148
E_{grav} [10^{51} erg]	-3.2074	-3.6701	-4.0330	-4.5283	-4.5004	-4.1419
E_{rot} [10^{50} erg]	0.442	1.748	2.625	4.465	4.555	2.991
E_{bind} [10^{50} erg]	-5.754	-7.558	-8.810	-11.214	-11.296	-9.280
β [%]	1.3769	4.7639	6.5092	9.8608	10.121	7.2206
J [10^{50} g cm^2/s]	0.37747	0.91512	1.1968	2.1951	2.4816	1.3602

Table 11.2: Physical quantities of the constructed initial models. The central density is $\rho_c = 2.0 \times 10^9$ g/cm^3 for all models. M_{high} is the mass for all material if $\rho > 5.248 \times 10^7$ g/cm^3, and M_{med} if 5.248×10^7 g/cm$^3 > \rho > 1.047 \times 10^7$ g/cm^3 . In the non-rotating case ($\rho_c = 2.0 \times 10^9$ g/cm^3, $M = 1.4\ M_\odot$) M_{high} and M_{med} are 1.268 $M_\odot$ (90.6 %) and 1.110 $M_\odot$ (7.9 %), respectively. Furthermore, the non-rotating star possesses the following quantities: $r = 2.1905 \times 10^8$ cm, $E_{int} = 2.5228 \times 10^{51}$ erg, $E_{grav} = -3.0275 \times 10^{51}$ erg, $E_{rot} = 0.000 \times 10^{50}$ erg, and $E_{bind} \equiv E_{int} + E_{grav} + E_{rot} = -5.047 \times 10^{50}$ erg.

model	16j_{const}adr05	16v_{const}adr02
Ω_c [rad/s]	6.4076	10.120
A [$r_{equator}$]	0.5	0.2
$r_{equator}/r_{pol}$	2.183	2.183
M [$M_\odot$]	1.8025	1.7067
M_{high} [$M_\odot$]	1.534	1.493
M_{high}/M [%]	85.1	87.5
M_{med} [$M_\odot$]	0.191	0.157
M_{med}/M [%]	10.6	9.2
r_{pol} [10^8cm]	1.8087	1.8134
$r_{equator}$ [10^8cm]	3.9481	3.95858
E_{int} [10^{51} erg]	3.0072	2.9678
E_{grav} [10^{51} erg]	-4.2779	-4.0604
E_{rot} [10^{50} erg]	3.163	2.393
E_{bind} [10^{50} erg]	-9.544	-8.533
β [%]	7.3941	5.8933
J [10^{50} g cm^2/s]	1.3785	1.0535

Table 11.3: The same parameters as in Table 11.2 for the “exotic” j_{const} and v_{const} rotators

It is important to note that the coefficients of the rotation law in Table 11.2 are only valid for this particular model and not necessarily for the whole sequence. To avoid convergence problems in the Newton-Raphson iteration scheme [PTVF03], a stellar model yielding a desired central angular velocity was constructed initially. Then the axis ratio was not increased but the coefficients c_1 to c_5 were adjusted in order to obtain the desired rotation law.

The rotation law was not fitted for an exact overlap with the proposed rotation laws (cf. chapter 3). In contrast, the value of the angular velocity Ω_c, the peak value of Ω, and the total mass were emulated, which is not seen as constraints considering the multitude of proposed rotation laws (N. Langer, private communication). The mass accretion from a Keplerian disc implies a critically rotating surface of the AWD rotators which can not easily be incorporated because the initial model algorithm aborts when mass shedding for a model is detected. Therefore it is assumed that the surfaces of most constructed models in this study do not rotate critically. This is not problematic since the outer layers of a star do not affect the nuclear burning in the interior.

Fig. 11.2 shows the density profile and Ω for both spatial and mass coordinates (the corresponding plots for the other considered models are listed in appendix B, Figs. B.1 to B.7). The latter is plotted for the cases of either enclosed spherical or cylindrical shells since both definitions of the mass coordinate are commonly used in the literature. Note that for the underlying cylindrical rotation (cf. Eq. (5.35)), only the cylindrical mass coordinate is adequate to describe Ω. Nevertheless, since the rotation law is derived for shell like rotation (cf. section 3.6), the dashed line may serve as an approximation for shell like rotation: it represents the mass enclosed by a sphere with radius r that reaches Ω in (and only in) the equatorial plane.

The grey thick contour line encloses densities greater than 5.25×10^7 g/cm^3 and the red line densities greater than 1.05×10^7 g/cm^3. These density thresholds roughly indicate the region up to which burning to iron group elements (IGEs) and intermediate mass elements (IMEs) takes place (cf. section 7.2) if the star has not expanded while the flame is propagating outwards. The white contour line at $\rho = 10^4$ g/cm^3 indicates the stellar surface.

Fig. 11.3 illustrates the mass proportions that fall into those density regimes for the rigid, $j - const.$, and AWD rotator series, for which the axis ratio a is decreased in each case. Since the burning products are closely related to the material densities, those proportions which apparently depend on the rotation law are of importance in the SN Ia context, as described in chapters 12 and 13.

11.6 Distribution of specific angular momentum

A WD is is well described by the barotropic equation of state which demands a cylindrical rotation law (Eq. (5.35)) and therefore fulfils the conditions of a *ho-*

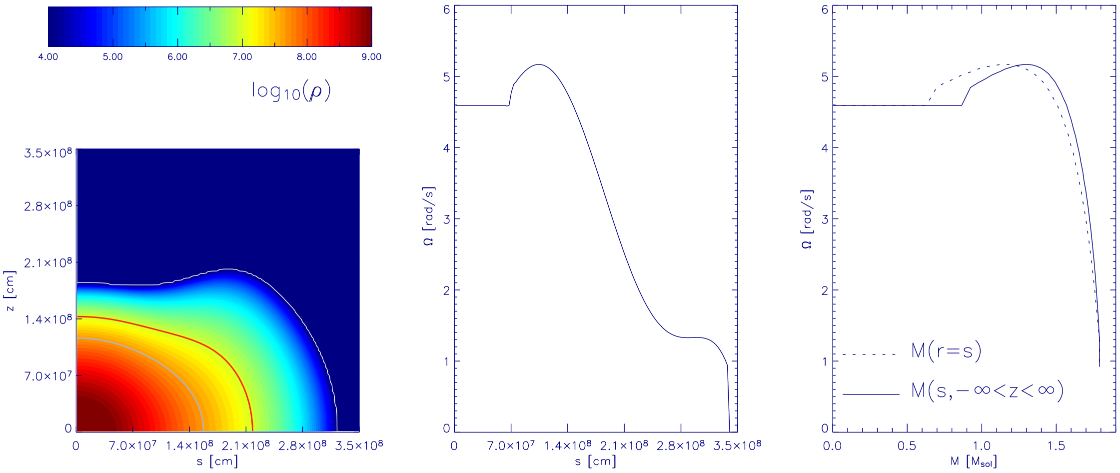

Figure 11.2: Density contour lines and the rotation law both in spatial and in mass coordinates for the 14AWD4 model. Note that the extent of the convective core (i.e., the rigidly rotating inner part) is estimated following Ref. [YL04].

mentropic star (i.e., entropy is constant in time and space). For the latter it can be shown that a necessary (but not sufficient) condition for stability is the *Solberg criterion* [Tas78], [KS82], [YL04]:

$$\frac{\mathrm{d}}{\mathrm{d}\,s}\left(\frac{\mathrm{d}\,J}{\mathrm{d}\,M}\right) \equiv \frac{\mathrm{d}}{\mathrm{d}\,s}\left(j\right) = \frac{\mathrm{d}}{\mathrm{d}\,s}\left(s^2\,\Omega\right) = \frac{\mathrm{d}}{\mathrm{d}\,s}\left(s^4\,\Omega^2\right) + const. \quad \not< \; 0 \qquad (11.35)$$

Here, $\mathrm{d}\,M$ is a mass element with the corresponding angular momentum $\mathrm{d}\,J$, consequently j denotes the specific angular momentum and s is the distance from the rotational axis. Equation (11.35) demands that the specific angular momentum must necessarily increase outwards for stability. It is also known as *Rayleigh criterion* when applied to inviscid, incompressible fluids without gravitational interaction.

The impact of the criterion becomes clear when considering a slight displacement of a fluid element whose angular momentum is conserved. If Eq. (11.35) holds and the fluid element moves outwards, it reaches a position that is located amid particles with higher angular momentum. Since the displaced particle has less angular momentum, a smaller centrifugal force acts on it, which results in a deceleration of the outward motion. Similarly, a particle that moves inwards is driven outwards by the excess of angular momentum.

Fig. 11.4 shows the specific angular momentum of the constructed rotators. The Solberg criterion is fulfilled except in the outer layers that were not modelled for numerical reasons (cf. section 11.5). Note that AWDs fulfil the Solberg criterion globally [YL04] since the surface region rotates much faster with the Keplerian value.

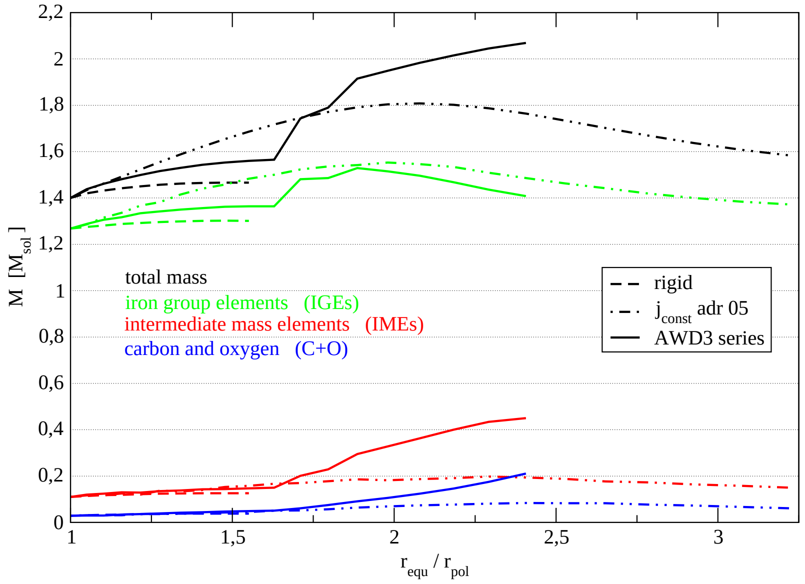

Figure 11.3: Fractions of the total mass in the high density regime ($\rho > 5.248 \times 10^7$ g/cm^3, “IGEs”), the medium density regime (5.248×10^7 g/cm^3 $> \rho > 1.047 \times 10^7$ g/cm^3, “IMEs”), and the low density regime ($\rho \leq 1.047 \times 10^7$ g/cm^3 , “C+O”) for different rotation laws versus the ratio of equatorial and polar radius

It is important to mention that the Solberg criterion has a limited significance on AWDs. *Stability* according to the Solberg criterion does not rule out any occurrence of instabilities. An accreting WD resides in a state of permanent perturbations by mass and angular momentum gain leading to a steady redistribution of angular momentum which in turn requires the appearance of instabilities (cf. section 3.2).

Altogether it can be stated that if the angular momentum decreased outwards, any accretion of material is unlikely since mass shedding occurs as described above.

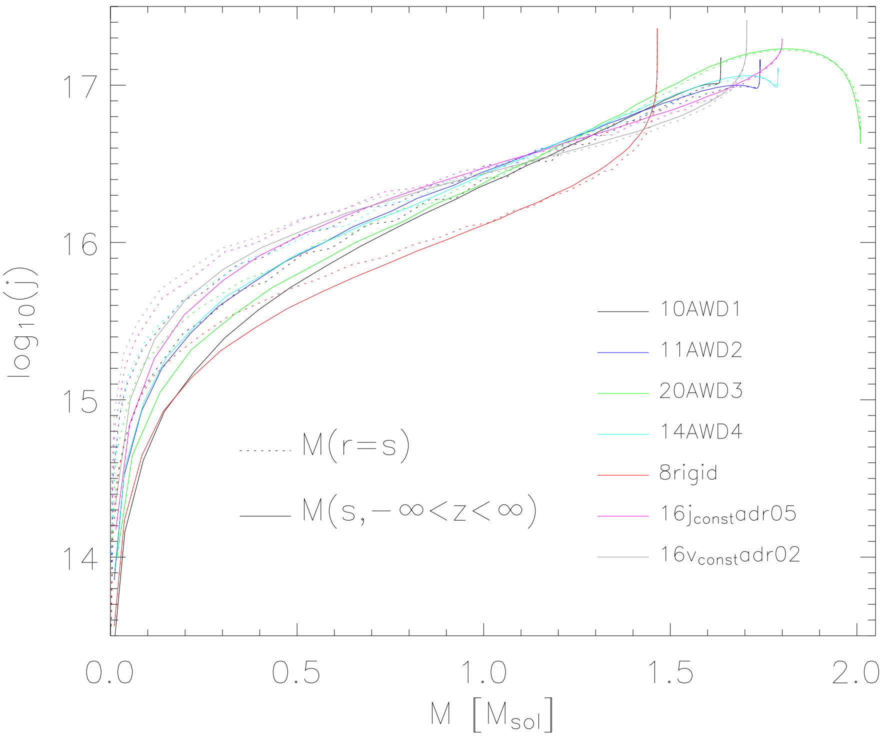

Figure 11.4: Specific angular momentum j in units of [cm^2/s] for rotators in this study. The solid line denotes the mass coordinate on cylinders, the dashed one represents the mass coordinate on spheres. Only at the stellar surface does j decrease with increasing distance from the rotational axis (note that the cylindrical as well as the spherical mass coordinate is a strict monotonic function of the position). Moreover, note that despite its name the j_{const} rotation law does not yield density distributions with constant specific angular momentum when the parameter A deviates from zero ($A = 0.5$ here).

Part III

Simulations of explosions of rotating White Dwarfs

12 Pure deflagrating rapid rotators

As speculated, e.g., in Ref. [YL04], rotation could be the parameter that is responsible for a variety of SN Ia features that cannot be explained by the current version of the deflagration model (cf. section 6.3). As outlined in chapter 3, the masses of some progenitor stars are perhaps super-Chandrasekhar. It is evident that a higher amount of progenitor mass may lead to more energetic explosions. Accordingly, nickel masses as inferred for SN 1991T could be the outcome of such an explosion.

In the following, the influence of rotation on the flame is introduced by the consideration of two typical explosions. Then an overview of the parameter space that is covered by this study is given. Explanations for the failure of rapid rotation in the pure deflagration scenario follow.

12.1 Following typical explosions

Due to the fact that the ignition scenario is found to have an impact on the explosion outcome (cf. section 4.2), both static (cf. section 8.1) and stochastic ignitions (cf. section 8.2) are tested in the framework of this thesis. The deflagration scenario for rapid rotators is analysed by means of the combustion of the 14AWD4 rotator (cf. section 11.5) which was separately ignited by both ignition realisations. The outcome of the two explosions can be regarded as typical for the deflagration of rapidly rotating WDs.

Fig. 12.1(a) shows the flame surface embedded in density profiles at four instants for the 14AWD4 rotator that is ignited in the stochastic ignition scenario. Unless stated differently, the simulations for this chapter were carried out for one hemisphere only (with the grid extensions described in section 9.2.2). Thus the contour plots — cross sections in the yz-plane along the rotation axis — exhibit equatorial symmetry. According to the threshold values for nuclear burning (cf. section 7.2), the red contour line encloses densities down to which intermediate mass elements (IMEs) can be produced. Material within the grey contour line is converted to iron group elements (IGEs) if burnt by the flame.

At $t = 0.1$ s, 363 ignitions are set *isotropically* in the interior of the star for the "14AWD4 $C_e = 5 \times 10^4$" explosion model (see Fig. 12.1(a)). Even at this early period, an agglomeration of the flame around the rotation axis (which points along the x axis) is visible. This trend is intensified when burning has ceased at $t = 1.5$ s, causing a noticeable amount of unburnt material in the equatorial plane.

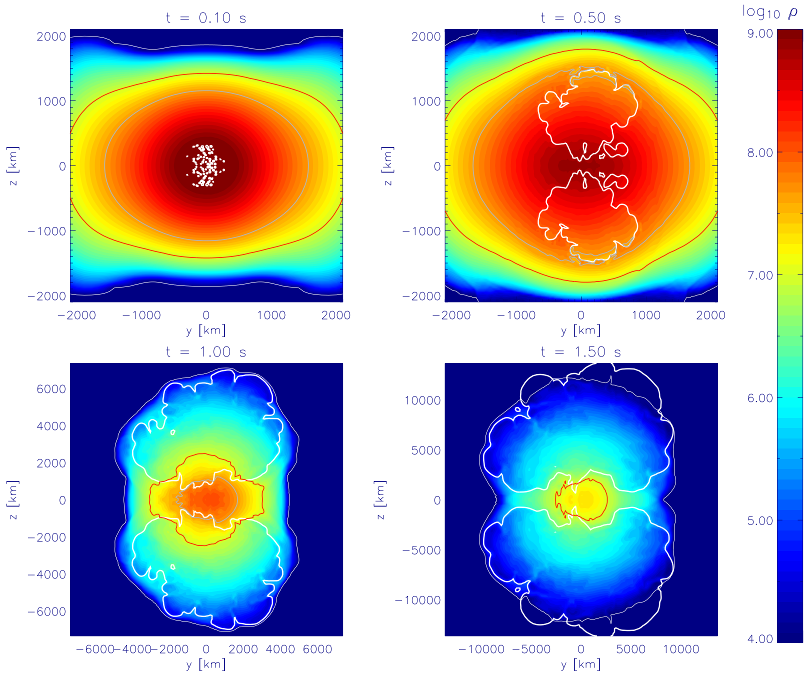

(a) “14AWD4 $C_e = 5 \times 10^4$” explosion model

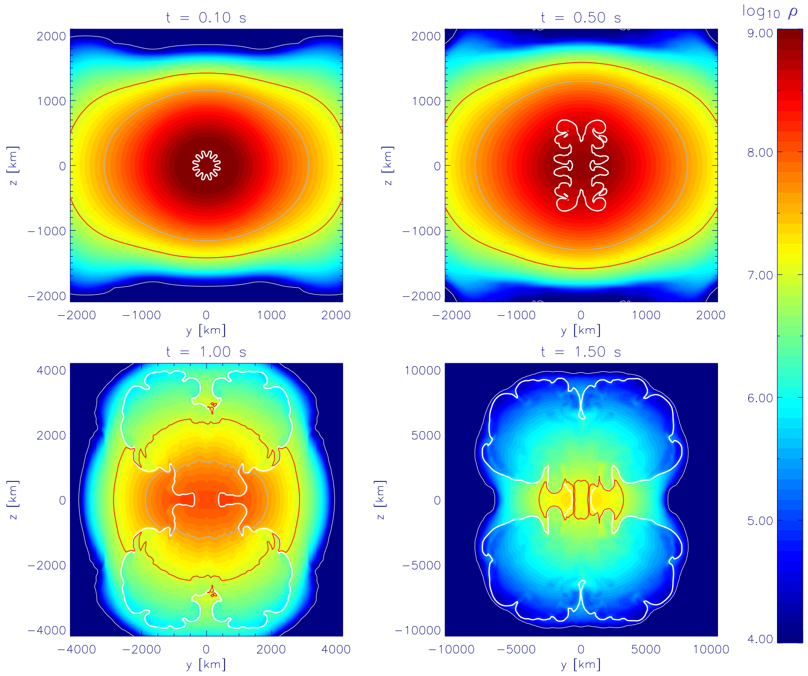

(b) “14AWD4 $c3$” explosion model

Figure 12.1: Density contour lines for the pure deflagration of the 14AWD4 rotator at different instants for stochastic ignition (upper panels) and $c3$ ignition (lower panels). Cross sections along the rotation axis of these simulations exhibiting equatorial symmetry are shown.

The same trend, namely preferred burning towards the poles and unburnt stellar material even close to the centre, emerges for $c3$ ignition (see Fig. 12.1(b)): the flame bulges that are located near the rotation axis evolve much faster compared to their equatorial counterparts, although they initially had the same size. However, note that unlike the case of stochastic ignition, the central region is at least partially burnt.

This anisotropic deflagration in rotating WDs is investigated in section 12.2. The influence of the free parameter of the stochastic ignition model (cf. section 8.2) is tested on the basis of one rotating WD model in section 12.3. Sections 12.4.1 and 12.4.2 present a parameter study concerning the rotation law for the $c3$ ignition and the stochastic ignition, respectively.

12.2 Impact of buoyancy

As stated in section 4.4.1, the ashes of SNe Ia are subject to buoyant motion. The existence of a preferred direction for the flame (see Figs. 12.1(a) and 12.1(b)) is caused by the buoyant force that acts anisotropically for rotators. Fig. 12.2(a) shows the gravitational acceleration $\boldsymbol{g}_{\mathrm{grav}}$ inside the 14AWD4 rotator. As a result of the lager density gradient along the rotation axis, $\boldsymbol{g}_{\mathrm{grav}}$ is stronger (indicated by longer arrays) in this direction compared to the equatorial plane. Buoyancy is caused by the effective gravitational acceleration $\boldsymbol{g}_{\mathrm{eff}}$ introduced in section 5.2, i.e., the gravitational acceleration including the centrifugal acceleration as plotted in Fig. 12.2(b). $\boldsymbol{g}_{\mathrm{eff}}$ is orthogonal to the coinciding isobaric and isopycnic surfaces (cf. section 5.2) and compensates the pressure gradient in hydrostatic equilibrium exactly. The difference in $\boldsymbol{g}_{\mathrm{eff}}$ along polar and equatorial direction is even larger than the difference in $\boldsymbol{g}_{\mathrm{grav}}$, which can be seen in Fig. 12.3.

Together with the Atwood number At (cf. Eq. (4.6)), $\boldsymbol{g}_{\mathrm{eff}}$ can be used to determine the velocity of a rising bubble. Fig. 12.4(b) shows the gradient of density of the exploding WD “14AWD4 $C_e = 5 \times 10^4$” at $t = 0.5$ s along various directions that are indicated in Fig. 12.4(a). The value of At does not strongly depend on the location of the flame inside the star, although a higher value of At in regions of stronger density gradient, i.e., along the rotation axis, is thinkable. At is always $\lesssim 0.5$. Nevertheless, due to its dependence on $\boldsymbol{g}_{\mathrm{eff}}$, the rising velocity v_b (cf. Eq. (4.5)) is affected by the position inside the star. The difference of $\boldsymbol{g}_{\mathrm{eff}}$ in polar and equatorial direction is given by a factor of $\lesssim 1.3$ (see Fig. 12.3). This means that according to Eq. (4.5), the rising velocity of ashes is greater by the factor of $\lesssim \sqrt{1.3}$ in the polar direction. The velocity of the fastest bubbles is of the order $\sim 10^8$ cm/s (with At $= 0.5$, $\boldsymbol{g}_{\mathrm{eff}} = 2 \times 10^{10}$ cm/s^2, and a bubble diameter of 10^8 cm), a value that is approximately 10 % of the speed of sound. Accordingly, smaller bubbles rise

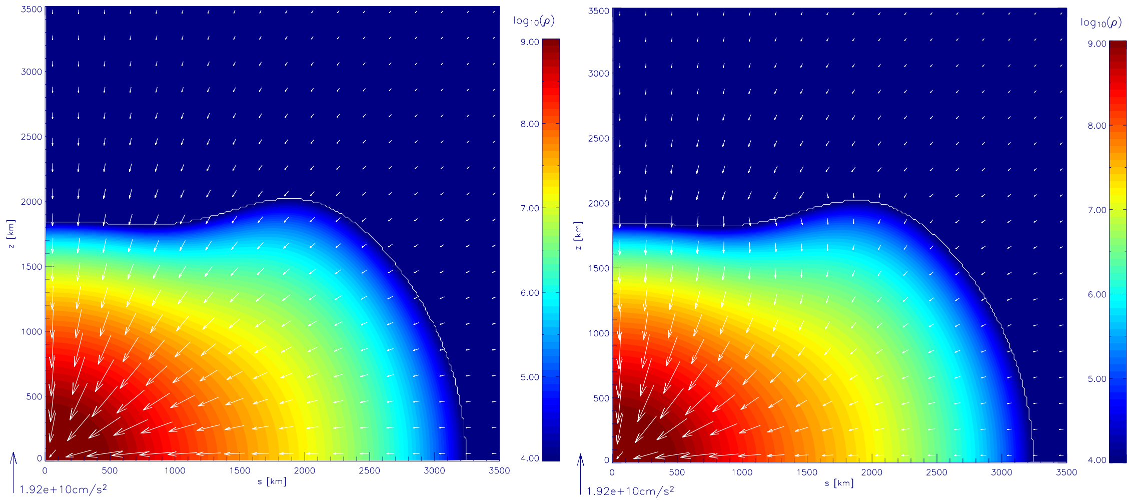

(a) $\boldsymbol{g}_{\mathrm{grav}}$

(b) $\boldsymbol{g}_{\mathrm{eff}}$

Figure 12.2: Density contour lines together with the gravitational acceleration $\boldsymbol{g}_{\mathrm{grav}}$ (Fig. 12.2(a)) and the effective gravitational acceleration $\boldsymbol{g}_{\mathrm{eff}}$ (Fig. 12.2(b)) that is indicated by arrows, respectively, for the 14AWD4 rotator. Note that $\boldsymbol{g}_{\mathrm{eff}}$ is orthogonal to the coinciding isobaric and isopycnic surfaces (outside the star, the centrifugal acceleration is zero).

more slowly. A lower limit for the rising speed is of the order of 10^6 cm/s (with $\mathrm{At} = 0.1$, a lower gravitational acceleration and the bubble dimension of 10^5 cm).

The difference in flame morphology between the polar and equatorial direction is greater than the factor $\sqrt{1.3}$ as can easily be seen in Figs. 12.1(a) and 12.1(b). The large difference in flame propagation speed can be explained by consequences which emerge from a small initial difference. As outlined in section 7.1.1, the propagation velocity of the flame consists of an advected component and the burning speed component normal to the flame surface. In the first case, buoyancy acts directly on the advection component and causes a slightly higher advection velocity in polar direction. Shortly after that, the burning speed is also indirectly influenced by these rising motions, due to the fact that turbulence is evoked by large scale motion (cf. section 4.5.2). The formation of turbulence causes an enhanced burning velocity that is no longer limited to the laminar value (cf. section 4.5). Therefore, fast burning is possible only in regions with sufficient turbulence.

The evolution of turbulence is shown in Fig. 12.5(a) where the subgrid scale velocity (cf. section 7.1.2) for the "14AWD4 $C_e = 5 \times 10^4$" explosion model is plotted. At $t = 0.5$ s, the strongest turbulent motion appears at the top of the flame near the poles. As argued, turbulence is much weaker close to the equatorial plane. As a consequence, the flame propagation is suppressed there and, accordingly, fuel

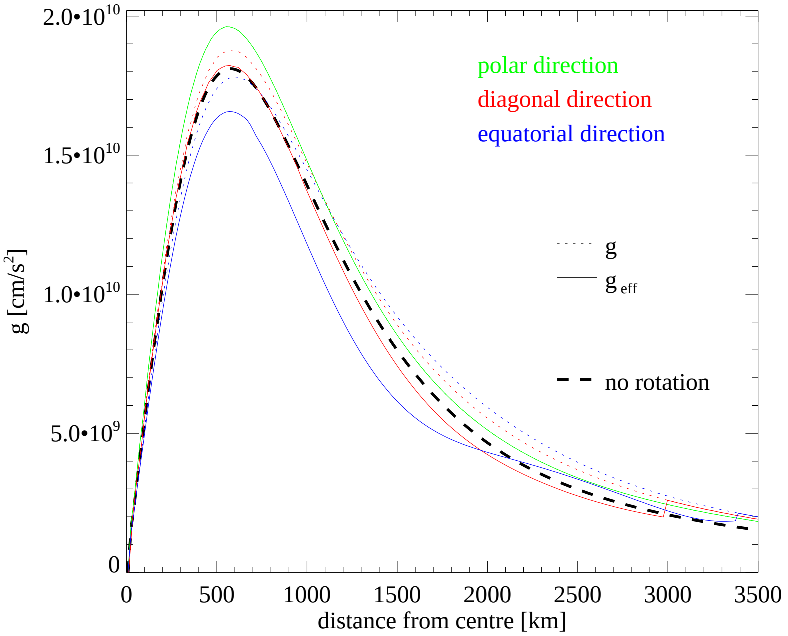

Figure 12.3: Gravitational acceleration $\boldsymbol{g}_{\mathrm{grav}}$ (dotted line) and the effective gravitational acceleration $\boldsymbol{g}_{\mathrm{eff}}$ (solid line) along the rotation axis, the stellar diagonal, and the equatorial plane for the 14AWD4 rotator. The edges of the red line (at ~ 3000 km) and the blue line (at ~ 3400 km) appear due to the absence of centrifugal acceleration outside the star. The dashed thick black line represents the spherically symmetric gravitational acceleration for the non-rotating star of equal central density.

remains unburnt at the centre.

The largest clumps of ash develop primarily in the polar direction due to the more effective buoyancy. As a consequence of their size (cf. Eq. (4.5)), those clumps rise fastest. Soon combustion is dominated by the largest flame bubbles, in turn enhancing turbulence.

The impact of buoyancy becomes apparent in an impressive manner for the extreme case of rotation that is so rapid that the maximum density no longer coincides with the central density but forms a ring in the equatorial plane (see appendix D, Fig. D.1). If a buoyant fluid element is located in the interior of the massive ring, it "rises" no longer towards the stellar surface but to the centre. However, the rotation laws that are needed to obtain such rotators are considered to be unrealistic in the SN Ia progenitor scenario (cf. chapter 3).

Turbulent combustion is characterised by the penetration of fuel and ashes. However, transport of material orthogonal to the rotation axis demands the exchange of angular momentum. The ashes enclosed by the outward burning flame need to

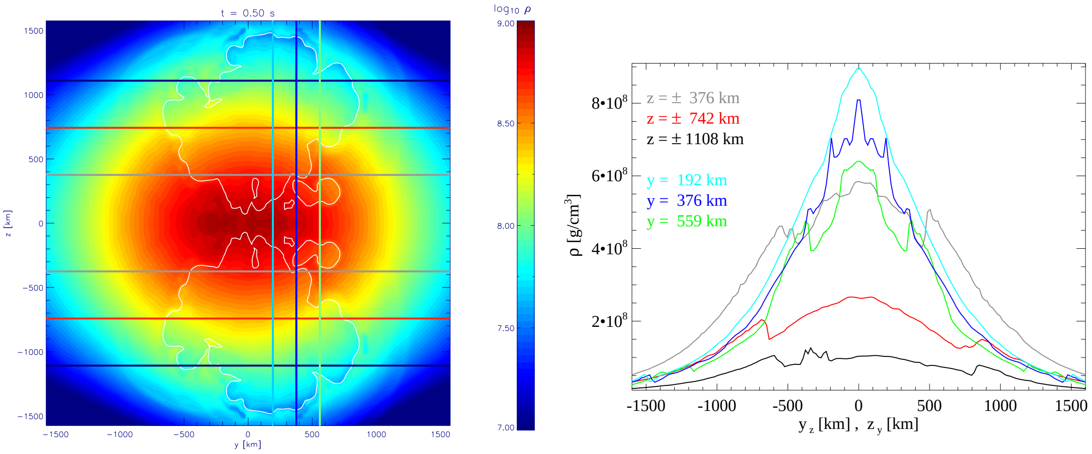

(a)

(b)

Figure 12.4: Density contour levels for the "14AWD4 $C_e = 5 \times 10^4$" explosion model (panel 12.4(a)) and density profiles along designated directions in the yz-plane (panel 12.4(b)) at $t = 0.5$ s. The straight lines in the contour plot indicate the directions along which the density contrast is extracted in Fig. 12.4(b). The colours correspond to those used for the one-dimensional density plot, respectively. The Atwood number At is accessible by comparing the density contrast between fuel and ashes, noticeable as jumps in density.

accept angular momentum whereas inflowing fuel has to give off angular momentum (see Fig. 11.4) for the rotation laws considered in the SN Ia context. The investigation of a potentially significant inhibition of turbulent combustion due to such a "barrier" in angular momentum exchange is not trivial in systems that exhibit a pressure gradient. An estimation of the influence of this effect can be achieved by looking at the radial velocities emerging during the explosion. From Fig. 12.5(b) it is apparent that any radial flow is much weaker in the equatorial plane compared to the polar regions burnt by the flame. This behaviour does not necessarily indicate the blocking of turbulent combustion by inefficient angular momentum exchange, because the absence of radial motions can also explained by the preferred burning direction caused by buoyancy as described before. However, inhibition of the angular momentum exchange between fuel and ashes is supported by the fact that inflowing (i.e., negative radial) velocities as the result of large scale Rayleigh-Taylor motion is also absent.

In summary, both the buoyancy that is enhanced at the poles in rotating WDs and the blocked mixing orthogonal to the rotation axis lead to a strongly anisotropic flame that leaves behind unburnt material at the stellar centre.

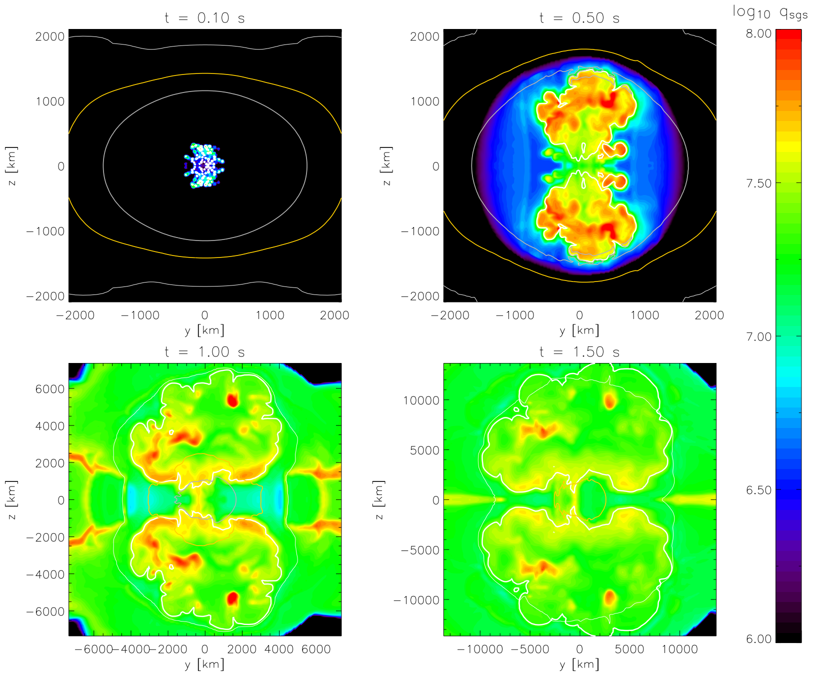

(a) turbulent velocities: “14AWD4 $C_e = 5 \times 10^4$” explosion model

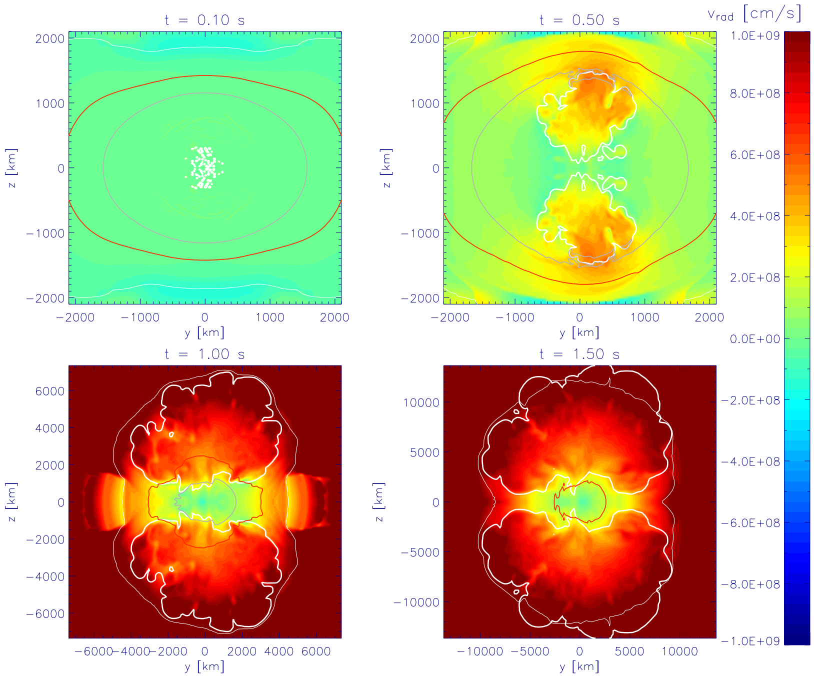

(b) radial velocities: “14AWD4 $C_e = 5 \times 10^4$” explosion model

Figure 12.5: Contour lines of the turbulent velocities (upper panels, Fig. 12.5(a); $q_{\mathrm{sgs}} \equiv \sqrt{3}\, v'(\Delta)$) and the radial velocities (lower panels, Fig. 12.5(b)) for the “14AWD4 $C_e = 5 \times 10^4$” explosion model at different instants (cf. Fig. 12.1(a) for the density contour levels of this explosion). Cross sections along the rotation axis of simulations exhibiting equatorial symmetry are shown.

C_e	5×10^1	5×10^3	5×10^4	5×10^5	5×10^7	10^4
mode	iso	iso	iso	iso	iso	dipole
Ω [π]	2	2	2	2	2	4
$I_{2\pi}$	13	152	391	809	19980	247
t = 5 s						
E_{kin} [10^{50} erg]	2.87	3.61	5.30	6.90	6.11	4.43
E_{tot} [10^{50} erg]	0.21	1.33	3.54	5.47	4.62	2.55
E_{nuc} [10^{51} erg]	1.050	1.182	1.420	1.619	1.535	1.310
IGEs [$M_\odot$]	0.40	0.51	0.69	0.79	0.74	0.62
[% M_{tot}]	20	25	34	39	37	31
IMEs [$M_\odot$]	0.51	0.46	0.41	0.46	0.45	0.40
[% M_{tot}]	25	23	20	23	23	20
C+O [$M_\odot$]	1.10	1.04	0.91	0.76	0.82	0.99
[% M_{tot}]	55	52	46	38	40	49

Table 12.1: Energetics and compositions for the deflagration study that is activated by stochastic ignition with different values for C_e in the 20AWD3 rotator ($M_{tot} = 2.01\ M_\odot$). Here Ω denotes the total spherical angle covered by the simulation domain.

12.3 Ignition speed in the stochastic ignition scenario

The stochastic ignition process (cf. section 8.2) contains one free parameter: the exponentiation parameter C_e that controls the overall speed of the creation of ignitions. Just as in the original work [SN06] (see Fig. 6.3(a)), this parameter was varied over a broad range in order to study the influence of C_e. For this reason, the 20AWD3 rotator (see appendix B, Fig. B.4) was ignited for C_e between 5×10^1 and 5×10^7 (see Table 12.1) in the isotropical mode, i.e., for ignitions that are placed without preference (cf. section 4.2). The evolution of the total energy and the composition of these simulations is summarised in Figs. 12.8(a) and 12.9(a), respectively.

Increasing C_e beyond the value 5×10^1 results in a higher amount of IGEs (see Table 12.1 and Fig. 12.9(a)). However, similar to the results of the original work that studies the combustion of non-rotating WDs, there exists a certain C_e, which in fact is not the largest value, but yields a maximum in energy output. This happens for $C_e = 5 \times 10^5$. This effect is explained by the fact that an even higher number of flame ignitions cannot further enhance the flame surface but, on the contrary, inhibits the growth of the flame surface and thus limits the energy generation (see Ref. [SN06], cf. also Ref. [RHNW06] for the discovery of the same trend for the static multi-spot ignition).

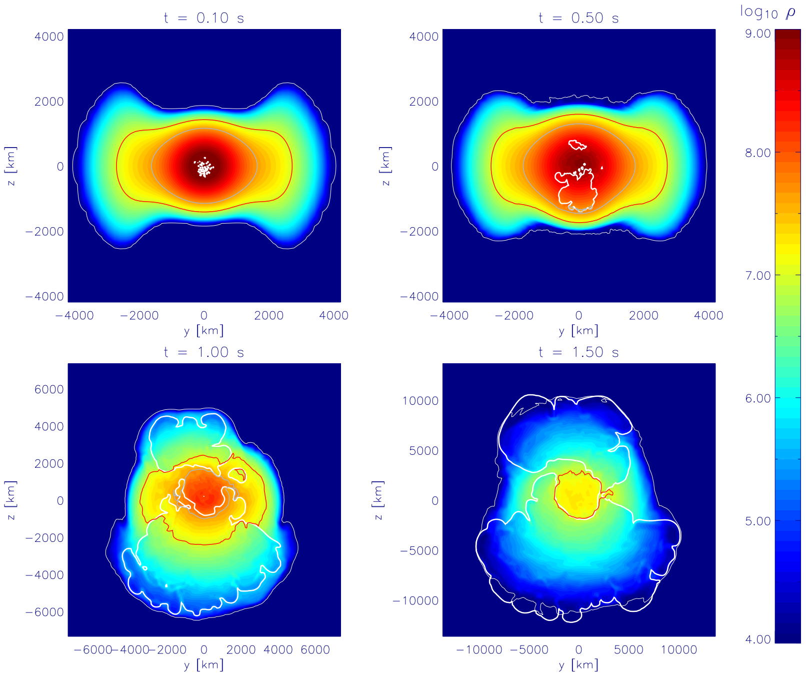

Figure 12.6: Density contour lines for the pure deflagration of the 20AWD3 rotator at different instants, ignited by the dipole jet flow scenario. Cross sections along the rotation axis of a full star simulation is shown.

However, employing the value $C_e = 5 \times 10^5$ amounts to burning the entire centre almost instantaneously because within the first tenth of a second 792 ignitions are initiated within a central region of the typical radius of ~ 350 km. Since high values of C_e not only seem unphysical but also cannot serve as a remedy for the problems arising for the stochastic ignition in combination with rotation (cf. section 12.4.2), the values of $C_e = 5 \times 10^3$ and $C_e = 5 \times 10^4$ were used in this work.

The dipole jet flow scenario — the incineration of a hemisphere mainly as described in section 8.2.2 — was also tested by means of the 20AWD3 rotator. However, as the impact of buoyancy already suggests (cf. section 12.2), this ignition realisation does not ameliorate the problem of remaining fuel close to the centre. If ignitions are set mainly in one hemisphere (without loss of generality, the southern one), the northern hemisphere is also burnt at a later time, but C and O are leftover in the core as Fig. 12.6 shows. In the non-rotating case, a strong off-centre ignition also leads to a delayed burning of the distant stellar part, but less centrally located fuel remains (F. Röpke, private communication).

A remarkable result emerges from a determination of the influence of the detailed location of randomly chosen ignition points (cf. section 8.2.2 for the method of placing ignitions). The "8rigid $C_e = 5 \times 10^3$" explosion model (see Table 12.3) was

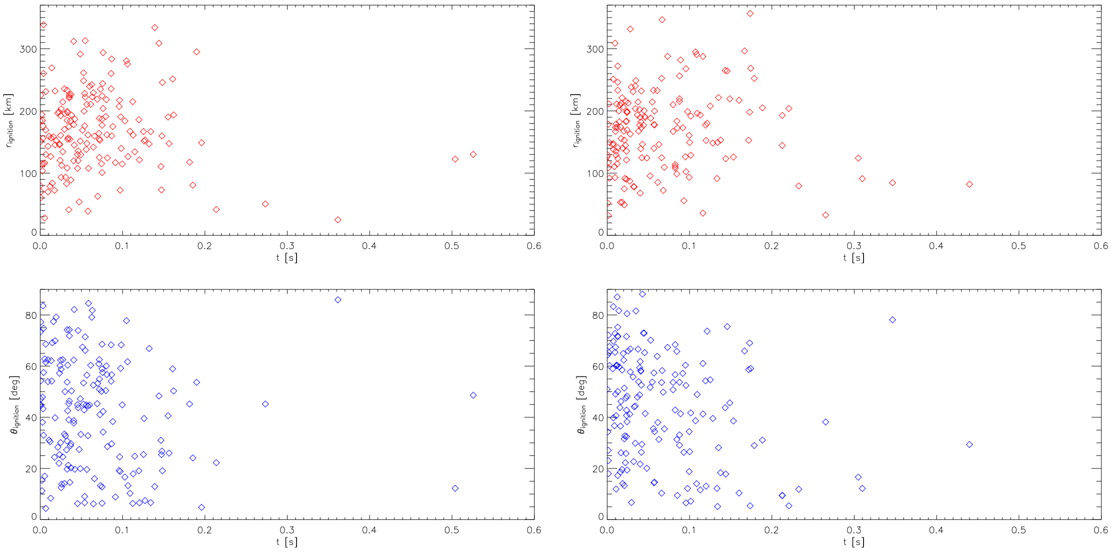

(a) 167 ignitions set within 0.53 s (b) 163 ignitions set within 0.44 s

Figure 12.7: Ignition radii (upper panels) and polar angles (lower panels) of the ignitions that are set in the “8rigid $C_e = 5 \times 10^3$” (Fig. 12.7(a)) and “8rigid* $C_e = 5 \times 10^3$” (Fig. 12.7(a)) explosion models, which only have two different seeds in the random number generator that arranges the ignitions

simulated twice. The only difference was a different seed for the random number generator which sets the ignition position within a shell whose number is determined by the Poisson process. Due to the randomness and nonlinearity of the problem, the total number of ignitions is not entirely but approximately the same: 167 vs. 163 ignitions were set during the simulations. However, the outcome of both explosions shows considerable differences, in particular the generated nuclear energy deviates by ~ 20 %.

Figs. 12.7(a) and 12.7(b) show the radii and polar angles of the initiated ignitions versus time for both simulations. Differences as a result of the randomly generated ignition locations are present, but don’t seem immense. As outlined in section 12.2, it is clear that the detailed ignition location plays a role particularly for the incineration of rotating stars because ignitions close to the rotation axis form more rapidly and dominate the explosion. Therefore, the influence of the random numbers is expected to be larger in rotating stars compared to their non-rotating counterparts. Anyway, the result that the exact locations of ignitions significantly alters the explosion outcome should be of interest for the SN Ia ignition research. Furthermore it could be related to the diversity among SNe Ia.

12.4 Variation of the rotation law

The influence of the rotation law on the pure deflagration scenario is investigated in the following. Rapidly rotating WDs can greatly exceed the canonical Chandrasekhar mass: the progenitor stars under consideration possess masses in the range of 1.40 $M_\odot$ (no rotation) and 2.01 $M_\odot$ (model 20AWD3).

An important conclusion can already be drawn by looking at the mass densities which the different WD models exhibit. The total mass increases by ~ 44 % from the non-rotating star to the 20AWD3 rotator. However, the mass fraction with densities greater than 5.25×10^7 g/cm^3 (the threshold density above which burning to IGEs takes place) grows by only ~ 16 %. The fraction of dense material within the star *decreases* from ~ 91 % in the non-rotating star to only ~ 73 % in the 20AWD3 rotator which — although heavier by ~ 0.6 $M_\odot$ — contains only ~ 0.2 $M_\odot$ more IGEs (see Figs. 12.10(a) and 12.10(b)). Therefore it is doubtful whether the pure deflagration of rapidly rotating super-Chandrasekhar-mass models yields significantly more ^{56}Ni compared to the non-rotating case.

The rotation law is varied for both the $c3$ ignition scenario (section 12.4.1) and the stochastic ignition scenario (section 12.4.2) in the following.

12.4.1 $c3$ ignition

Fig. 12.8(b) demonstrates the temporal evolution of the total energy E_{tot} for different rotators that are ignited with the $c3$ ignition. Note that the more massive WDs start from more negative values of total energy. This is caused by the larger gravitational energies E_{grav} for heavier stars (see Table 12.2). All simulations end in successful explosions that cause the star to unbind at $t \sim 1$ s, whereas this takes longest for the heaviest WD, 20AWD3. The differences in E_{tot} that are apparent in the beginning become smaller during the explosion process, which is caused by a higher amount of released nuclear energy E_{nuc} for the more massive WDs.

The non-rotating star exhibits the highest value of E_{tot} in the homologous expansion phase (cf. section 9.3). E_{tot} at $t = 5$ s consists mainly of kinetic energy E_{kin} of the ejecta (cf. Fig. 9.9 for the typical temporal evolution of the energy contributions). Accordingly, the ejecta are fastest for the non-rotating progenitor on average, as will be shown in section 12.7.

With respect to the stellar composition after the explosion, the following trend is visible from Table 12.2 and Figs. 12.9(b), 12.11(a), and 12.11(b): the heavier the progenitor, the more fuel is left unburnt. The amount of IGEs after 5 s ranges from 0.54 $M_\odot$ for the non-rotating star to 0.67 $M_\odot$ for the rapidly rotating model 20AWD3. However, the fraction of IGEs with respect to the total mass *decreases* for rapid rotation. Only 33 % of the total 2.01 $M_\odot$ is converted to IGEs for the 20AWD3 rotator. The amount of IMEs rises for more rapid rotation, its fraction

	norot	8rigid	10AWD1	11AWD2	14AWD4	20AWD3
M_{tot} $[M_\odot]$	1.40	1.47	1.64	1.74	1.79	2.01
Ω $[\pi]$	2	2	2	2	2	2
t = 0 s						
E_{grav} $[10^{51}\,\mathrm{erg}]$	-3.027	-3.204	-3.665	-4.027	-4.135	-4.518
E_{rot} $[10^{50}\,\mathrm{erg}]$	0.00	0.44	1.75	2.62	2.99	4.46
β [%]	0.00	1.38	4.78	6.50	7.22	9.87
t = 5 s						
E_{kin} $[10^{50}\,\mathrm{erg}]$	6.49	6.53	6.63	5.99	5.42	5.28
E_{tot} $[10^{50}\,\mathrm{erg}]$	5.89	5.87	5.74	4.84	4.09	3.50
E_{nuc} $[10^{51}\,\mathrm{erg}]$	1.076	1.129	1.291	1.318	1.289	1.419
IGEs $[M_\odot]$	0.54	0.56	0.65	0.65	0.64	0.67
$[\%\ M_{tot}]$	38	39	40	37	35	33
IMEs $[M_\odot]$	0.28	0.30	0.34	0.36	0.35	0.44
$[\%\ M_{tot}]$	20	20	20	21	20	22
C+O $[M_\odot]$	0.58	0.61	0.65	0.73	0.80	0.90
$[\%\ M_{tot}]$	42	41	40	42	45	45

Table 12.2: Energetics and compositions for the deflagration study that is initiated by the $c3$ ignition in different rotators. Here Ω denotes the total spherical angle covered by the simulation domain.

is remarkably constant at $\sim 20\ \%$ for all rotation laws. Combined with the fact that the amount of unburnt material becomes larger for faster rotators, this result indicates that the higher absolute amount of IMEs for the rapid rotators is not obtained “at the cost” of fuel in contrast to experimental observations (cf. section 12.7). It is a consequence of the small amount of produced IGEs.

12.4.2 Stochastic ignition

All in all, the trends regarding the outcome of the explosion that can be derived from the $c3$ ignition in section 12.4.1, remain valid for the stochastic ignition scenario. But the situation is aggravated, i.e., even less IGEs and IMEs are produced and even more fuel remains (see Table 12.3 and Figs. 12.8(c), 12.9(c), 12.11(a), and 12.11(b)). This is explained by the fact that, unlike the symmetric $c3$ ignition, the stochastically ignited bubbles are immediately subject to buoyant motion since the net buoyancy is not balanced by a symmetric alignment of the ashes, therefore having less time to burn the central region efficiently. For this reason, the $c3$ ignition may be considered as artificial only because it is unlikely — bearing in mind that the $c3$ ignition probably arises from a central one-point ignition — that within rotators

	norot	8rigid / 8rigid*	10AWD1	11AWD2	14AWD4	20AWD3
M_{tot} $[M_\odot]$	1.40	1.47	1.64	1.74	1.79	2.01
C_e	5×10^3	5×10^3	5×10^3	5×10^3	5×10^4	5×10^3
Ω $[\pi]$	2	2	2	2	2	2
$I_{2\pi}$	172	167 / 163	168	154	404	152
t = 0 s						
E_{grav} $[10^{51}\,\mathrm{erg}]$	-3.027	-3.204	-3.665	-4.027	-4.135	-4.518
E_{rot} $[10^{50}\,\mathrm{erg}]$	0.00	0.44	1.75	2.62	2.99	4.46
β [%]	0.00	1.38	4.78	6.50	7.22	9.87
t = 5 s						
E_{kin} $[10^{50}\,\mathrm{erg}]$	8.69	7.70 / 5.63	8.64	3.67	3.68	3.61
E_{tot} $[10^{50}\,\mathrm{erg}]$	8.16	7.04 / 4.82	7.84	1.95	1.97	1.33
E_{nuc} $[10^{51}\,\mathrm{erg}]$	1.282	1.234 / 1.005	1.495	1.016	1.073	1.182
IGEs $[M_\odot]$	0.67	0.63 / 0.50	0.79	0.47	0.52	0.51
$[\%\, M_{tot}]$	48	43 / 34	48	27	29	25
IMEs $[M_\odot]$	0.28	0.30 / 0.27	0.32	0.34	0.31	0.46
$[\%\, M_{tot}]$	20	20 / 19	20	20	17	23
C+O $[M_\odot]$	0.45	0.54 / 0.70	0.53	0.93	0.96	1.04
$[\%\, M_{tot}]$	32	37 / 47	32	53	54	52

Table 12.3: Energetics and compositions for the deflagration study that is activated by the stochastic ignition with $C_e = 5 \times 10^3$ ($C_e = 5 \times 10^4$ for 14AWD4) in different rotators (* note the different values for both simulations with the 8rigid rotator that initially only vary the seed for the random number generator used for the stochastic ignition process). Here Ω denotes the total spherical angle covered by the simulation domain.

such a flame morphology could ever evolve.

Fluctuations in the composition between different progenitor models are more distinct for stochastic ignition compared to $c3$ ignition. This is due to the fact that not only the overall number of ignitions but also the specific locations of the ignitions influence the explosion outcome (cf. section 12.3).

Noticeable is the "success" of the non-rotating and the 10AWD1 (see appendix B, Fig. B.2) progenitor models combined with the stochastic ignition. Both models share the low influence of rotation in the central stellar region. Note that the angular velocity of the 10AWD1 rotator is comparably low in the core because an efficient angular momentum transport caused by convective pre-SN Ia motion is *not* admitted. Thus, the multi-spot ignition that is consistent with many features of the "Branch normal" (cf. section 2.1) events for non-rotating WDs [SN06], is also successful for the 10AWD1 rotator. In addition, even more fuel is available for the 10AWD1 rotator to power the explosion. However, employing rotation laws similar to the one of the 10AWD1 rotator is not a good “recipe” to generate powerful SN Ia explosions, since the convective phase is necessary for the initiation of the thermonuclear runaway (L. Iapichino and S.-C. Yoon, private communication; cf. section 4.1).

From the “14AWD4 $C_e = 5 \times 10^4$” explosion model it can be seen that IMEs are not generated “at the cost” of C and O but that of IGEs. Since a higher value of C_e ($C_e = 5 \times 10^4$ for the 14AWD4 rotator but 5×10^3 elsewhere) leads to more IGEs (cf. section 12.3), the lack of IMEs in favour of IGEs for the 14AWD4 rotator (see Fig. 12.11(b)) confirms the close relationship between IGEs and IMEs: a more energetic explosion, resulting in a comparably high amount of IGEs, causes such a rapid expansion of the star that the burning to IMEs ceases early and leaves behind a large amount of unburnt material.

The “16j_{const}adr05 $C_e = 5 \times 10^3$” and “16v_{const}adr02 $C_e = 5 \times 10^3$” explosion models are only capable of generating a small amount of IGEs (see Table 12.4). Indeed, neither the j_{const} nor the v_{const} rotation law are considered as realistic in terms of accreting WD rotation (cf. chapter 3).

12.5 Influence of numerical resolution

All simulations for this work were done in three spatial dimensions. At least one hemisphere or even a full star were considered. Therefore, the resolution was chosen to be relatively coarse (cf. section 9.2.2): the spacing of the initial flame grid was 7.5×10^5 cm. In order to get an estimate of the accuracy of all simulations, the “8rigid $C_e = 5 \times 10^4$” explosion model was redone with doubled resolution.

The outcome of both the coarse and the fine simulations are summarised in Table 12.5. As a result of higher spatial resolution, a larger number of ignitions, namely 1291 as compared to 421, that are smaller in size could be initiated. Although the impact of stochastic ignition on the explosion outcome is known (cf. section 12.3), both simulations are in accordance to a high degree with respect to the energetics and compositions. This could be due to the fact that the exponentiation parameter used for the resolution study is comparably high. Thus, stochastic effects could cancel out each other, leading to a more homogeneous explosion.

Fig. 12.12 shows the flame surface of the highly resolved “8rigid $C_e = 5 \times 10^4$” simulation at four instants within a hemisphere. The typically emerging Rayleigh-Taylor “mushrooms” of ash burning towards the stellar surface are clearly visible from these three-dimensional plots. The flame surface is coloured according to the value of the turbulent velocity fluctuations. Note that these are highest in gaps and in the space between the mushrooms, since there the shear motion is largest.

Although the resolution study is done only on the basis of two simulations, the result indicates that the resolution employed for most of the simulations is sufficient.

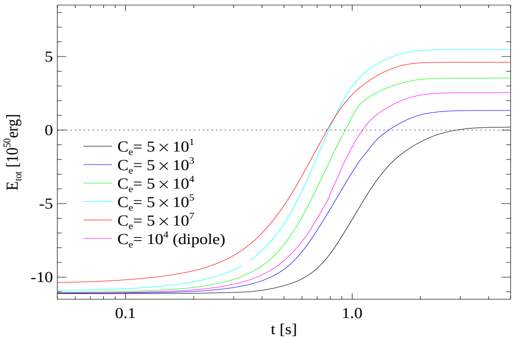

(a) stochastic ignition: 20AWD3

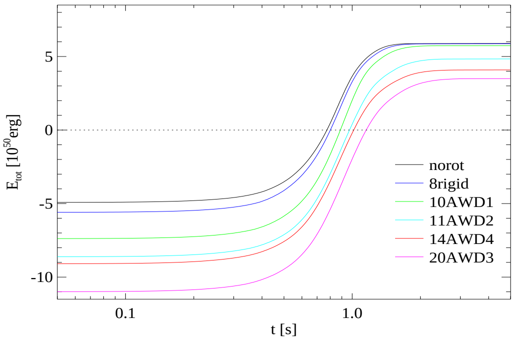

(b) rotation law: $c3$ ignition

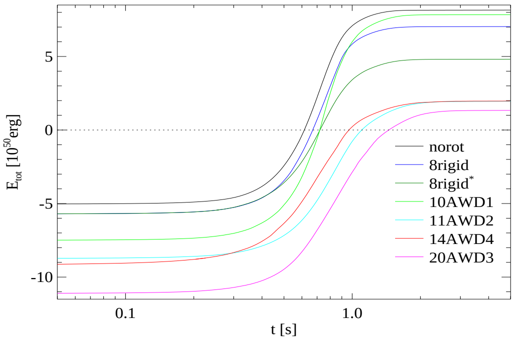

(c) rotation law: stochastic ignition

Figure 12.8: Temporal evolution of the total energy for the deflagration study that is initiated by stochastic ignition with different values for C_e in the 20AWD3 rotator (Fig. 12.8(a)), by $c3$ ignition in different rotators (Fig. 12.8(b)), and by stochastic ignition in different rotators ($C_e = 5 \times 10^4$ for the 14AWD4 rotator, else $C_e = 5\times10^3$) (Fig. 12.8(c))

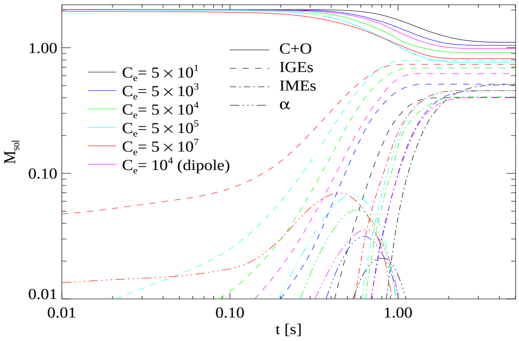

(a) stochastic ignition: 20AWD3

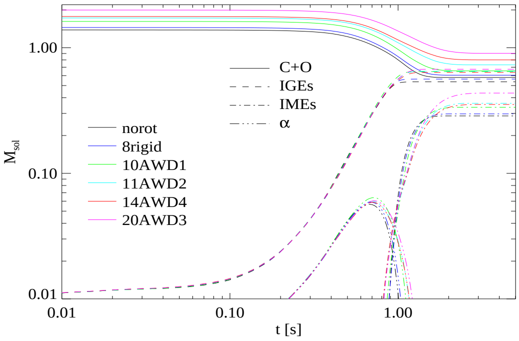

(b) rotation law: $c3$ ignition

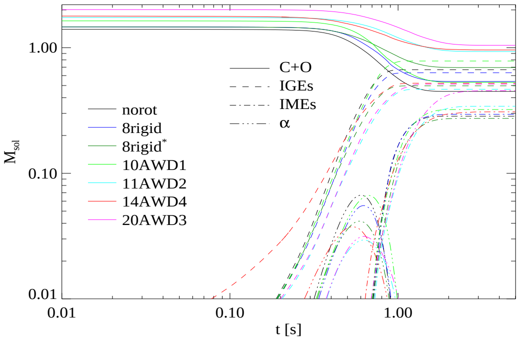

(c) rotation law: stochastic ignition

Figure 12.9: Temporal evolution of the composition for the deflagration study that is initiated by stochastic ignition with different values for C_e in the 20AWD3 rotator (Fig. 12.9(a)), by $c3$ ignition in different rotators (Fig. 12.9(b)), and by stochastic ignition in different rotators (Fig. 12.9(c))

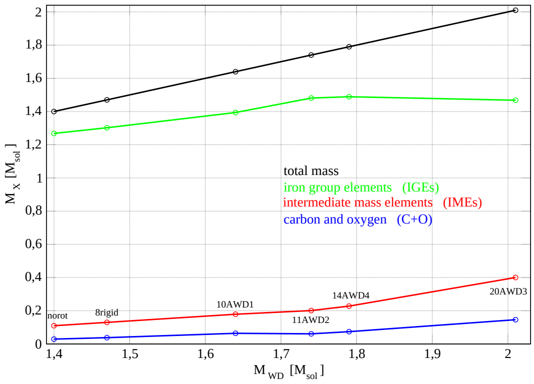

(a) no expansion: absolute fractions

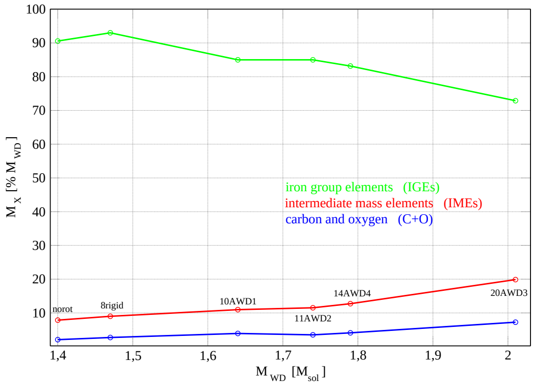

(b) no expansion: relative fractions

Figure 12.10: Estimate of the burning products if the stars were not expanding during the burning process. The figure shows the fractions of the total mass in the high density regime ($\rho > 5.25 \times 10^7 \mathrm{g/cm}^3$, "IGEs"), the medium density regime ($5.25 \times 10^7 \mathrm{g/cm}^3 > \rho > 1.05 \times 10^7$ g/cm^3, "IMEs"), and the low density regime ($\rho \leq 1.05 \times 10^7$ g/cm^3 , "C+O").

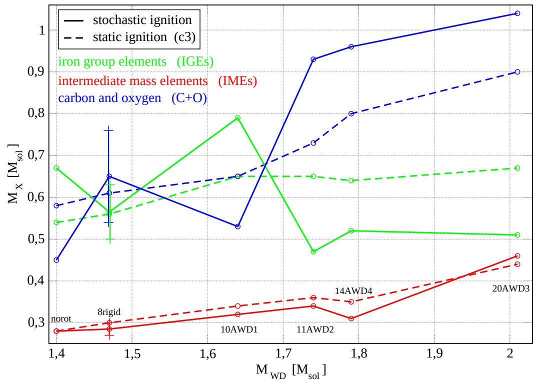

(a) pure deflagration: absolute fractions

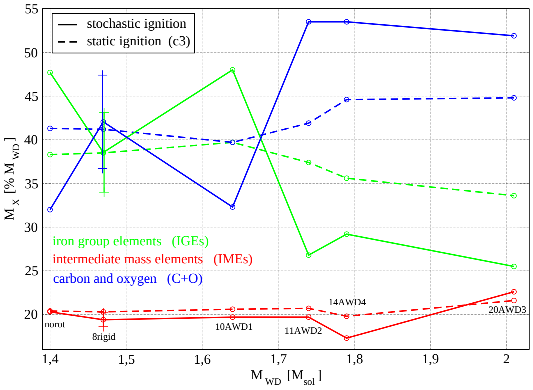

(b) pure deflagration: relative fractions

Figure 12.11: Burning products after $t = 5$ s as the outcome of simulations that are ignited by stochastic ignition (solid lines) and $c3$ ignition (dashed lines). Note the influence of the stochastic burning on the explosion outcome as can be seen for the 8rigid rotator: there the burning products are taken as the mean of two identical simulations that differ only in the random numbers for stochastic ignition.

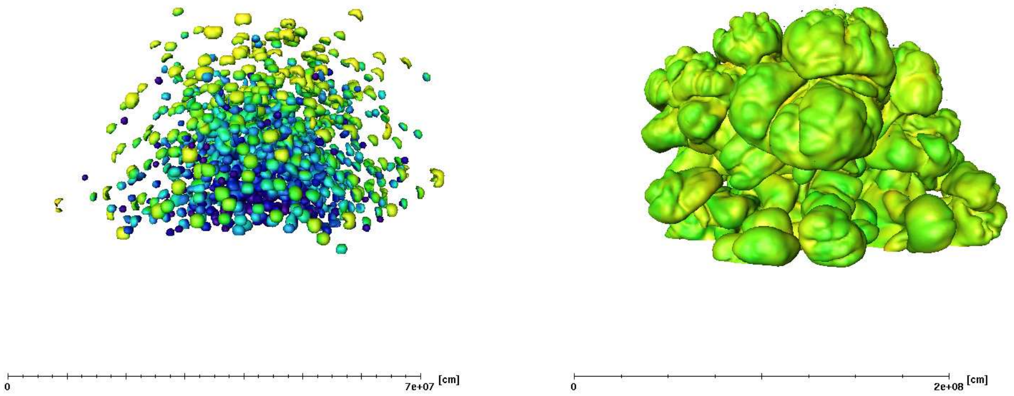

(a) $t = 0.1$ s

(b) $t = 0.5$ s

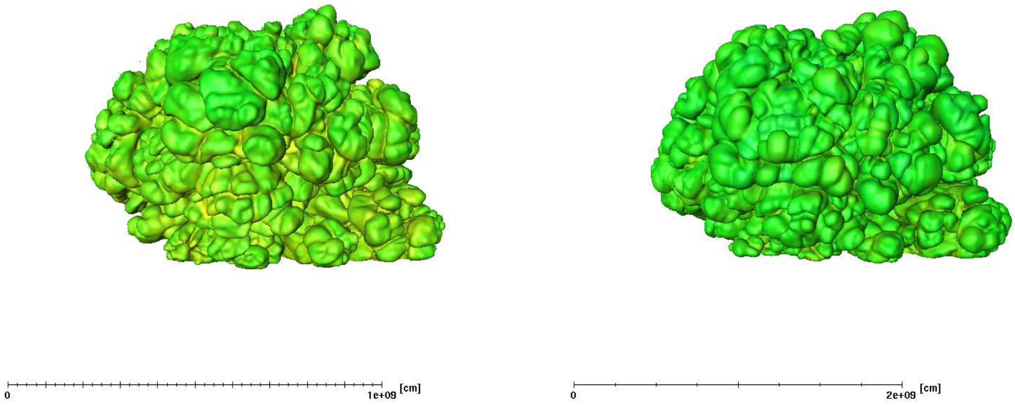

(c) $t = 1.0$ s

(d) $t = 1.5$ s

Figure 12.12: Flame surface for the highly resolved "8rigid $C_e = 5 \times 10^4$" explosion model. The initial flame grid spacing is $\Delta x = 3.75 \times 10^5$ cm. Only the simulated hemisphere is shown, which may hide the fact that the explosion is quite aspherical even for the critical rigid rotator. The surface colours denote the value of the amount of turbulent velocity fluctuations, ranging from dark blue (10^6 cm/s) over green and yellow to red (10^8 cm/s).

	$16j_{const}$adr05	$16v_{const}$adr02
M_{tot} $[M_\odot]$	1.80	1.71
C_e	5×10^3	5×10^3
Ω $[\pi]$	2	2
$I_{2\pi}$	159	158
t = 0 s		
E_{grav} $[10^{51}\,\mathrm{erg}]$	-4.271	-4.056
E_{rot} $[10^{50}\,\mathrm{erg}]$	3.16	2.39
β [%]	7.40	5.89
t = 5 s		
E_{kin} $[10^{50}\,\mathrm{erg}]$	1.66	1.29
E_{tot} $[10^{50}\,\mathrm{erg}]$	-0.75	-1.11
E_{nuc} $[10^{51}\,\mathrm{erg}]$	0.817	0.679
IGEs $[M_\odot]$	0.34	0.29
$[\%\,M_{tot}]$	19	17
IMEs $[M_\odot]$	0.34	0.27
$[\%\,M_{tot}]$	19	16
C+O $[M_\odot]$	1.12	1.15
$[\%\,M_{tot}]$	62	67

Table 12.4: Energetics and compositions for the deflagration study that is activated by stochastic ignition with $C_e = 5 \times 10^3$ in the $16j_{const}$adr05 and $16v_{const}$adr02 rotators. Here Ω denotes the total spherical angle covered by the simulation domain.

12.6 Shear motion during the explosion

It is a common belief that the shear introduced by differential rotation can enhance the explosion strength by increasing the flame surface. Although rotating WDs exhibit high rotation velocities (the surface of the 8rigid rotator moves with 2.5 % of the speed of light), within the entire span of time during which burning takes place ($t \lesssim 1.5$ s) the direct influence of rotation on the flame surface is limited. The critical rigid rotator 8rigid accomplishes only half a rotation if the burning induced expansion is neglected. The latter arranges a slowdown of the star as soon as the thermonuclear runaway is initiated as a result of angular momentum conservation.

Fig. 12.13 presents the rotation law profile by means of the averaged velocities arising at certain distances to the rotation axis. In view of Fig. 11.2, the kink in angular velocity Ω does not make an impact on the track speed within the WD (in Fig. 12.13, it is slightly visible at a distance of 680 km).

Unless a distinct jump in Ω occurs — which is not the case for smooth differential rotation — , the flame will not be significantly influenced by rotation in a direct way

cells per octant	128	256
mode	iso	iso
Ω [π]	2	2
$I_{2\pi}$	421	1291
t = 5 s		
E_{kin} [10^{50} erg]	8.46	8.17
E_{tot} [10^{50} erg]	7.87	7.56
E_{nuc} [10^{51} erg]	1.322	1.302
IGEs [$M_\odot$]	0.70	0.69
[% M_{tot}]	48	47
IMEs [$M_\odot$]	0.28	0.28
[% M_{tot}]	19	19
C+O [$M_\odot$]	0.49	0.50
[% M_{tot}]	33	34

Table 12.5: Energetics and compositions for the deflagration study that is activated by stochastic ignition with $C_e = 5 \times 10^4$ in the 8rigid rotator ($M_{tot} = 1.47\ M_\odot$). The resolution is doubled for the simulation summarised in the right column. Here Ω denotes the total spherical angle covered by the simulation domain.

(but, as described in section 12.2, due to buoyant and angular momentum effects).

It might be the case that, as proposed in Ref. [YL04], rotation could trigger a deflagration-to-detonation transition (cf. section 4.3.1) since the outer layers still rotate rapidly when the outward burning flame causes a slowdown of the WD. The resulting gradient in velocity due to burning is higher than by differential rotation (cf. Fig. 12.13 at $t = 0.9$ s and $y \sim 4400$ km) and could possibly generate a detonation if the flame surface is increased abruptly and therefore also the released energy. However, because the knowledge of the initiation of a deflagration-to-detonation transition in WD matter is only rudimental, the transition to detonation in rapidly rotating WDs is beyond the scope of this work but may be investigated in the future.

12.7 Interpretation with respect to spectral features

An inspection of the composition and the kinematics of the ejecta in the homologous expansion phase allows a prediction of spectral features even without employing a detailed postprocessing study. Regarding rotation, the most serious discrepancy between the simulation results and observations is the prediction of C and O at low radial expansion velocities, i.e., close to the centre. This result, already a problem for the non-rotating deflagration model, grows more acute for rapid rotation.

Fig. 12.14 shows the total and fractional mass densities after $t = 5$ s for the “norot

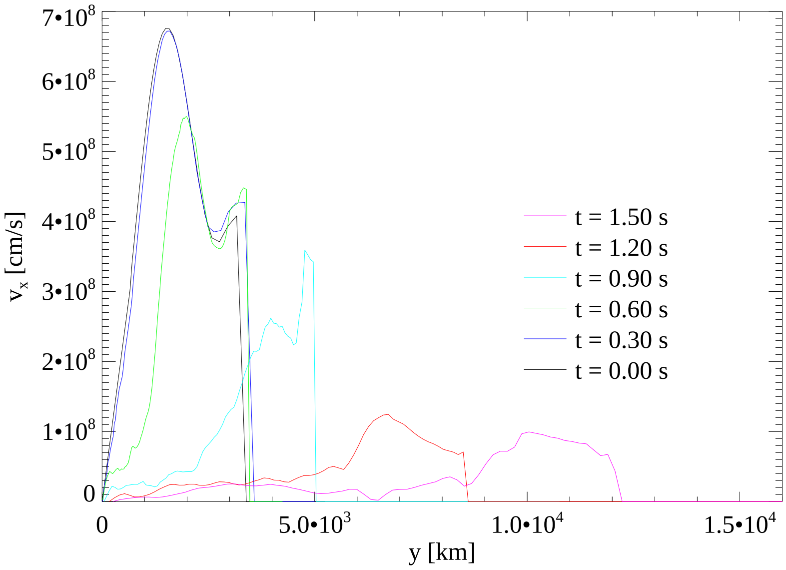

Figure 12.13: Mean velocities in x-direction (in the yz-plane) as function of the distance to the rotation axis y at different times

$c3$" and "20AWD3 $c3$" explosion models (for the sake of demonstration, only the $c3$ ignition — the results are qualitatively in accordance with those of the stochastic ignition — is presented here). It is derived from observations (cf. section 2.1.1) that the IMEs should be located in the outer regions and enclose the IGEs for normal SNe Ia, whereas C and O shouldn't be present near the centre at all. However, as a result of the turbulent combustion whose driving force is the Rayleigh-Taylor motion, the species are mixed throughout the stellar interior. Furthermore, the existence of a significant amount of fuel in the core is inconsistent with observations.

$c3$ ignition appears to be rather unrealistic because the implied symmetries are still visible after $t = 5$ s in the non-rotating case. A clear trend that becomes stronger for more rapid rotation emerges for all explosions considered in this investigation: the flame, initially almost only burning towards the stellar poles, generates IGEs there. Later when the flame approaches the equatorial plane and the density has already dropped, IMEs are produced between the polar and equatorial directions. Finally, burning ceases even before the central part and the equatorial plane could be burnt.

A further remarkable trend arises for the species in radial velocity space. As can be seen from Fig. 12.15, broad lines (i.e., lines covering a wide range of radial velocities) are expected for all species from the explosion models both in the non-rotating case and for the 14AWD4 rotator. The distinct peak of C and O at low radial velocities for the rapid rotator, indicating a considerable amount of unburnt material close to

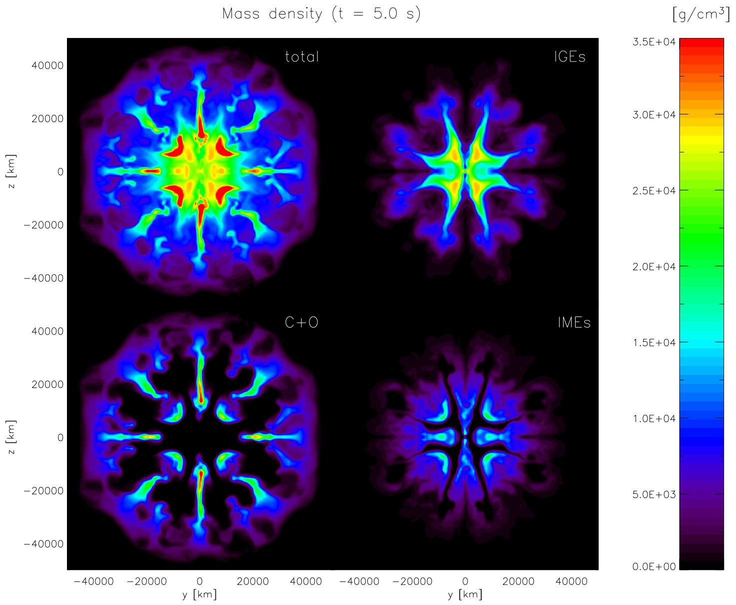

(a) “norot $c3$” explosion model

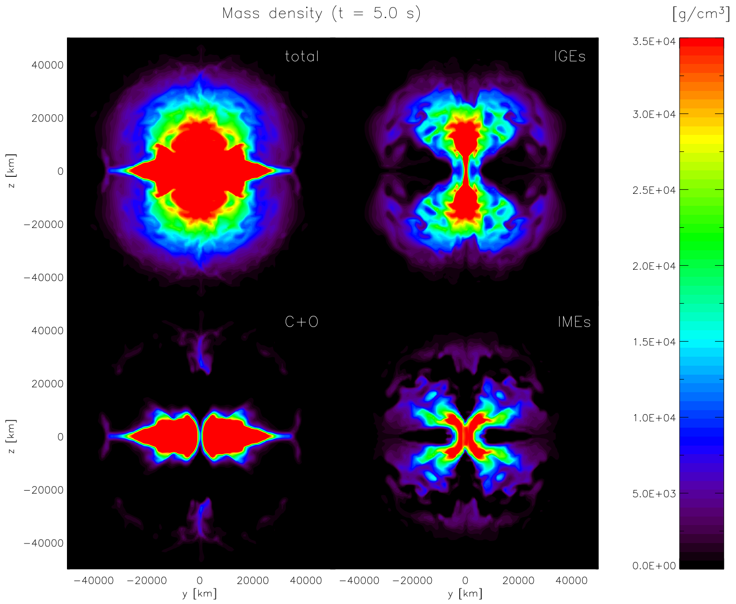

(b) “20AWD3 $c3$” explosion model

Figure 12.14: Total and fractional mass densities after $t = 5$ s for the “norot $c3$” (12.14(a)) and “20AWD3 $c3$” (12.14(b)) explosion models. A mixing of the species throughout the star emerges in both scenarios, particularly the rapid rotator leaves fuel in the stellar core. Cross sections along the rotation axis of simulations exhibiting equatorial symmetry are shown.

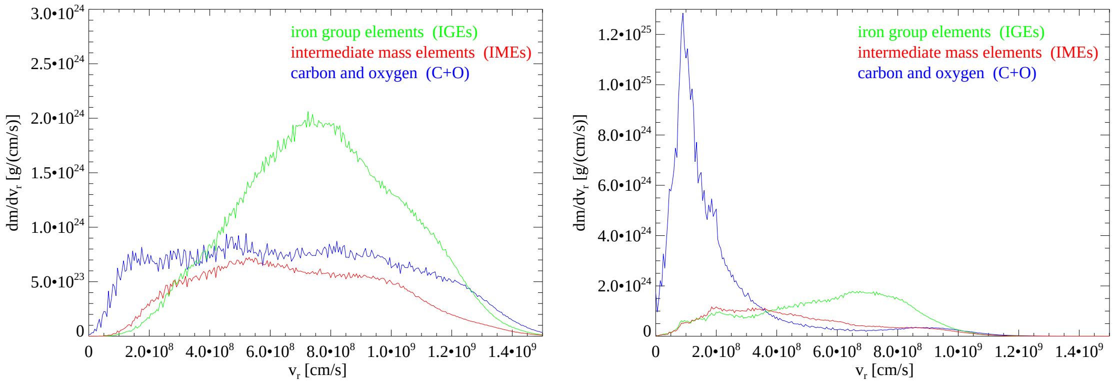

(a) "norot $C_e = 5 \times 10^4$"

(b) "14AWD4 $C_e = 5 \times 10^4$"

Figure 12.15: Probability density functions in radial velocity space for the "norot $C_e = 5 \times 10^4$" (Fig. 12.15(a)) and "14AWD4 $C_e = 5 \times 10^4$" (Fig. 12.15(b)) explosion models

the centre, severely contradicts the bulk of observations.

The highest radial velocities in the non-rotating case are $\lesssim 15 \times 10^8$ g/cm^3. Consequently, high velocity features (cf. section 2.2) cannot be explained by the deflagration model in its current implementation. In the rotating case, the radial velocities are even smaller ($\lesssim 10 \times 10^8$ g/cm^3), although the rotating progenitors include a noticeable amount of rotational kinetic energy. This is basically due to the fact that the gravitational attraction of the rotators is greater (cf. Table 12.1) and in addition the released energy is comparatively small because of incomplete burning.

Fig. 12.16 compares the initially available rotational energy (bottom of the bars) and the kinetic energies of the ejecta after $t = 5$ s (top of the bars) for different WD models. Except for the 10AWD1 rotator without convective core, the disposable kinetic energies become successively smaller for increasing strength of rotation. Note that for the "20AWD3 $C_e = 5 \times 10^3$" explosion model, the kinetic energy after $t = 5$ s is even less than the kinetic energy initially present in the rotation motion.

Faced with this unambiguous result in opposition to observations for deflagrated rapid rotators, the question of compatibility of rotation and deflagration arises. If rotation of the progenitor star was proven beyond doubt, to what extent is rotation allowed to be developed and the pure deflagration model not ruled out at the same time? The answer is as follows: rotation that is so rapid that the stellar mass is significantly enhanced (say by more than $\gtrsim 0.2\ M_\odot$), is incompatible with the pure deflagration scenario in its present realisation. Of course, this statement is imprecise since different rotation laws may lead to identical stellar masses. But more precisely, if the stellar interior of a heavy WD rotates rigidly as demanded by the accepted pre-SN Ia scenario (unlike the 10AWD1 rotator), no SN Ia will be the outcome if the pure deflagration scenario is valid.

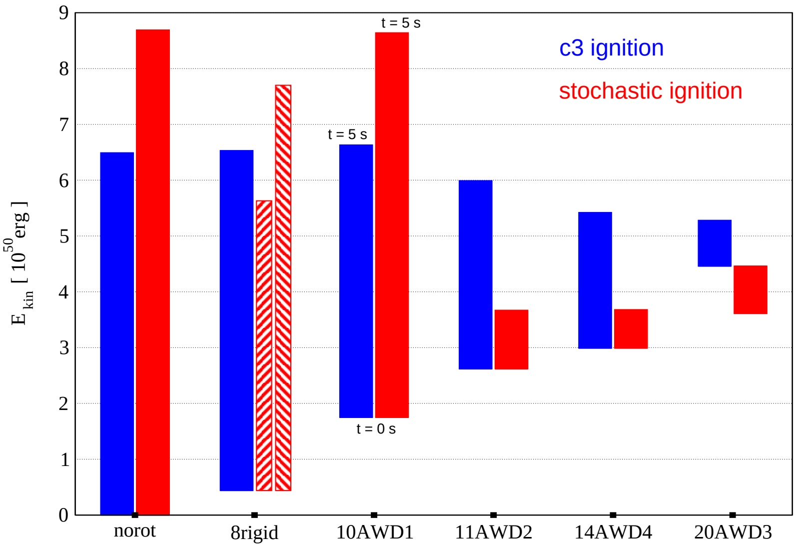

Figure 12.16: Initially available rotational energy (bottom of the bars) and kinetic energy of the ejecta after $t = 5$ s (top of the bars) for successively heavier WD models

Of outstanding interest is the critically rotating rigid rotator, whose mass is increased only slightly by 0.07 $M_\odot$ (the 8rigid rotator, see Fig. B.1) as the possible outcome of a evolutionary scenario that is dominated by braking magnetic torques or efficient viscous angular momentum transport. Comparing Figs. 12.17(a) and 12.17(b) with 12.14(a) and 12.15(a) respectively, it can be stated that although rotation does not improve the shortcomings of the implemented deflagration model, a deflagration of the critical rigid rotator yields approximately the same results as the deflagration of the non-rotating star. Hence, as soon as the present limitations of the non-rotating deflagration model are corrected, a critically and rigidly rotating WD is conceivable as a SN Ia progenitor in the pure deflagration model.

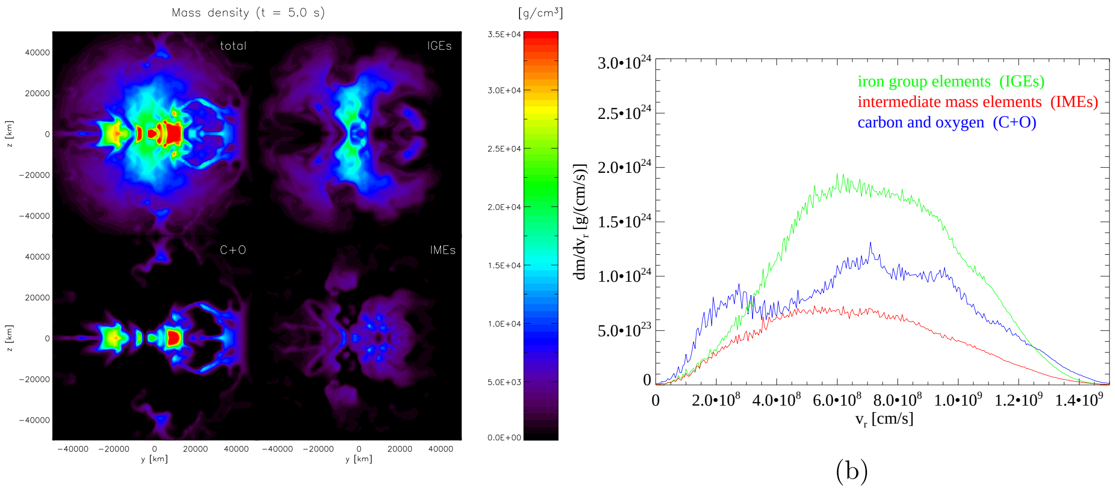

(b)

(a)

Figure 12.17: Total and fractional mass densities after $t = 5$ s for the “8rigid $C_e = 5 \times 10^4$” explosion model (Fig. 12.17(a); cross sections along the rotation axis of simulations exhibiting equatorial symmetry are shown) and the probability density function in radial velocity space for the same scenario (Fig. 12.17(b))

13 Prompt detonation studies

As shown in sections 11.5 and 12.4, a major obstacle for the pure deflagration scenario is the fact that additional stellar material due to rapid rotation exists mainly at lower densities (cf. Figs. 11.3 and 12.10(a)). As soon as the deflagration is initiated, the stellar material becomes less dense. A considerable amount of fuel is left unburnt because its density is too low for nuclear reactions.

However, if the WD is burnt in such a rapid manner before it expands — this is achieved by a sonically propagating reaction, i.e., a detonation — the situation is different.

13.1 Prompt detonation of rotators in the past

The reason why the deflagration scenario arose in the early 1980ies is the fact that the prompt detonation of a non-rotating Chandrasekhar mass WD was found to result in an excess of iron group elements (IGEs) ($\gtrsim 1.25\ M_\odot$) and a lack of intermediate mass elements (IMEs; $\lesssim 0.15\ M_\odot$). The possibility of stellar rotation to escape this problem by lifting the dense material was realised in Ref. [SMH92]. However, the authors concluded that the bulk of WD matter was nevertheless burnt to IGEs and, accordingly, even rapid rotation did not change the situation. Whenever a significant amount of IMEs was obtained by rotation in their study, the amount of IGEs was simultaneously too high, namely super-Chandrasekhar.

From a contemporary point of view, the cited work has to be considered in a different way for two reasons. On the one hand, today's observations agree that there exist at least some very luminous SNe Ia as SN 1991T with more than one solar mass of ^{56}Ni which need an explanation. Whereas the frequently occurring subluminous SNe Ia could be explained by the deflagration scenario (cf. chapter 12), the involvement of an detonation process seems unavoidable for very overluminous SNe Ia: the high amount of ^{56}Ni, together with a considerable amount of IMEs that is necessary for the SN Ia classification imply a super-Chandrasekhar-mass progenitor star that is not in tune with the pure deflagration model (cf. chapter 12). On the other hand, the j_{const} rotation law was employed in Ref. [SMH92]. However, recent studies justify the assumption that there is no reason why an accreting WD should rotate more rapidly in the interior than at the surface layers [YL04]. As presented in the following, the prompt detonation of accreting WDs, i.e., those stars whose rotation laws obey the characteristics presented in section 3.4.2, offers possibilities in terms of strong SNe Ia events that cannot be explained by the pure deflagration scenario exclusively.

A considerable amount of ^{56}Ni is obtained if the flame crosses dense material in the pure deflagration scenario (however, note that for densities $\rho \gtrsim 3 \times 10^9$ g/cm^3 adverse electron capturing becomes important). However, a sufficient amount of IMEs can only be achieved for a noticeable amount of less dense material within the progenitor in the prompt detonation scenario. An estimate for the burning products of detonating WDs can be obtained by looking at the material densities present in the hydrostatic case, because the detonation front incinerates the star before changes in the stellar structure can occur. From Fig. 11.3 it is clear that for the AWD3 series, less IGEs and, at the same time, more IMEs are generated. The 22AWD3 model ($r_{equator}/r_{pol} = 2.4$) contains 1.41 $M_\odot$ of IGEs and 0.45 $M_\odot$ of IMEs. In contrast, the j_{const} sequence used in Ref. [SMH92] always produces more IGEs and less IMEs. It is assumed that for densities of $\rho > 5.25 \times 10^7$ g/cm^3, IGEs are generated. At lower densities down to $\rho > 1.05 \times 10^7$ g/cm^3, the detonation results in IMEs. Below this density threshold, no burning takes place.

Caution is advised with this estimate since, as described in section 7.2, these density threshold values are obtained from a *deflagration* run. However, nuclear burning is not merely a function of density, and therefore the threshold values could be different for detonations. As written in section 5.4, the NSE also depends on the temperature which is usually higher for detonations compared to deflagrations, which brings an indirect dependence of NSE adjustment on the burning mode. However, the aim of the work presented in this chapter is to display the possibilities that prompt detonations of accreting WD rotators yield and not a quantitative analysis of detonating WDs.

13.2 Following a prompt detonation

Because of the lack of highly structured turbulent flow that forms in the context of turbulent combustion, the resolution of the computational grid was chosen to be much coarser (initially, $\Delta x = 1.2 \times 10^7$ cm) for prompt detonations, so that even a full star simulation could be realised on a personal computer. Fig. 13.1(a) shows the density contours of the “22AWD3 detonation” explosion model which is centrally ignited. Even though the outcome concerning the composition is clear — the density dependent burning implemented in the hydrodynamics code should end with exactly the same amount of species that has been previously estimated by means of the hydrostatic model — the explosion gives insight into the spectral features that are anticipated by the simulation. The burning front (white thick line) moves outwards with the density dependent velocity as described in section 7.1.2 (it does not stop when burning ceases but propagates steadily outside once burning

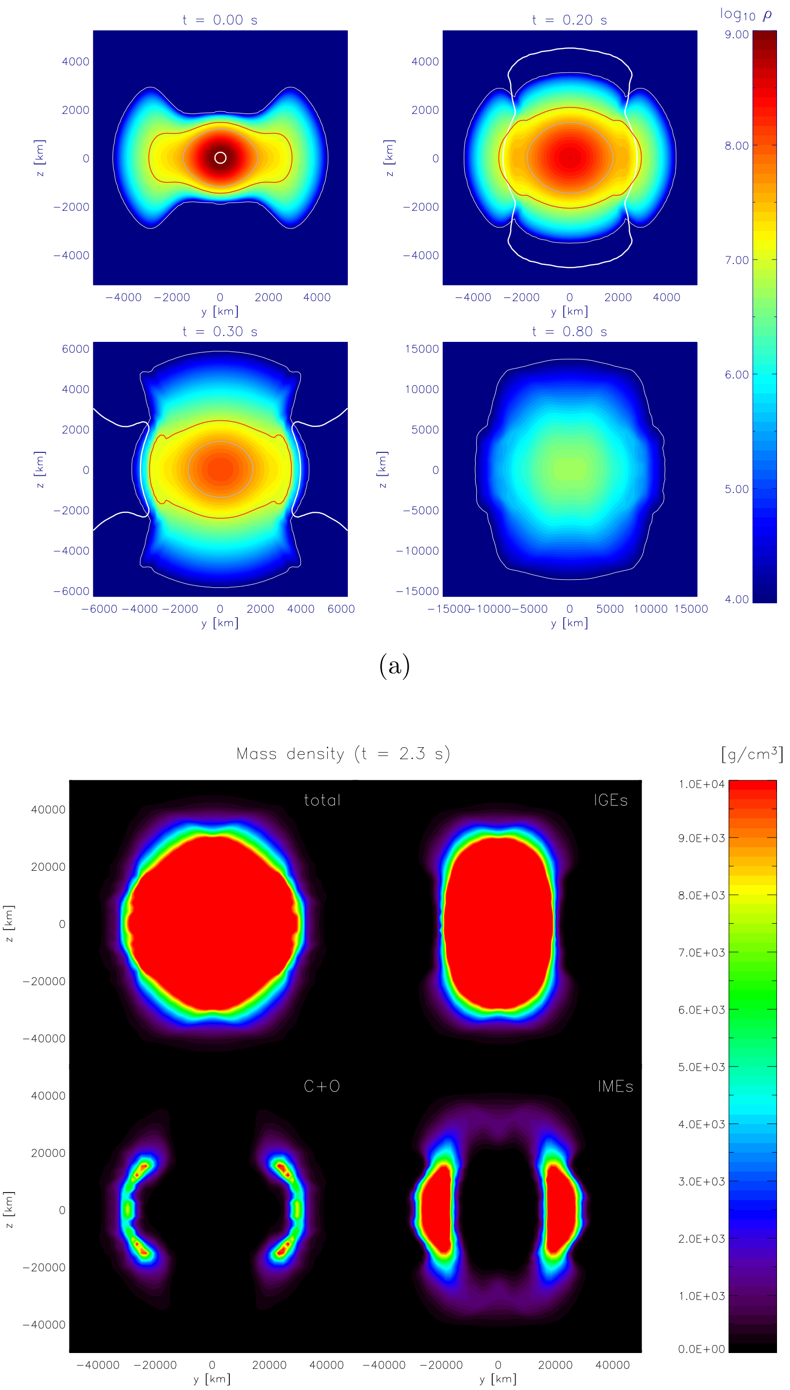

(a)

(b)

Figure 13.1: Density contour lines for the prompt detonation of the 22AWD3 rotator at different instants (upper panels, the white thick line represents the detonation front) and the total as well as fractional mass densities after $t = 2.3$ s for the same explosion model. Cross sections along the rotation axis of a full star simulation are shown.

	density	hydro	postproc
M_{tot} [$M_{\odot}$]	2.07	2.07 / 2.12 *	2.12
t = 0 s			
E_{grav} [10^{51} erg]	-4.500	-4.497	
E_{rot} [10^{50} erg]	4.55	4.55	
β [%]	10.11	10.12	
t = 10 s			
E_{kin} [10^{50} erg]	15.88		
E_{tot} [10^{50} erg]	15.30		
E_{nuc} [10^{51} erg]	2.650		
IGEs [$M_{\odot}$]	1.41	1.47	1.75
[% M_{tot}]	68	71	83
IMEs [$M_{\odot}$]	0.45	0.42	0.29
[% M_{tot}]	22	20	14
C+O [$M_{\odot}$]	0.21	0.18	0.08
[% M_{tot}]	10	9	3

Table 13.1: Quantities for the "22AWD3 detonation" explosion model from the initial model ("density" column), the hydrodynamics code ("hydro" column), and the postprocessing ("postproc" column) (* total mass of tracer particles)

has terminated for numerical reasons).

The high amount of IMEs for the 22AWD3 rotator, predicted between the grey and the red contour line, is caused by the peak in angular velocity that leads to an equatorial bulge of low dense material that is typical for accreting WD rotation. The density stratification along the equatorial plane is enlarged (cf. Fig. B.5).

Table 13.1 summarises the values that are derived directly from the rotating initial model ("density" column) and those obtained by the hydrodynamics code. Deviations in the composition and, above all, the total stellar mass are clearly visible. The difference in composition after t = 10 s can be explained by errors occurring due to the transformation of the initial model to a coarse grid and hydrodynamical instabilities of the star (burning ceases after $t \lesssim 0.3$ s, any pulsating motions before that time affect the composition) and further due to the discretisation of burning by the level set method. The mass of the tracer particles adds up to 2.12 $M_{\odot}$, which exceeds the stellar mass of the 22AWD3 rotator by more than 2 %. This is caused by the fact that only a small number of tracer particles, namely 15^3, are employed (cf. section 7.4).

Compared to the subsonic deflagrations, the entire explosion proceeds faster for detonations. Fig. 13.2 visually describes the evolution of the energy contributions of the turbulent deflagration of a similar rotator and of the "22AWD3 detonation"

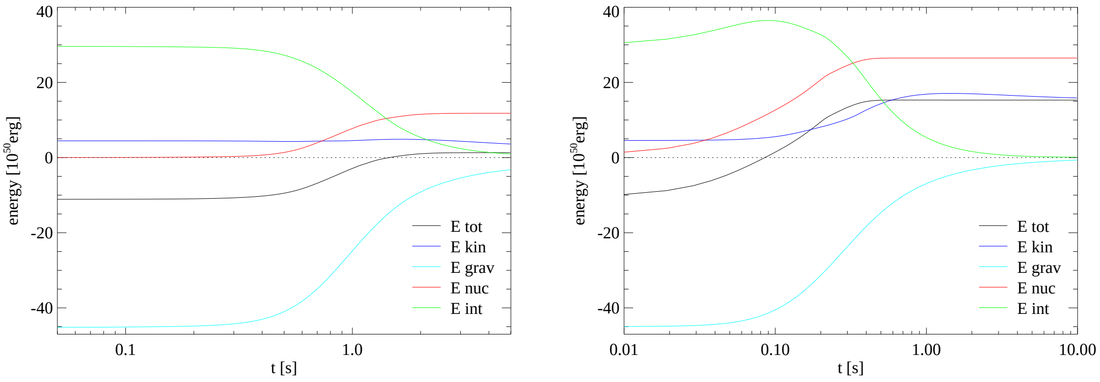

(a) “20AWD3 deflagration $C_e = 5 \times 10^3$”

(b) “22AWD3 detonation”

Figure 13.2: Evolution of the energy fractions for a deflagration scenario (Fig. 13.2(a)) and the prompt detonation (Fig. 13.2(b))

explosion model. The high temperatures caused by the detonation lead to a noticeable peak in the internal energy at $t \sim 0.1$ s. The nuclear energy released by the detonation exceeds E_{nuc} for the deflagration scenario by the factor of ~ 2.5. It leads to an early unbinding of the star (which is hardly achieved in the deflagration case for the specific deflagration scenario) and furthermore to ejecta whose overall kinetic energy is increased by the factor of ~ 3. Even though completely different burning modes are adopted, the energetics are not entirely different. Furthermore, E_{nuc} could be decreased by assuming a lower carbon-to-oxygen ratio (cf. section 6.2). It was fixed to $X(^{12}C) = 0.5$ for the detonation study. However, several publications indicate that in the WD's interior it is less than 0.5 [CA75], [UNYW99], [HS02], [LHT+06] which results in a less energetic explosion.

13.3 Expected spectral features

The most striking property with respect to spectral features is the extreme distribution of species even in the homologous expansion phase. Fig. 13.1(b) shows cross sections along the rotation axis for the total and fractional mass densities at $t = 2.3$ s. Note that the extent of the ejecta at that time approximately corresponds to the expansion that is reached for pure deflagration studies after $t = 5$ s. Whereas IMEs are *only* present in a torus in the equatorial plane, IGEs break out at the poles and therefore are already visible at an early period. No fuel is left at the centre. The noticeable adjustment of the species should lead to a strong dependence on the line of sight.

As already stated, the higher amount of released nuclear energy leads to more energetic ejecta. Fig. 13.3(b) shows the resulting radial velocities at $t = 5$ s for

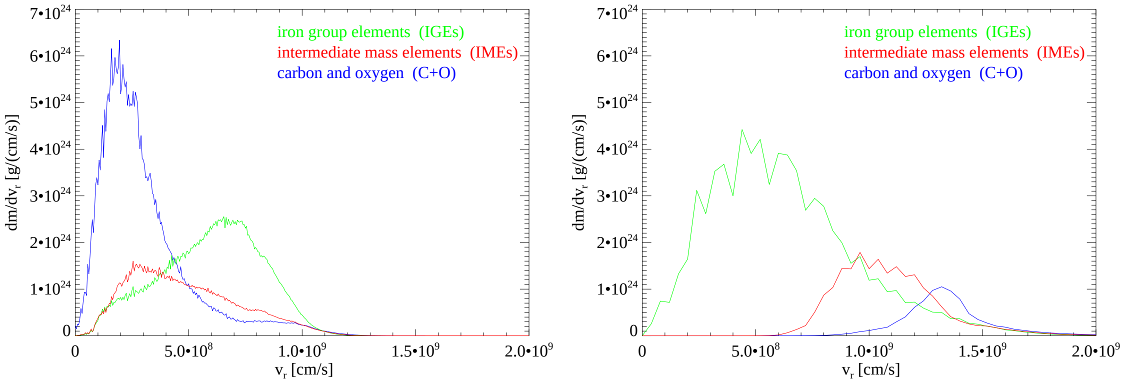

(a) “20AWD3 deflagration $C_e = 5 \times 10^3$”

(b) “22AWD3 detonation”

Figure 13.3: Probability density functions in radial velocity space for the deflagration scenario (Fig. 13.3(a)) and the prompt detonation (Fig. 13.3(b)) at $t = 5$ s. The velocity increments are different for the deflagration and detonation simulation ($dv = 5 \times 10^6$ cm/s and $dv = 4 \times 10^7$ cm/s, respectively) as a result of the different resolution for both hydrodynamics simulations.

the different species. No fuel appears at low velocities, which is promising in the SN Ia context. IGEs are encountered over a broad range of velocities but are most prominent at lower radial velocities ($v_r \sim 5 \times 10^3$ km/s). IMEs are found at some higher velocities, and are most prominent at $v_r \sim 10 \times 10^3$ km/s. In addition, some of the ejecta exhibit velocities up to $v_r \sim 20 \times 10^3$ km/s. Therefore, high velocity features (HVFs) could arise from prompt detonations of rapidly rotating WDs. The composition structure and velocity agree fairly well with restrictions that have been derived for SN 1991T by a synthetic spectrum [FBHB99]. Further benefits of the prompt detonation of the 22AWD3 rotator arise from recent work on three-dimensional spectral synthesis for early spectra [TMMN06]. It was found that a thick torus — similar to the one embodied by the IMEs — can naturally explain the diversity in observed strength of the HVFs by covering parts of the star.

13.4 Postprocessing of the prompt detonation

Thanks to F. Röpke who made postprocessing data of the “22AWD3 detonation” explosion model available, insight into the composition resulting from that scenario is more profound (cf. Ref. [THRT04] for more details on the postprocessing code relating to SNe Ia). For example, the composition emerging from the postprocessing can be compared to the composition of the hydrodynamics code by evaluating the tracer data. Unfortunately, the significance of a direct comparison of the composition can not be considered as an independent test of the accuracy of the nuclear burning

IMEs	$[M_\odot]$	IGEs	$[M_\odot]$
^{28}Si	0.15	^{56}Ni	1.48
^{32}S	0.08	^{58}Ni	0.13
^{36}Ar	0.02	^{57}Ni	0.05
^{40}Ca	0.02	^{54}Fe	0.05
^{24}Mg	0.01	^{60}Zn	0.01
		^{52}Fe	0.01
		^{55}Co	0.01
		^{62}Zn	0.01

Table 13.2: Composition of various species for explosion scenario of “22AWD3 detonation” from the postprocessing calculation. All species exceeding the amount of $5\times10^{-3}\ M_\odot$ are listed.

(cf. section 7.2). Its usefulness is limited since the composition obtained by the postprocessing results from the (potentially incorrect) density thresholds for nuclear energy release. Any difference in composition indicates that the released energy is incorrect to some degree, which might have influenced the process of the entire explosion. Otherwise, even the lack of deviations cannot guarantee the correctness of the composition since the result is biased in either case by the assumptions made for burning. However, as stated above, the aim of this chapter is to display the feasibility of detonations in WD matter to produce IMEs. Since it can be shown that they are not missing at all in spite of high detonation temperatures, further work may be spent on this topic in order to derive quantitative results.

Although the difference is clearly present when looking at the composition assumed for the hydrodynamics and obtained from the postprocessing (see Table 13.1; middle and right column, respectively), *a significant amount of IMEs resulting from the prompt detonation of an accreting WD rotator* is derived by postprocessing: Even though it is not large compared to SNe Ia, 0.29 $M_\odot$ is generated within the 22AWD3 rotator; a number that compares fairly well for SN 1991T-like events which exhibit more than a solar mass of ^{56}Ni and a small amount of 0.2 to 0.3 $M_\odot$ of IMEs (P. Mazzali, private communication). Table 13.2 lists all isotopes of IGEs and IMEs that exceed five-tenth of a percent of a solar mass. The amount of ^{56}Ni, namely 1.48 $M_\odot$, is extraordinarily high and should lead to very bright SNe Ia by serving as the energy source for the light curve (cf. section 5.4). As a result of high temperatures, fewer neutron-rich isotopes among IGEs are produced. Whereas the radioactive decay of ^{56}Ni supplies the energy for the light emitted by the SN Ia ejecta, the presence of other iron group nuclei enhances the opacity of the ejecta and causes a broadening of the light curve [RHN02b]. The ratio of ^{56}Ni / ^{58}Ni = 11 for the “22AWD3 detonation” explosion model.

13.5 Detonating rotators: only an exotic scenario?

As derived in the previous sections, the prompt detonation of a rapidly rotating WD fulfils the criteria of superluminous SNe Ia regarding spectral and bolometric features. Therefore it represents an explanation for the rather small number of SN 1991T-like explosions. The spectral evidence against the prompt detonation scenario has been shown to be not valid for a rapid rotator in this investigation.

Support for the deflagration scenario is also derived by considering the ignition episode (cf. section 4.3.1). But it may still be the case that the initiation of detonations is favoured within rotating stars. This topic may be the subject of future work.

The prompt detonation may be seen as nothing but a deflagration-to-detonation transition (DDT, cf. section 4.3.1) happening at an early period, namely already at the initiation of the explosion. Albeit there is an entirely different distinction to the DDT scenario: the transition itself, whose existence is questionable, is not needed in the context of the prompt detonation.

Assuming that the entire span of SNe Ia observations can be explained by the deflagration scenario for the subluminous and normal SNe Ia and the detonation scenario for the superluminous ones and accepting that two entirely different burning modes exist in parallel, a question arises: what causes the WDs to either not rotate at all (then the deflagration model is most successful) or, in contrast, to rotate very rapidly in order to permit the production of IMEs for the detonation? If it can be shown that rotation has an impact on the selection of the burning mode leading to a detonation, a basic approach for this hypothetical coexistence is found.

It can be summarised that a prompt detonation is able to explain a subgroup of SNe Ia observations, as long as the rotation, above all in the outer layers, is rapid enough.

14 Conclusions

The influence of rotation of the progenitor star on the SN Ia explosion is investigated in this thesis.

It has been shown that the amount of iron group elements is not significantly increased, although the rotating WD models are notably heavier than their non-rotating counterparts. Due to the centrifugal expansion, rotators contain more material at low densities in general, thus the amount of material capable of burning to iron group elements is only weakly increased if the star is burnt by a deflagration. Furthermore, due to rotationally induced non-isotropic buoyancy effects and, at the same time, inhibition of effective mixing parallel to the equatorial plane, the flame develops a clear direction preference towards the stellar poles. This leads to comparably weak and anisotropic explosions that leave behind unburnt material at the centre and in the equatorial plane. However, no significant effects of shear motion acting on the flame are observed. Deflagrations of rapid rotators do not cause high velocity features but result in overall low expansion velocities. Rapid rotation of the progenitor star as proposed in Ref. [YL04] is ruled out in combination with the present realisation of the pure deflagration scenario. The incineration of the critical rigid rotator shows similar features as the non-rotating scenario. Therefore, critical rigid rotation could generally be possible in the deflagration context.

The prompt detonation of rapidly rotating WDs represents a promising model for the explanation of superluminous SNe Ia events with the amount of ^{56}Ni that is derived for SN 1991T. The exclusion of the prompt detonation scenario for SNe Ia is disproved by taking into account the fact that intermediate mass elements can be generated within rapid rotators. The exhibition of high velocity features is predicted for the ejecta. Promptly detonation of rapidly rotating WDs can not account for a large part of SNe Ia events but could be the explosion scenario for the rarely observed and extremely bright SNe Ia events.

Rotation of the progenitor star is unlikely to be the parameter that causes the observed variation in peak luminosities among SNe Ia. Rapid rotation of the progenitor star that is derived by an accretion study can lead to a great variety in explosion strength in the deflagration scenario, but only within a range that is ruled out for observational reasons. Otherwise, even the possible critical rigid rotation can not account for a significant spread in the explosion outcome.

15 Zusammenfassung der Arbeit

Den Supernovae des Typs Ia (SNe Ia) wird seit Ende der 1990er Jahre besondere Bedeutung beigemessen. Denn wenn sie als Standardkerzen eingesetzt werden, legen sie eine momentan beschleunigte Expansion des Universums nahe, was folglich auf einen neuen Beitrag zum Gesamtinhalt des Universums, die Dunkle Energie, schließen lässt. Entfernte SNe Ia erscheinen nämlich weniger hell, als man es in einem Universum ohne eine heutzutage beschleunigte Expansion erwarten würde. Um SNe Ia für die Vermessung des Universums heranziehen zu können, muss man allerdings die Beobachtungsdaten standardisieren, denn immer genauere Beobachtungen bringen eine intrinsische Streuung hinsichtlich ihrer Helligkeit zu Tage, welche in derselben Größenordnung wie dieses kosmologische Phänomen liegt. Die Standardisierung wird bislang vorgenommen, ohne dass die eigentliche Ursache der Verschiedenartigkeit bekannt ist, denn die Übereinstimmung der abgeleiteten kosmologischen Daten mit denjenigen unabhängiger Methoden verleitet dazu, die Standardisierung unverstanden einzusetzen.

So muss ein Explosionsmechanismus gefunden werden, welcher eine Variation der Helligkeit von SNe Ia über eine Größenordnung erklärt, welche auf den Massenbereich von $0,1 - 1,0$ Sonnenmassen der Energiequelle radioaktiven Nickels, ^{56}Ni, schließen lässt. Seit Mitte der 1990er Jahre liefert die turbulenten Deflagration als Explosionsmodell viel versprechende Resultate: Eine Unterschall-Flamme verbrennt einen Weißen Zwergstern aus Kohlenstoff und Sauerstoff, wobei die Flammenoberfläche aufgrund turbulenter Strömungen derart vergrößert wird, dass die Explosion auf eine ausreichende Stärke anwächst, um das im SN Ia - Kontext nötige völlige Zerreißen des Sterns zu bewirken. Die dreidimensionalen Hydrodynamik-Simulationen zeigen zudem, dass mittels der turbulenten Deflagration die für diese Supernovaklasse typischen mittelschweren Elemente erzeugt werden können und auch die typische Menge an ^{56}Ni, um den Großteil der SNe Ia - Beobachtungen zu erklären.

Allerdings weist das reine Deflagrationsszenario in der aktuellen Implementierung noch Unzulänglichkeiten auf: Die leuchtkräftigsten Ereignisse können bislang nicht erklärt werden, denn diese erfordern die Produktion von rund einer Sonnenmasse an ^{56}Ni, deutlich mehr als der Maximalwert im Deflagrationsmodell von ca. 0,6 Sonnenmassen. Auch hinsichtlich spektraler Eigenschaften von SNe Ia lässt das Deflagrationsmodell Schlussfolgerungen zu, die mit Beobachtungen nicht in Einklang zu bringen sind: Kohlenstoff und Sauerstoff bleiben in größeren Mengen in der Sternmitte unverbrannt zurück, zudem sind die Reaktionsprodukte über das ganze Stern-

innere vermischt und nicht, wie die Beobachtungen nahelegen, geschichtet. Auch die mittlerweile häufig nachgewiesenen Spektrallinien besonders schneller mittelschwerer Elemente verlangen nach einer Erklärung.
Bislang wurde schnelle Rotation des Vorläufersterns, wie sie von einer Sternentstehungsstudie vorhergesagt wird — ein Weißer Zwergstern akkretiert Materie und deren Drehimpuls von einem nichtentarteten Begleitstern über eine Keplersche Akkretionsscheibe — , in den Simulationen vernachlässigt. Es ist Ziel dieser Arbeit, den Einfluss der Rotation auf die SN Ia - Explosion zu untersuchen. Es ist zu erwarten, dass die resultierenden Simulationen deutliche Unterschiede zum nichtrotierenden Fall aufweisen, denn rotierende Vorläufersterne können wesentlich schwerer sein: nicht nur ca. 1,4 Sonnenmassen, das ist der Wert, bei welchem im nichtrotierenden Fall die Gravitationskraft stärker wird als der entgegenwirkende Druckgradient, sondern bis zu ca. 2,1 Sonnenmassen. Neben diesem größeren Materiereservoir, welches für die Erklärung großer Mengen an ^{56}Ni in Frage kommt, könnte außerdem die nach außen brennende Flamme von der Rotation beeinflusst werden. Zusätzliche Scherung könnte die Explosion verstärken.

Für die Untersuchung des Einflusses von Rotation auf die Sternexplosion mussten zunächst sich im hydrostatischen Gleichgewicht befindliche rotierende Anfangsmodelle erzeugt werden, welche ein Rotationsprofil aufweisen, das dem akkretierender Weißer Zwergsterne entspricht. Bevor diese gezündet werden konnten, war weiterhin der Hydrodynamik-Code zu modifizieren. Es wurde durch die Implementierung eines Multipol-Poissonsolvers sichergestellt, dass das Gravitationspotential auch für Sterne, welche aufgrund ihrer Rotation deutlich von der spährischen Gestalt abweichen, akkurat berechnet werden kann. Zudem wurden die Algorithmen des expandierenden Rechengitters und der Zündroutine hinsichtlich der Rotation erweitert.

Die Berücksichtigung schneller Rotation des Vorläufersterns kann die Beschränkungen des reinen Deflagrationsszenarios nicht beseitigen. Im Gegenteil, die Unzulänglichkeiten werden noch verschärft. Aufgrund der Tatsache, dass rotierende Weiße Zwergsterne zwar schwerer sind, die zusätzliche Masse aber größtenteils niedrige Dichten aufweist, steht nicht viel mehr Materie zur Verfügung, welche potentiell zu ^{56}Ni verbrannt werden könnte. Zudem entwickelt die Flamme, welche Auftriebskräften unterliegt, in schnellen Rotatoren eine klare Vorzugsrichtung zu den Sternpolen. Weil auch noch der für die turbulente Verbrennung notwendige Materieaustausch senkrecht zur Rotationsachse gehemmt ist aufgrund des auszutauschenden Drehimpulses, ergibt sich folgendes Bild für die Deflagration schneller Rotatoren: Zu viel unverbranntes Material bleibt in klarem Widerspruch zu Beobachtungen im Sternzentrum und nahe der Äquatorialebene zurück. Die Explosionen fallen deshalb im Vergleich zum nichtrotierenden Szenario schwach aus. Dieser Trend ist auch auf die Tatsache zurückzuführen, dass die betrachteten Vorläufersterne zwar sehr schnell rotieren, jedoch zu langsam sind, um die Flammenausbreitung direkt durch

Scherbewegungen zu beeinflussen. Explosionsprodukte mit sehr schnellen Ausbreitungsgeschwindigkeiten, wie in frühen Spektren beobachtet, können nicht erklärt werden.
Folglich ist die schnelle Rotation des Vorläufersterns mit dem Deflagrationsszenario nicht vereinbar und somit unwahrscheinlich. Sollten allerdings solch schnell rotierende Weiße Zwergsterne als Vorgänger für SNe Ia nachgewiesen werden, ist es das Deflagrationsszenario, das nicht aufrechterhalten werden kann. Von besonderer Bedeutung ist die kritische starre Rotation. Dieser Fall könnte als Evolutionsergebnis akkretierender Weißer Zwergsterne im Einfluss starker Magnetfelder eintreten, die Gesamtmasse des Sterns ist aber kaum erhöht, und auch an der Masse des erzeugten ^{56}Ni ändert sich im Vergleich zum nichtrotierenden Szenario kaum etwas. Allerdings kommen kritisch und starr rotierende Weiße Zwergsterne als Vorläufersterne von SNe Ia im reinen Deflagrationsszenario in Frage, sofern es gelingt, die Unzulänglichkeiten des Deflagrationsmodells im nichtrotierenden Fall zu beseitigen.

Eine grundlegend andere Situation ergibt sich aus der sofortigen Detonation von schnell rotierenden Weißen Zwergsternen. Die im Vergleich zur Deflagration schnellere Detonation verbrennt nichtexpandiertes Sternmaterial und erzeugt einen großen Anteil an ^{56}Ni. Die bislang anerkannte Vorstellung, dass annähernd keine mittelschweren Elemente aus der Detonation von Weißen Zwergsternen resultieren, ist widerlegt, sofern ein Rotationsgesetz zugrunde liegt, das im Einklang mit der Akkretions-Vorgeschichte steht. Sowohl in bolometrischer als auch spektraler Hinsicht ist die sofortige Detonation schnell rotierender Weißer Zwergsterne ein vielversprechendes Explosionsszenario für die leuchtstärksten SNe Ia.
Unter der Annahme, dass tatsächlich zwei unterschiedliche Brennmodi für die Erklärung des ganzen Spektrums der SNe Ia - Ereignisse vonnöten sind, und zwar die turbulente Deflagration für wenig leuchtstarke bis normale SNe Ia und die sofortige Detonation für die sehr leuchtstarken SNe Ia, stellt sich folgende Frage: Was veranlasst die Vorgängersterne, einerseits für eine erfolgreiche Deflagration fast gar nicht, andererseits aber für eine erfolgreiche Detonation äußerst schnell zu rotieren? Dieser Sachverhalt sollte untersucht werden, wenn die sofortige Detonation für die Erklärung leuchtstarker Ereignisse herangezogen wird.

Aus der großen Vielfalt an Rotationsgesetzen, welche sich aus Akkretionsstudien ableiten lässt, resultiert eine ebenso breite Streuung hinsichtlich der Explosionsergebnisse Weißer Zwergsterne. Da allerdings der Großteil der Resultate nicht mit den Beobachtungen von SNe Ia in Einklang zu bringen ist, kann die schnelle Rotation des Vorgängersterns nicht die anfangs erwähnte Klasseninhomogenität erklären. Doch erst wenn die Natur des Explosionsszenarios bzw. der Explosionsszenarien der SNe Ia geklärt ist, kann das Potential dieser herausragenden astronomischen Ereignisse ohne Mutmaßungen voll ausgeschöpft werden.

Lebenslauf

Name		Jan Michael Manfred Pfannes
Geburtsdatum und -ort		8. Feburar 1979 in Dettelbach
Staatsangehörigkeit		deutsch
Schule	1985 - 1989	Volksschule Dettelbach
	1989 - 1998	Armin-Knab-Gymnasium Kitzingen
	1998	*Abitur* am 26. Juni
Zivildienst		Mainfränkische Werkstätten GmbH Kitzingen (1998 - 1999)
Studium	1999 - 2002	Bayerische Julius-Maximilians-Universität Würzburg Fakultät für Physik und Astronomie Hauptfach: Physik Nebenfach: Psychologie
	2001	*Vordiplom Physik* am 23. August
	2002 - 2003	Physics Department State University of New York at Buffalo New York, USA Auslandsstipendium des DAAD
	2003	Abschluss: *Master of Science* am 1. Juni 2003 Masterarbeit: "Energy Propagation in Granular Chains"
Promotion	seit 2003	Bayerische Julius-Maximilians-Universität Würzburg Institut für Theoretische Physik und Astrophysik Lehrstuhl für Astronomie Dissertation: "Rotating White Dwarf Explosions"
	seit 2005	Mitglied des *Graduiertenkollegs "Theoretische Astrophysik und Teilchenphysik"* der DFG

Würzburg, im Juni 2006

A Cycle of the hydrodynamics code

The Newtonian finite-volume hydrodynamics code, PROMETHEUS, employed in this investigation represents a future trend for the original version [FMA89] towards full-blown simulations of SNe Ia. Its handling of the hydrodynamics is based on the Piecewise Parabolic Method [CW84], and is a Godunov type upwind scheme [God59] which preserves third-order accuracy in space. The level set front tracking scheme (cf. section 7.1.1) is a guarantee for a defined model of the reaction zone, which is necessary to model turbulent combustion properly.

The code employed for this thesis works as follows:

- Before the time integration is started, the following steps are carried out:
  - The three-dimensional computational grid (cf. chapter 9) capable of housing the WD is constructed.
  - The density profile, ρ_{ijk}, velocity components, $v(x, y, z)_{ijk}$, temperature profile, T_{ijk}, and composition, X_{ijk} of the rotating WD are set onto the grid. For the (ρ, T, X) distribution, the equation of state (cf. section 7.3) is subsequently called in order to obtain pressure p_{ijk} and energy density e_{ijk}.
  - The tracer particles are assigned in a manner which is consistent with the density profile of the WD (cf. section 7.4).
  - In the case of a static ignition at $t = 0$ s, the level set is arranged according to the flame surface (cf. section 8.1). The burning routine provides the energy release (cf. section 7.2) and flame velocity (cf. section 7.1.2).
- The time integration is started, whereby the following steps are performed within half a cycle, i.e., one time step:
  - The velocities of the grid are determined (cf. section 9.2).
  - The time step size is chosen to satisfy the Courant-Friedrich-Levy (CFL) condition.
  - According to the *operator splitting* method, sequential one-dimensional sweeps, each of them solving Riemann problems, are performed:

    A x-sweep for every y- and z-coordinate is arranged, followed by the calculation of the gravitational acceleration and a call of the equation

  of state in order to obtain the new temperatures for the corresponding values of (ρ, p, e). The following y- and z-sweeps obey the same pattern.
  - The gravitational potential is computed (cf. section 10.2) and averaged with its old values in order to preserve second order accuracy in time according to the Strang-splitting. Then velocity and energy is updated.
  - The level set is propagated according to the advection and the burning speed contribution. In case of deflagrations, the subgrid energy is computed (cf. section 7.1.2). The tracer particles are advected to their new positions.
  - Burning according to the level set is arranged (cf. section 7.2). Since it is not directly coupled to the hydrodynamical advection and the burning time step is usually much shorter compared to the CFL condition, it is treated independently by organising as many burning time steps as necessary to complete the CFL time step.

- Apart from the following changes, the second half of the cycle elapses in the same way as the first half:
  - In order to preserve second order accuracy in time, the sweep direction is reversed to the sequence of z, y, x since the operator splitting method violates time symmetry.
  - The grid is not moved.
  - In case of the stochastic ignition, ignition is carried out before burning takes place (cf. section 8.2).

B Constructed initial models

In the following, the rotating initial models created with the method introduced in chapter 11 are summarised. The central density ρ_c of all models is 2.0×10^9 g/cm^3 and coincides with the maximum density inside the star. The thick grey contour line encloses densities greater than 5.25×10^7 g/cm^3, and the red line densities greater than 1.05×10^7 g/cm^3. The white contour line marks the density of 10^4 g/cm^3 and serves as an indicator of the stellar surface.

Note that only the cylindrical mass coordinate (solid line in the right panels) describes cylindrical rotation properly.

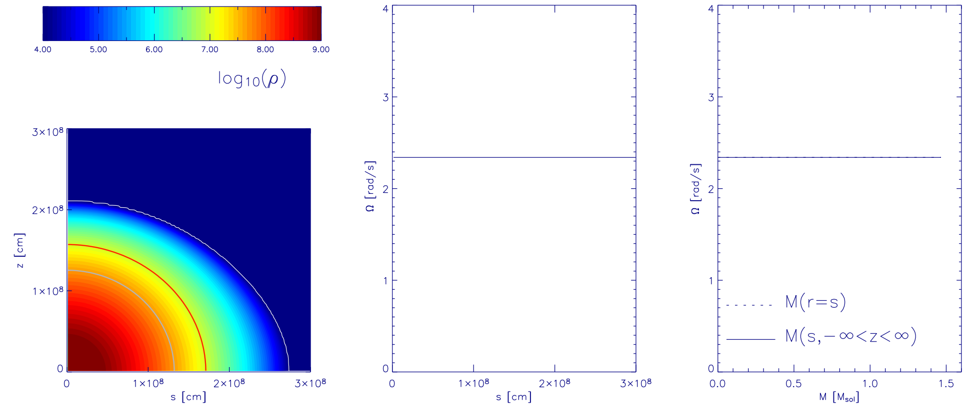

Figure B.1: Density contour lines and the rotation law both in spatial and in mass coordinates for the 8rigid model

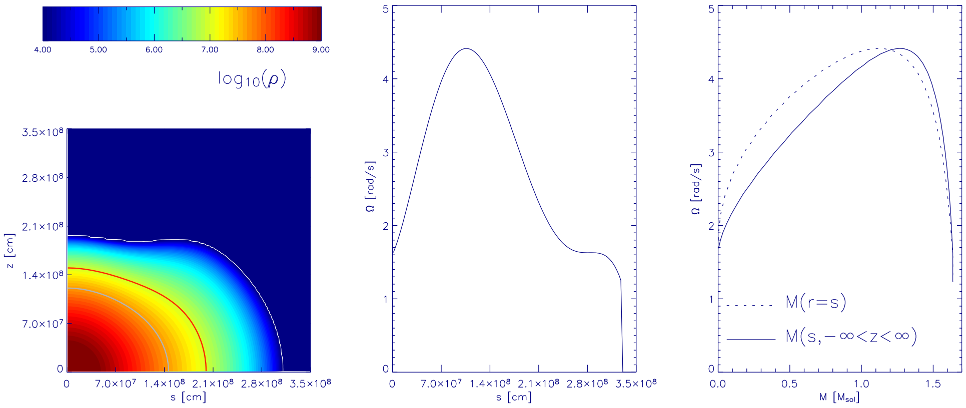

Figure B.2: Density contour lines and the rotation law both in spatial and in mass coordinates for the 10AWD1 model

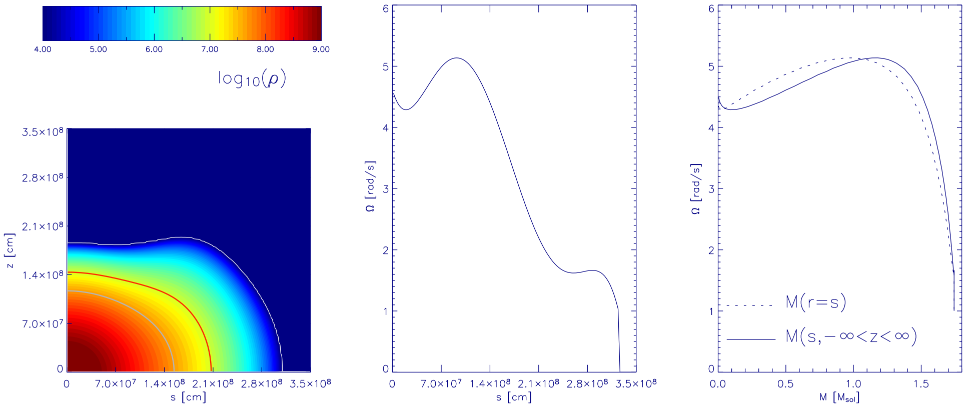

Figure B.3: Density contour lines and the rotation law both in spatial and in mass coordinates for the 11AWD2 model

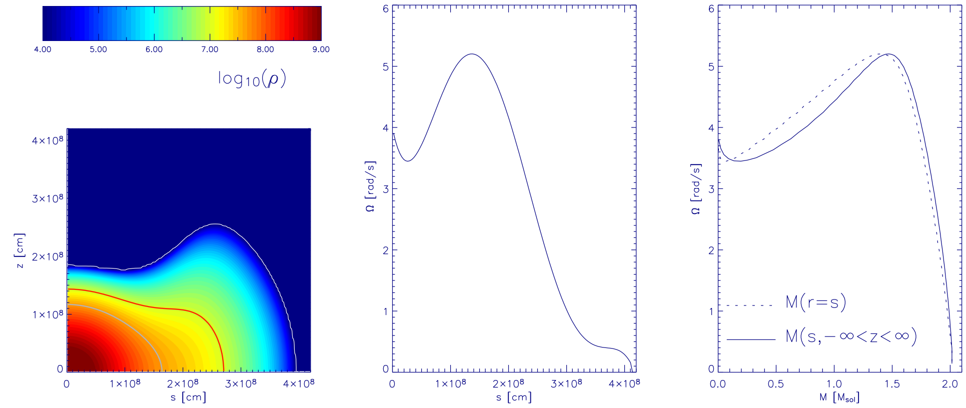

Figure B.4: Density contour lines and the rotation law both in spatial and in mass coordinates for the 20AWD3 model

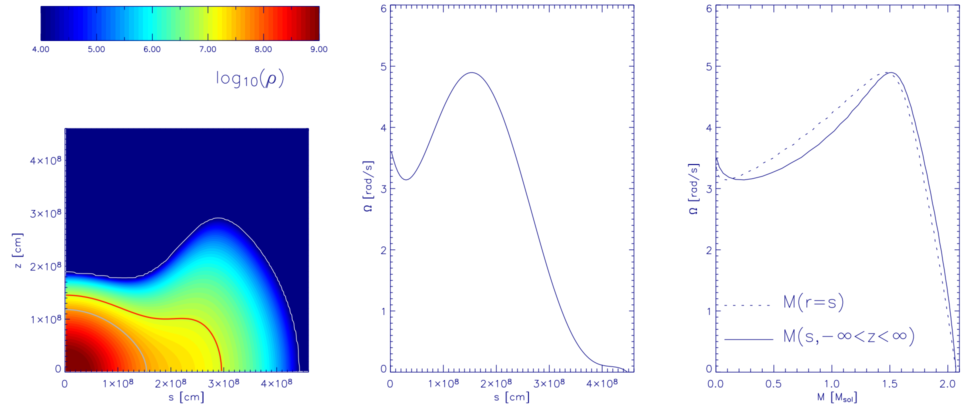

Figure B.5: Density contour lines and the rotation law both in spatial and in mass coordinates for the 22AWD3 model

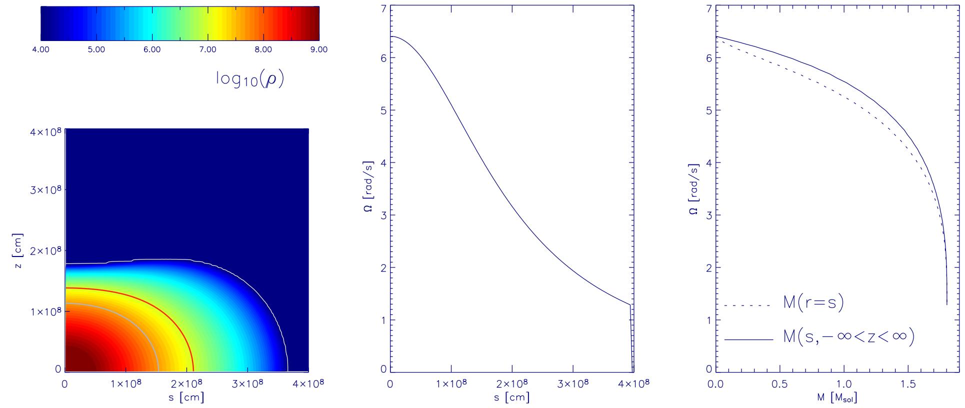

Figure B.6: Density contour lines and the rotation law both in spatial and in mass coordinates for the 16jconstadr05 model

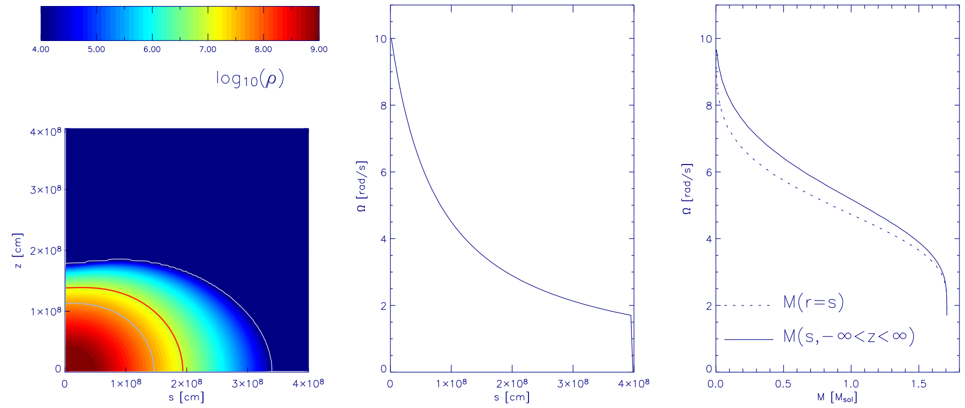

Figure B.7: Density contour lines and the rotation law both in spatial and in mass coordinates for the 16vconstadr02 model

C Test of hydrostatic stability

The test for hydrostatic stability on the grid of the hydrodynamics simulation as presented in chapter 9 for the 20AWD3 rotator is enlarged to the 8rigid and 10AWD1 rotators in the following.

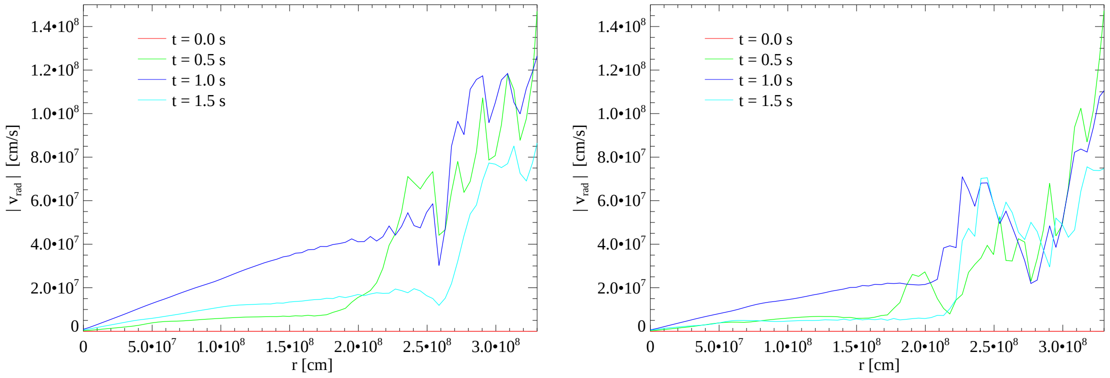

(a) 8rigid

(b) 10AWD1

Figure C.1: Modulus of the radial velocity as a function of the central distance at four different times for the 8rigid rotator (Fig. C.1(a)) and the 10AWD1 rotator (Fig. C.1(b))

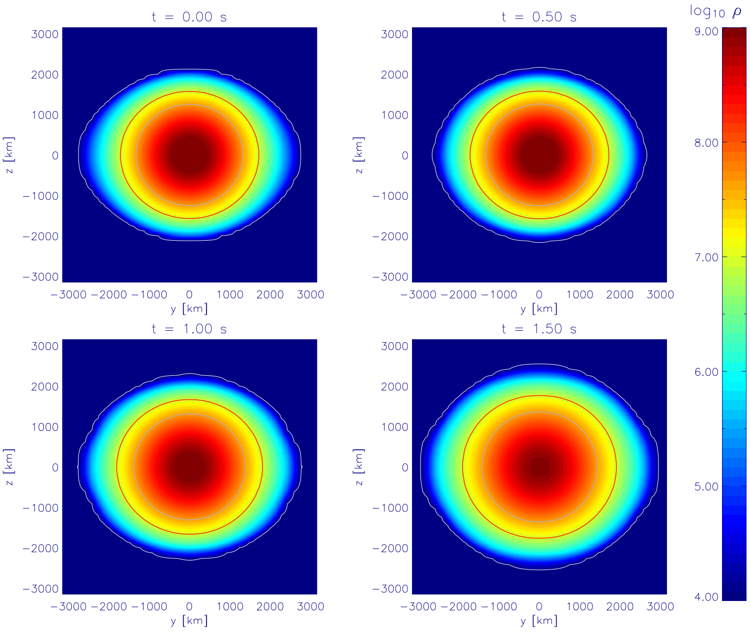

Figure C.2: Density contours for the 8rigid rotator during the test for hydrostatic stability. Equatorial symmetry is assumed.

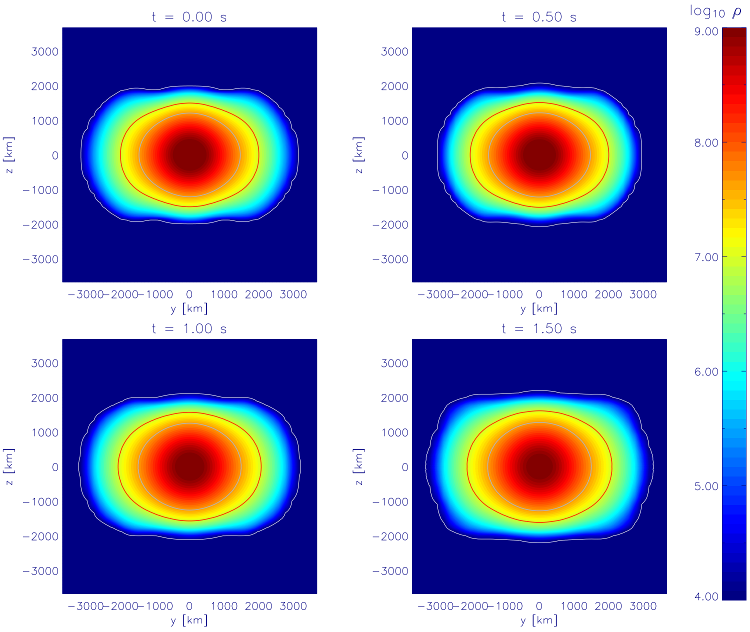

Figure C.3: Density contours for the 10AWD1 rotator during the test for hydrostatic stability. Equatorial symmetry is assumed.

D Impact of buoyancy

The effective gravitational acceleration, i.e., the gravitational acceleration that is corrected for the centrifugal acceleration, is plotted on top of the density contour lines for the $25j_{const}$adr02 rotator in Fig. D.1.

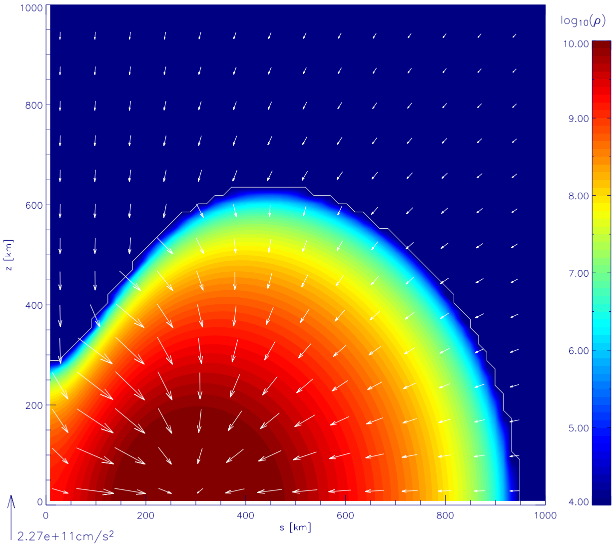

Figure D.1: Density contour lines and the effective gravitational acceleration (indicated by arrows) of the $25j_{const}$adr02 model. Due to the fact that the maximum density is not located at the stellar centre, buoyant motion occurs towards the centre in the torus of dense material.

This model for hydrostatic equilibrium demonstrates the effect of the density stratification on buoyant motion. Central and maximum densities do not coincide for the $25j_{const}$adr02 model. In contrast, a torus of dense material has formed at the equator. Buoyant material "rises" towards the centre of the star if it is located inside the dense torus.

However, by no means can the $25j_{const}$adr02 rotator be considered as a SN Ia progenitor: its mass is too high ($M = 3.09\ M_\odot$), the rotation law unrealistic (cf. chapter 3), the maximum angular velocity too high ($\Omega_c = 164.5$ rad/s), and the maximum density too high ($\rho_{max} = 2.7 \times 10^{10}$ g/cm^3).

The modulus of the gravitational acceleration and the modulus of the effective gravitational acceleration is plotted for the polar direction, diagonal direction, and

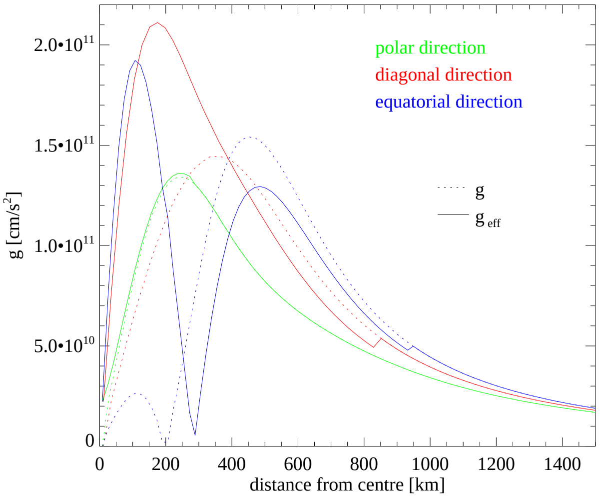

Figure D.2: *Modulus* of the gravitational acceleration (dashed) and the effective gravitational acceleration (solid) along the rotation axis, the stellar diagonal, and the equatorial plane for the $25j_{const}$adr02 rotator

equatorial direction in Fig. D.2. Note the large impact of the centrifugal acceleration, leading to a shift in direction of g_{grav} at $s \sim 200$ km and g_{eff} at $s \sim 300$ km (this is the position of the highest density, see Fig. D.1) in the equatorial plane. At the position of the highest density, the pressure gradient together with the effective gravity vanish. The edges of the red and the blue line (at $\sim$ 830 and $\sim$ 940 km, respectively) appear due to the absence of centrifugal acceleration outside the star.

Bibliography

[ABW85] W. D. Arnett, D. Branch, and J. C. Wheeler. Hubble's constant and exploding carbon-oxygen white dwarf models for Type I supernovae. *Nature*, 314:337–+, March 1985.

[AGR$^+$06] P. Astier, J. Guy, N. Regnault, R. Pain, E. Aubourg, D. Balam, S. Basa, R. G. Carlberg, S. Fabbro, D. Fouchez, I. M. Hook, D. A. Howell, H. Lafoux, J. D. Neill, N. Palanque-Delabrouille, K. Perrett, C. J. Pritchet, J. Rich, M. Sullivan, R. Taillet, G. Aldering, P. Antilogus, V. Arsenijevic, C. Balland, S. Baumont, J. Bronder, H. Courtois, R. S. Ellis, M. Filiol, A. C. Gonçalves, A. Goobar, D. Guide, D. Hardin, V. Lusset, C. Lidman, R. McMahon, M. Mouchet, A. Mourao, S. Perlmutter, P. Ripoche, C. Tao, and N. Walton. The Supernova Legacy Survey: measurement of Ω_M, Ω_Λ and w from the first year data set. *A&A*, 447:31–48, February 2006.

[Arn69] D. W. Arnett. A Possible Model of Supernovae: Detonation of ^{12}C. *Ap&SS*, 5:180–+, 1969.

[Arn82] W. D. Arnett. Type I supernovae. I - Analytic solutions for the early part of the light curve. *ApJ*, 253:785–797, February 1982.

[BBB$^+$05] C. Badenes, K. Borkowski, E. Bravo, J. P. Hughes, and U. Hwang. Exploring the Physics of Type Ia Supernovae Through the X-ray Spectra of their Remnants . *Memorie della Societa Astronomica Italiana*, 76:555–+, 2005.

[BBH$^+$05a] C. Badenes, K. J. Borkowski, J. P. Hughes, U. Hwang, and E. Bravo. Constraints on the Physics of Type Ia Supernovae from the X-Ray Spectrum of the Tycho Supernova Remnant. *ArXiv Astrophysics e-prints*, November 2005.

[BBH$^+$05b] D. Branch, E. Baron, N. Hall, M. Melakayil, and J. Parrent. Comparative Direct Analysis of Type Ia Supernova Spectra. I. SN 1994D. *PASP*, 117:545–552, June 2005.

[BBR05] K. Belczynski, T. Bulik, and A. J. Ruiter. New Constraints on Type Ia Supernova Progenitor Models. *ApJ*, 629:915–921, August 2005.

[BCPB90] W. Benz, A. G. W. Cameron, W. H. Press, and R. L. Bowers. Dynamic mass exchange in doubly degenerate binaries. I - 0.9 and 1.2 solar mass stars. *ApJ*, 348:647–667, January 1990.

[BDL$^+$06] S. Blondin, L. Dessart, B. Leibundgut, D. Branch, P. Höflich, J. L. Tonry, T. Matheson, R. J. Foley, R. Chornock, A. V. Filippenko, J. Sollerman, J. Spyromilio, R. P. Kirshner, W. M. Wood-Vasey, A. Clocchiatti, C. Aguilera, B. Barris, A. C. Becker, P. Challis, R. Covarrubias, T. M. Davis, P. Garnavich, M. Hicken, S. Jha, K. Krisciunas, W. Li, A. Miceli, G. Miknaitis, G. Pignata, J. L. Prieto, A. Rest, A. G. Riess, M. E. Salvo, B. P. Schmidt, R. C. Smith, C. W. Stubbs, and N. B. Suntzeff. Using Line Profiles to Test the Fraternity of Type Ia Supernovae at High and Low Redshifts. *AJ*, 131:1648–1666, March 2006.

[BDR$^+$04] J. B. Bell, M. S. Day, C. A. Rendleman, S. E. Woosley, and M. Zingale. Direct Numerical Simulations of Type Ia Supernovae Flames. II. The Rayleigh-Taylor Instability. *ApJ*, 608:883–906, June 2004.

[Bee74] A. Beer. Vistas in astronomy. Volume 16. *Vistas in Astronomy*, 16, 1974.

[BFN93] D. Branch, A. Fisher, and P. Nugent. On the relative frequencies of spectroscopically normal and peculiar type Ia supernovae. *AJ*, 106:2383–2391, dec 1993.

[BK86] S. I. Blinnikov and A. M. Khokhlov. Initiation of detonation in supernovae. *NASA STI/Recon Technical Report N*, 87:27574–+, 1986.

[BKN$^+$05] L. Berger, D. Koester, R. Napiwotzki, I. N. Reid, and B. Zuckerman. Rotation velocities of white dwarfs determined from the Ca II K line. *A&A*, 444:565–571, December 2005.

[BMP$^+$06] C. Balland, M. Mouchet, R. Pain, N. A. Walton, R. Amanullah, P. Astier, R. S. Ellis, S. Fabbro, A. Goobar, D. Hardin, I. M. Hook, M. J. Irwin, R. G. McMahon, J. M. Mendez, P. Ruiz-Lapuente, G. Sainton, K. Schahmaneche, and V. Stanishev. Spectroscopy of twelve type Ia supernovae at intermediate redshift. *A&A*, 445:387–402, January 2006.

[Bra98] D. Branch. Type Ia Supernovae and the Hubble Constant. *ARA&A*, 36:17–56, 1998.

[BRB96] D. Branch, W. Romanishin, and E. Baron. Statistical Connections between the Properties of Type Ia Supernovae and the B-V Colors of Their Parent Galaxies, and the Value of H_0. *ApJ*, 465:73–+, July 1996.

[BSMM99] I. N. Bronstein, K. A. Semendjajew, G. Musiol, and H. Mühlig. *Taschenbuch der Mathematik*. Verlag Harri Deutsch, Frankfurt am Main, Thun, 4th edition, 1999.

[BTF94] O. S. Bartunov, D. Y. Tsvetkov, and I. V. Filimonova. Distribution of supernovae relative to spiral arms and H II regions. *PASP*, 106:1276–1284, December 1994.

[CA75] R. G. Couch and W. D. Arnett. Carbon ignition and burning in degenerate stellar cores. *ApJ*, 196:791–803, March 1975.

[CET99] E. Cappellaro, R. Evans, and M. Turatto. A new determination of supernova rates and a comparison with indicators for galactic star formation. *A&A*, 351:459–466, November 1999.

[Cha61] S. Chandrasekhar. *Hydrodynamic and Hydromagnetic Stability*. Oxford University Press, Ely House, London W. 1, 1st edition, 1961.

[CIT98] S. Cassisi, I. J. Iben, and A. Tornambe. Hydrogen-accreting Carbon-Oxygen White Dwarfs. *ApJ*, 496:376–+, March 1998.

[CLV00] G. Contardo, B. Leibundgut, and W. D. Vacca. Epochs of maximum light and bolometric light curves of type Ia supernovae. *A&A*, 359:876–886, jul 2000.

[CM69] S. A. Colgate and C. McKee. Early Supernova Luminosity. *ApJ*, 157:623–+, August 1969.

[Cox68] J. P. Cox. *Principles of stellar structure - Vol.1: Physical principles; Vol.2: Applications to stars.* New York: Gordon and Breach, 1968, 1968.

[COZK02] G. F. Carnevale, P. Orlandi, Y. Zhou, and R. C. Kloosterziel. Rotational suppression of Rayleigh Taylor instability. *Journal of Fluid Mechanics*, 457:181–190, April 2002.

[CW84] P. Colella and P. R. Woodward. The Piecewise Parabolic Method (PPM) for Gas-Dynamical Simulations. *Journal of Computational Physics*, 54:174–201, September 1984.

[CYL+98] R. G. Carlberg, H. K. C. Yee, H. Lin, M. Swicki, C. W. Shepherd, E. Ellingson, S. L. Morris, D. Schade, J. E. Hesser, J. B. Hutchings, J. B. Oke, D. Patton, G. Wirth, M. Balogh, F. D. A. Hartwick, C. J. Pritchet, R. Abraham, and T. Smecker-Hane. Omega_M and the CNOC Surveys. In V. Mueller, S. Gottloeber, J. P. Muecket, and J. Wambsganss, editors, *Large Scale Structure: Tracks and Traces*, pages 119–126, 1998.

[dAB+00] P. de Bernardis, P. A. R. Ade, J. J. Bock, J. R. Bond, J. Borrill, A. Boscaleri, K. Coble, B. P. Crill, G. De Gasperis, P. C. Farese, P. G. Ferreira, K. Ganga, M. Giacometti, E. Hivon, V. V. Hristov, A. Iacoangeli, A. H. Jaffe, A. E. Lange, L. Martinis, S. Masi, P. V. Mason, P. D. Mauskopf, A. Melchiorri, L. Miglio, T. Montroy, C. B. Netterfield, E. Pascale, F. Piacentini, D. Pogosyan, S. Prunet, S. Rao, G. Romeo, J. E. Ruhl, F. Scaramuzzi, D. Sforna, and N. Vittorio. A flat Universe from high-resolution maps of the cosmic microwave background radiation. *Nature*, 404:955–959, April 2000.

[Dam39] G. Damköhler. In "Jahrbuch der deutschen Luftfahrtforschung", 1939.

[Dem98] W. Demtröder. *Experimentalphysik 4: Kern-, Teilchen- und Astrophysik*. Springer Verlag, Berlin Heidelberg New York, 1st edition, 1998.

[DI81] R. H. Durisen and J. N. Imamura. Improved secular stability limits for differentially rotating polytropes and degenerate dwarfs. *ApJ*, 243:612–616, January 1981.

[DT50] R. M. Davies and G. Taylor. The Mechanics of Large Bubbles Rising through Extended Liquids and through Liquids in Tubes. *Royal Society of London Proceedings Series A*, 200:375–390, February 1950.

[Dur75] R. H. Durisen. Upper mass limits for stable rotating white dwarfs. *ApJ*, 199:179–183, July 1975.

[EM85] Y. Eriguchi and E. Müller. A general computational method for obtaining equilibria of self-gravitating and rotating gases. *A&A*, 146:260–268, May 1985.

[FBHB99] A. Fisher, D. Branch, K. Hatano, and E. Baron. On the spectrum and nature of the peculiar Type Ia supernova 1991T. *MNRAS*, 304:67–74, March 1999.

[FFL+05] R. J. Foley, A. V. Filippenko, D. C. Leonard, A. G. Riess, P. Nugent, and S. Perlmutter. A Definitive Measurement of Time Dilation in the Spectral Evolution of the Moderate-Redshift Type Ia Supernova 1997ex. *ApJ*, 626:L11–L14, June 2005.

[Fil97] A. V. Filippenko. Optical Spectra of Supernovae. *ARA&A*, 35:309–355, 1997.

[Fli93] J. Fliegner. Diplomarbeit, Universität Göttingen, 1993.

[FMA89] B. A. Fryxell, E. Müller, and W. D. Arnett. Hydrodynamics and nuclear burning. *MPA Green Report*, 449, 1989.

[Fri95] U. Frisch. *Turbulence — The Legacy of A. N. Kolmogorov.* Cambridge University Press, Cambridge, 1995.

[FRM+05] M. A. Ferry, J. Rhodes, R. Massey, F. W. High, and SNAP Collaboration. Improving the Image Simulations for SNAP. *American Astronomical Society Meeting Abstracts*, 207:–+, December 2005.

[GAA+05] T. S. C. P. G. Garavini, G. Aldering, A. Amadon, R. Amanullah, P. Astier, C. Balland, G. Blanc, A. Conley, T. Dahlen, S. E. Deustua, R. E. S. Fabbro, V. Fadeyev, X. Fan, G. Folatelli, B. Frye, E. L. Gates, R. Gibbons, G. Goldhaber, B. Goldman, A. Goobar, D. E. Groom, J. Haissinski, D. Hardin, I. Hook, D. A. Howell, S. Kent, A. G. Kim, R. A. Knop, M. Kowalski, N. Kuznetsova, B. C. L. C. Lidman, J. Mendez, G. J. Miller, M. Moniez, M. Mouchet, A. Mourao, H. Newberg, S. Nobili, P. E. Nugent, R. Pain, O. Perdereau, S. Perlmutter, R. Quimby, N. Regnault, J. Rich, G. T. Richards, P. Ruiz-Lapuente, B. E. Schaefer, K. Schahmaneche, E. Smith, A. L. Spadafora, V. Stanishev, R. C. Thomas, N. A. Walton, L. Wang, and W. M. Wood-Vasey. Spectroscopic Observations and Analysis of the Unusual Type Ia SN 1999ac. *ArXiv Astrophysics e-prints*, July 2005.

[GAN+05] J. Guy, P. Astier, S. Nobili, N. Regnault, and R. Pain. SALT: a spectral adaptive light curve template for type Ia supernovae. *A&A*, 443:781–791, December 2005.

[GGI+96] J. Gutierrez, E. Garcia-Berro, I. J. Iben, J. Isern, J. Labay, and R. Canal. The Final Evolution of ONeMg Electron-Degenerate Cores. *ApJ*, 459:701–+, March 1996.

[GHF+04] C. L. Gerardy, P. Höflich, R. A. Fesen, G. H. Marion, K. Nomoto, R. Quimby, B. E. Schaefer, L. Wang, and J. C. Wheeler. SN 2003du: Signatures of the Circumstellar Environment in a Normal Type Ia Supernova? *ApJ*, 607:391–405, May 2004.

[GJC+98] P. M. Garnavich, S. Jha, P. Challis, A. Clocchiatti, A. Diercks, A. V. Filippenko, R. L. Gilliland, C. J. Hogan, R. P. Kirshner, B. Leibundgut, M. M. Phillips, D. Reiss, A. G. Riess, B. P. Schmidt, R. A. Schommer, R. C. Smith, J. Spyromilio, C. Stubbs, N. B. Suntzeff, J. Tonry, and S. M. Carroll. Supernova Limits on the Cosmic Equation of State. *ApJ*, 509:74–79, December 1998.

[GL88] J. Glimm and X. L. Li. Validation of the Sharp Wheeler bubble merger model from experimental and computational data. *Physics of Fluids*, 31:2077–2085, August 1988.

[GN05] I. Golombek and J. C. Niemeyer. A model for multidimensional delayed detonations in SN Ia explosions. *A&A*, 438:611–616, August 2005.

[God59] S. K. Godunov. Finite difference method for numerical computation of discontinous solution of the equations of fluid dynamics. *Matematicheskii Sbornik*, 47:271, 1959.

[Gol04] I. Golombek. Zweidimensionale Simulationen verzögerter Detonationen in weißen Zwergen. Diplomarbeit, Julius-Maximilians-Universität Würzburg, May 2004.

[GTW93] R. D. Gehrz, J. W. Truran, and R. E. Williams. Classical novae - Contributions to the interstellar medium. In E. H. Levy and J. I. Lunine, editors, *Protostars and Planets III*, pages 75–95, 1993.

[Hac86] I. Hachisu. A versatile method for obtaining structures of rapidly rotating stars. *ApJS*, 61:479–507, July 1986.

[HBF+99] K. Hatano, D. Branch, A. Fisher, E. Baron, and A. V. Filippenko. On the High-Velocity Ejecta of the Type Ia Supernova SN 1994D. *ApJ*, 525:881–885, November 1999.

[HE82] I. Hachisu and Y. Eriguchi. Bifurcation and Fission of Three Dimensional, Rigidly Rotating and Self-Gravitating Polytropes. *Progress of Theoretical Physics*, 68:206–221, July 1982.

[HF60] F. Hoyle and W. A. Fowler. Nucleosynthesis in Supernovae. *ApJ*, 132:565–+, nov 1960.

[HHA+05] I. M. Hook, D. A. Howell, G. Aldering, R. Amanullah, M. S. Burns, A. Conley, S. E. Deustua, R. Ellis, S. Fabbro, V. Fadeyev, G. Folatelli, G. Garavini, R. Gibbons, G. Goldhaber, A. Goobar, D. E. Groom, A. G. Kim, R. A. Knop, M. Kowalski, C. Lidman, S. Nobili, P. E. Nugent, R. Pain, C. R. Pennypacker, S. Perlmutter, P. Ruiz-Lapuente,

G. Sainton, B. E. Schaefer, E. Smith, A. L. Spadafora, V. Stanishev, R. C. Thomas, N. A. Walton, L. Wang, and W. M. Wood-Vasey. Spectra of High-Redshift Type Ia Supernovae and a Comparison with Their Low-Redshift Counterparts. *AJ*, 130:2788–2803, December 2005.

[HHWW01] D. A. Howell, P. Höflich, L. Wang, and J. C. Wheeler. Evidence for Asphericity in a Subluminous Type Ia Supernova: Spectropolarimetry of SN 1999by. *ApJ*, 556:302–321, July 2001.

[HK03] I. Hachisu and M. Kato. RX J0513.9-6951: The First Example of Accretion Wind Evolution, a Key Evolutionary Process to Type Ia Supernovae. *ApJ*, 590:445–459, June 2003.

[HN00] W. Hillebrandt and J. C. Niemeyer. Type Ia Supernova Explosion Models. *ARA&A*, 38:191–230, 2000.

[How01] D. A. Howell. The Progenitors of Subluminous Type Ia Supernovae. *ApJ*, 554:L193–L196, June 2001.

[HP06] Z. Han and P. Podsiadlowski. A single-degenerate model for the progenitor of the Type Ia supernova 2002ic. *MNRAS*, 368:1095–1100, May 2006.

[HPS$^+$96] M. Hamuy, M. M. Phillips, N. B. Suntzeff, R. A. Schommer, J. Maza, and R. Aviles. The Absolute Luminosities of the Calan/Tololo Type Ia Supernovae. *AJ*, 112:2391–+, December 1996.

[HS02] P. Höflich and J. Stein. On the Thermonuclear Runaway in Type Ia Supernovae: How to Run Away? *ApJ*, 568:779–790, April 2002.

[HT96] W. R. Hix and F.-K. Thielemann. Silicon Burning. I. Neutronization and the Physics of Quasi-Equilibrium. *ApJ*, 460:869–+, April 1996.

[HT99] W. Hix and F. K. Thielemann. Computational methods for nucleosynthesis and nuclear energy generation. *J. Comp. and Appl. Math.*, 109:321–351, 1999.

[IBHN06] L. Iapichino, M. Brüggen, W. Hillebrandt, and J. C. Niemeyer. The ignition of thermonuclear flames in type Ia supernovae. *A&A*, 450:655–666, May 2006.

[IT84] I. Iben and A. V. Tutukov. Supernovae of type I as end products of the evolution of binaries with components of moderate initial mass (M not greater than about 9 solar masses). *ApJS*, 54:335–372, February 1984.

[Jac98] J. D. Jackson. *Classical Electrodynamics.* John Wiley & Sons, Inc., New York, 3rd edition, 1998.

[Jam64] R. A. James. The Structure and Stability of Rotating Gas Masses. *ApJ*, 140:552–+, August 1964.

[JBC⁺06] S. Jha, D. Branch, R. Chornock, R. J. Foley, W. Li, B. J. Swift, D. Casebeer, and A. V. Filippenko. Late-Time Spectroscopy of SN 2002cx: The Prototype of a New Subclass of Type Ia Supernovae. *ArXiv Astrophysics e-prints*, February 2006.

[Kan03] C. Kanzow. *Vorlesungsskript: Nichtlineare Gleichungssysteme.* Julius-Maximilians-Universität Würzburg, Institut für Angewandte Mathematik und Statistik, 2003.

[KEH89] H. Komatsu, Y. Eriguchi, and I. Hachisu. Rapidly rotating general relativistic stars. I - Numerical method and its application to uniformly rotating polytropes. *MNRAS*, 237:355–379, March 1989.

[KGC⁺05] K. Krisciunas, P. M. Garnavich, P. Challis, J. L. Prieto, A. G. Riess, B. Barris, C. Aguilera, A. C. Becker, S. Blondin, R. Chornock, A. Clocchiatti, R. Covarrubias, A. V. Filippenko, R. J. Foley, M. Hicken, S. Jha, R. P. Kirshner, B. Leibundgut, W. Li, T. Matheson, A. Miceli, G. Miknaitis, A. Rest, M. E. Salvo, B. P. Schmidt, R. C. Smith, J. Sollerman, J. Spyromilio, C. W. Stubbs, N. B. Suntzeff, J. L. Tonry, and W. M. Wood-Vasey. Hubble Space Telescope Observations of Nine High-Redshift ESSENCE Supernovae. *AJ*, 130:2453–2472, December 2005.

[Kho89] A. M. Khokhlov. The structure of detonation waves in supernovae. *MNRAS*, 239:785–808, aug 1989.

[Kho91] A. M. Khokhlov. Delayed detonation model for type Ia supernovae. *A&A*, 245:114–128, May 1991.

[Kho93] A. Khokhlov. Flame Modeling in Supernovae. *ApJ*, 419:L77+, dec 1993.

[KMP⁺05] R. Kotak, W. P. S. Meikle, G. Pignata, M. Stehle, S. J. Smartt, S. Benetti, W. Hillebrandt, D. J. Lennon, P. A. Mazzali, F. Patat, and M. Turatto. Spectroscopy of the type Ia supernova SN 2002er: Days -11 to +215. *A&A*, 436:1021–1031, June 2005.

[KNTW04] D. Kasen, P. Nugent, R. C. Thomas, and L. Wang. Could There Be a Hole in Type Ia Supernovae? *ApJ*, 610:876–887, August 2004.

[KNW$^+$03] D. Kasen, P. Nugent, L. Wang, D. A. Howell, J. C. Wheeler, P. Höflich, D. Baade, E. Baron, and P. H. Hauschildt. Analysis of the Flux and Polarization Spectra of the Type Ia Supernova SN 2001el: Exploring the Geometry of the High-Velocity Ejecta. *ApJ*, 593:788–808, August 2003.

[Kol41] A. N. Kolmogorov. The local structure of turbulence in incompressible viscous fluid for very large Reynolds number. *Dokl. Akad. Nauk SSSR*, 30:299–303, 1941.

[KOW98] C. Koen, J. A. Orosz, and R. A. Wade. KPD 0422+5421: a new short-period subdwarf B/white dwarf binary. *MNRAS*, 300:695–704, November 1998.

[KS82] E. Knobloch and H. C. Spruit. Stability of differential rotation in stars. *A&A*, 113:261–268, September 1982.

[Kv97] P. Kahabka and E. P. J. van den Heuvel. Luminous Supersoft X-Ray Sources. *ARA&A*, 35:69–100, 1997.

[KWG06] M. Kuhlen, S. E. Woosley, and G. A. Glatzmaier. Carbon Ignition in Type Ia Supernovae. II. A Three-dimensional Numerical Model. *ApJ*, 640:407–416, March 2006.

[LAH05] E. Livne, S. M. Asida, and P. Höflich. On the Sensitivity of Deflagrations in a Chandrasekhar Mass White Dwarf to Initial Conditions. *ApJ*, 632:443–449, October 2005.

[Lei00] B. Leibundgut. Type Ia Supernovae. *A&A Rev.*, 10:179–209, 2000.

[LFT$^+$01] W. Li, A. V. Filippenko, R. R. Treffers, A. G. Riess, J. Hu, and Y. Qiu. A High Intrinsic Peculiarity Rate among Type Ia Supernovae. *ApJ*, 546:734–743, January 2001.

[LHF$^+$05] C. Lidman, D. A. Howell, G. Folatelli, G. Garavini, S. Nobili, G. Aldering, R. Amanullah, P. Antilogus, P. Astier, G. Blanc, M. S. Burns, A. Conley, S. E. Deustua, M. Doi, R. Ellis, S. Fabbro, V. Fadeyev, R. Gibbons, G. Goldhaber, A. Goobar, D. E. Groom, I. Hook, N. Kashikawa, A. G. Kim, R. A. Knop, B. C. Lee, J. Mendez, T. Morokuma, K. Motohara, P. E. Nugent, R. Pain, S. Perlmutter, V. Prasad, R. Quimby, J. Raux, N. Regnault, P. Ruiz-Lapuente, G. Sainton, B. E. Schaefer, K. Schahmaneche, E. Smith, A. L. Spadafora, V. Stanishev, N. A. Walton, L. Wang, W. M. Wood-Vasey, and N. Yasuda (The

Supernova Cosmology Project). Spectroscopic confirmation of high-redshift supernovae with the ESO VLT. *A&A*, 430:843–851, February 2005.

[LHT$^+$06] P. Lesaffre, Z. Han, C. A. Tout, P. Podsiadlowski, and R. G. Martin. The C flash and the ignition conditions of Type Ia supernovae. *MNRAS*, 368:187–195, May 2006.

[LHW$^+$00] A. M. Lisewski, W. Hillebrandt, S. E. Woosley, J. C. Niemeyer, and A. R. Kerstein. Distributed Burning in Type Ia Supernovae: A Statistical Approach. *ApJ*, 537:405–413, July 2000.

[Liv00] M. Livio. The progenitors of type ia supernovae. In J. C. Niemeyer and J. W. Truran, editors, *Type I Supernovae: Theory and Cosmology*, pages 33–48, 2000.

[LL91] L. D. Landau and E. M. Lifschitz. *Hydrodynamik*, volume 6 of *Lehrbuch der theoretischen Physik*. Akademie Verlag, Berlin, 1991.

[LLF$^+$05] D. C. Leonard, W. Li, A. V. Filippenko, R. J. Foley, and R. Chornock. Evidence for Spectropolarimetric Diversity in Type Ia Supernovae. *ApJ*, 632:450–475, October 2005.

[LO67] D. Lynden-Bell and J. P. Ostriker. On the stability of differentially rotating bodies. *MNRAS*, 136:293–+, 1967.

[Mai05] A. Maier. Detonationsfronten in teilweise verbranntem Sternmaterial. Diplomarbeit, Julius-Maximilians-Universität Würzburg, January 2005.

[MBA$^+$05] P. A. Mazzali, S. Benetti, G. Altavilla, G. Blanc, E. Cappellaro, N. Elias-Rosa, G. Garavini, A. Goobar, A. Harutyunyan, R. Kotak, B. Leibundgut, P. Lundqvist, S. Mattila, J. Mendez, S. Nobili, R. Pain, A. Pastorello, F. Patat, G. Pignata, P. Podsiadlowski, P. Ruiz-Lapuente, M. Salvo, B. P. Schmidt, J. Sollerman, V. Stanishev, M. Stehle, C. Tout, M. Turatto, and W. Hillebrandt. High-Velocity Features: A Ubiquitous Property of Type Ia Supernovae. *ApJ*, 623:L37–L40, April 2005.

[MBF$^+$05] T. Matheson, S. Blondin, R. J. Foley, R. Chornock, A. V. Filippenko, B. Leibundgut, R. C. Smith, J. Sollerman, J. Spyromilio, R. P. Kirshner, A. Clocchiatti, C. Aguilera, B. Barris, A. C. Becker, P. Challis, R. Covarrubias, P. Garnavich, M. Hicken, S. Jha, K. Krisciunas, W. Li, A. Miceli, G. Miknaitis, J. L. Prieto, A. Rest, A. G. Riess, M. E. Salvo, B. P. Schmidt, C. W. Stubbs, N. B. Suntzeff, and J. L.

Tonry. Spectroscopy of High-Redshift Supernovae from the ESSENCE Project: The First 2 Years. *AJ*, 129:2352–2375, May 2005.

[MBS+05] P. A. Mazzali, S. Benetti, M. Stehle, D. Branch, J. Deng, K. Maeda, K. Nomoto, and M. Hamuy. High-velocity features in the spectra of the Type Ia supernova SN 1999ee: a property of the explosion or evidence of circumstellar interaction? *MNRAS*, 357:200–206, February 2005.

[MDP05] F. Mannucci, M. Della Valle, and N. Panagia. Two populations of progenitors for type Ia SNe? *ArXiv Astrophysics e-prints*, October 2005.

[MDT95] P. A. Mazzali, I. J. Danziger, and M. Turatto. A study of the properties of the peculiar SN Ia 1991T through models of its evolving early-time spectrum. *A&A*, 297:509–+, May 1995.

[ME85] E. Müller and Y. Eriguchi. Equilibrium models of differentially rotating, completely catalyzed, zero-temperature configurations with central densities intermediate to white dwarf and neutron star densities. *A&A*, 152:325–335, November 1985.

[MHW+06] G. H. Marion, P. Höflich, J. C. Wheeler, E. L. Robinson, C. L. Gerardy, and W. D. Vacca. Low Carbon Abundance in Type Ia Supernovae. *ArXiv Astrophysics e-prints*, January 2006.

[ML90] R. Mochkovitch and M. Livio. The coalescence of white dwarfs and type I supernovae - The merged configuration. *A&A*, 236:378–384, September 1990.

[MLS+05] S. Mattila, P. Lundqvist, J. Sollerman, C. Kozma, E. Baron, C. Fransson, B. Leibundgut, and K. Nomoto. Early and late time VLT spectroscopy of SN 2001el - progenitor constraints for a type Ia supernova. *A&A*, 443:649–662, November 2005.

[Mü94] E. Müller. Galactic Dynamics and N-Body Simulations. In *Lecture Notes in Physics*, volume 433, pages 313–363. Ed. G. Contopoulos, N. K. Spyrou, & L. Vlahos. Berlin Heidelberg: Springer-Verlag, 1994.

[NH95a] J. C. Niemeyer and W. Hillebrandt. Microscopic Instabilities of Nuclear Flames in Type Ia Supernovae. *ApJ*, 452:779–+, October 1995.

[NH95b] J. C. Niemeyer and W. Hillebrandt. Turbulent Nuclear Flames in Type Ia Supernovae. *ApJ*, 452:769–+, October 1995.

[NHW96] J. C. Niemeyer, W. Hillebrandt, and S. E. Woosley. Off-Center Deflagrations in Chandrasekhar Mass Type Ia Supernova Models. *ApJ*, 471:903–+, November 1996.

[Nie95] J. C. Niemeyer. *On the propagation of thermonuclear flames in type Ia supernovae*. PhD thesis, MPA, Munich, Germany: Technical University, 1995.

[Nie99] J. C. Niemeyer. Can Deflagration-Detonation Transitions Occur in Type Ia Supernovae? *ApJ*, 523:L57–L60, September 1999.

[NK91] K. Nomoto and Y. Kondo. Conditions for accretion-induced collapse of white dwarfs. *ApJ*, 367:L19–L22, January 1991.

[NK97] J. C. Niemeyer and A. R. Kerstein. Burning regimes of nuclear flames in SN Ia explosions. *New Astronomy*, 2:239–244, August 1997.

[NNS79] K. Nomoto, K. Nariai, and D. Sugimoto. Rapid Mass Accretion onto White Dwarfs and Formation of an Extended Envelope. *PASJ*, 31:287–298, 1979.

[Nol99] W. Nolting. *Klassische Mechanik*. Vieweg & Sohn Verlagsgesellschaft mbH, Braunschweig/Wiesbaden, 5th edition, 1999.

[NP84] R. Nandkumar and C. J. Pethick. Transport coefficients of dense matter in the liquid metal regime. *MNRAS*, 209:511–524, August 1984.

[NS77] K. Nomoto and D. Sugimoto. Rejuvenation of Helium White Dwarfs by Mass Accretion. *PASJ*, 29:765–780, 1977.

[NSD$^+$05] K. Nomoto, T. Suzuki, J. Deng, T. Uenishi, and I. Hachisu. Progenitors of Type Ia Supernovae: Circumstellar Interaction, Rotation, and Steady Hydrogen Burning. In M. Turatto, S. Benetti, L. Zampieri, and W. Shea, editors, *ASP Conf. Ser. 342: 1604-2004: Supernovae as Cosmological Lighthouses*, pages 105–+, December 2005.

[NSKH06] K. Nomoto, H. Saio, M. Kato, and I. Hachisu. Thermal Stability of White Dwarfs Accreting Hydrogen-rich Matter and Progenitors of Type Ia Supernovae. *ArXiv Astrophysics e-prints*, March 2006.

[NTY84] K. Nomoto, F.-K. Thielemann, and K. Yokoi. Accreting white dwarf models of Type I supernovae. III - Carbon deflagration supernovae. *ApJ*, 286:644–658, November 1984.

[NUK^{+}00] K. Nomoto, H. Umeda, C. Kobayashi, I. Hachisu, M. Kato, and T. Tsujimoto. Type Ia supernovae: Progenitors and evolution with redshift. In S. S. Holt and W. W. Zhang, editors, *American Institute of Physics Conference Series*, pages 35–52, 2000.

[NW97] J. C. Niemeyer and S. E. Woosley. The Thermonuclear Explosion of Chandrasekhar Mass White Dwarfs. *ApJ*, 475:740–+, February 1997.

[OB68] J. P. Ostriker and P. Bodenheimer. Rapidly Rotating Stars. II. Massive White Dwarfs. *ApJ*, 151:1089–+, March 1968.

[OS88] S. Osher and J. A. Sethian. Fronts propagating with curvature dependent speed: Algorithms based in hamilton-jacobi formulations. *Journal of Computational Physics*, 79:12–49, 1988.

[Pac91] B. Paczynski. A polytropic model of an accretion disk, a boundary layer, and a star. *ApJ*, 370:597–603, April 1991.

[PAG^{+}99] S. Perlmutter, G. Aldering, G. Goldhaber, R. A. Knop, P. Nugent, P. G. Castro, S. Deustua, S. Fabbro, A. Goobar, D. E. Groom, I. M. Hook, A. G. Kim, M. Y. Kim, J. C. Lee, N. J. Nunes, R. Pain, C. R. Pennypacker, R. Quimby, C. Lidman, R. S. Ellis, M. Irwin, R. G. McMahon, P. Ruiz-Lapuente, N. Walton, B. Schaefer, B. J. Boyle, A. V. Filippenko, T. Matheson, A. S. Fruchter, N. Panagia, H. J. M. Newberg, W. J. Couch, and The Supernova Cosmology Project. Measurements of Omega and Lambda from 42 High-Redshift Supernovae. *ApJ*, 517:565–586, jun 1999.

[Pet99] N. Peters. The turbulent burning velocity for large-scale and small-scale turbulence. *J. Fluid Mech.*, 384:107–132, 1999.

[PGG^{+}97] S. Perlmutter, S. Gabi, G. Goldhaber, A. Goobar, D. E. Groom, I. M. Hook, A. G. Kim, M. Y. Kim, J. C. Lee, R. Pain, C. R. Pennypacker, I. A. Small, R. S. Ellis, R. G. McMahon, B. J. Boyle, P. S. Bunclark, D. Carter, M. J. Irwin, K. Glazebrook, H. J. M. Newberg, A. V. Filippenko, T. Matheson, M. Dopita, W. J. Couch, and The Supernova Cosmology Project. Measurements of the Cosmological Parameters Omega and Lambda from the First Seven Supernovae at $z \geq 0.35$. *ApJ*, 483:565–+, jul 1997.

[Phi93] M. M. Phillips. The absolute magnitudes of Type Ia supernovae. *ApJ*, 413:L105–L108, August 1993.

[PN91] R. Popham and R. Narayan. Does accretion cease when a star approaches breakup? *ApJ*, 370:604–614, April 1991.

[Poc94] A. Pocheau. Scale invariance in turbulent front propagation. *Phys. Rev. E*, 49:1109–1122, 1994.

[Psk77] I. P. Pskovskii. Light curves, color curves, and expansion velocity of type I supernovae as functions of the rate of brightness decline. *Soviet Astronomy*, 21:675–682, December 1977.

[PTVF03] W. H. Press, S. A. Teukolsky, W. T. Vetterling, and B. P. Flannery. *Numerical Recipes in Fortran 77: The Art of Scientific Computing.* Cambridge University Press, Cambridge, UK, 2nd edition, 2003.

[QHK$^+$06] R. Quimby, P. Höflich, S. J. Kannappan, E. Rykoff, W. Rujopakarn, C. W. Akerlof, C. L. Gerardy, and J. C. Wheeler. SN 2005cg: Explosion Physics and Circumstellar Interaction of a Normal Type Ia Supernova in a Low-Luminosity Host. *ApJ*, 636:400–405, January 2006.

[RCM$^+$04] P. Ruiz-Lapuente, F. Comeron, J. Méndez, R. Canal, S. J. Smartt, A. V. Filippenko, R. L. Kurucz, R. Chornock, R. J. Foley, V. Stanishev, and R. Ibata. The binary progenitor of Tycho Brahe's 1572 supernova. *Nature*, 431:1069–1072, October 2004.

[Rea84] K. I. Read. Experimental investigation of turbulent mixing by Rayleigh-Taylor instability. *Physica D Nonlinear Phenomena*, 12:45–58, July 1984.

[Rei01] M. Reinecke. *Modeling and simulation of turbulent combustion in Type Ia supernovae.* PhD thesis, MPA Garching, June 2001.

[RFC$^+$98] A. G. Riess, A. V. Filippenko, P. Challis, A. Clocchiatti, A. Diercks, P. M. Garnavich, R. L. Gilliland, C. J. Hogan, S. Jha, R. P. Kirshner, B. Leibundgut, M. M. Phillips, D. Reiss, B. P. Schmidt, R. A. Schommer, R. C. Smith, J. Spyromilio, C. Stubbs, N. B. Suntzeff, and J. Tonry. Observational Evidence from Supernovae for an Accelerating Universe and a Cosmological Constant. *AJ*, 116:1009–1038, September 1998.

[RFL$^+$99] A. G. Riess, A. V. Filippenko, W. Li, R. R. Treffers, B. P. Schmidt, Y. Qiu, J. Hu, M. Armstrong, C. Faranda, E. Thouvenot, and C. Buil. The Rise Time of Nearby Type Ia Supernovae. *AJ*, 118:2675–2688, December 1999.

[RGH05] F. K. Röpke, M. Gieseler, and W. Hillebrandt. Type Ia Supernova Diversity from 3-dimensional Models. In M. Turatto, S. Benetti, L. Zampieri, and W. Shea, editors, *ASP Conf. Ser. 342: 1604-2004: Supernovae as Cosmological Lighthouses*, pages 397–+, December 2005.

[RH04] F. K. Röpke and W. Hillebrandt. The case against the progenitor's carbon-to-oxygen ratio as a source of peak luminosity variations in type Ia supernovae. *A&A*, 420:L1–L4, June 2004.

[RH05a] F. K. Röpke and W. Hillebrandt. Full-star type Ia supernova explosion models. *A&A*, 431:635–645, February 2005.

[RH05b] F. K. Röpke and W. Hillebrandt. The distributed burning regime in type Ia supernova models. *A&A*, 429:L29–L32, January 2005.

[RHN$^+$99] M. Reinecke, W. Hillebrandt, J. C. Niemeyer, R. Klein, and A. Gröbl. A new model for deflagration fronts in reactive fluids. *A&A*, 347:724–733, jul 1999.

[RHN02a] M. Reinecke, W. Hillebrandt, and J. C. Niemeyer. Refined numerical models for multidimensional type Ia supernova simulations. *A&A*, 386:936–943, May 2002.

[RHN02b] M. Reinecke, W. Hillebrandt, and J. C. Niemeyer. Three-dimensional simulations of type Ia supernovae. *A&A*, 391:1167–1172, September 2002.

[RHNW06] F. K. Röpke, W. Hillebrandt, J. C. Niemeyer, and S. E. Woosley. Multi-spot ignition in type Ia supernova models. *A&A*, 448:1–14, March 2006.

[Ric22] L. F. Richardson. *Weather prediction by numerical process.* Cambridge University Press, Cambridge, 1922.

[RS95] F. A. Rasio and S. L. Shapiro. Hydrodynamics of binary coalescence. 2: Polytropes with gamma = 5/3. *ApJ*, 438:887–903, January 1995.

[RST$^+$04] A. G. Riess, L. Strolger, J. Tonry, S. Casertano, H. C. Ferguson, B. Mobasher, P. Challis, A. V. Filippenko, S. Jha, W. Li, R. Chornock, R. P. Kirshner, B. Leibundgut, M. Dickinson, M. Livio, M. Giavalisco, C. C. Steidel, T. Benítez, and Z. Tsvetanov. Type Ia Supernova Discoveries at $z > 1$ from the Hubble Space Telescope: Evidence for Past Deceleration and Constraints on Dark Energy Evolution. *ApJ*, 607:665–687, June 2004.

[Rö03] F. K. Röpke. *On the Stability of Thermonuclear Flames in Type Ia supernova Explosions.* PhD thesis, MPA Garching, July 2003.

[Rö05] F. K. Röpke. Following multi-dimensional type Ia supernova explosion models to homologous expansion. *A&A*, 432:969–983, March 2005.

[SB05] E. Scannapieco and L. Bildsten. The Type Ia Supernova Rate. *ApJ*, 629:L85–L88, August 2005.

[Sch01] F. Schmitz. *Vorlesungsskript: Einführung in die Hydrodynamik*. Julius-Maximilians-Universität Würzburg, Institut für Theoretische Physik und Astrophysik, 2001.

[Sch04] W. Schmidt. *Turbulent Thermonuclear Combusiton in Degenerate Stars*. PhD thesis, MPA Garching, February 2004.

[Sha18] H. Shapley. Studies based on the colors and magnitudes in stellar clusters. VIII. The luminosities and distances of 139 Cepheid variables. *ApJ*, 48:279–294, December 1918.

[Sha99] G. J. Sharpe. The structure of steady detonation waves in Type Ia supernovae: pathological detonations in C-O cores. *MNRAS*, 310:1039–1052, dec 1999.

[Shc43] K. I. Shchelkin. *J. Tech. Phys.*, 13:520, 1943.

[SLP$^+$06] M. Sullivan, D. Le Borgne, C. J. Pritchet, A. Hodsman, J. D. Neill, D. A Howell, R. G Carlberg, P. Astier, E. Aubourg, D. Balam, S. Basa, A. Conley, S. Fabbro, D. Fouchez, J. Guy, I. Hook, R. Pain, N. Palanque-Delabrouille, K. Perrett, N. Regnault, J. Rich, R. Taillet, S. Baumont, J. Bronder, R. S. Ellis, M. Filiol, V. Lusset, S. Perlmutter, P. Ripoche, and C. Tao. Rates and properties of type Ia supernovae as a function of mass and star-formation in their host galaxies. *ArXiv Astrophysics e-prints*, May 2006.

[SMBH05] M. Stehle, P. A. Mazzali, S. Benetti, and W. Hillebrandt. Abundance stratification in Type Ia supernovae - I. The case of SN 2002bo. *MNRAS*, 360:1231–1243, July 2005.

[SMH92] M. Steinmetz, E. Müller, and W. Hillebrandt. Carbon Detonations in Rapidly Rotating White Dwarfs. *A&A*, 254:177–+, February 1992.

[SN85] H. Saio and K. Nomoto. Evolution of a merging pair of C + O white dwarfs to form a single neutron star. *A&A*, 150:L21–L23, September 1985.

[SN98] H. Saio and K. Nomoto. Inward Propagation of Nuclear-burning Shells in Merging C-O and He White Dwarfs. *ApJ*, 500:388–+, June 1998.

[SN04] H. Saio and K. Nomoto. Off-Center Carbon Ignition in Rapidly Rotating, Accreting Carbon-Oxygen White Dwarfs. *ApJ*, 615:444–449, November 2004.

[SN06] W. Schmidt and J. C. Niemeyer. Thermonuclear supernova simulations with stochastic ignition. *A&A*, 446:627–633, February 2006.

[SNH06] W. Schmidt, J. C. Niemeyer, and W. Hillebrandt. A localised subgrid scale model for fluid dynamical simulations in astrophysics. I. Theory and numerical tests. *A&A*, 450:265–281, April 2006.

[SNHR06] W. Schmidt, J. C. Niemeyer, W. Hillebrandt, and F. K. Röpke. A localised subgrid scale model for fluid dynamical simulations in astrophysics. II. Application to type Ia supernovae. *A&A*, 450:283–294, April 2006.

[SST$^+$99] A. Saha, A. Sandage, G. A. Tammann, L. Labhardt, F. D. Macchetto, and N. Panagia. Cepheid Calibration of the Peak Brightness of Type Ia Supernovae. IX. SN 1989B in NGC 3627. *ApJ*, 522:802–838, September 1999.

[ST83] S. L. Shapiro and S. A. Teukolsky. *Black holes, white dwarfs, and neutron stars: The physics of compact objects.* Research supported by the National Science Foundation. New York, Wiley-Interscience, 1983, 663 p., 1983.

[Ste90] M. Steinmetz. Kohlenstoff-Detonationen in differentiell rotierenden, stark deformierten Weißen Zwergen. Diplomarbeit, Technische Universität München, October 1990.

[SVP$^+$03] D. N. Spergel, L. Verde, H. V. Peiris, E. Komatsu, M. R. Nolta, C. L. Bennett, M. Halpern, G. Hinshaw, N. Jarosik, A. Kogut, M. Limon, S. S. Meyer, L. Page, G. S. Tucker, J. L. Weiland, E. Wollack, and E. L. Wright. First-Year Wilkinson Microwave Anisotropy Probe (WMAP) Observations: Determination of Cosmological Parameters. *ApJS*, 148:175–194, September 2003.

[SY05] J.-E. Solheim and L. R. Yungelson. The White Dwarfs in AM CVn Systems – Candidates for SN Ia? In D. Koester and S. Moehler, editors, *ASP Conf. Ser. 334: 14th European Workshop on White Dwarfs*, pages 387–+, 2005.

[TAC67] J. W. Truran, W. D. Arnett, and A. G. W. Cameron. Nucleosynthesis in supernova shock waves. *Canadian Journal of Physics*, 45:2315–+, 1967.

[Tas78] J.-L. Tassoul. *Theory of rotating stars.* Princeton University Press, Princeton, New Jersey, 1978.

[TBB$^+$04] R. C. Thomas, D. Branch, E. Baron, K. Nomoto, W. Li, and A. V. Filippenko. On the Geometry of the High-Velocity Ejecta of the Peculiar Type Ia Supernova 2000cx. *ApJ*, 601:1019–1030, February 2004.

[THR05] C. Travaglio, W. Hillebrandt, and M. Reinecke. Metallicity effect in multi-dimensional SNIa nucleosynthesis. *A&A*, 443:1007–1011, December 2005.

[THRT04] C. Travaglio, W. Hillebrandt, M. Reinecke, and F.-K. Thielemann. Nucleosynthesis in multi-dimensional SN Ia explosions. *A&A*, 425:1029–1040, October 2004.

[TMMN06] M. Tanaka, P. A. Mazzali, K. Maeda, and K. Nomoto. 3D Models for High Velocity Features in Type Ia Supernovae. *ArXiv Astrophysics e-prints*, March 2006.

[TS00] F. X. Timmes and F. D. Swesty. The Accuracy, Consistency, and Speed of an Electron-Positron Equation of State Based on Table Interpolation of the Helmholtz Free Energy. *ApJS*, 126:501–516, February 2000.

[TW92] F. X. Timmes and S. E. Woosley. The conductive propagation of nuclear flames. I - Degenerate C + O and O + NE + MG white dwarfs. *ApJ*, 396:649–667, September 1992.

[UB99] A. Unsöld and B. Baschek. *Der neue Kosmos*. Springer-Verlag, 1999.

[UNYW99] H. Umeda, K. Nomoto, H. Yamaoka, and S. Wanajo. Evolution of 3-9 $M_\odot$ Stars for Z=0.001-0.03 and Metallicity Effects on Type Ia Supernovae. *ApJ*, 513:861–868, March 1999.

[vLF05] S. van den Bergh, W. Li, and A. V. Filippenko. Classifications of the Host Galaxies of Supernovae, Set III. *PASP*, 117:773–782, August 2005.

[Wan05] L. Wang. Dust around Type Ia Supernovae. *ApJ*, 635:L33–L36, December 2005.

[WB06] R. Waldman and Z. Barkat. The Evolution of Low Mass Helium Stars towards Supernova Type I Explosion. *ArXiv Astrophysics e-prints*, May 2006.

[WBH$^+$03] L. Wang, D. Baade, P. Höflich, A. Khokhlov, J. C. Wheeler, D. Kasen, P. E. Nugent, S. Perlmutter, C. Fransson, and P. Lundqvist. Spectropolarimetry of SN 2001el in NGC 1448: Asphericity of a Normal Type Ia Supernova. *ApJ*, 591:1110–1128, July 2003.

[WBH+04a] L. Wang, D. Baade, P. Höflich, J. C. Wheeler, K. Kawabata, A. Khokhlov, K. Nomoto, and F. Patat. Pre-Maximum Spectropolarimetry of the Type Ia SN 2004dt. *ArXiv Astrophysics e-prints*, September 2004.

[WBH+04b] L. Wang, D. Baade, P. Höflich, J. C. Wheeler, K. Kawabata, and K. Nomoto. On the Hydrogen Emission from the Type Ia Supernova SN 2002ic. *ApJ*, 604:L53–L56, March 2004.

[Web84] R. F. Webbink. Double white dwarfs as progenitors of R Coronae Borealis stars and Type I supernovae. *ApJ*, 277:355–360, February 1984.

[Wei68] V. Weidemann. White Dwarfs. *ARA&A*, 6:351–+, 1968.

[Whi98] M. White. Complementary Measures of the Mass Density and Cosmological Constant. *ApJ*, 506:495–501, October 1998.

[Woo90] S. E. Woosley. Type I Supernovae: Carbon Deflagration and Detonation. In *Supernovae*, pages 182–212. Petsckek A. G., ed., Springer Verlag, Berlin, 1990.

[WS06] W. M. Wood-Vasey and J. L. Sokoloski. Novae as a Mechanism for Producing Cavities around the Progenitors of SN 2002ic and Other SNe Ia. *ArXiv Astrophysics e-prints*, May 2006.

[WSC+06] L. Wang, M. Strovink, A. Conley, G. Goldhaber, M. Kowalski, S. Perlmutter, and J. Siegrist. Nonlinear Decline-Rate Dependence and Intrinsic Variation of Type Ia Supernova Luminosities. *ApJ*, 641:50–69, April 2006.

[WTW86] S. E. Woosley, R. E. Taam, and T. A. Weaver. Models for Type I supernova. I - Detonations in white dwarfs. *ApJ*, 301:601–623, February 1986.

[WW86] S. E. Woosley and T. A. Weaver. The physics of supernova explosions. *ARA&A*, 24:205–253, 1986.

[WW94] S. E. Woosley and T. A. Weaver. Supernovae. In S. A. Bludman, R. Mochkovitch, and J. Zinn-Justin, editors, *Les Houches Session LIV*, North-Holland, 1994.

[WW04] S. Wunsch and S. E. Woosley. Convection and Off-Center Ignition in Type Ia Supernovae. *ApJ*, 616:1102–1108, December 2004.

[WWH97] L. Wang, J. C. Wheeler, and P. Höflich. Polarimetry of the Type Ia Supernova SN 1996X. *ApJ*, 476:L27+, February 1997.

[WWK04] S. E. Woosley, S. Wunsch, and M. Kuhlen. Carbon Ignition in Type Ia Supernovae: An Analytic Model. *ApJ*, 607:921–930, June 2004.

[YL03] S.-C. Yoon and N. Langer. The first binary star evolution model producing a Chandrasekhar mass white dwarf. *A&A*, 412:L53–L56, December 2003.

[YL04] S.-C. Yoon and N. Langer. Presupernova evolution of accreting white dwarfs with rotation. *A&A*, 419:623–644, May 2004.

[YL05] S.-C. Yoon and N. Langer. On the evolution of rapidly rotating massive white dwarfs towards supernovae or collapses. *A&A*, 435:967–985, June 2005.

[YLS04] S.-C. Yoon, N. Langer, and S. Scheithauer. Effects of rotation on the helium burning shell source in accreting white dwarfs. *A&A*, 425:217–228, October 2004.

[ZWB$^+$05] M. Zingale, S. E. Woosley, J. B. Bell, M. S. Day, and C. A. Rendleman. The Physics of Flames in Type Ia Supernovae. *Journal of Physics Conference Series*, 16:405, 2005.

[ZWR$^+$05] M. Zingale, S. E. Woosley, C. A. Rendleman, M. S. Day, and J. B. Bell. Three-dimensional Numerical Simulations of Rayleigh-Taylor Unstable Flames in Type Ia Supernovae. *ApJ*, 632:1021–1034, October 2005.

Acknowledgment

I thank my advisor Prof. Dr. Jens Niemeyer for offering me the opportunity to investigate the present challenging topic in numerical astrophysics. His supervision allowed me to pursue various ideas, and at the same time prevented me from getting lost in details.

The discussions with Prof. Dr. Friedrich Schmitz have always been enlightening. He offered insights into the theory of rotating stars and was a contact person regarding the modernisation of numerical codes.

Dr. Harald Dimmelmeier assisted me in the effects of general relativity on the rotating stellar models. Discussions with Dr. Luigi Iapichino about the SN Ia research in general and the ignition process in detail complemented the theoretical background. Dr. Ewald Müller provided his program for the generation of rotating stars. The structuring of the hydrodynamics code by Dr. Martin Reinecke allowed for an efficient program. Dr. Friedrich Röpke arranged the postprocessing of the detonation data and made his hybrid grid implementation available. Dr. Wolfram Schmidt provided the localised subgrid model and the stochastic ignition routine. Dr. Sung-Chul Yoon was available for questions concerning the WD rotation and supplied a table for the temperature profile of rotators. Furthermore, discussions with Dominik Elsässer and Markus Meyer about astronomy have been valuable. I thank all these persons for their helpful suggestions.

Special thanks go to my roommate Andreas Maier, not only because of the friendly atmosphere in our office. Discussions with him yielded additional points of view and inspired me to consider new aspects. In his position as a system administrator he further guaranteed stable operation of the local machines, which is a premise for uninterrupted work. Andreas Vetter facilitated a frictionless utilisation of the CIP-Pool machines on which most of the calculations were performed.

Dr. Charles Becker critically read the thesis.

I appreciate my parents' support during the entire duration of my study, which was the fundament for a life and work without financial worries. My girlfriend Katharina not only did a detailed check of the manuscript but also lightened the work load among other things in stressful times.